

Designing a Robotic Port System for Laparo-Endoscopic Single-site Surgery

Von der Fakultät für Maschinenbau
der Gottfried Wilhelm Leibniz Universität Hannover

zur Erlangung des akademischen Grades
Doktor-Ingenieur

genehmigte Dissertation

von

Ernar Amanov

2019

1. Referentin: Prof. Dr.-Ing. Jessica Burgner-Kahrs
2. Referentin: Prof. Dr.-Ing. Annika Raatz
Gutachter: PD Dr.-Med. Florian Imkamp

Tag der Promotion: 14.10.2019

The acknowledgement is probably always written at the end, when everything else is already done. This moment lets me go back several years and review the way to today. When I came to Germany as a teenager, I could hardly imagine sitting here and submitting my thesis. Many important decisions have determined the direction and I have met many great people along the way. At this point I would like to thank my family, who taught me early that education is very important and has always supported and challenged me along the way. I would like to thank all the people I have made friends with along the way and who have always shaped me. I thank my great colleagues, for the fun time and encouragement in difficult times. We were colleagues, but today we are friends! I thank Jessica for her dedication, motivation and supervising over the last 6 years! I thank Florian for the great cooperation, great exchange, and the review of my work! I thank Professor Raatz for acting as co-examiner! And of course I thank my partner, Josie, who has supported, encouraged and endured me over the years!

Current research and development in the field of surgical interventions aim to reduce the invasiveness by using few incisions or natural orifices in the body to access the surgical site. Considering surgeries in the abdominal cavity, the Laparo-Endoscopic Single-site Surgery (LESS) can be performed through a single incision in the navel, reducing blood loss, post-operative trauma, and improving the cosmetic outcome. However, LESS results in less intuitive instrument control, impaired ergonomic, loss of depth and haptic perception, and restriction of instrument positioning by a single incision. Robot-assisted surgery addresses these shortcomings, by introducing highly articulated, flexible robotic instruments, ergonomic control consoles with 3D visualization, and intuitive instrument control algorithms. The flexible robotic instruments are usually introduced into the abdomen via a rigid straight port, such that the positioning of the tools and therefore the accessibility of anatomical structures is still constrained by the incision location. To address this limitation, articulated ports for LESS are proposed by recent research works. However, they focus on only a few aspects, which are relevant to the surgery, such that a design considering all requirements for LESS has not been proposed yet. This partially originates in the lack of anatomical data of specific applications. Further, no general design guidelines exist and only a few evaluation metrics are proposed. To target these challenges, this thesis focuses on the design of an articulated robotic port for LESS partial nephrectomy. A novel approach is introduced, acquiring the available abdominal workspace, integrated into the surgical workflow. Based on several generated patient datasets and developed metrics, design parameter optimization is conducted. Analyzing the surgical procedure, a comprehensive requirement list is established and applied to design a robotic system, proposing a tendon-driven continuum robot as the articulated port structure. Especially, the aspects of stiffening and sterile design are addressed. In various experimental evaluations, the reachability, the stiffness, and the overall design are evaluated. The findings identify layer jamming as the superior stiffening method. Further, the articulated port is proven to enhance the accessibility of anatomical structures and offer a patient and incision location independent design.

Keywords: minimally-invasive surgery, continuum robots design, partial nephrectomy

Die aktuelle Forschung und Entwicklung auf dem Gebiet der chirurgischen Eingriffe zielt darauf ab, die Invasivität zu reduzieren, indem nur wenige Schnitte oder gar natürliche Öffnungen im Körper für den Zugang zur Operationsstelle verwendet werden. Bei Operationen in der Bauchhöhle kann die sogenannte Laparo-Endoscopic Single-site Surgery (LESS) durch nur einen einzigen Schnitt im Nabel durchgeführt werden, wodurch Blutverlust, und postoperative Traumata reduziert und das kosmetische Ergebnis verbessert werden.

Andererseits führt LESS zu einer weniger intuitiven Instrumentenbedienung, zu beeinträchtigter Ergonomie, zum Verlust von Tiefen, haptischer Wahrnehmung, sowie zur Einschränkung der Instrumentenpositionierung durch einen einzigen Schnitt. Die robotergestützte Chirurgie behebt diese Mängel durch die Einführung von hochartikulierten, flexiblen Roboterinstrumenten, ergonomischen Bedienpulten mit 3D-Visualisierung und intuitiven Instrumentenkontrollalgorithmen. Die flexiblen Roboterinstrumente werden in der Regel über eine starre gerade Zuführung in den Bauch inseriert, so dass die Positionierung der Werkzeuge und damit die Zugänglichkeit der anatomischen Strukturen durch die Inzisionsstelle noch eingeschränkt sind. Um dieser Einschränkung entgegenzuwirken, werden in jüngeren Forschungsarbeiten artikulierbare Ports für LESS vorgeschlagen. Sie konzentrieren sich jedoch auf wenige Aspekte, die für die Operation relevant sind, so dass ein Design unter Berücksichtigung aller Anforderungen an LESS noch nicht vorgeschlagen wurde. Dies liegt zum Teil daran, dass es an anatomischen Daten für bestimmte Anwendungen fehlt. Andererseits gibt es keine allgemeinen Gestaltungsrichtlinien und es werden nur wenige Bewertungskriterien vorgeschlagen. Um diese Herausforderungen zu bewältigen, konzentriert sich diese Arbeit auf das Design eines artikulierbaren Roboterports für die LESS partielle Nephrektomie. Ein neuartiger Ansatz zur Erfassung des verfügbaren abdominalen Arbeitsbereichs wird vorgestellt, welcher in den chirurgischen Arbeitsablauf integriert ist. Basierend auf mehreren generierten Patientendatensätzen und entwickelten Metriken wird eine Designparameteroptimierung durchgeführt. Bei der Analyse des chirurgischen Verfahrens wird eine vollständige Anforderungsliste erstellt und für den Entwurf eines Robotersystems verwendet, in dem ein seilzug-gesteuerter Kontinuumsroboter als artikulierbare Portstruktur vorgeschlagen wird. Insbesondere werden die Aspekte der Versteifung und des sterilen Designs behandelt.

In verschiedenen experimentellen Evaluierungen werden die Erreichbarkeit, die Steifigkeit und das Gesamtkonzept bewertet. Die Ergebnisse identifizieren die schichtweise Verklemmung als die überlegene Versteifungsmethode. Darüber hinaus hat sich gezeigt, dass der artikulierbare Port die Zugänglichkeit verbessert und ein patienten- und einschnitt unabhängiges Design bietet.

Schlagwörter: minimal-invasive Chirurgie, Kontinuumsroboter-Design, partielle Nephrectomy

CONTENTS

Acronyms	xiii
I INTRODUCTION AND STATE OF THE ART	1
1 MEDICAL MOTIVATION	3
1.1 Kidney Anatomy Fundamentals	3
1.2 Kidney Cancer	4
1.3 Partial Nephrectomy	5
1.4 Partial Nephrectomy Access Approach	7
1.5 Problem Statement	8
2 STATE OF THE ART	13
2.1 Manual Commercial Tools	13
2.1.1 Manual Devices Dilemma	15
2.2 Robotic LESS Systems	16
2.2.1 Elastic Port	17
2.2.2 Rigid Port	18
2.2.3 Articulated Port	21
2.3 Miniature Platform	23
2.4 Conclusion	24
3 CHALLENGES AND CONTRIBUTION	29
3.1 Contributions	31
II CONSTRAINTS AND REQUIREMENTS	33
4 ANATOMICAL CONSTRAINTS	35
4.1 Definitions	35
4.1.1 Abdominal Space	36
4.1.2 Region of Interest	36
4.1.3 Incision Location	36
4.2 Acquisition	37
4.2.1 Measurement Workflow	38
4.2.2 Post-Processing	39
4.3 Results	39
5 FORCE CONSTRAINTS	43
5.1 Task Definitions	43
5.1.1 Tearing Loading Case	43
5.1.2 Spreading Loading Case	44
5.1.3 Lifting and Partial Lifting Loading Case	44
5.1.4 Pulling Loading Case	45
5.1.5 Suturing Loading Case	45
5.2 Acquisition	45
5.3 Results	46

5.3.1	Tearing	46
5.3.2	Spreading	47
5.3.3	Partial Lifting	47
5.4	Conclusion	47
III	ROBOT SYSTEM DESIGN	49
6	ROBOTIC SYSTEM VISION	51
6.1	Envisioned Surgical Workflow	51
6.2	Overall Design	52
6.3	Sterility Concept	54
6.4	Requirements summary	55
7	STIFFENING METHOD	57
7.1	Tendon Tensioning Stiffening	57
7.2	Friction Based Stiffening	58
7.3	Fluidic Stiffening	58
7.4	Fluidic Shape Locking	58
7.5	Jamming Stiffening	59
7.6	Thermo-Active Stiffening	60
7.7	Rheological Stiffening	61
7.8	Shape Memory Alloy (SMA)	61
7.9	Electroactive Polymers (EAP)	62
7.10	Stiffening Method Selection	62
7.11	Conclusion	64
8	ROBOTIC SYSTEM DESIGN	67
8.1	Articulated Port Design Approaches	67
8.1.1	Tendon Routing	68
8.1.2	Backbone Design	69
8.2	Working Channel Design	70
8.2.1	Jamming Method Integration	70
8.3	Tendon Displacement	71
8.4	Manipulator Design Decision	73
8.5	Coupling Mechanisms Design	74
8.5.1	Magnetic Coupling	74
8.5.2	Friction Coupling	75
8.5.3	Shape-Locking Coupling	75
8.5.4	Coupling Mechanism Decision	75
8.6	Actuation Unit Design	77
8.7	Translational DoF Approaches	77
8.7.1	Translational DoF Design Decision	78
9	DESIGN PARAMETERIZATION	79
9.1	Parameter Definition and Differentiation	79
9.2	Kinematic Modeling: Constant Curvature Approach	81
9.2.1	Constant Curvature Approach: General Idea	82
9.2.2	Robot Dependent Mapping	82
9.2.3	Robot Independent Mapping	84
9.2.4	Several Segments	85

9.2.5	Translational Degree of Freedom	85
9.3	Parameter Optimization	86
9.3.1	Input	87
9.3.2	Optimization	88
9.3.3	Output	91
9.4	Optimization Execution and Results	91
9.5	Conclusion	94
IV	EVALUATIONS	97
10	REACHABILITY	99
10.1	Reachability Evaluation Prototype	99
10.1.1	Articulated Port	99
10.1.2	Actuation Unit	100
10.1.3	Translation Degree of Freedom	101
10.1.4	Phantom Design	101
10.2	Evaluation Execution	103
10.3	Results	104
10.4	Discussion	104
11	STIFFNESS	107
11.1	Experimental Test Bench	107
11.2	Force/Torque Sensor Data Processing	109
11.3	Torsional Stiffness Increase by Structure	111
11.3.1	Evaluation Set Up	112
11.3.2	Results	112
11.4	Jamming Stiffening	113
11.4.1	Layer Jamming - Tendon Tension Stiffening Prototype	114
11.4.2	Layer Jamming - Granular Jamming Prototype	115
11.4.3	Pure Layer Jamming Evaluation	117
11.4.4	Layer Jamming with Tendon Tension Stiffening Evaluation	119
11.4.5	Layer and Granular Jamming Evaluation	121
11.5	Discussion	123
12	STABILITY	129
12.1	Experimental Set Up	129
12.2	Data Processing	130
12.3	Results	130
12.4	Discussion	131
13	STERILE PROTOTYPE FUNCTIONALITY	133
13.1	Manipulator Prototype	133
13.2	Actuation Unit	134
13.3	Coupling Flow Evaluation	135
13.4	Actuation Evaluation	136
13.5	Discussion	137
14	EVALUATION CONCLUSION	139
V	CONCLUSION	141
15	CONTRIBUTION SUMMARY	143

16 OUTLOOK	145
BIBLIOGRAPHY	147
VI APPENDIX	157
A ANATOMICAL ABDOMINAL SPACES	159
B DESIGN OPTIMIZATION RESULTS	161
C DETAILED PROTOTYPE PARAMETERS	167
D EVALUATION RESULTS	169
D.1 Reachability Results	169
D.2 Stability Results	171
E REPRINT PERMISSIONS	173
CURRICULUM VITAE	174
OWN PUBLICATIONS	177
SUPERVISED STUDENT THESES	179

AS	Abdominal Space
ATPP	Acrylic-based Thermoplastic Polymer
CT	Computed Tomography
DoF	Degree of Freedom
DC	Direct Current
EAP	Electroactive Polymer
ERF	Electro-Rheological Fluid
FDA	Food and Drug Administration
IL	Incision Location
LESS	Laparo-Endoscopic Single-site Surgery
LMPA	Low Melting Point Alloy
LMPP	Low Melting Point Polymer
MRF	Magneto-Rheological Fluid
NOTES	Natural Orifices Transluminal Endoscopic Surgery
OD	Outer Diameter
OR	Operation Room
PCL	Polycaprolactone
PID	Proportional-Integral-Derivative
PLA	Poly lactide
RCC	Renal Cell Carcinoma
R-LESS	Robotic Laparo-Endoscopic Single-site Surgery
RoI	Region of Interest
SMA	Shape Memory Alloy
TDCR	Tendon-Driven Continuum Robot
TP	Target Point
UHMWP	Ultra-High-Molecular-Weight Polyethylene

Part I

INTRODUCTION AND STATE OF THE ART

This chapter provides fundamental knowledge about the selected application in this thesis. First, the kidney anatomy and function, possible sources of carcinogenic development, and its symptoms are described. Since the focus of this work is on minimally-invasive surgical treatment of kidney cancer, a summary of surgical procedures and techniques leads over to the description of applied instruments. In a concluding discussion, drawbacks of techniques and instrumentation are presented and desired solutions are stated.

1.1 KIDNEY ANATOMY FUNDAMENTALS

The kidneys are essential organs responsible for the waste, water, and salt management in mammals. This is necessary for preserving the electrolyte and water balance in the body tissue fluids. There are two kidneys located lateral¹ left and right to the spine as shown in Figure 1a. They are supplied by the renal vein (branch of the inferior vena cava) and renal artery (branch of the aorta), located medial to the kidneys. The kidneys excrete urine over the ureter running caudal². The kidneys are further located at the posterior³ abdominal wall behind the peritoneum (retroperitoneal) separated from the peritoneal cavity by the pararenal fat (Figure 1b). They are about 11-14 cm in length, 4-7 cm in width, and 4 cm thick and are encapsulated into a robust Gerota's fascia providing fixation and protection (Figure 1c).

¹ description of the relative anatomical location; located away from the mid line of the human body, the opposite is medial: toward the human body mid line

² description of the relative anatomical location; located toward the feet, the opposite is cranial: toward the head

³ description of the relative anatomical location; located toward the back, the opposite is anterior: toward the front

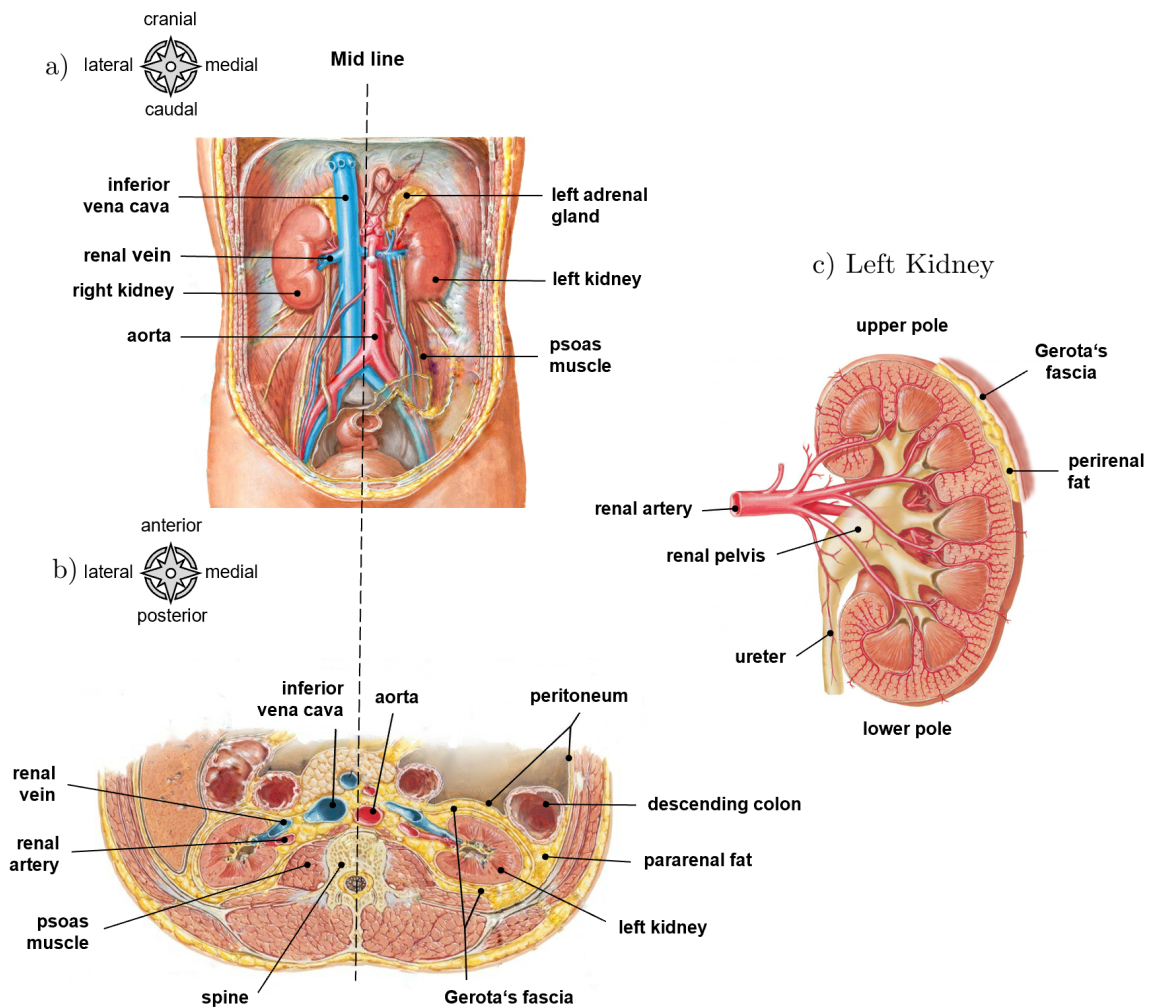


Figure 1: Kidney anatomy fundamentals: a) Location in the peritoneal cavity anterior view; b) Location in the peritoneal cavity caudal view; c) Left kidney cross section.

Reprinted from (Netter, 2019), ©2019, with kind permission from Elsevier.

1.2 KIDNEY CANCER

There exist different kinds of kidney cancer. Renal cell carcinoma is the most common type, accounting for about 85% of diagnoses, originating from within the kidney cells. Urothelial carcinoma accounts for approximately 10-15% and originates in the renal pelvis (Figure 1c). Rare kidney cancer types are Sarcoma, Wilms tumor (most common in children), and Lymphoma, according to American Society of Clinical Oncology. In this thesis, the Renal cell carcinoma (RCC) is considered since it is the most common kidney cancer type.

Various reasons can promote kidney cancer, such as genetic tendency (Linehan et al., 2009), adiposity, chronic kidney insufficiency, smoking, alcohol, or extensive exposure to e.g. X-rays (Cho et al., 2011). There are usually no symptoms in the early stages of renal cell carcinoma and they are diagnosed coincidentally during other examinations. Symptoms of renal cell carcinoma can be blood in the urine, low back pain, weight loss, absence of hunger, fever, a lump on side, belly or back, anemia (low number of red blood cells).

In 2016, 16 thousand of new kidney cancer cases were reported by the Association of Population Based Cancer Registries in Germany. This is equivalent to 3.6 % of all newly reported cancer cases. A study over 40 European countries by Ferlay et al., 2015 reports 115,200 new kidney cancer cases in 2012 with a mortality of 49,000. This statistic reveals kidney cancer as the 9th most common cancer type in Europe. The average age of diagnosed patients lies between 65 and 70 years for men and over 70 years for women. In the published statistic prognoses for kidney cancer by American Cancer Society, 73,820 adults will be diagnosed with kidney cancer in the USA in 2019, from which 14,770 are estimated to be lethal. The average diagnosis age is 65 years. This is the 6th most common cancer for men and the 8th most common cancer for women in the USA. Considering the demographic trends, new kidney cancer diagnoses are expected to rise in the future.

The cancer development is classified into four stages. In the first stage, the carcinogenic cells remain inside the kidney and do not exceed the size of 7 cm. Above this size, cancer enters the second stage, while remaining inside the kidney. When the carcinogenic cells spread to the surrounding veins but do not extend beyond Gerota's fascia, it is considered as stage III kidney cancer. If the Gerota's fascia is penetrated or the cells spread to other organs such as lymph, cancer has reached its last stage IV (Ljungberg, Albiges, et al., 2019). The most sufficient treatment is the surgical removal of carcinogenic cells. This can be done either in the removal of the whole organ (radical nephrectomy) or organ-preserving (partial nephrectomy) way. In the later only the tumor is resected. This approach has been shown beneficial, since the operated kidney partially maintains its renal functionality, supporting the healthy kidney (Mir et al., 2017). Partial nephrectomy is preferred for tumors in the early stages (I and II), and can be applied to stage III, if anatomically possible. Radical nephrectomy can be performed for stage II-IV (Ljungberg, Bensalah, et al., 2015). Which approach to choose should be decided for each case. Partial nephrectomy has been shown superior in terms of oncological and functional outcomes in extensive evaluations (Ljungberg, Bensalah, et al., 2015, Van Poppel et al., 2011). Therefore, partial nephrectomy is the actual golden standard for surgical kidney cancer treatment.

In this thesis, partial nephrectomy is considered. But, since the surgical procedure is similar for both approaches, the findings of this work are transferable to radical nephrectomy.

1.3 PARTIAL NEPHRECTOMY

Partial nephrectomy belongs to the extraluminal surgeries, which are performed outside a lumen. Surgeries in the abdominal or thoracic (chest) cavities are defined as extraluminal. Surgeries performed only through a natural orifice (lumen), such as gastrointestinal surgery through the esophagus or ureteroscopy⁴ are called intraluminal. A transluminal surgery approach foresees instrument deployment through a natural orifice followed by an internal incision trespassing the lumen.

Independent from the access approach to the surgical site, certain steps are performed during the partial nephrectomy as illustrated in Figure 2 on the example of the left kidney. After the access to the peritoneal cavity is established, in the first step, the descending colon has to be separated from the peritoneum around the kidney (Figure 2a-b). The colon is connected to the peritoneum by adhesions spread out the whole cavity. Second, the renal vein and artery

⁴ kidney stone removal with a flexible tool inserted through the bladder and the ureter.

need to be identified for later blood support interruption during tumor resection. To do so, the peritoneum is incised at the lower kidney pole first and then the major vessels (aorta and vena cava) are followed cranially to the renal pelvis (Figure 2c).

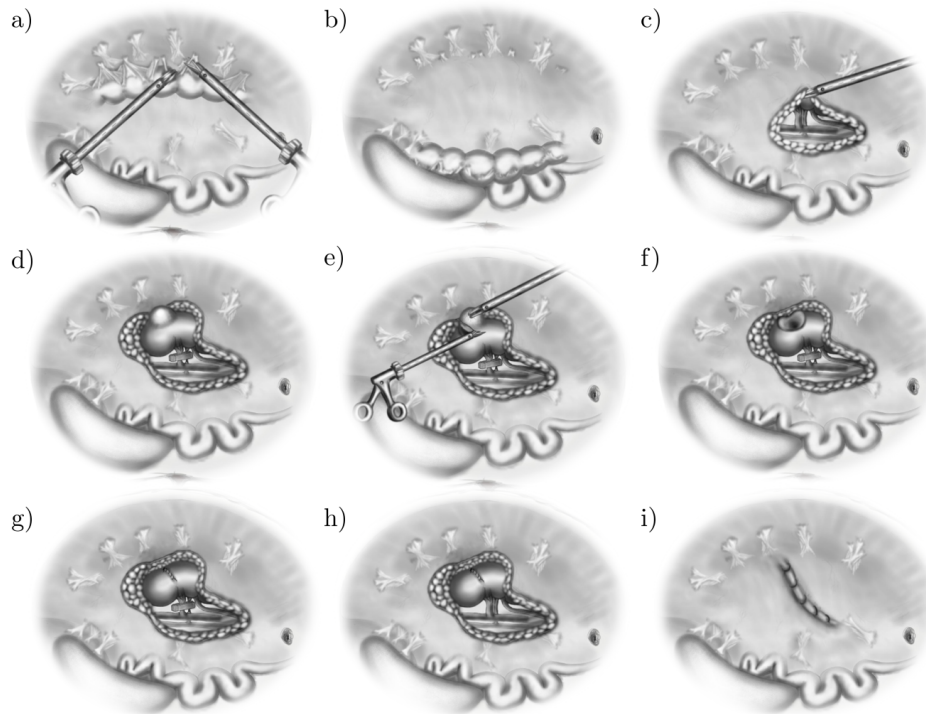


Figure 2: Partial nephrectomy surgical procedure: a) Dissecting the descending colon; b) Descending colon shifted medially after dissection; c) Renal artery and vein identification from lower kidney pole to the renal pelvis; d) Peritoneum removal around the tumor; e) Vessel clipping and tumor resection; f) After tumor resection; g) Wound suturing; h) Reestablishing the blood support; i) Peritoneum reconstruction.

The renal vessels sometimes exhibit branches involved in the blood circuit. It is important to find all branches. Subsequently, peritoneum around the tumor is incised to provide access to the tumor. Sometimes, the whole kidney is separated from the surrounding pararenal fat (kidney mobilization), to enable more sufficient access to the tumor. When clamping the renal artery, vein, and their branches (Figure 2d) to interrupt the blood flow (ischemia) and therefore to reduce blood loss during tumor resection, it is recommended to not clamp venous branches to permit drainage. Subsequently, the tumor is separated from healthy tissue (Figure 2e). Renal ischemia should not exceed 30 minutes to preserve renal function. Generally, partial nephrectomy is feasible without ischemia, but tumor resection might be impaired considerably due to intense perfusion and bleeding at the resected site. After the tumor is resected completely (Figure 2f), the resection site is coagulated⁵ and sutured (Figure 2g). After clip removal blood support can be reestablished (Figure 2h). Finally, the peritoneum is reconstructed for kidney anchoring and protection (Figure 2i). Further details on the surgical steps of partial nephrectomy can be found in Shields et al., 2017 and Rosenblatt et al., 2008.

⁵ blood changing from fluid to a gel (blood clotting): is performed during the surgery through denaturing the tissue by heat or chemical agents

1.4 PARTIAL NEPHRECTOMY ACCESS APPROACH

To enable the described surgical steps above, access to the surgical site has to be established. Generally, the patient is positioned on the contralateral side and is overstretched to expose the kidney as shown in Figure 3a-c. Thereby, the tumor-bearing kidney is located upright in the operating field. The initial standard approach was the open surgery, associated with a large incision in the abdominal wall (open laparotomy), such that the surgeons could work with their hands and standard instruments such as a scalpel or scissors (Figure 3a).

With the advance of imaging technology and novel surgical tool designs, a new, laparoscopic approach performed through several small incisions in the abdominal wall became feasible (Figure 3c). Comparison of open and laparoscopic surgeries studies showed reduced trauma, blood loss, risk of infection, and recovery time (Velanovich, 2000, Reifsnnyder et al., 2012). Laparoscopic access to the kidney can be performed in the retroperitoneal approach (access below the ribs on the kidney site), or the transperitoneal approach (from the anterior abdominal wall). In this thesis, the transperitoneal approach is considered since it provides more space in the abdomen (Hudgens et al., 2007). By default, there is no free space in the human abdomen. To provide space for tool manipulation, CO₂ is insufflated into the abdomen through one of the ports, which provides an extra interface as shown in (Figure 3b), thus creating a stable pressure of 15 mmHg during surgery.

Usually, three to four incisions are necessary for two instruments, one endoscope (thin shaft with an integrated light source and a camera), and one for irrigation or suction. The incisions are prepared with so-called ports, as rigid tubes fit into the incision tissue enabling instrument insertion and exchange without stressing the abdominal wall (Figure 3c). The ports also seal the abdomen preventing CO₂ leakage. The tools and the endoscope used for the laparoscopic surgery are rigid and straight and commonly have a diameter of 5-10 mm. Different instrument tips can be used, such as grippers, or scissors. Such procedures belong to the so-called minimally-invasive surgeries providing advantages for the patient. Hence, the multi-port laparoscopic approach became the golden standard for many indications in the abdominal space, such as cholecystectomy (gallbladder removal), prostatectomy (prostate removal), or nephrectomy.

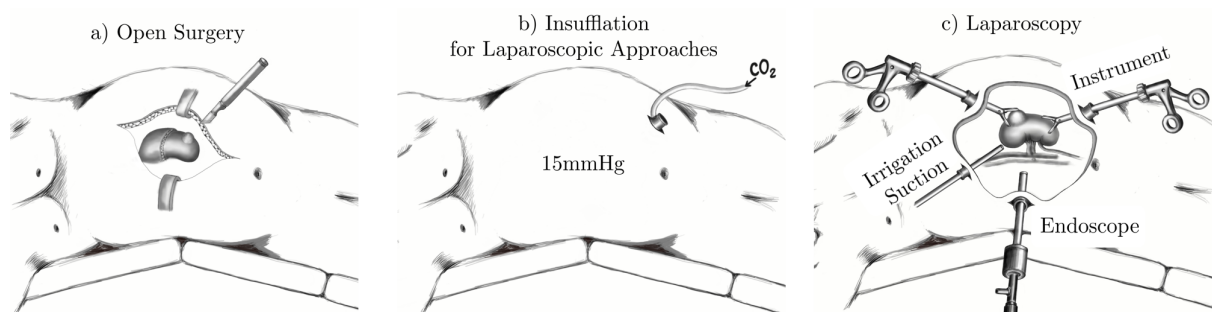


Figure 3: Surgery approaches for partial nephrectomy: a) Open laparotomy with a large single incision; b) Patient overstretched lateral mount after insufflation with a port for insufflation; c) Laparoscopic approach with two instruments, an endoscope, and irrigation/suction tube.

Besides the described laparoscopic procedure with multiple ports, a logical step towards reducing invasiveness is reducing the number of incisions. A so-called laparo-endoscopic single-site surgery (LESS) was proposed using only one incision (< 30 mm) with one port as shown

in Figure 4a. LESS is the natural evolution of minimally-invasive surgery. Studies were conducted to compare the conventional multi-port laparoscopy and LESS, of which some show no significant differences (Raman et al., 2009, Raybourn et al., 2010). However, Jeong et al., 2009 and Park et al., 2015 showed improvements in postoperative pain and superior cosmetic outcomes using LESS. Advantages for the clinics would encounter shorter hospital stays and fewer medications.

Further, specialized prebent tools are introduced to improve tissue manipulation. These tools can be deployed through an elastic port. They can be arranged parallelly or crossed as shown in Figure 4b/c. Commercially available prebent tools offer 5DoF including grasping (Figure 4b). The endoscope is inserted through an additional port channel between the instruments. The tools can be exchanged, pivoted inside the port, and translated. Another tool alternative is tools with a flexible articulated distal section, such as SILSTM Dessect (Medtronic, Minneapolis, MN, USA) as shown in Figure 4c. These tools are foreseen for the crossed arrangement.

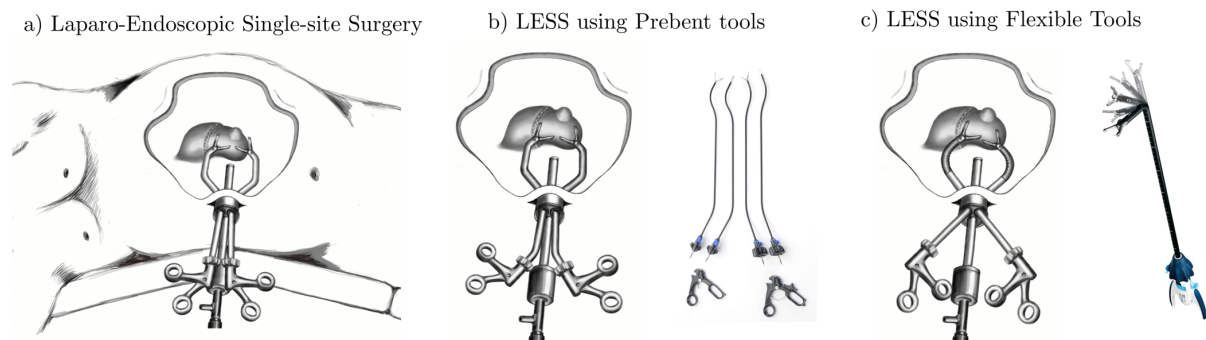


Figure 4: Laparo-Endoscopic Single-site Surgery: a) General approach through a single incision (here not through the navel for the sake of the illustration); b) Concept of using prebent instruments to restore the triangulation and commercial instrument example HiQ LS Series (©Olympus Corporation, Tokyo, Japan); c) Flexible instruments in the crossed approach with a commercial flexible instruments example SILSTMShears, (©Medtronic, Minneapolis, MN, USA).

For the LESS approach, a special elastic port with several instrument channels is placed in a single incision. Such ports are offered commercially with three or four channels as Triport or Quadport (Olympus Corporation, Tokyo, Japan) or SILSTM Port (Medtronic, Minneapolis, MN, USA) as shown in Figure 5.

1.5 PROBLEM STATEMENT

In order to understand the limitations of LESS, it is necessary to define the limitations that have emerged with the development of minimally-invasive surgery.

Considering open surgery, a large incision in the abdominal wall enables free hand and eye positioning around the surgical site. A human hand with a surgical tool can be approximated to have 7DoF including grasping⁶ (Baik, 2010, Kakar et al., 2011) as shown in Figure 6a. The surgeon is able to receive haptic and visual feedback (including depth perception), process the information immediately, and intuitively coordinate the movements of hands and eyes. This

⁶ Following this assumption robotic instruments were developed successfully for the da Vinci[®] robot series (Intuitive Surgical Inc., Sunnyvale, CA, USA), which are perceived as very intuitive in the surgeons community.

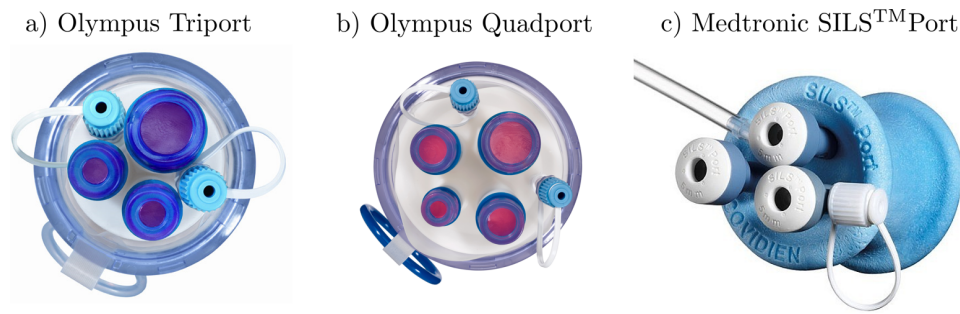


Figure 5: Elastic ports for LESS: a) Triport (©Olympus Corporation, Tokyo, Japan); b) Quadport (©Olympus Corporation, Tokyo, Japan); c) SILS™ Port (©Medtronic, Minneapolis, MN, USA).

can be considered as the ideal case from the surgeon's perspective. This is also the reason why even today complicated cases tend to be solved in open surgery. The ideal requirements are:

- Unrestricted camera positioning
- Unrestricted tool positioning
- 7DoF for the tools (including grasping)
- Intuitive tool control
- Depth perception (3D vision)
- Haptic feedback

With the introduction of the laparoscopic approach, the positioning of the tools (hand) and the endoscope (eye) is restricted to the incision locations. The hands (tools) and the eye (endoscope) have been decoupled and are manipulated by the surgeon and the assistant, requiring communication and teamwork. The 7DoF of the hand had to be abstracted to 5DoF by straight rigid tools (Figure 6b). The tool manipulation through an incision results in a so-called fulcrum effect, the surgeon's hand moves in one direction outside the human body, and the tool moves in another direction in the peritoneal cavity. Additionally, the varying lever arm depending on the insertion depth alters the translation of the movements as a relationship of the internal and external parts of the tool. Both effects are illustrated in Figure 6d. Further, the falsified haptic feedback (through the incision and the long shaft) and the lack of depth perception (2D endoscope images) are counterintuitive and require additional surgical training compared to open surgery.

To compensate for the limitation of the incision location, geometric dependencies were defined as a concept of triangulation. This is described by three terms (Hudgens et al., 2007):

- Angle between instruments
- Plane between instruments
- Visual angle

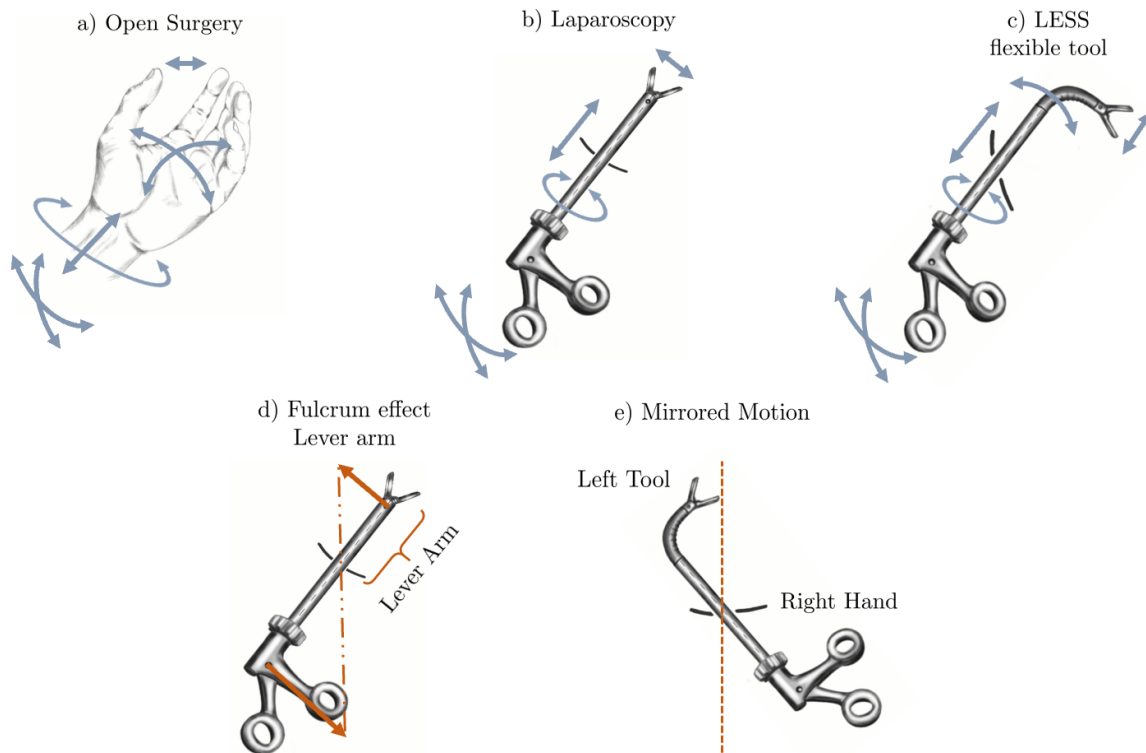


Figure 6: Degrees of freedom for: a) Open surgery; b) Laparoscopic surgery; c) Laparo-Endoscopic Single-site Surgery (LESS) with a flexible instrument. In d) the fulcrum effect and the lever arm motion transmission for minimally-invasive surgeries are illustrated; In e) the mirrored motion for LESS is depicted.

as shown in Figure 7a. The angle between the instruments is defined as the angle between their straight shafts. The plane between the tools is the plane defined by and bounded by the lines of the straight instruments. The vision angle is between the instrument plane and the straight endoscope shaft. For sufficient visualization and tissue manipulation, the instrument angle should be between 60° - 90° , and the vision angle should be larger than 30° (increased depth perception as stated in Hudgens et al., 2007). Further, for sufficient visualization, the endoscope should be placed between the instruments. While the triangulation can locally compensate for the incision restriction, the instrument angle would decrease when approaching remote regions from the endoscope incision, decreasing the quality of the triangulation. This means that unrestricted positioning of the instruments and visibility within the abdomen is not guaranteed. To be able to establish this arrangement, the location of the incisions is important. The following rules are recommended for tools and endoscope incision locations (Rosenblatt et al., 2008):

- Triangle arrangement showing upwards or downwards
- Endoscope on the top or bottom respectively
- Four fingers between the endoscope and a tool port
- Five fingers between the tool ports

as illustrated in Figure 7b/c.

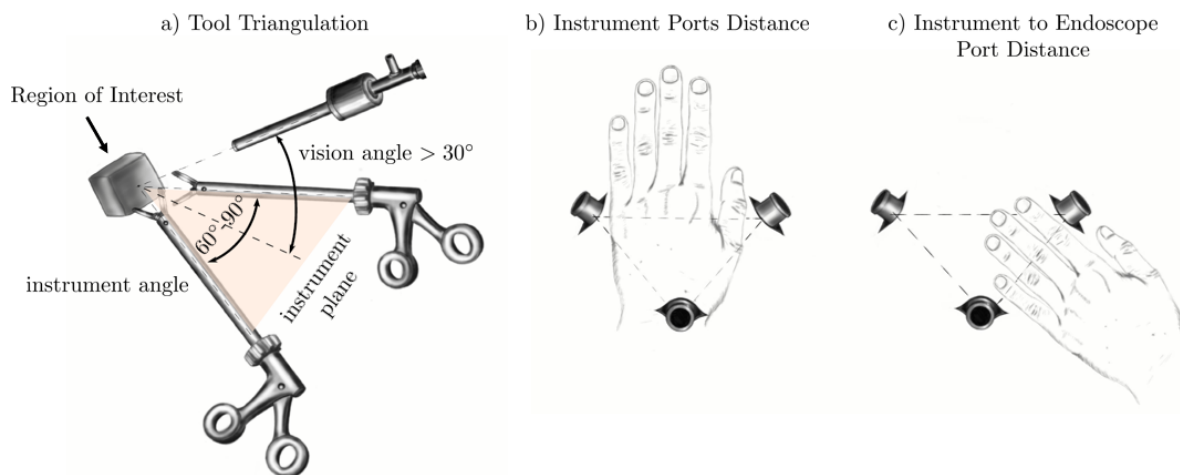


Figure 7: Geometric rules for port locations for laparoscopic surgeries: a) Instruments and endoscope arrangement inside the abdomen; b) Location and distance of the instrument ports; c) Location and distance of the endoscope and instrument ports.

The LESS approach maintains the mentioned limitations of laparoscopy and restricts the tool's motion further by only one port. The concept of triangulation has to be provided by bent or flexible tools. Deployed through the same port, the instruments can further clash with each other constraining the range of motion additionally. Applying tool crossing and the use of flexible tools provides higher range of motion, better ergonomics in comparison to a parallel insertion, and even higher number of DoF (6DoF), as illustrated in Figure 6c.

The drawback of the crossed tool approach is a mirrored tool control; the tool on the left side inside the abdomen is controlled by the opposite hand (Figure 6e). It has been shown that training for LESS exhibits a flatter learning curve (Canes et al., 2010, Andonian et al., 2010).

In summary, the LESS approach is very beneficial for patients, but has many limitations for surgeons. This leads to a relatively low application of LESS in comparison to multi-port laparoscopic approaches (Imkamp et al., 2014).

2

STATE OF THE ART

To address the limitations of LESS stated in the previous chapter, different approaches were proposed. Since the problem statement is very similar to the field of Natural Orifices Transluminal Endoscopic Surgery (NOTES), which considers the introduction of tools through natural body openings, solutions for NOTES are considered here as well. Manual tools with increased DoF (in comparison to straight, rigid tools) address some challenges. Further, this chapter presents the robotic approaches for laparoscopic surgery.

2.1 MANUAL COMMERCIAL TOOLS

Several approaches aimed to improve intuitive instrument control and increase the DoF for a manual crossed instrument approach. An instrument, RealHand™ (Novare Surgical Systems, Cupertino, CA, USA), with a 2DoF articulated distal section was introduced to compensate the fulcrum effect. With overall 7DoF, this tool restores the human hand DoF (Figure 8a) and provides the locking of the bent section.

Autonomy Laparo-Angle instruments (Cambridge Endoscopic Devices, Framingham, MA, USA) similarly provide 7DoF (Figure 8b), mimicking the surgeon's hands movements (no fulcrum effect). A locking mechanism for the bending section ensures that the curved tool shape is maintained. Both instruments were clinically evaluated as summarized in Yoshiki, 2016.

A relatively new commercial laparoscopic tool is the FlexDex™ (FlexDex Surgical, Brighton, MI, USA). It has 7DoF and aims to improve intuitive tool control with a special purely mechanic handle (Figure 8c). Successful clinical trials on laparoscopic partial nephrectomy were conducted in Vigneswaran, 2017. Although it is not yet practicable for LESS approaches, it can potentially be used as a single crossed incision approach, similar to other laparoscopic instruments.

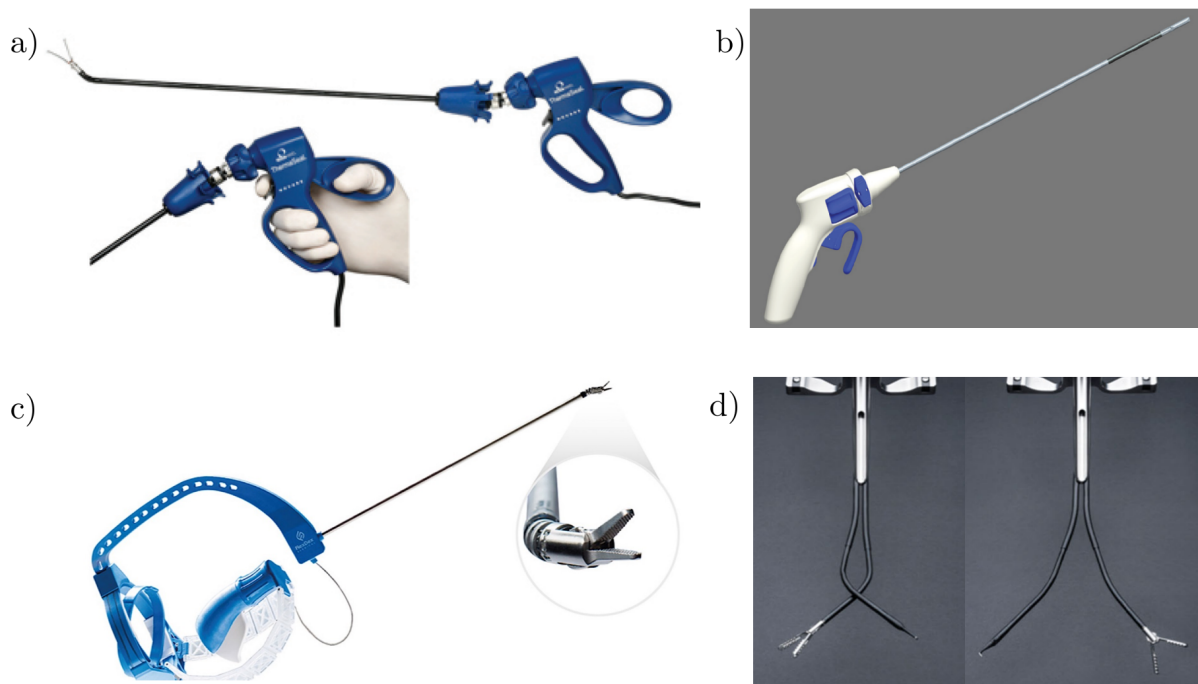


Figure 8: Manual straight rigid tools with highly articulated tips. a) RealHand™ (©Novare Surgical Systems, Cupertino, CA, USA); b) Autonomy Laparo-Angle instruments (©Cambridge Endoscopic Devices, Framingham, MA, USA); c) FlexDex™ (©FlexDex Surgical, Brighton, MI, USA); d) SymphonX (Fortimedix Surgical B.V., Geelen, Netherlands) (reprinted from (Berducci et al., 2016), ©2015, with kind permission from Springer Nature.)

The SymphonX™ Surgical Platform (Fortimedix Surgical B.V., Geelen, Netherlands) proposes articulated tools inserted through a 15 mm rigid port mounted on a customized platform. The rigid port provides three 5 mm channels for two parallelly introduced tools, one camera, and a 3 mm channel for further tools, such as a suction or irrigation tube (Figure 8d). The tools offer 5DoF. It is reported that the design offers better ergonomics (Berducci et al., 2016). The main advantage of this approach is the parallel insertion of the tools avoiding mirroring.

Semi-manual instruments with a similar structure as presented above and partially motorized DoF were introduced with the JAIMY Advanced System (Endocontrol Medical, La Tronche, France), as illustrated in Figure 9a, and the Dex Surgical (Lamidey Noury Medical, Verrières le Buisson, France) providing 7DoF, as shown in Figure 9b. They are primarily designed for laparoscopic surgeries.

Several instruments were proposed and applied for NOTES, e.g. colonoscopy, requiring deployment in a tortuous narrow environment. In this way the shaft is passively flexible for its most length and possesses a short articulated end section with up to 4DoF.

The information mentioned below is partly taken from the two summaries by Patel et al., 2014 and Vitiello et al., 2013.

The Transport System (USGI Medical, San Clemente, CA, USA) provides a four DoF articulated tip with four channels (7, 6, 4, and 4mm) (Figure 10a). For visualization, a flexible endoscope can be inserted. It is 18 mm in diameter and has a so-called shape locking mechanism, providing increased stability. However, the triangulation is poor, since common instruments were inserted through the channels. The Cobra was an improved version of the Transport in-

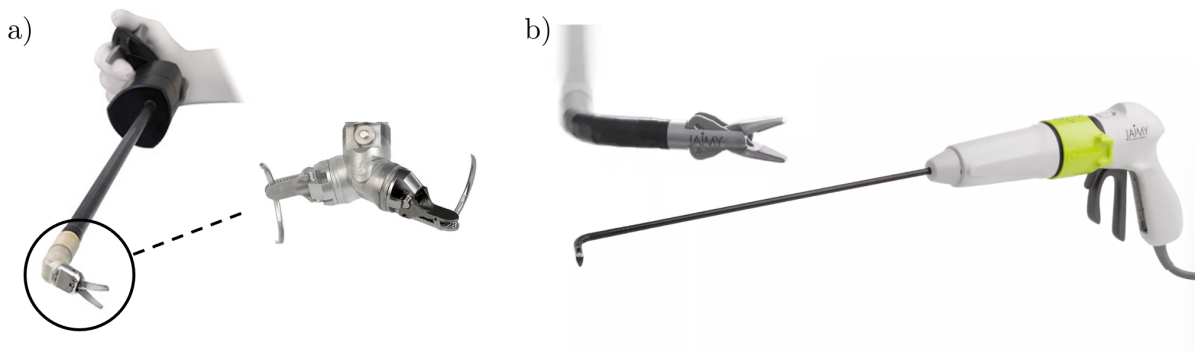


Figure 9: Semi-manual tools with highly articulated motorized tips: a) JAIMY Advanced System (©Endocontrol Medical, La Tronche, France); b) Dex Surgical (©Lamidey Noury Medical, Verrières le Buisson, France).

cluding three unfoldable arms providing working channels for the instruments and a flexible endoscope (Figure 10b). However, smooth manual control of the overtube tip and the instruments is difficult and the device has to be removed for tool exchange.

The Anubiscope[®] (KARL STORZ SE & Co. KG, Tuttlingen, Germany) has a 16 mm four way flexible end section with a 18 mm diameter tip and carries two unfoldable arms with working channels of 4.2 mm diameter each. A further 3.4 mm channel is located within the shaft (Figure 10c). Clinical trials were conducted in Perretta et al., 2013 showing its feasibility. However, the triangulation is reported to be poor and manual tool control is challenging.

The R-Scope (Olympus Corporation, Tokyo, Japan) has a 14.3 mm shaft diameter with two 2.8 mm channels. It provides two sections which can bent independently (Figure 10d). The working channels allow the use of instruments, but do not enable instrument triangulation. This issue was targeted by the Endosamurai with two unfoldable arms including working channels and an additional channel for suction. The control of the device is, however, still challenging (Figure 10e).

The Direct Drive Endoscopic System (DDES) (Boston Scientific, Marlborough, MA, USA) is a 2DoF articulated flexible shaft providing three working channels with two unfoldable arms and one additional channel (Figure 10f). It has a diameter of 22 mm and includes specially designed tools offering additionally 5DoF. Inadequate triangulation and interference of the tools with the optical axis were reported as drawbacks.

2.1.1.1 Manual Devices Dilemma

If considering the increase in DoF to restore the human hand dexterity, many successful approaches with up to 7DoF have been shown above, facilitating even complex surgical tasks such as suturing. Also, sufficient triangulation can be provided. Concerning the intuitive control of the proposed surgical tool, some tools improve intuitive manipulation by addressing the fulcrum effect. Only the SymphonX[™] Surgical Platform specifically considers LESS, avoiding both, the fulcrum effect and tool mirroring.

Manual control of the articulated flexible port systems, proposed for NOTES, shows limitations in precision and intuitive control. Manipulating high DoF tools, articulated endoscopes, and e.g. irrigation or suction through the same port, result in the remaining challenge of poor

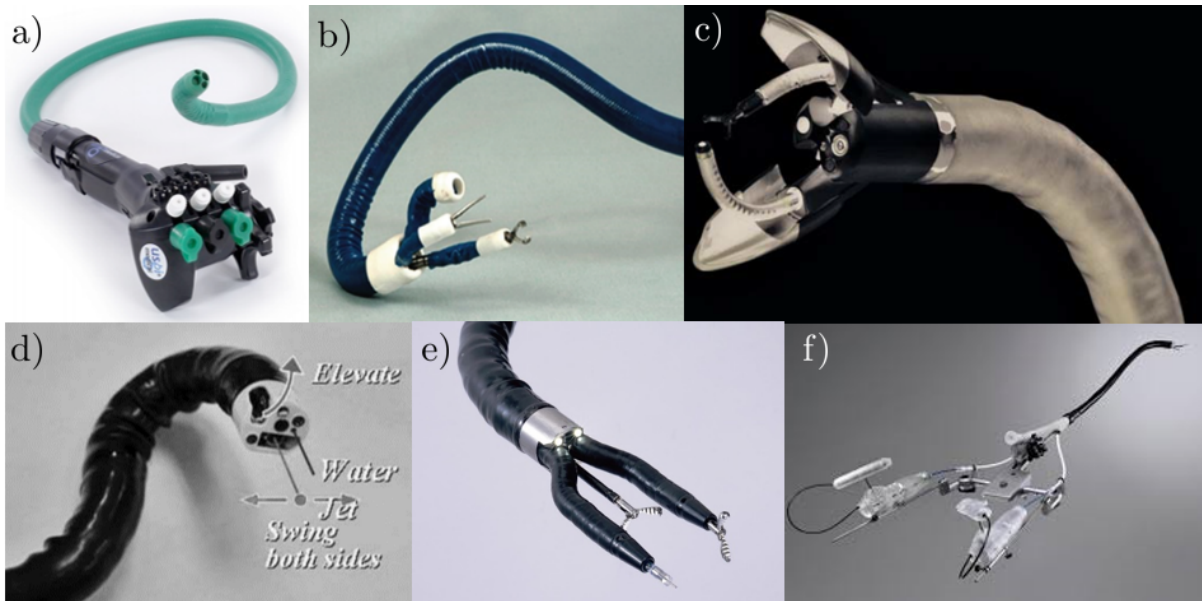


Figure 10: Manual articulated ports: a) Transport System (©USGI Medical, San Clemente, CA, USA); b) Cobra (©USGI Medical, San Clemente, CA, USA); c) Anubiscope® (©KARL STORZ SE & Co. KG, Tuttlingen, Germany); d) R-Scope (©Olympus Corporation, Tokyo, Japan), e) Endosamurai (©Olympus Corporation, Tokyo, Japan); f) Direct Drive Endoscopic System (©Boston Scientific, Marlborough, MA, USA).

ergonomics for surgeons. This has been shown in a recent review by Epstein et al., 2018. In addition, depth perception is still missing for the mentioned tools above, since the surgeon only has a 2D monitor as visual feedback. Motion scaling, precision increase, and tremor reduction is addressed by semi-manual devices, showing the advantages of partially robotic solutions.

Indeed, robotic approaches can address also depth perception loss and ergonomic limitations by dividing the robotic surgical system into a robotic device at the surgical table and a remote control console. Robots can be teleoperated from distance in a comfortable sitting position, receiving visual feedback in a binocular 3D-view. Further, robotic solutions, can overcome human limitations by compensating for natural hand tremor, motion scaling for increased precision (Prasad et al., 2004), and navigation. Helpful assisting functions such as automated endoscope tool following can be achieved, restoring the hand-eye coordination.

Studies showed that robotic approaches lead to faster completion of complex tasks such as suturing (Falahatkar et al., 2010) and showed a steeper learning curve (Jayaraman et al., 2010) indicating benefits for less experienced surgeons. Therefore, this work further focuses on existing robot-assisted LESS (R-LESS) approaches.

2.2 ROBOTIC LESS SYSTEMS

Research in the field of minimally-invasive surgery is strongly focused on the development of dexterous surgical instruments, while the design space of robotic ports remains mostly unexplored. Therefore, this thesis particularly focuses on the design of the robotic port structure. First, the existing R-LESS and NOTES approaches are classified into four main port structure

groups.

The most simple approach is to introduce robotic tools through an elastic port and use them in a crossed arrangement. Large robotic arms (usually serial kinematics) carry and manipulate dexterous laparoscopic tools. Through the robotic approach, tool mirroring can be reversed providing more intuitive control. This structure is summarized under Elastic Port and is illustrated in Figure 11a.

The second structure type foresees a rigid straight port, which does not allow for individual pivoting of the introduced tools as shown in Figure 11b. This structure is called Rigid Port. The instruments can be rigidly installed within the port or can be exchangeable. A camera is often rigidly installed within the port or offers certain DoF in itself. The actuation pack of the instruments can be designed more compact compared to the Elastic Port approach and has a smaller spacial footprint since the tools do not require pivoting. However, the whole port might be mounted on a serial robot to provide additional DoF.

The third approach replaces the straight rigid port by an articulated port, being able to bend actively itself and additionally allowing for highly articulated tool deployment, as shown in Figure 11c. This group is described as Articulated Port. Similarly to the rigid ports, the actuation pack allows for space-efficient designs. Further, pivoting around the incision is not necessary, since the port itself provides additional DoF.

The last group disclaims a port and introduces a defoldable or reconfigurable robotic platform that is only connected by cables to the outside of the abdomen and is held by an external magnetic field. This group is defined as Miniature Platform and is shown in Figure 11d. The external magnetic field needs to be mounted on some robotic arm or requires manual control to enable repositioning of the platform inside the abdomen. The embedded actuation avoids an external actuation pack and instruments can be attached/detached offering a modular design.

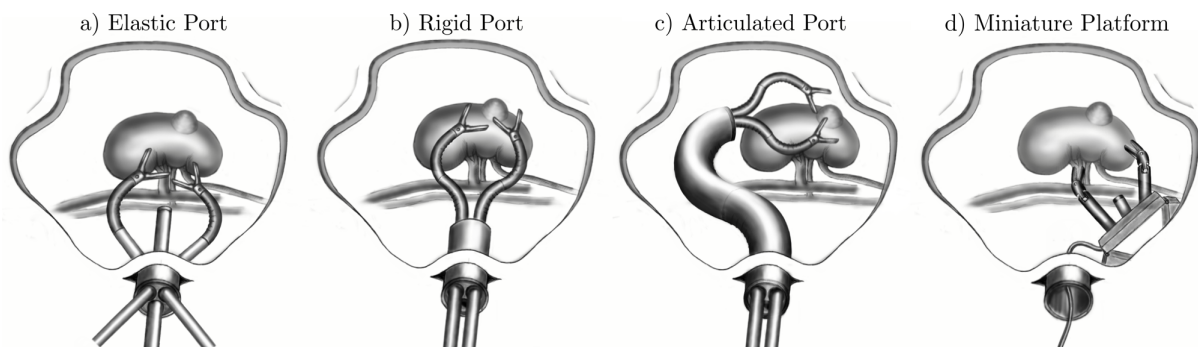


Figure 11: Port structure classification: a) Elastic Port; b) Rigid Port; c) Articulated Port; d) Miniature Platform.

2.2.1 Elastic Port

Similar to the approach using manual instruments, a specific elastic port is placed inside the incision offering several channels (depending on the overall system) for robotic instruments and an endoscope. Further, an insufflation interface is provided. The elastic nature of the

port allows to pivot the instruments inside. Only view systems utilize this port structure as presented in the following.

commercial The only commercial robotic systems utilizing this port structure are the da Vinci® Surgery System Series (Intuitive Surgical Inc., Sunnyvale, CA, USA) with its Single-Site® technology. Special flexible instruments are deployed through rigid curved guiding cannulae (Figure 12a) to improve triangulation. The guiding cannulae and the tools are carried by serial robotic arms, providing pivoting and translation of the tools (Figure 12b), resulting in overall 6DoF per tool. This system is FDA¹ approved for clinical use and was evaluated for different applications such as radical prostatectomy and nephrectomy (Kaouk, Goel, et al., 2009), colectomy (Ostrowitz et al., 2009), radical cystectomy², or partial nephrectomy (Kaouk and Goel, 2009).

research A research system with a similar structure proposed by Hwang et al., 2017 disclaims curved cannulae. Instead, highly articulated tools with rigid joints and links (9DoF) are carried by a robotic arm (Figure 12c) and are introduced through an elastic port into the peritoneal cavity. The three additional DoF per tool provide increased dexterity at the tip and have a payload over 15 N. Preliminary tests performing peg transfer³ on a human abdominal phantom are demonstrated.

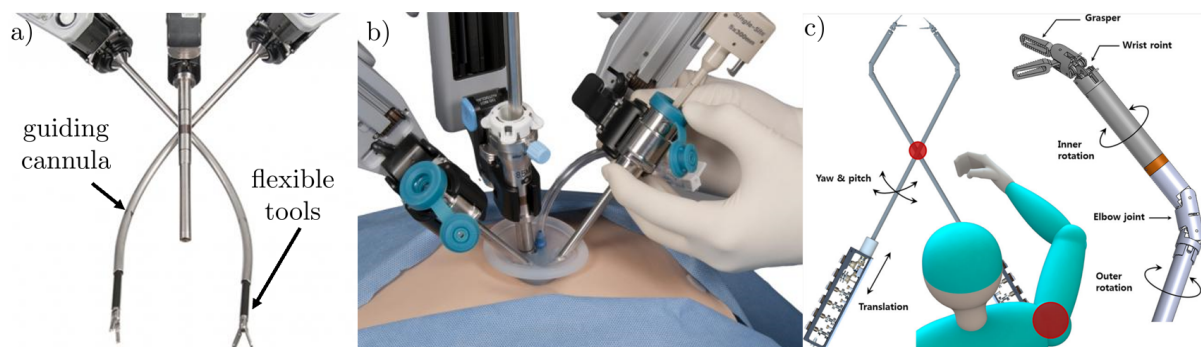


Figure 12: Robotic systems introduced through an elastic port: Da Vinci® robotic system with equipped Single-Site® (©Intuitive Surgical Inc., Sunnyvale, CA, USA) technology showing the flexible instruments in a) and external robotic arms in b); c) Research R-LESS system with 9DoF per tool (reprinted from (Hwang et al., 2017) with permission from John Wiley & Sons, Ltd.; Copyright ©2017 John Wiley & Sons, Ltd.)

2.2.2 Rigid Port

The rigid port approach foresees a straight rigid cylinder port allowing for instrument deployment and insufflation. The spacial footprint is improved since the robotic system can be

¹ US Food and Drug Administration, a major robotic-assisted surgery approval institution

² bowel resection of the large bowel (colon)

³ A standard surgical skill training for laparoscopic tools, moving small objects from A to B; the transfer of an object from one instrument to another is performed in between.

mounted permanently or on a single serial kinematic arm. Further, instrument clashing is avoided through parallel instrument deployment.

commercial The only recently FDA approved R-LESS system commercially available is the da Vinci SP[®] (Intuitive Surgical Inc., Sunnyvale, CA, USA) with a 25 mm rigid port, three articulated arms, and an articulated endoscope. The arms partially consist of joints and rigid links (proximal), and distal hyper-redundant (large number of joints and links) sections. They offer 7DoF (Figure 13a), which enhances intuitive control. The system was successfully evaluated in several clinical studies for applications such as prostatectomy or partial nephrectomy as reported in Kaouk, G. P. Haber, et al., 2014.

The SPORT Surgical System (Titan Medical Inc., Toronto, Canada) based on the previous research results by Ding et al., 2013 is meant for abdominal surgeries. This robotic system consists of a straight rigid 25 mm cylindrical port, which includes a wide range 2D camera. Two hyper-redundant arms with 8DoF and an articulated endoscope with 6DoF (Figure 13b) can be introduced and exchanged through the port. The actuation pack is mounted on a 4DoF robotic arm. Currently, this system is not approved by any responsible institution but a variety of studies with experienced surgeons are reported on the manufacturer website, including prostatectomy, and partial nephrectomy.

The SurgiBot[™] (TransEnterix Surgical Inc., Morrisville, NC, USA) is mounted on a planar passive arm with several DoF. A straight rigid port includes two manually adjustable flexible instrument tubes providing triangulation for the inserted 5DoF tools (Figure 13c). One further instrument and an endoscope can be introduced through the port. The design originated from the manual Spider system introduced in G.-P. Haber et al., 2012. No relevant studies are shown in the literature. After FDA approval rejection, further development was abandoned.

The Virtual Incision System (Virtual Incision Corp, Lincoln, NB, USA) proposes a straight shaft (port) equipped with two 28 mm in diameter 6DoF serial tools and enables insertion of a flexible endoscope. The port is manually positioned within the incision, is mounted on a passive arm, and can be rotated about its central axis during surgery. The initial design was reported in Wortman et al., 2013 and in-vivo trials were performed successfully (Dolghi et al., 2011).

research Xu et al. proposed a similar system to the SPORT Surgical System with two push-pull rod actuated flexible robot arms providing 6DoF (6.35 mm diameter) each and a 3DoF camera unit (Xu et al., 2015). The design is relatively small with only 12 mm due to its unfoldable design, as shown in (Figure 14a). The highly articulated tools are integrated into a straight rigid port mounted on an industrial serial robot (6DoF). Successful suturing and grape peeling was performed.

Similar to the da Vinci SP[®], a system proposed by Wang et al., 2018 consists of two robotic arms with a mixture of joints and rigid links, and hyper-redundant sections. However, it has 8DoF including grasping and possesses an integrated stiffening method. The number of arms is limited to two. An articulated camera arm is permanently integrated into the port (Figure 14b). The robotic tools are introduced through a rigid straight port with 22 mm in diameter mounted on a passive arm with several DoF. The stiffening method allows for relatively high loads. Animal tissue resection studies were performed while teleoperating the articulated arms.

A parallel kinematic chain system was proposed by Matich et al., 2015 (Figure 14e). A 38 mm

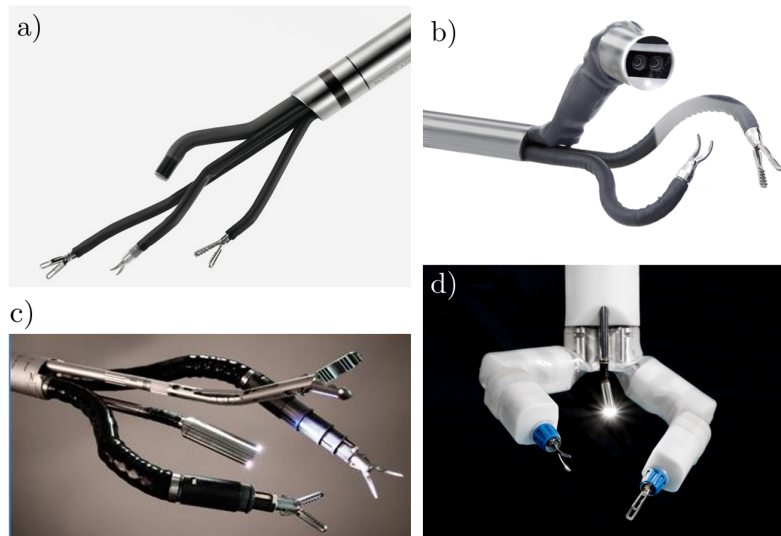


Figure 13: Commercial R-LESS systems with straight rigid ports: a) Da Vinci SP[®] System (©Intuitive Surgical Inc., Sunnyvale, CA, USA); b) SPORT Surgical System (©Titan Medical Inc., Toronto, Canada); c) SurgiBot[™] (©TransEnterix Surgical Inc., Morrisville, NC, USA); d) The Virtual Incision System (©Virtual Incision Corp, Lincoln, NB, USA).

large straight port is equipped with a 3D camera and carries two parallel kinematic robotic arms providing 6DoF each. Through the parallel kinematic structure, increased loads and dynamic performance can be accomplished. Since the robot is designed for transanal procedures (NOTES), its workspace is limited.

Kobayashi et al., 2015 proposes a similar structure reducing the straight port size to 25 mm (Figure 14c). Additional to two 6DoF articulated robotic arms, an articulated camera unit is provided. The whole robot is mounted on a larger robot arm providing pivoting, translation, and rotation. Animal tissue resection was shown successfully. A similar structure with a straight rigid port and two parallel robotic arms was investigated by Li et al., 2019.

Serial kinematics instruments deployed through a straight port, as proposed by Petroni et al., 2013, were presented as alternatives for LESS as well. A 30 mm straight rigid cannula equipped with a camera allows for the insertion of two articulated robotic arms (6DoF each). This structure was improved in terms of outer diameter and payload by Yung et al., 2017 (Figure 14d), introducing special tool locking mechanisms. With this mechanism, the lumen in the straight port remains free after the articulated robotic arm is deployed and offers space for further instruments. The tools can be exchanged for both designs. The overall system is anchored to a swivel system with 3DoF. Yung et al., 2017 reported increased loads up to 5 N and showed promising results performing multiple porcine cholecystectomies⁴ (LESS).

Hendrick et al., 2015 proposed a robotic system with two concentric tube robots for prostatic hyperplasia treatment (Figure 14f). The robotic arms provide 3DoF each, although up to 6DoF could be possible. Due to the space-efficient size of concentric tube robots, they can be deployed through a 8.3 mm large straight rigid cylinder equipped with an endoscope. The whole robot is mounted on a frame providing 3DoF.

⁴ Surgical removal of the gallbladder

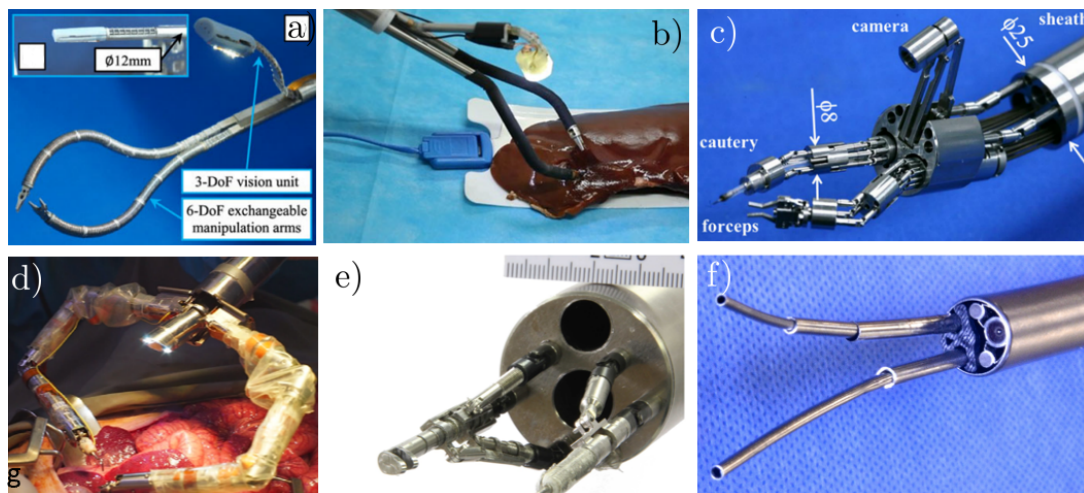


Figure 14: Research Robotic LESS systems with straight rigid ports: a) With articulated camera and continuum arms (reprinted from (Xu et al., 2015), ©2015 IEEE); b) With articulated camera and joint based arms (reprinted from (Wang et al., 2018) with permission from John Wiley & Sons, Ltd; Copyright ©2017 John Wiley & Sons, Ltd.); c) With parallel kinematic arms (reprinted from (Kobayashi et al., 2015) with permission from John Wiley & Sons, Ltd; ©2014 John Wiley & Sons, Ltd.) d) With serial kinematic arms (reprinted from (Yung et al., 2017), ©2017, with kind permission from Springer Nature); e) With parallel kinematic arms (reprinted from (Matich et al., 2015), ©2015 IEEE); f) With concentric tube arms (reprinted from (Hendrick et al., 2015), ©2015 SAGE Publications).

2.2.3 Articulated Port

Articulated ports exhibit a flexible shaft with several DoF, which allows for the deployment of additional articulated tools. This design is particularly advantageous for applications in tortuous, confined spaces such as the colon or throat. Although the space is not restricted in abdominal operations, access via an articulated port provides better instrument positioning and is less restricted by the incision site.

commercial Thakkar et al., 2015 introduced a tendon-actuated hyper-redundant manipulator with the ability of follow-the-leader motion⁵. This motion is achieved by alternatively sliding and stiffening two concentric hyper-redundant structures and is predestined for NOTES with narrow tortuous paths. Arbitrary shapes can be achieved with a maximum angle between two links of 10° . This approach resulted in an FDA approved commercial product, the Flex[®] Robotic System (Medrobotics Corporation, Raynham, MA, USA), as illustrated in Figure 15a. It carries an integrated 3D camera at the tip and allows the exchange of two 3 mm articulated instruments. Recent studies show feasibility using the Flex[®] Robotic System for transoral robotic surgeries (Sethi et al., 2020) and endoscopic submucosal dissection (Moura et al., 2019).

The NeoGuide Endoscopy System (Intuitive Surgical Inc., Sunnyvale, CA, USA) is a robotic flexible endoscope consisting of 16 8 cm long serial motorized sections (Eickhoff et al., 2007), as shown in Figure 15b. It is meant to reduce discomfort during colonoscopy by sensing the distance to the colon wall (sensor at the tip) and automatically adjusting its shape. Flexi-

⁵ A motion where the whole body of the manipulator stays on the path that the tip took during deployment



Figure 15: Commercial articulated port systems: a) Flex[®] Robotic System (©Medrobotics Corporation, Raynham, MA, USA); b) NeoGuide Endoscopy System (©Intuitive Surgical Inc., Sunnyvale, CA, USA); c) ViaCath (©Hansen Medical, Norwood, MA, USA).

ble instruments can then be deployed and exchanged. First clinical studies were promising (Eisenberg et al., 2010), however, the system is not FDA approved and further development is not reported.

The STRAS is a robotic system based on the Anubiscope[®] with a flexible port and two articulated instruments. The port is composed of a 57 cm long flexible passive section, a 22 cm articulated distal section (3DoF), and has an overall diameter of 18 mm. Up to three instruments with 4DoF can be deployed and exchanged through the port (De Donno et al., 2013). It is proposed for endoluminal or transluminal surgeries, e.g. colonic endoscopic submucosal dissection. Performing the surgical task in a phantom and in-vivo trials has been shown as feasible. However, the system is not FDA approved and no further reports on development are available.

The ViaCath (Hansen Medical, Norwood, MA, USA) was proposed for stomach surgeries introduced through the esophagus (NOTES). It consists of an overtube, smaller 7DoF instruments, and a camera unit which can be deployed (Figure 15c). The overtube represents an articulated port which exhibits a long, flexible passive section and two tendon actuated distal sections with overall 3DoF. The articulated sections consist of joints and rigid links. The system was evaluated on in-vivo porcine models (Abbott et al., 2007). Further developments were stopped due to the acquisition by Hansen Medical.

research Y. J. Kim et al., 2013 introduced an articulated cylindrical (22 mm diameter) port structure composed of flexible flap layers. It provides 4DoF for two active 200 mm sections and one inner lumen as a channel (Figure 16a). By encapsulating the flaps inside an air-proof membrane and applying vacuum, the stiffness of the port can be varied due to increased friction between the flaps. In the paper, no instruments were used for deployment and the articulated robot had no camera modules integrated. The proposed application is extraluminal surgery in the abdominal cavity, but no studies were conducted.

Roppenecker et al., 2014 proposed a monolithically 3D-printed structure as an articulated port providing two working channels and an additional camera channel (Figure 16b). The 3D-printed structure consists of flexure hinges and can be bent using tendons with 2DoF up to 240°. It has an overall diameter of 14.4 mm. Common flexible laparoscopic instruments and endoscopes can be deployed and exchanged. The channels can be actuated in an unfolding manner, providing triangulation. The overall length can be modified based on a modular approach. The modularity and the sterile 3D-printing method are the key features of the system and are proposed for LESS and NOTES at the same time. No further studies are reported.

Despite the manual actuation of this system, this work is included in this chapter due to its relevant contributions.

Another actuation principle was proposed by Cianchetti et al., 2014 (Figure 16e). The robot design addresses the safe use by being actuated with pneumatic bellows. They expand when pressurized, causing a bending of the structure. With three parallel pressure chambers, one segment provides two bending DoF and one elongation DoF (when all chambers are pressurized at the same time). Several segments can be stacked upon each other. A prototype with two segments of 32 mm diameter and 50-81 mm has been realized. Additionally, this approach also provides a stiffening method with granular jamming for increased shape stability. No working channels were introduced. The desired application is LESS in the abdominal cavity.

Roh et al., 2015 suggested an articulated 4DoF port for R-LESS with two tendon-actuated segments (Figure 16d). The overall diameter is 30 mm and the lengths of the segments are 150 mm and 100 mm. The port includes two permanently attached multi-DoF robotic arms and an articulated camera unit with 3DoF. It consists of identical rolling joints, while the joints are rotated around 90° degrees to each other in an alternating manner to assure bending in two directions. Through tensioning all tendons simultaneously, the stiffness of the port can be varied. The port has been shown to improve the accessibility of an abdominal phantom qualitatively. Further, peg transfer and suturing have been shown.

Rosen et al., 2017 proposed another hyper-redundant port with 2DoF (Figure 16f). The joints are arranged alternately to provide bending in two directions. The overall diameter is 12 mm and allows for bending angles of 180°. Two channels are provided for commonly used 2.3 mm flexible instruments and two channels for 1.2 mm scanning fiberscopes for 3D-visualization. The port allows for two further bending DoF for each tool to provide triangulation. The port is proposed for transnasal skull base surgery (NOTES).

The Korea Advanced Institute of Science and Technology developed a system (K-Flex) for NOTES/LESS with two articulated segments port of 17 mm diameter and 4DoF (Figure 16g). It includes a fixed camera in the port shaft and allows for tool insertion through two 4.2 mm working channels. The port consists of flexure hinges and allows for high payloads. While an animal gallbladder resection trial is reported to be successfully performed on their website, no publication can be found.

Shang, Noonan, et al., 2011 proposed a 7DoF universal joint structure with embedded actuation for NOTES. The overall articulated port diameter is 12.5 mm, offers two 2.8 mm working channels, and one further 2.5 mm visualization channel. Five serial links result in a robot length of 185 mm. Porcine trials showed first feasibility results.

2.3 MINIATURE PLATFORM

Some researchers proposed mobile platforms carrying instruments and a camera, while they are controlled inside the body by an external force such as a magnetic field. (Lehman et al., 2009) used a miniaturized platform with two unfolding arms equipped with tools (e.g. grippers) and a stereo vision unit (Figure 17b). It is meant to be introduced transorally into the peritoneal cavity (NOTES). Each arm possesses three DoF. The platform contains a permanent magnet and the surgeon can manually control the platform by an external magnet outside

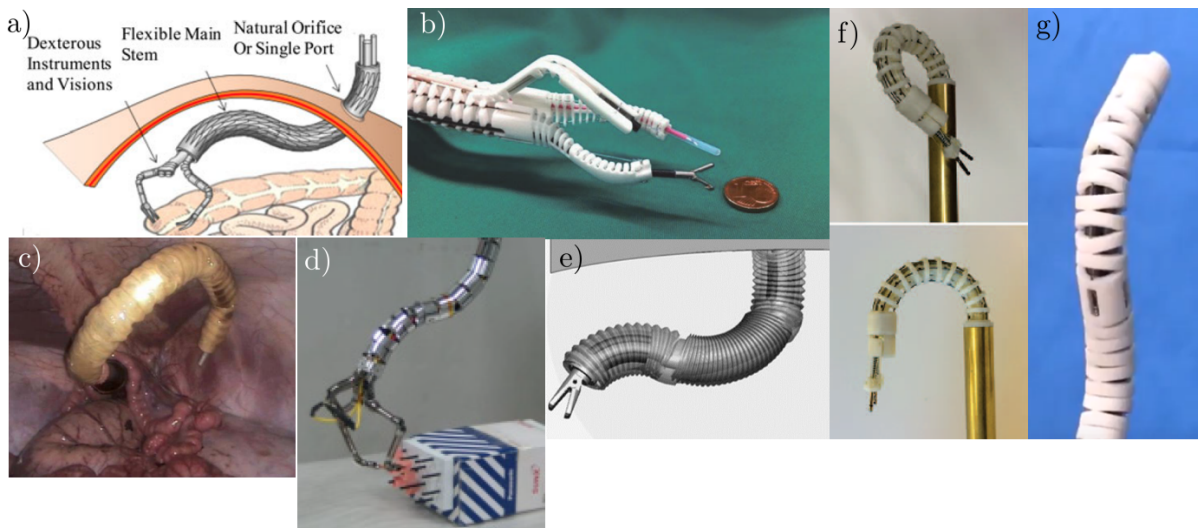


Figure 16: Research articulated robotic LESS ports: a) Flexible layer jamming structure (reprinted from (Y. J. Kim et al., 2013), ©2013 IEEE); b) Sterile modular flexure hinge 3D-printed structure (reprinted from (Roppenecker et al., 2014), ©2014 IEEE); c) i-Snake serial joint structure (reprinted from (Shang, Noonan, et al., 2011), ©2011 IEEE); d) Rolling joint structure (reprinted from (Roh et al., 2015), ©2015, with kind permission from Springer Nature); e) Soft fluidic chambers structure (reprinted from (Cianchetti et al., 2014), ©2014, with kind permission from Mary Ann Liebert, Inc.); f) Hyper-redundant structure (reprinted from (Rosen et al., 2017), ©2017 IEEE); g) 3D-printed flexure hinge structure¹

¹ K-Flex system from KAIST, <http://easyendosurgical.com>, accessed on 23.08.2019

the body. The platform is supplied with external power.

Tortora et al., 2013 proposed a similar device with a triangular platform carrying permanent magnets (Figure 17a). The improvement here, is the modular structure of the device allowing for different tools to dock to the platform. In the paper, the authors propose a 2DoF camera module, a 2DoF gripper, and a 4DoF serial manipulator. The platform is positioned by an external magnetic field, manually controlled by the surgeon.

Using an external magnetic field, internal magnets integrated into miniature robots can be actuated, as proposed by Garbin et al., 2015. The work is limited to a single tissue retractor providing 1DoF. An internal camera platform with integrated 3DoF held at the abdominal wall by an external magnet was proposed by Terry et al., 2012. The camera platform is also fixed to an incision port. A similar approach of a miniature camera held by an external magnetic field was investigated by Liu et al., 2018, providing 2DoF. By moving the external magnetic anchor, the camera can be positioned anywhere on the abdominal wall. It is connected with a wire through the port used for one of the instruments, thus avoiding the need of an additional incision for an endoscope.

2.4 CONCLUSION

In order to preserve the benefits of LESS for the patient and restore the benefits of open or at least laparoscopic surgery for the surgeon, advanced manual instruments have been proposed for LESS and NOTES. While the triangulation, the DoF, and partially, the intuitive instrument manipulation (removing the fulcrum effect and mirrored motion) can be restored, the lack of depth perception, falsified haptic feedback, decoupled hand-eye coordination, and the restric-

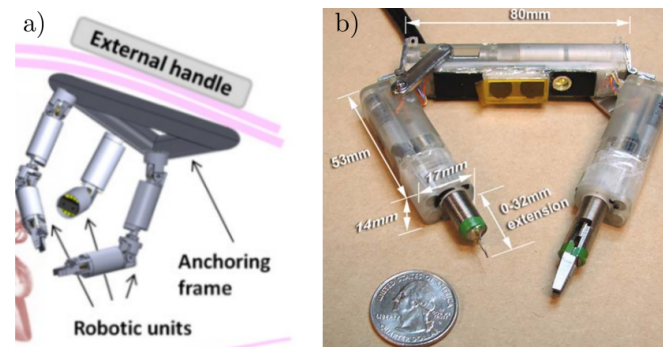


Figure 17: Miniature platform structure: a) With an articulated camera and two articulated arms (reprinted from (Tortora et al., 2013), ©2013 IEEE); b) With fixed camera and two articulated tools (reprinted from (Lehman et al., 2009), ©2008, with kind permission from Springer Nature.)

tion of the incision location are still present.

By introducing robotics to minimally-invasive surgery, depth perception using 3D imaging in a remote control console can be regained. The coordination of vision and instruments can be achieved by one surgeon and can additionally be supported by assisting functions keeping the instruments in the endoscope field of view. Motion scaling and tremor filtering can even enhance the surgical skill beyond human capabilities during open surgery. Further, for the first time, the surgeon can operate from distance in a comfortable position.

Robotic LESS has been shown to be comparable to standard laparoscopic procedures in clinical terms, such as blood loss, surgery time, less postoperative pain and port relative complications (e.g. port infections), and better cosmetic outcomes through a single incision (navel) especially (Liatsikos et al., 2012, Autorino et al., 2013). Therefore, a robotic approach is preferable for LESS. As the integration of haptic feedback progresses through the use of miniature sensors in robotic instruments and motorized input devices to transmit forces, the limitation of operating through a single incision remains.

There are two restrictions which occur: The restriction of instrument triangulation and the restriction of the field of view. Using elastic ports, the restriction of the field of view can be compensated by angled or flexible endoscopes. Pivoting endoscopes in the incision is sufficient, as shown in Figure 18a. In the case of rigid ports, a fixed installed camera is highly restricting the visualization of the region of interest and the instruments (Figure 18b, top). Articulated cameras can compensate for this restriction (Figure 18b, bottom). For the articulated port and the miniature platform, the camera can be positioned within a wide range inside the peritoneal cavity. Being aligned with the instruments, they offer an efficient visualization of the surgical site and the instruments (Figure 18c-d). Because the miniature platform is actuated by the external magnetic field, it always needs contact with the abdominal wall. This might result in some visualization restrictions. The articulated port, on the other hand, is restricted by its structure.

The best triangulation is provided, when the surgical site is located symmetrically between the instruments and the instrument angle is approximately 60° - 90° , as mentioned in the introduction. Considering the elastic port, the proposed systems are designed to create triangulation when the surgical site is accessible on a straight line (further line of deployment) from the incision location. The further the surgical site deviates from this line, the less suf-

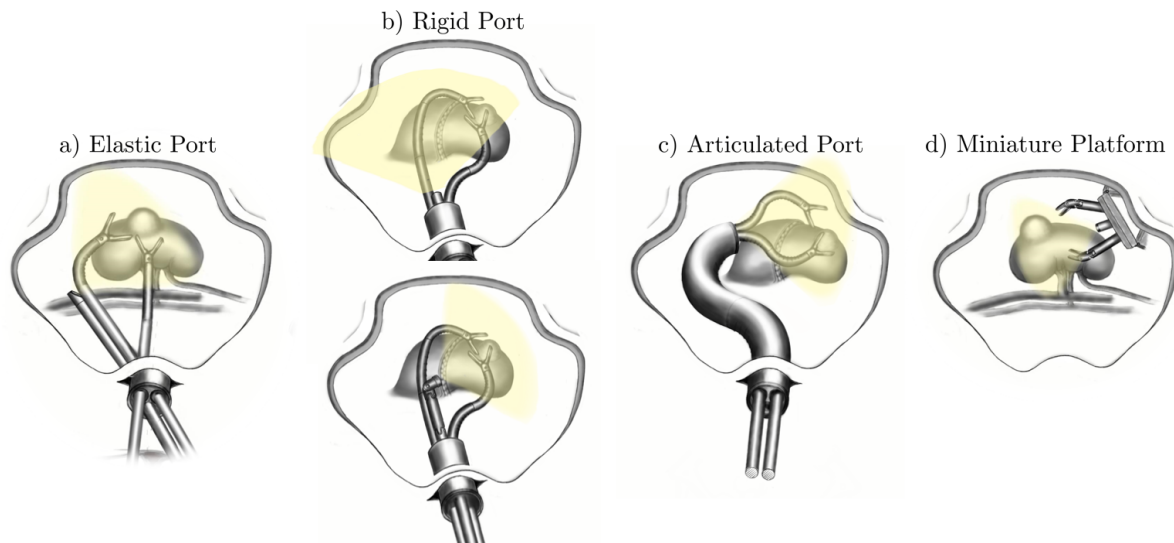


Figure 18: Overcoming visualization restrictions using different port structures: a) Through elastic ports with angled endoscopes; b) Through a straight port with an articulated camera unit (bottom), fixed cameras provide restricted vision (top); c) Through an articulated port with fixed cameras; d) Through a miniature platform with fixed cameras.

ficient becomes the triangulation of these tools, as shown in Figure 19a. The full range of motion of each DoF must be utilized, which leads to operations at the joint boundaries and the loss of DoF.

A similar case occurs for the straight ports. The instruments need to operate at their workspace borders with increased deviation from the line of deployment (Figure 19b), resulting in worse triangulation and loss of DoF. To compensate for this scenario, kidney mobilization is performed, as described in the introduction, requiring a considerable amount of surgery time and invasive dissection of the peritoneal fat and the peritoneum around the kidney.

The miniature platform and the articulated port can avoid this scenario being able to position and orient the instruments around the kidney such that the instruments are aligned with the line of deployment, as shown in Figure 19c-d. This enables the same triangulation independent from the location of the surgical site and the incision location. Thus, the miniature platform and the articulated port are the two solutions to restore the free positioning and orientation of the instruments (hands) and the camera (eye) referring to open surgery. Further, the complexity of the deployed instruments and the camera unit can potentially be decreased utilizing articulated ports or miniature platforms.

Comparing both port structures, the miniature platform is still in the early stages and faces embedded actuation miniaturization challenges limiting the available DoF for the instruments. The articulated port offers the deployment of broadly proposed articulated flexible tools and provides several segments with several DoF for independent position and orientation control. Therefore, the articulated port structure is further considered in this thesis.

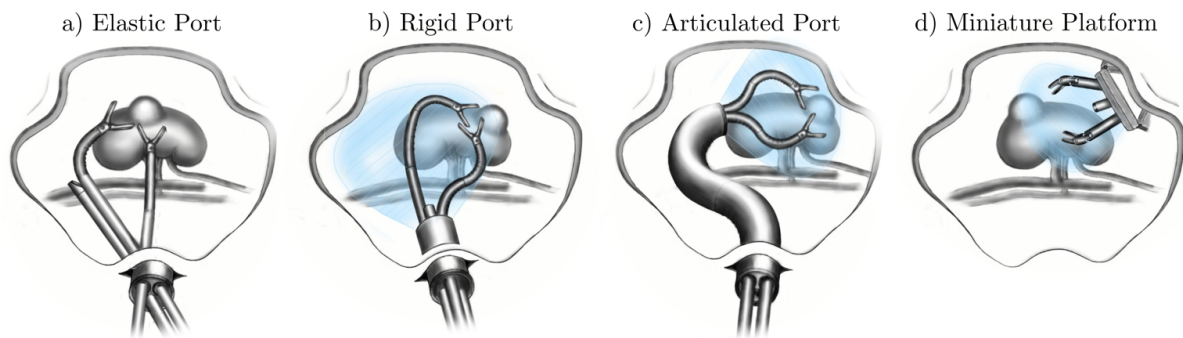


Figure 19: Instrument workspace restrictions: a) Through an elastic port, flexible instruments operate at their workspace borders; b) Through a straight port, articulated instruments operate at their workspace borders; c) Through the articulated port, instruments use their workspace optimally; d) Using a miniature platform, instruments use their workspace optimally.

3

CHALLENGES AND CONTRIBUTION

The introduction described the surgical procedure for partial nephrectomy and LESS. Based on this description, the following requirements are formulated for the surgical port system:

- Outer diameter below 30 mm
- Two instrument working channels
- Camera
- One additional working channel for suction or irrigation
- Tool exchange
- Structural stiffness and flexibility
- Sterility

The articulated robotic port state of the art parameters are summarized in Table 1 and Table 2 for NOTES, and in Table 3 for LESS. Considering the requirements above, none of the existing designs addresses all of them. Considering NOTES, either an additional channel is missing or the payload is not investigated. LESS designs either lack instrument channels or cameras, instrument exchange is not provided, or payload is not addressed. For both applications, the aspect of sterility has only been considered by Roppenecker et al., 2014 and by the Flex[®] Robotic System (FDA approved medical device). While NOTES designs exhibit similar features compared to manual commercial flexible endoscopes with established sterilization procedures, the sterilization of robotic parts (electronics) is not explored. For LESS in general, the concept of sterile design and sterilization considerations are addressed. The sterile manufacturing process by Roppenecker et al., 2014 is promising. However, it foresees manual actuation, such that the sterilization of robotic components is not discussed. The adaptation

of the Flex[®] Robotic System is not possible for LESS since the design proposes a sequential insertion by articulating only the most distal section with two DoF. The rearrangement of the whole posture requires full retraction and deployment. It is suitable for tortuous, natural orifices pathways, but not efficient for movements in free space. An articulated port design addressing all the mentioned requirements constitutes a challenge in the current state of the art.

This results in the relatively less mature development state of LESS systems in comparison to NOTES, which is reflected in the rudimentary and rare trials/studies (Table 1, 2 and 3, last row). Several prototypes for NOTES are evaluated in animal trials, while none of the prototypes for LESS exceed the stage of the evaluation on a phantom. This indicates the demand for more research in this field.

A broader challenge is the lack of a common design parameter space. This can be observed for NOTES and LESS considering the number of DoF, the articulated lengths, the number of articulated sections, and the maximum curvature. Although it is intuitively appropriate to aim for more DoF or higher curvatures, there exists no quantitative reference value. This is due to the lack of anatomical data for specific applications, and respective metrics, to support design decisions and assessment. Soft tissue environments are challenging to measure compared to bony structures, that can be extracted from preoperative images and are not altered during the surgery. The evaluation of the proposed systems is therefore usually limited to the performance of surgical tasks using instruments or evaluations of stiffening. In general, a design guideline for articulated ports for LESS is demanded to enhance the research in this field.

Table 1: Parameter summary of articulated robotic NOTES ports.

For trials: C=Cadaver, H=Human, P=Phantom, A=Animal

For camera: I=Inserted, F=Fixed, A=Articulated

¹ Calculated based on the data provided in the literature

² Only the most distal link can be articulated

³ Degani et al., 2006

	Roppenecker et al., 2014	Thakkar et al., 2015	NeoGuide	STRAS
		Flex [®] Robotic System		
Outer \varnothing [mm]	13 ¹	15	no data	18
DoF	2	2 ²	15	3
Segment lengths x (mm/mm)	1 (80)	600	1480	220
Max Curvature m^{-1}	52	13 ³	no data	no data
Instrument Channels x (mm)	2 (2.8/2.8)	2	no data	2 (4.2/4.2)
Additional Channels (mm)	no	no	no	no
Tool Exchange	yes	yes	yes	yes
Camera	I 2DoF	F	F	F
Payload	yes (no data)	no data	no data	no data
Sterility	Y	Y (FDA approved)	FDA rejection	no data
Trials/Studies	none	P,A,H	C	P,A

Table 2: Parameter summary of articulated robotic NOTES ports (second part).
 For trials: C=Cadaver, H=Human, P=Phantom, A=Animal
 For camera: I=Inserted, F=Fixed, A=Articulated

	ViaCath	Rosen et al., 2017	K-Flex KAIST	Shang, Noonan, et al., 2011
Outer \varnothing [mm]	16	12	17	12.5
DoF	3	2	4	7
Segment lengths x (mm/mm)	2 (10/25)	81	-	3 (35),2 (40)
Max Curvature m^{-1}	no data	30.2	-	21.2
Instrument Channels x (mm)	no data	2 (2.3/2.3)	2 (4.2/4.2)	1 (3)
Additional Channels (mm)	no	no	no	no
Tool Exchange	yes	yes	yes	yes
Camera	I	I	F	F
Payload	no data	no data	no data	no data
Sterility	no data	no data	no data	no data
Trials/Studies	P,A	none	P,A	P,A

Table 3: Parameter summary of articulated robotic NOTES ports.
 For trials: C=Cadaver, H=Human, P=Phantom, A=Animal
 For camera: I=Inserted, F=Fixed, A=Articulated

¹ Calculated based on the data provided in the literature
² Permanently integrated instruments
³ Shiva et al., 2016
⁴ Y. J. Kim et al., 2014

	Y. J. Kim et al., 2013	Roppenecker et al., 2014	Roh et al., 2015	Cianchetti et al., 2014
Outer \varnothing [mm]	22	13 ¹	30	32
DoF	4	2	4	6
Segment lengths x (mm/mm)	2 (200/200)	1 (80)	2 (150/100)	2 (50-81/50-81)
Max Curvature m^{-1}	no data	52	10	39.3
Instrument Channels x (mm)	1 (18))	2 (2.8/2.8)	none ²	none
Additional Channels (mm)	none	none	none	none
Tool Exchange	yes	yes	no	no
Camera	none	I 2DoF	F 3DoF	none
Payload	2N	no data	no 3N ³	1.5N ⁴
Sterility	no data	yes	no data	no data
Trials/Studies	none	none	P	none

3.1 CONTRIBUTIONS

This thesis contributes to advancing the field of robotic Laparo-Endoscopic Single-site Surgery (LESS) by investigating the potential of an articulated robotic port. While the focus of research often lies on the design of multi degrees of freedom instruments to provide precise and intuitive control, the port design itself is still neglected.

The main goal of this thesis is to design a robotic articulated port for single-site partial nephrectomy based on the definition of comprehensive requirements. A general design structure is proposed by studying the current laparoscopic surgical procedure with an expert in the field of oncological urology. For the first time, the surgical workspace in the peritoneal cavity is acquired during laparoscopic partial nephrectomy procedures on real patients. The

collected data, in combination with the formulated surgical task objectives, is used to determine the port parameters and optimize the segment lengths. A patient and incision location independent design is introduced and experimentally evaluated using a port prototype and an abdominal phantom. Sufficient reachability and orientation inside the abdomen is proven to be possible without moving the kidney.

To counter the flexible nature of an articulated port, stiffening methods are integrated and evaluated. A direct comparison of granular and layer jamming is performed for the first time in the same port prototype. Further, stiffening synergy effects between tendon tension stiffening, granular jamming, and layer jamming are investigated.

Design of a robotic articulated port for surgical use, including actuation, stiffening integration, tool deployment, and exchange is proposed. The state of the art is extended by addressing a sterile coupling mechanism and the integration into the overall surgical workflow.

Although this work focuses on the specific application of single-site partial nephrectomy, a guideline for general requirements and anatomical workspace acquisition for LESS is provided. The abdominal measurement results are further applicable to other ports or clinical studies. The measurement approach itself can be transferred to other abdominal applications. As far as the results of the stiffening method are concerned, the results contribute to general research on the stiffness increase of flexible manipulators.

Part II

CONSTRAINTS AND REQUIREMENTS

4

ANATOMICAL CONSTRAINTS

To provide a basis for design parameterization, the geometric anatomical constraints must be measured. Considering the selected application of partial nephrectomy, the following relevant anatomical structures are identified: the abdominal free space in the insufflated state with the abdominal wall as a boundary (Abdominal Space), the peritoneum over the kidney (Region of Interest), and the incision locations for the single-port (Incision Location). In the region of interest, points can be defined which must be accessible (Target Points). A suitable measuring approach for clinical use is developed and described, the data post-processing is demonstrated, and the results are presented.

4.1 DEFINITIONS

The common medical imaging technology for partial nephrectomy, computed tomography (CT), creates images of different tissue types, while the patient lies on her/his back without free space in the abdomen. In the operation room (OR), the patient is mounted in an over-stretched lateral position for kidney exposure, as described in the introduction of this thesis. Since the abdomen and the abdominal organs consists mostly of soft tissue they shift depending on the patient positioning. Insufflation (positive pressure of $15\text{mmHg} = 2\text{kN/m}^2$) inside the abdomen is used to create free space pushing the organs, and especially the abdominal wall, away from each other. In a non-insufflated state, there is no free space inside the peritoneal cavity for instruments. This free space cannot be captured by preoperative imaging. After the insufflation, anatomical regions can be differentiated: The Abdominal Space (AS), the Region of Interest (RoI), and Incision Location (IL).

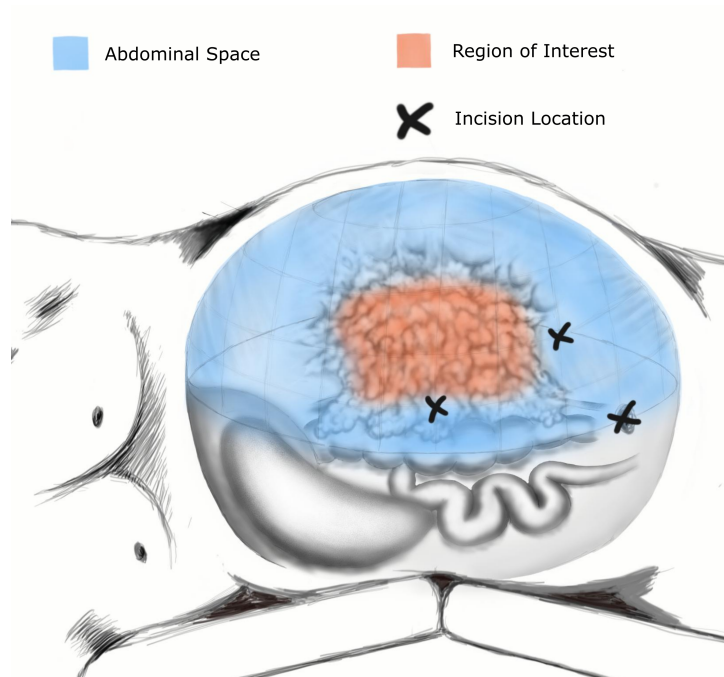


Figure 20: Anatomical regions: The abdominal space (AS) in blue, the region of interest (RoI) in red, and the incision locations (IL) as black crosses.

4.1.1 *Abdominal Space*

The abdominal space describes the volume in the peritoneal cavity created by the positive gas (CO_2) pressure after the intestine is separated from the peritoneum (Figure 20, blue space). The abdominal space is restricted by its borders: posterior by the posterior abdominal wall and the peritoneum covering the kidney, anterior by the anterior abdominal wall, medial by the intestines, other intraperitoneal¹ organs, cranial by the diaphragm, and caudal by the pelvic cavity. It is measured in cm^3 . The abdominal space contains gas only.

4.1.2 *Region of Interest*

The region of interest is an area that is defined by the peritoneum surface covering the kidney when the patient is in the lateral position and the abdominal cavity is insufflated (Figure 20, red surface). The area is measured in cm^2 . Here, the overall surface is of interest, as the tumor can appear anywhere on the kidney. By ensuring coverage of the whole RoI, the tumor at any location can be reached and resected.

4.1.3 *Incision Location*

The incision location is defined as a percutaneous² incision in the abdominal wall through which the robot must be inserted into the peritoneal cavity (Figure 20, black cross). Here it is

¹ located inside the peritoneal cavity

² through the skin

described as a point in 3D space on the anterior abdominal wall in mm. A preferred IL is the navel due to positive cosmetic outcomes.

4.2 ACQUISITION

The goal of defining and measuring these geometric characteristics, is to provide a dataset that can be used for the articulated port design parameter optimization. This data set should then contain the anatomical constraints mentioned above in order to fully describe the surgical workspace. Therefore, a data set is defined by the following features: the abdominal space, the region of interest, and the incision location. One patient can provide several data sets, as multiple incision locations can be selected, which will change the geometric relationship of the features to one another and thus alter the design parameters. In order to measure the surgically available space in the peritoneal cavity, a measurement setup in the OR is desirable for data acquisition. Since the ideal case would be to measure after insufflation, a sterile measurement approach is desired. In addition, the measurement procedure should not prolong the operation or significantly impede the surgical workflow.

Ideally, the abdominal space would be measured from the inside in a non-tactile manner, e.g. using a stereo camera. Such measurements would need compatible hardware and software for data post-processing. In this thesis, an alternative, more approachable method is chosen. Using a passive 6 axis measurement arm the FaroArm[®] and the Faro ScanArm[®] (Faro Europe GmbH & Co. KG, Kortnal-Münchingen, Germany), a tactile and a non-tactile measurement is possible. The provider offers a specific software (Cam2Measure) including several measuring modes and data post-processing. The arm has a length of 2.7 m and an accuracy of 41 μm for tactile measurements and 25 μm for non-tactile measurements. Non-tactile data acquisition is preferable for sterile measurements. However, internal measurements can only be performed tactilely, as the entire LaserArm[®] is too large and not sterile to be inserted through the incision.

To acquire enough data to create a closed volume and measure the defined features, the anterior abdominal wall is scanned using the ScanArm[®] from the outside. Further, the region of interest and the posterior abdominal wall are measured tactilely from the inside³. To be able to collect points inside the body, the measuring arm needs a sterile tip. A sterile cylindrical shaft is chosen and a suitable adapter for fixation on the arm is designed. The shaft has to be calibrated to find a transformation between the joint angles and the tip position of the shaft when fixed on the measuring arm. The calibration was performed using a spheric calibration and the calibration software provided by the manufacturer. For an efficient calibration, a sphere with a predefined radius is positioned at the tip. Since the shaft has a cylindrical shape, it does not exhibit a sphere at its tip. Hence, a calibrating shaft was built, having the same length. It consists of a cylindrical carbon tube with 6 mm diameter, and a cone-shaped brass transition piece with a glued steel sphere tip of 2.5 mm radius. The calibration accuracy was 1.2 mm. This value is sufficient for the intended application, since the tactile measurement of soft tissue is implicitly linked to certain deviations.

³ The measurements were conducted with the patients' acceptance and approval of the Ethical Review Board of Hannover Medical School.

4.2.1 Measurement Workflow

The measurements are conducted during the surgery in the OR. Therefore, the measuring arm is placed next to the patient at an approximate distance of 1 m anterior to the patient. Parallel to this, the placement of the first port and the insufflation of the relaxed patient's abdomen take place. At this point, the measurement procedure interrupts the surgery, as shown in Figure 21(0-1). First, the anterior abdominal wall is scanned from the outside non-tactilely. As a result of the scan, a point cloud is obtained (Figure 21(1)). Additionally, a surface of the foot of the patient table is measured with the ScanArm, which defines a plane parallel to the patient as a reference for data post-processing (Figure 21(2)).

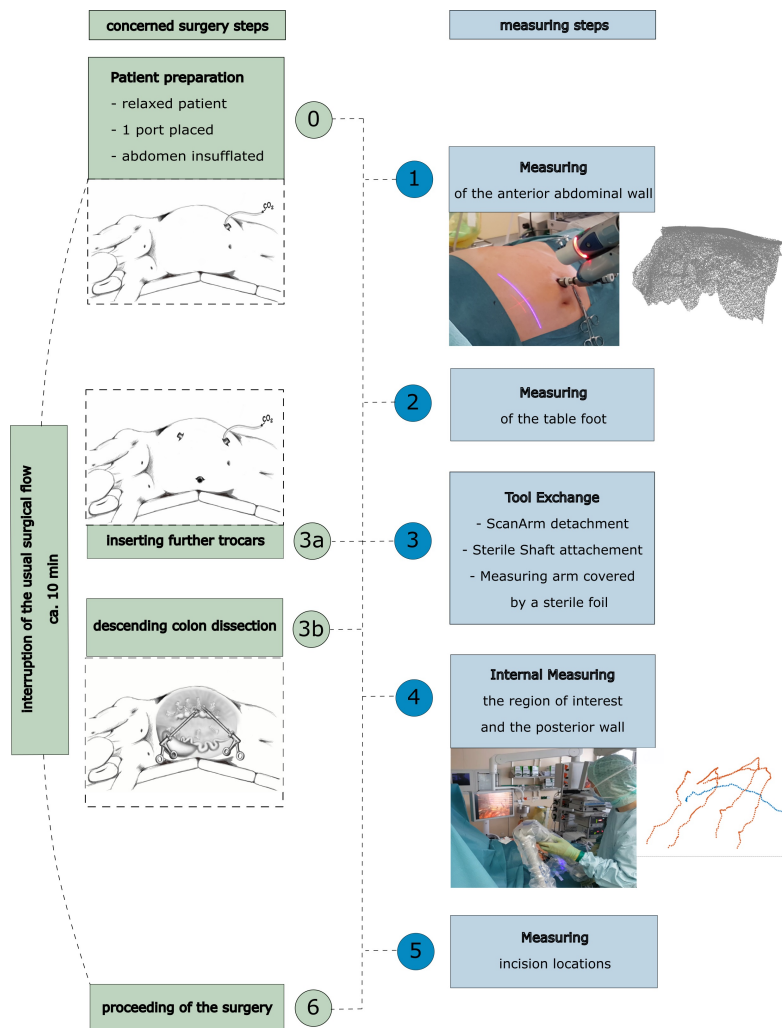


Figure 21: Data acquisition workflow: The external measurements of the anterior abdominal wall take place after the placement of the first port; The internal measurements take place after the instrument and the endoscope ports are placed. The dissection of the descending colon is performed when the left kidney is considered.

The ScanArm is detached to use the sterile shaft. Further, the whole measuring arm is covered by a sterile foil, to prevent patient contamination (Figure 21(3)). Meanwhile, the surgery proceeds to the next step, and two ports used for the surgical tools are placed. With the tools, the

descending colon is dissected (Figure 21(3a-3b)). In the fourth step of the surgery, the internal measurements are conducted. The sterile shaft is inserted through one of the ports. Several lines (3-5), consisting of several points (7-15), are measured by touching the peritoneum covering the kidney and a part of the posterior wall with the shaft's tip as shown in Figure 21(4). The border to the posterior wall is marked by the blue line. The surgeon's freedom of movement is restricted in the OR, so that the acquisition of additional data in the abdomen is complicated and leads to an undesired prolongation of the operation. Finally, three possible incision locations for LESS are measured outside the patient with the shaft. One of the IL is always the navel, as it provides the best cosmetic result. The other two are chosen by the surgeon based on his experience (Figure 21(5)). With the identification of the renal vessels, the operation can then be performed as normal. (Figure 21(6)). The surgery is prolonged for about 10 minutes by the overall measurement procedure.

4.2.2 Post-Processing

To create a closed volume, all measured features have to be combined to a single point cloud. Originally, all points are measured with respect to the measurement arm's coordinate system that lies in its base. First, all points are rotated, such that one coordinate axis is parallel to the measured patient table base. The second axis is defined as the vertical axis of the FaroArm[®]. The third axis is calculated by the cross product of the two existing axes (Figure 22(1)). Second, the RoI is extracted from the red lines by considering only the points below the blue line and interpolating the lines to a surface using *meshgrid*⁴. The result is a point cloud. The geometrical center of mass is used as a reference point to set the location limits along the y-axis. The limits to the side of the diaphragm and the pelvic cavity are set, such that the extension of the volume in the y-axis is 350 mm symmetrically to the geometrical center of mass of the RoI, as shown in Figure 22(2). Subsequently, the scanned abdominal wall and the uncut red lines are extrapolated to the borders on the y-axis using *meshgrid* as well (Figure 22(3)). Planes perpendicular to the y-axis are created, such that they close the space, as shown in Figure 22(4). Further, a horizontal plane perpendicular to the z-axis at the height of the navel is created, such that it closes the volume from the bottom. All surfaces created following steps (2) to (4) are then combined. For orientation optimization purposes, the RoI is converted to a polygon surface to obtain the surface normal vectors, and the workspace is divided into voxels with a voxel side length of 5 mm as a compromise between accuracy and computational efficiency. The voxels inside the workspace are indexed with one and voxels outside with zero for optimization purposes (Figure 22(5)).

4.3 RESULTS

Overall, 9 patients were measured. For each patient, three incision locations were defined, resulting in 27 data sets. An example abdominal space is shown in Figure 23 with all features and the resulting abdominal space volume. Having the voxel representation of the abdominal space, the available volume can be calculated. All measurements are taken by the same surgeon and prolong the surgery insignificantly by approximately 10 minutes. No complications for the patients occurred during the measurements.

⁴ a customized function interpolating/extrapolating points to a 3-dimensional grid

The datasets are used for design parameter optimization. Target point positions and their normal vectors (Figure 23) can be defined as objectives for the optimization algorithm. The outer boundary of the abdominal space provides data for collision avoidance. All acquired workspaces can be found in the Appendix A.

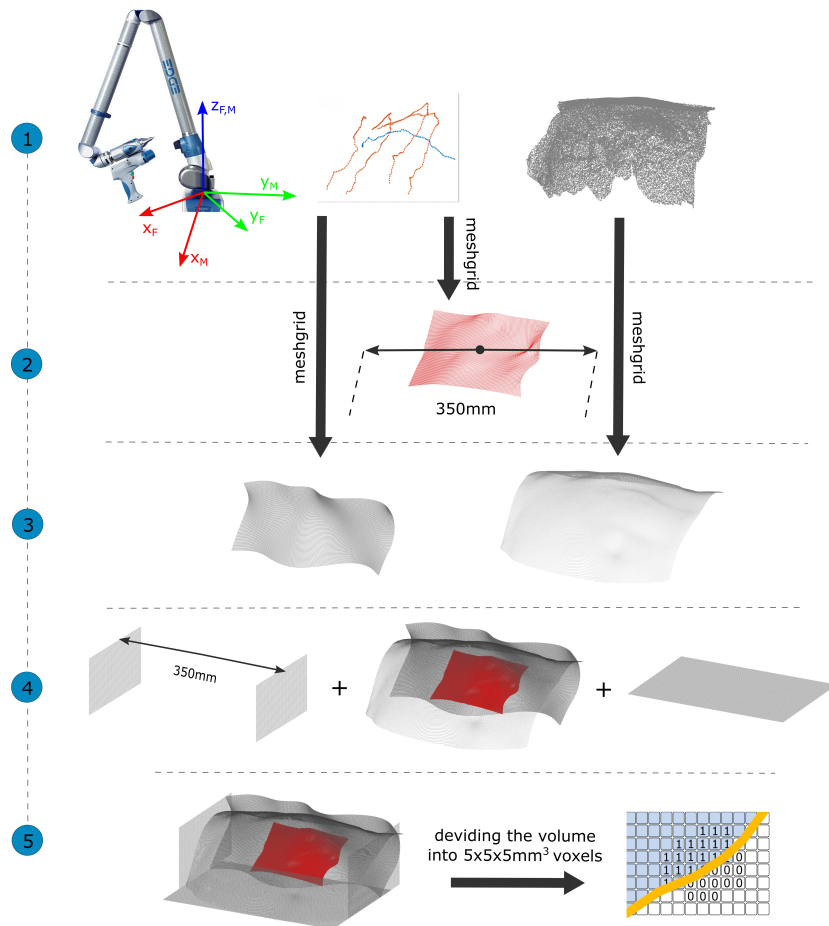


Figure 22: Data post-processing: 1) Rotation of the coordinate system of the FaroArm[®] (©Faro Europe GmbH & Co. KG, Kortnal-Münchingen, Germany) for measurements; 2) Interpolation of the RoI and defining the volume limits on the y-axis; 3) Extrapolation of the anterior (in front) abdominal wall and the posterior (in the back) abdominal wall; 4) Generation of bottom and limiting planes on y-axis; 5) Combining the created point cloud to a closed data set and transforming the volume into a voxelized grid.

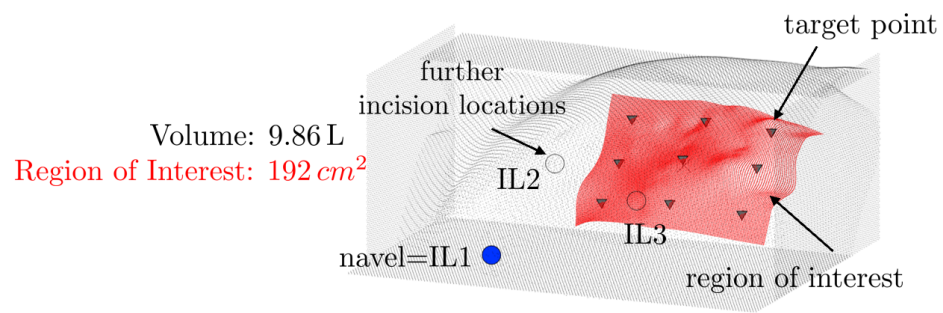


Figure 23: Abdominal space example including target points on the RoI and three incision locations. The volume can be calculated from the voxel representation of the abdominal space. The area of the RoI is calculated by integrating the sub-areas between the red points.

5

FORCE CONSTRAINTS

Besides anatomical geometric constraints, partial nephrectomy exerts certain tissue manipulation forces onto the robot structure. Considering the surgical steps presented in the introduction, specific tasks including tissue interactions are identified in this section. The tasks presented correspond to particular load cases. In order to quantify these in an experimental setup, the different load cases are replicated using porcine kidneys and a tool equipped with a force sensor. The evaluation results serve as a basis for the prototypical assessment with regard to stiffness.

5.1 TASK DEFINITIONS

In order to identify specific tasks during surgery, the surgical steps mentioned in the introduction are considered. Figure 24 shows relevant instrument-tissue interactions. The tasks result from the surgeon's experience in performing laparoscopic surgery with straight instruments. The corresponding loading cases are defined below.

5.1.1 *Tearing Loading Case*

A common task is to dissect the peritoneum and pararenal fat to access some of the anatomical structures, such as the renal vessels (renal vein and artery) or the tumor itself. This can be performed by tearing the tissue. A closed gripper or a suction tube can be used, applying force to the tissue in a certain direction until it tears, as shown in Figure 24a. This loading case is defined as tearing. No data on this loading case is found in the literature.

5.1.2 Spreading Loading Case

For the same task of exposing certain anatomical structures, two tools can alternatively be used to create or enlarge an opening. Grippers or a suction tube are mostly used while moving in opposite directions and spreading the tissue, as shown in Figure 24b. This loading case is defined as spreading. No data on this loading case is found in the literature.

5.1.3 Lifting and Partial Lifting Loading Case

Once a sufficient opening has been created by tearing or spreading, tissue can be moved (non-invasively) to further expose anatomical structures. This usually involves elevating the pararenal fat tissue or the kidney itself to expose the renal vessels and the ureter, as shown in Figure 24c. This loading case is defined as partial lifting. No data on this loading case is found in the literature.

If complete mobilisation of the kidney is considered, the kidney is lifted and moved around in order to create the most adequate access to the tumor. The load is equivalent to the weight of a human kidney and is defined as lifting. Lifting the kidney is also required when performing a radical nephrectomy.

Human kidney weight is reported to range between 125-170 grams (Boron et al., 2009).

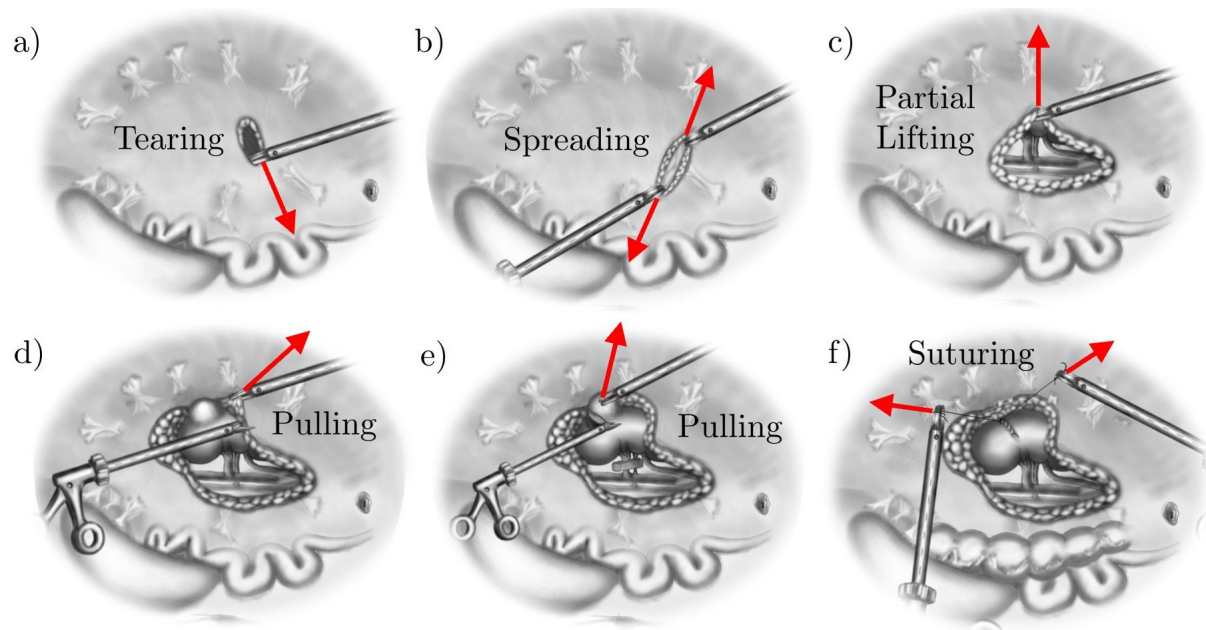


Figure 24: Surgical task identifications with applied forces: a) Tearing the tissue with an instrument; b) Spreading an existing opening with two instruments; c) Lifting the tissue to expose anatomical structures; d-e) Pulling tissue to provide tension and facilitate resection; f) Suturing the wound after tumor resection.

5.1.4 Pulling Loading Case

The most common task is the dissection of the tissue using scissors. A standard method for performing this task is to pull tissue with a gripper to tension it and cut the tensioned tissue with scissors, as shown in Figure 24d for access to the renal vessels and in Figure 24e for tumor resection. Since this is the most common case, the pulling forces are measured in relation to the haptic feedback for robotic surgery (U. Kim et al., 2015). A gripper is equipped with miniature force sensors and is evaluated on tissue phantoms that measure the gripping and tensile forces. A maximum pulling force of 1.47 N is reported.

5.1.5 Suturing Loading Case

The suture is used to reconstruct the tissue after resection of the tumor or dissection of the peritoneum. In this task, two grippers must handle a suture needle and thread to close a wound by piercing the tissue and tying a knot, as shown in Figure 24f. The forces required to pierce the tissue were determined by Okamura et al., 2004 with forces of 2.5 N. Kitagawa et al., 2005 investigated knot tying forces for various suture materials. Using human hands, forces between 1-4 N were measured as a function of the suture material.

5.2 ACQUISITION

While data for lifting, pulling and suturing are given in the literature, data for tissue tearing, spreading and partial lifting must be recorded. To quantify the different load cases, porcine kidneys are used as test objects. It is well-known that porcine anatomy is sufficiently close to human anatomy and has similar tissue characteristics. An experimental test bench is designed and built to perform the evaluation and measure the forces. The surgical scenario is replicated by a wooden plate with an inclination of 30° to an aluminum base plate and two openings attached to the same aluminum plate, as shown in Figure 25a. The ports consist of

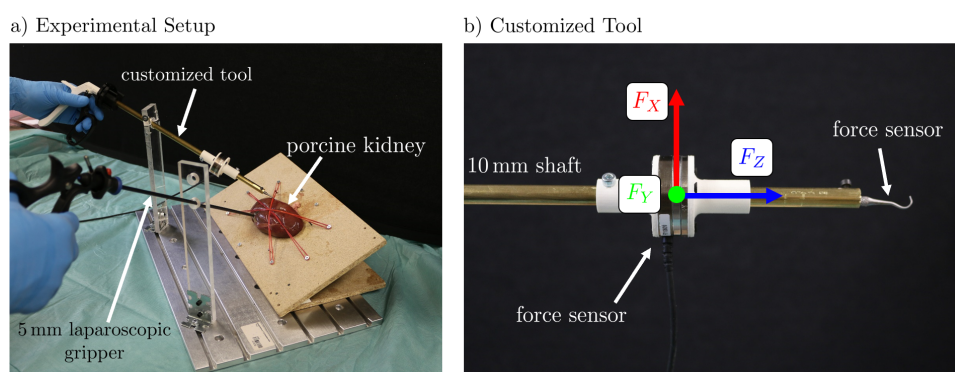


Figure 25: Experimental loading case set up: a) Overall test bench showing the fixed porcine kidney and two tools approaching the kidney through two ports; b) Customized tool for force measurements enabling force measurements in three directions.

two acrylic glass bars and allow the use of instruments. The wooden plate and the ports are arranged in such a way that sufficient triangulation is guaranteed. Two tools are used for the experiments, a laparoscopic 5 mm tool (HiQ+ series grasping forceps, Olympus Corporation,

Tokyo, Japan) and a custom tool with integrated force/torque sensor (ATI Mini40, ATI Industrial Automation, Apex, NC, USA), as shown in Figure 25b. The sensor enables measuring of three forces with an accuracy of $50^{-1}/25^{-1}$ N in x/y and z direction. The customized tool shaft has a diameter of 10 mm and is equipped with a hook at the tip to enable some tissue interaction.

The kidneys are attached to the wooden board with three elastic bands crossing in the middle of the kidney, as shown in Figure 26, which replicates the kidney fixation in the peritoneum. Each loading case was performed by an experienced surgeon three times on two different porcine kidneys. Tearing is shown in Figure 26a, spreading in Figure 26b, and partial lifting in Figure 26c. During a single measurement repetition, the typical motion for the respective loading case is repeated several times. The forces were samples with 40 Hz.

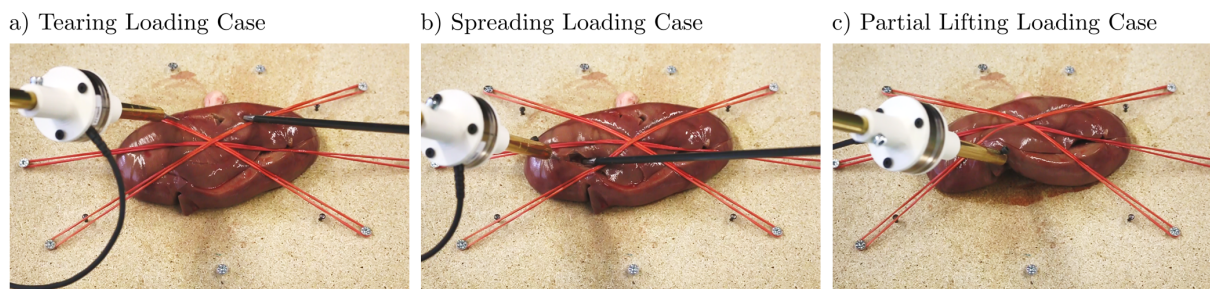


Figure 26: Experimental loading case evaluation with porcine kidneys attached to a wooden plate by elastic bands: a) Tearing; b) Spreading; c) Partial lifting.

5.3 RESULTS

The results are shown in Figure 27 for the three loading cases and two kidneys each. The three forces, F_X , F_Y , and F_Z , and the resulting force F_{res} , defined by the square root of the sum of the squares of each component, can be depicted. The forces are given in Newton. The number of samples is shown on the horizontal axis. Each plot presents the results of the three repetitions on one kidney. The data is concatenated and the repetitions are indicated by a black dotted line.

5.3.1 Tearing

Figure 27a shows the results of both kidneys for the tearing loading case. The force magnitude of both kidneys is quite different. While a force maximum of 2.95 N is recorded for the first kidney, the force maximum value for the second kidney reaches 8.04 N. Since the tearing is performed until the tissue begins to tear, it depends on the penetration depth of the customized tool. For the second kidney, higher depths were evaluated, resulting in higher tearing forces. A typical force course for tearing can be observed, first rising and then decreasing abruptly when the tissue tears. Several peaks per repetition indicate several tearing motions.

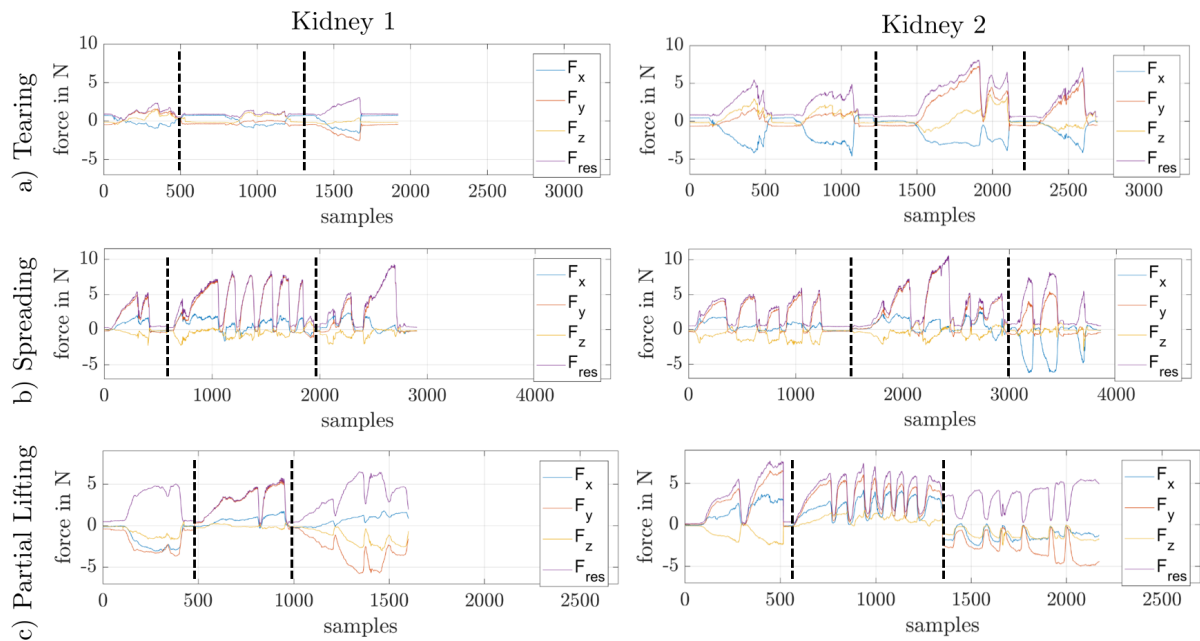


Figure 27: Loading case experimental results showing individual and resulting forces over all repetitions for both kidneys, black dashed lines indicate the repetitions: a) Tearing loading case; b) Spreading loading case; c) Partial lifting loading case.

5.3.2 Spreading

The spreading results are shown in Figure 27b. The force course with several peaks reflects the typically repeated motion of spreading the tissue and tool rearrangement. Here, similar values for both kidneys are recorded with a maximum of 10.6 N. This loading case requires the greatest force achieved during the entire force evaluation.

5.3.3 Partial Lifting

The partial lifting results are illustrated in Figure 27c. Forces up to 7.69 N are observed. The peaks correspond to the repeated partial lifting motions during a duration of measurement repetition. The peaks correspond to the repeated partial lifting movements during a measurement repetition period. Due to the connection of the kidney to the surrounding tissue, the partial lifting requires higher forces than those needed to lift a mobilized kidney alone.

5.4 CONCLUSION

The quantified required forces for typical surgical tasks during partial nephrectomy are summarized in Table 4. Although the forces act directly on the deployed instruments, they propagate further to the articulated port and are utilized in the evaluation part of this thesis to assess the achieved stiffness with the articulated port prototype. The generated experimental results in this chapter are understood as an initial study results of forces required for tearing, spreading, and partial lifting.

Table 4: Force requirement result for 6 different loading cases. Median, 25th and 75th percentile, and minimum and maximum values are depicted.

	Tearing	Spreading	Partial Lifting	Pulling	Lifting	Suturing
Median in N	0.93	2.28	3.52	-	-	-
25 Percentile in N	0.81	0.63	1.57	-	-	-
75 Percentile in N	2.67	4.63	4.9	-	-	-
Maximum in N	8.04	10.6	7.69	1.47	1.67	2.5/4

Part III

ROBOT SYSTEM DESIGN

6

ROBOTIC SYSTEM VISION

This chapter contains general design decisions and formulates constraints for the parameter design space. First, this chapter discusses the robotic articulated port to be integrated into the surgical workflow and proposes the master-slave control paradigm. After discussing the sterility concept, the overall design is presented and divided into several design units. The structure of the articulated port is designed to be a tendon-driven continuum robot. Each unit must meet certain requirements, which are summarized and amplified in this chapter. Throughout the chapter, the articulated robot is also referred to as a manipulator.

6.1 ENVISIONED SURGICAL WORKFLOW

Considering the surgical procedure of partial nephrectomy, the composition of the main protagonists in the operating room is important. The composition proposed in this thesis is shown in Figure 28. The patient is placed on the table in the middle of the room. The anaesthetist is on the side of the patient's head and the assistant nurse is close to the patient's feet. The robotic system and the assistant surgeon are positioned anterior to the patient. The surgeon controls the robot from a distance and uses a console for control. This is the so-called master-slave control paradigm. The other paradigm is patient-side control, where the surgeon sits at the patient's bedside. The console provides two input devices for teleoperation of the articulated port or the surgical instruments used. The motion of the input devices is mapped to the motion of the robotic tools. The advantage of this concept is the ergonomic working position for the surgeon. Switching between instrument control is provided. The surgeon receives 3D images on a 3D monitor as visual feedback. Wearing 3D glasses enables depth perception.

Once the composition is determined, the workflow can begin with the preparation of the patient, placing the patient in a laterally overstretched position. An incision is made at the navel

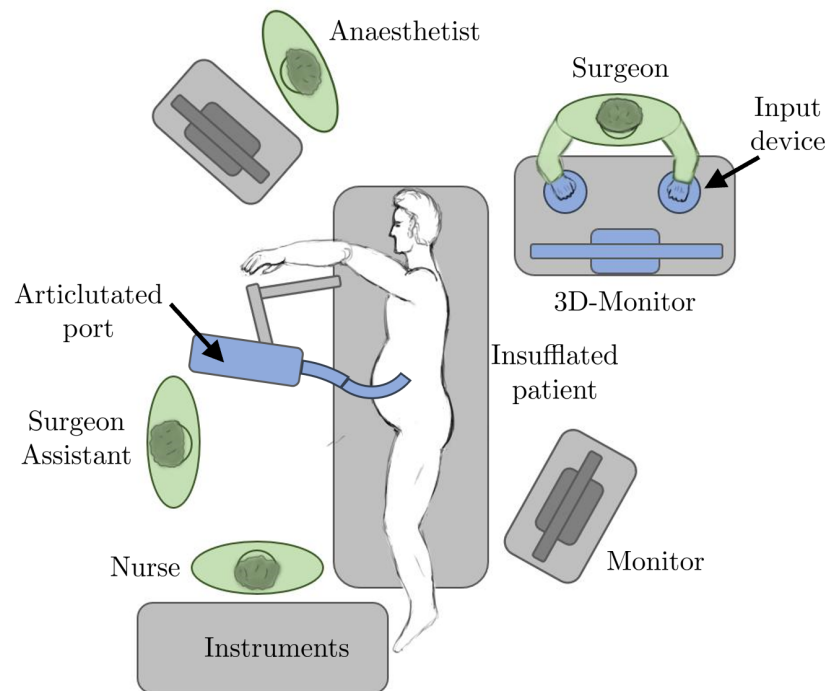


Figure 28: Composition in the operation room using the robotic articulated port for LESS partial nephrectomy.

and a port is inserted, which provides an insufflation interface and is airtight. The robot is mounted on a passive articulated arm and inserted into the port. Now, the surgeon can start to teleoperate the robot by deploying it into the peritoneal cavity with visual feedback from an integrated camera. The articulated port is deployed into the body until the desired location is achieved. The surgeon can activate a stiffening method to solidify the articulated port to provide increased stability. Subsequently, surgical instruments are attached to the robotic system by the assistant surgeon or a nurse, and the instruments are deployed and articulated. To access various anatomical structures, the surgeon can release the stiffening, reposition the articulated port, stiffen it again, and proceed with the surgery. The surgeon can request an instrument exchange at any time by communicating with the surgical staff. The irrigation or suction instruments are controlled by the assistant manually. They are introduced through an additional channel in the articulated port. The surgery then follows the steps described in the introduction of this thesis. The tumor can be evacuated with the retraction of the articulated port. The passive articulated arm that carries the robot can be moved to the side so that the assistant surgeon has enough space to manually suture the incision at the navel. The surgical workflow is summarized in Figure 29.

6.2 OVERALL DESIGN

In addition to the articulated port, the overall system design requires further units: an actuation unit, a rigid port, a mounting arm, and a single DoF translation unit, as shown in Figure 30.

Here, the general structure of the articulated port is presented first. In the state of the art sec-

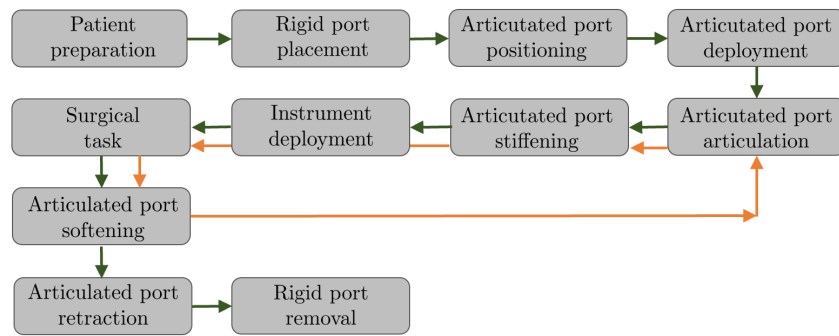


Figure 29: Envisioned surgical workflow using the articulated port.

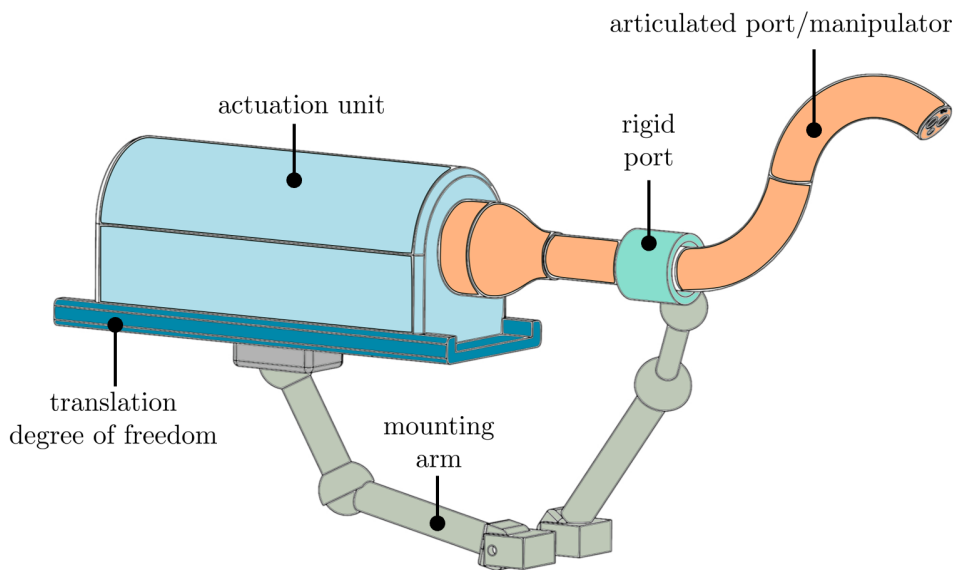


Figure 30: Overall robotic system design showing the identified units.

tion of this thesis, flexure hinges, serial, hyper-redundant, or fluidic structures are proposed as articulated ports. Serial structures exhibit relatively long rigid links and joints inhibiting the deployment and exchange of the instruments. Fluidic actuators are space expensive, such that the available space for working channels is limited. Hyper-redundant designs and flexure hinges have been shown to provide sufficient stability in combination with tendon-actuation. However, they are limited to achieve high curvature due to the alternating joint arrangement: two consecutive joints are rotationally displaced by 90° , allowing for bending in two directions. In this work, an alternative structure for an articulated port is proposed: a tendon-driven continuum structure. It was used for the construction of flexible miniature instruments that offer high maneuverability. The continuum structure allows for bending in two directions at any point along the whole length, increasing the maximum bending curvature.

The actuation unit handles the degrees of freedom of the tendon-driven articulated port. DC motors are selected as actuators in this thesis because of their precision, their established control algorithms and their compact design.

An additional translational degree of freedom is beneficial to allow the articulated port to

be introduced into the peritoneal cavity. In addition, this allows a variation of the insertion length, which can vary due to the different sizes of the abdominal cavity of each patient. All aforementioned units must be carried by a mounting arm. The passive mounting arm allows for the positioning of the units and stabilizes its posture. To reduce the load on the incision during translation and bending of the articulated port, a rigid port is introduced to straighten the articulated port at the incision site and outside the human body. Further, the rigid port is air-proof and provides an insufflation interface. It is mounted on an articulated passive arm and is fixed to the patient's table.

6.3 STERILITY CONCEPT

For use in the OR, the components of the entire robotic system must be sterile. This can be achieved by prior sterilisation and sterile production of the components, as well as encapsulation of non-sterile components into a sterile cover. One can distinguish between single- and multi-use instruments. Single-use components will be disposed of after first use in the OR. They are usually manufactured and sealed in a sterile environment. In the OR, they are unsealed right before their use and are handled with sterile gloves by the assistant surgeon or the surgeon. Flexible laparoscopic instruments often require sterile manufacturing. The reason for this is their complex wire-driven design and structures that are difficult to access, requiring time-consuming and costly sterilization procedures. In particular, the risk of residual contamination within the complex tool structure motivates the trend towards disposable tools.

Multi-use instruments require cleaning, disinfection and the application of an instrument dependent sterilization method, as stated in the guidelines by The German Society for Sterile Goods Supply (Deutsche Gesellschaft für Sterilgutversorgung e.V.¹). Considering the flexible structure and the intended application, steam pressure sterilisation (Kramer et al., 2008) is recommended as the sterilisation method, which, according to DIN EN 285, provides for temperatures of 134 ° and pressures between 0.03-3 bar. This requires components with appropriate specifications and a design that allows pressure compensation. Other sterilization methods that require lower temperatures and atmospheric pressures, such as sterilization with ethylene oxide (C₂H₄O), formaldehyde (CH₂O) or hydrogen peroxide (H₂O₂), require further consideration of hazardous substances.

Alternatively, the instruments and devices can be covered by a sterile foil. This approach is commonly used for various devices in the OR. It has been proposed for the sterile use of actuation units for concentric tube continuum robots in Burgner et al., 2013. In addition, the FDA-approved surgical robots of the da Vinci® series use a sterile cover between the serial robot arms and surgical articulated instruments, as proposed in the US patent of Cooper et al., 2011.

The rigid port in this work, including the mounting station, can be designed as a multi-use sterilizable unit. It has a simple structure and no confined spaces. Such components are already designed as multi-use nowadays. The mounting arm is already a common gadget in the OR, and is sterilized prior each intervention. The manipulator cannot be encapsulated, as tools have to be deployed through its inner lumen. Since the manipulator is also a highly

¹ Risk assessment and preparation classification of medical devices, <https://www.dgsv-ev.de>, accessed on 12.06.2019

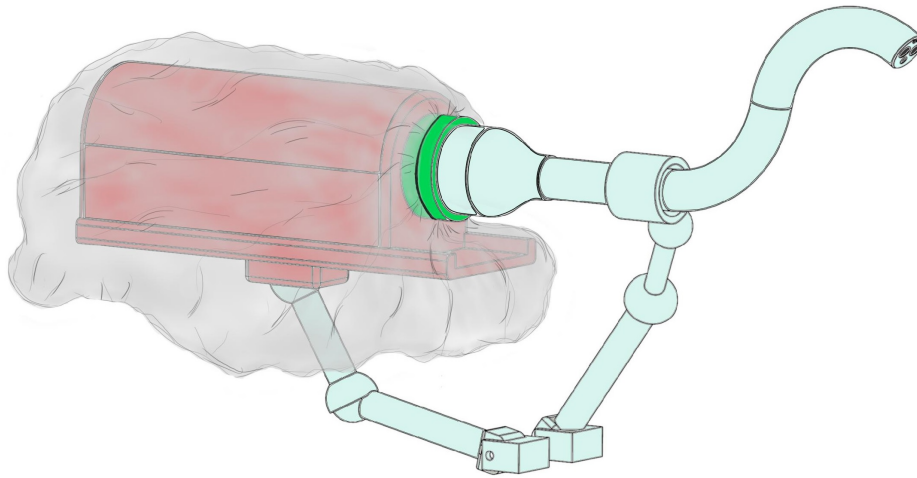


Figure 31: Overall robotic design with sterile components. Turquoise: sterile single-use articulated port, sterile multi-use mounting arms, sterile multi-use rigid port; red: non-sterile multi-use actuation unit and translational mechanism covered by a sterile foil; Green: Coupling mechanism containing the foil.

flexible tool with a complex structure, it is more reasonable to design it as a single-use instrument. Since the actuation unit contains the motors and precision mechanical components, it is too expensive to design it to be single-use. To enable multi-use, the actuation unit can be sterilizable or encapsulated with a sterile foil. For sterilization, the motors must either be sterilizable or installed in an airtight chamber within the actuation unit. State of the art sterilization techniques place further requirements on the actuator design, such as heat and moisture resistance and negative and positive air pressures, as specified in the chapter on sterilization requirements in this thesis. In addition, the actuation unit may exceed the dimensions of the available sterilization equipment. A sterile foil represents an effective and resource-saving alternative.

Since the articulated port is designed as single-use and the actuation unit as multi-use, a coupling between the two must be established. This sterility concept involves some adjustments to the overall design of the robot system, as shown in Figure 31. An additional unit is used to create a coupling between the articulated port and the actuation unit.

6.4 REQUIREMENTS SUMMARY

Some requirements are already listed in the sections challenges and contributions and are extended here as follows:

- Outer diameter < 30 mm
- Two instrument working channels (8 mm)
- Visual feedback
- One additional working channel for suction or irrigation (4 mm)

- Tool exchange
- Payload (1.47-10.6 N)
- Sterility (detachable articulated port)
- Temperature $< 40^{\circ}$
- Voltages < 50 V or currents < 50 mA (Bumiller et al., 2018)

The overall diameter must remain below 30 mm to limit invasiveness. Two working channels for instruments and an additional channel for irrigation or suction are required. The size of the instrument channels is set to 8 mm, as the proposed flexible instruments have a diameter of approximately 5 mm. In addition, the channels must provide sufficient space for the introduction of other surgical consumables such as needles and clips. The smaller channel is defined to be 4 mm, as the suction and irrigation tools do not need to be rigid and can be designed smaller than, for example, a gripper. The articulated port functions also a flexible endoscope. Therefore it offers 3D visualization with a stereo camera and a light source. The tool exchange via all three channels is another requirement that has to be fulfilled. As already investigated earlier in this thesis, the articulated port must provide stability when exposed to forces associated with specific surgical tasks. The payload ranges from 1.47-10.6 N. The sterility, as discussed previously in this chapter, is established by a coupling mechanism between the actuation unit and the articulated port. Hence, the design needs to provide the corresponding attachment or detachment of the articulated port. Additional safety requirements are identified which might affect the stiffening methods.

The tissue must not be exposed to dangerous temperatures, currents or voltages as listed above. Temperatures above 40° are critical for soft tissue. Currents above 50 mA can be fatal to humans. The current is also dependent on the voltage to which a person is exposed. An adult human body has a resistance of about 1000 ohm. Therefore a voltage above 50 V should be avoided (Bumiller et al., 2018).

7

STIFFENING METHOD

The aim of this chapter is to find a suitable stiffening method for the considered tendon-driven continuum manipulator for single-site surgery. The methods are classified according to the activation stimuli that lead to a stiffening reaction. After reviewing the state of the art, potential candidates are evaluated, taking into account the requirements for safe use in the human body and the stiffening potential. Particular attention is paid to methods that have proven to be practicable for flexible robots. Stiffness is defined here as the bending resistance under applied loads.

7.1 TENDON TENSIONING STIFFENING

One way to increase the stiffness of tendon-driven continuum robots is to tension all tendons simultaneously. Only mechanical stimuli are required for this. Since the tendons are already part of the manipulator, no design changes are required. Depending on the type of tendon control (e.g. DC motors) a fast stiffening can be achieved, but the resulting increase in stiffness is relatively small. This stiffening effect has been proven by several researchers. In Shiva et al., 2016 the stiffening by tendon tension is used for a fluidic soft robot. A stiffness increase of 2.3 can be realized. A combination of fluidic chamber inflation and tendon tension is used. A hyper-redundant tendon-driven manipulator consisting of rolling joints can increase its stiffness if antagonistic tendons are tensioned simultaneously. The achieved stiffening increase reaches 2.5 as shown by Y. J. Kim et al., 2014.

7.2 FRICTION BASED STIFFENING

Friction force increase between two surfaces due to normal force increase can be used as a stiffening method. Degani et al., 2006 propose a tendon-driven snake-like robot structure consisting of several vertebrae. Simultaneous tensioning of the tendons increases the friction between the vertebral surfaces and the torque required to bend the robot also increases. Mahvash et al., 2011 quantify this effect in another study. Evaluating a 40 mm long probe with a 6 mm outer diameter, a maximum force of 0.75 N is needed to deflect the most proximal link. Tendon tensions of approximately 20 N are required. This stiffening method is effective but strongly depends on the surface area. Further, the sliding angle between two vertebrae is limited to about 11° inhibiting the manipulator's range of motion.

7.3 FLUIDIC STIFFENING

In general, fluid-driven continuum robots consist of several fluidic chambers, which can expand or contract as the internal pressure increases. Through a certain arrangement of the chambers, bending, twisting or expansion/contraction can be achieved. When the chambers are pressurized, the stiffness increases naturally. This effect is also demonstrated by Shiva et al., 2016 as mentioned in the previous paragraph. Manti et al., 2016 reports in a review about stiffening methods, stiffness factors of up to 10 using fluidic chambers. Suzumori et al., 2013 propose a design with the emphasis on increasing stiffness. Proposed is a manipulator structure with one chamber in its centre surrounded by 5 other chambers (circular arrangement). When pressure is applied, the central chamber contracts and the outer chambers lengthen, creating tension inside the manipulator. Compared to a manipulator with only elongated chambers, a 3-5 times increase in stiffness is shown. A monolithic 3D-printed tendon-driven continuum robot with a pressure chamber in the middle of the structure is proposed by Kundrat et al., 2016. This approach uses a combination of tendons and a fluidic chamber, which counteract each other and increase the overall stability of the structure. This design offers the possibility of simultaneous actuation and stiffening. However, the chambers take up most of the space of the manipulator and offer little space for working channels.

7.4 FLUIDIC SHAPE LOCKING

This method exploits the increase in stiffness by interlocking geometric structures (e.g. gear teeth). If the manipulator must be flexible, the structures do not interlock. The stiffness is increased by interlocking the structures. Using an actuation mechanism to shift the structures into a locking position, increases the stiffness. One possible locking activation mechanism is a fluidic chamber. A chamber running through the center of the manipulator shifts the locking structures radially towards each other when expanding (pressurized). A prototype introduced by A. Loeve et al., 2012, uses the shape locking of wires as a result of pressurizing a central fluidic chamber. It is shown that the designed tool (5.5 mm diameter) can hold its bent shape when pressurized. The prototype, however, does not offer a working channel. Yamashita et al., 2009 propose a locking mechanism using a vacuum instead of positive pressure. When the air in the gap between two flexible tubes with teeth is evacuated, the teeth are pushed into each other by atmospheric pressure and interlock. A 16 mm thick manipulator can withstand

forces up to 1.6 N on a 150 mm lever arm before deforming. A stiffness increase factor is not provided. The prototype offers one working channel. Using a vacuum for shape locking is also proposed by Moses et al., 2013. The manipulator consists of long flexible beams with a cross-section such that they can be fit into each other shaping a cylindrical manipulator. While bending, the beams can slide along each other, maintaining the cylindrical cross-section of the manipulator. The whole manipulator is encapsulated into a membrane. When applying a vacuum, the beams are jammed against each other and interlock. A stiffness increase factor of 2.5 is reported. However, the proposed design is too large for surgical interventions (40 mm diameter).

7.5 JAMMING STIFFENING

A similar way to increase the stiffness is provided by using jamming methods. Although they are also based on increased friction between structures, they propose very specific well established designs and should be mentioned in a category on their own.

granular jamming Granular jamming utilizes a vacuum chamber filled with granules of any shape or material. By evacuating the air, the granules will be pushed against each other by the atmospheric pressure and jam, resulting in a stiffer shape. In the soft state, the chamber is flexible and the granules can move freely. It is a simple design and many different materials can be exploited to investigate their stiffening potential. N. G. Cheng, Lobovsky, et al., 2012 originally proposed a manipulator, which has a spring backbone surrounding several vacuum chambers filled with granules and actuated by tendons. The manipulator is able to hold its weight and exhibits a stiffness of 0.08 N/mm. This can be achieved in combination with tendon tensioning. A. J. Loeve et al., 2010 use only granules in vacuum and reach stiffnesses of 0.15 N/mm. Ranzani, Cianchetti, Gerboni, Falco, et al., 2016 use granular jamming in a soft fluidic actuated manipulator for minimally-invasive surgeries. Due to the limited space and other structures of the manipulator, granular jamming is only performed inside a cylinder with 8 mm diameter. This way, the stiffness can be increased by 1.73.

Multiple applications are proposed for granular jamming, such as pneumatic grippers. Further works are summarized by Manti et al., 2016 and report stiffness increase factors of up to 40. The efficiency of granular jamming seems to depend on the overall design and the integration inside the flexible manipulator. Further, Jiang et al., 2014 show that the membrane influences the stiffening outcome as well. Yanagida et al., 2013 demonstrate the dependence of stiffness by means of granular jamming on the cross-sectional area, vacuum level and the granulate material used. Salt performs best out of several materials in this work. Other works show coffee as superior granule material in terms of stiffness increase.

layer jamming Layer jamming exploits friction forces between flat thin structures due to an applied vacuum. The original layer jamming prototype proposed by Y. J. Kim et al., 2013 consists of thin flaps of PET film (0.12 mm) or paper that are spirally wound and sewn together at specific points to form a cylinder (Figure 32). By encapsulating this cylinder into multiple membranes and creating a vacuum inside them leads to jamming between the flaps, exploiting their surface friction. In the soft state the manipulator allows deflection and can be operated by means of tendons. In the rigid state a 400 mm long manipulator has a rigidity

of 0.2 N/mm. It further provides an approximately 18 mm in diameter large working channel. The production, however, is complex and time consuming. Simple planar shapes with different designs have been investigated, summarized by Manti et al., 2016, and can lead to a stiffness increase factor of up to 10. A robotic finger using layer jamming is proposed by Wall et al., 2015, reporting a stiffening increase factors of up to 8 for bending experiments. The layer jamming approach has also proved useful as a basic structure for shoes or furniture in Ou et al., 2014. Choi et al., 2018 shows the dependence of layer jamming stiffening on the flap material and the vacuum level. Blankemeyer et al., 2017 evaluated different factors influencing the stiffness of layer jamming: the number of overlapping layers, friction surface variation, and abrasive behavior of flap materials. In conclusion, no work presents a dedicated design of a continuum robot using layer jamming.



Figure 32: Layer jamming manipulator with helically wrapped flaps and two actuated segments (reprinted from (Y. J. Kim et al., 2013), ©2013 IEEE).

7.6 THERMO-ACTIVE STIFFENING

Thermo-active stiffening utilizes the viscosity variation of materials due to heat exposure. Several materials can be utilized.

wax Wax is proposed in N. G. Cheng, Gopinath, et al., 2014 as a coat for 3D-printed structures. When heated to 70 °C, the wax becomes soft and actuation is possible. High stiffness (3 N) and stiffness factors (25-10⁴) are reported. To induce heat, wires are used which glow as a result of electrical currents (6-8 A). However, the applied currents and temperatures are not suitable for use within the human body.

low melting point polymers (lmp) Low melting point polymers reduce their stiffness at relatively low temperatures similar to wax. A generally available material is polycaprolactone (PCL) with a melting point of 60 °C. Balasubramanian et al., 2014 investigate 3D-printed structures made of an acrylic-based thermoplastic polymer (ATPP). A Young's modulus of 1 GPa in the stiff state and 13.5 MPa in the soft state are reported. A temperature of 80 °C is necessary. A state transition within 2.4 s can be achieved. Similar to wax, the temperatures exceed acceptable limits.

low melting point alloys (lmpa) Low melting point alloys are metal alloys, which have a low melting point <100 °C. They change their mechanical properties faster than wax and low melting point polymers. Tonazzini et al., 2016 investigate the properties of the Field's metal alloy (HiTech Alloys, WA, USA), consisting of bismuth (32.5%), indium (51%), and tin (16.5%). A cylindrical probe is covered by a helical conductive wire to induce heat and melt the alloy. The required temperature reaches 62 °C using 1.1 A. A Young's modulus of 0.9 GPa is reported in this work, although the alloy is supposed to reach about 3 GPa. A stiffness increase factor of 700 with respect to the soft state can be measured. Wang et al., 2018 introduce a robotic LESS system using flexible manipulators with an integrated LMPA with a melting point of 45 °C. The LMPA is filled into the free space of a 8.5 mm thick and 50 mm long tendon-driven flexible section. The phase transition of the alloy is controlled by an inductive foil and a water stream through the manipulator. Water temperatures between 55-70 °C are tested. At 70 °C a change between the rigid and the soft state was achieved within 5 s. In an experimental investigation, the stiffening increase is 4.12 and the stiffness reaches up to 4 N/mm on a lever arm of 140 mm. Although this method reaches high stiffness and is applied to a miniaturized robotic surgical tool, the reported temperatures are hazardous to the human body.

7.7 RHEOLOGICAL STIFFENING

Rheological fluids are suspensions of small particles (in micrometers) dispersed in a carrier fluid such as oil. Electrically polarizable particles respond to an external electrical field changing the fluid's viscosity (electro-rheological fluid (ERF)). Ferromagnetic particles show the same effect when exposed to a magnetic field (magneto-rheological fluid (MRF)). This approach is effective, however, the stiffening potential is relatively low. Considering electro-rheological fluids, the stiffness reaches 5 kPa. The magneto-rheological fluid reaches 100 kPa (Olabi et al., 2007). They are mostly applied in automotive suspensions, brakes or clutches. Another drawback when considering the application in this thesis are the activation currents (1-2 A) for magnetic fields and their high voltages (2-5 kV).

7.8 SHAPE MEMORY ALLOY (SMA)

Shape memory alloys can be used as a stiffening mechanism due to their ability to change their shape when exposed to heat. Usually, they are used as rods or springs, which can change their lengths and therefore provide stiffening of the structure similar to tendon tension stiffening. As activation stimuli, electrical current is used to increase the temperature inside an SMA actuator. For surgical means, nitinol is often proposed since it is biocompatible. Temperatures

depend on the alloy and range from 47-95 °C (Y. Kim, S. S. Cheng, and Desai, 2018, Henke et al., 2016). Henke et al., 2016 use a square frame (105x110 mm²) equipped with SMA actuators that reaches stiffness of 1.73 N/mm, increasing the stiffness by a factor of 14.6. Although the results are efficient, they are based on a setup that cannot be transferred to a continuum robot structure in this work. Y. Kim, S. S. Cheng, and Desai, 2018 use SMA in a continuum robot for minimally-invasive surgery and report a stiffness increase by 4 with a 12.6 mm diameter manipulator. A stiffness of 0.15 N/mm is stated. The clear drawback is the high temperature incompatible with the surgical application inside the human body.

7.9 ELECTROACTIVE POLYMERS (EAP)

Electroactive polymers respond with deformation to electric fields. This deformation can be utilized for stiffening. They are divided into two major groups: the ionic EAP and the electronic EAP. A basic ionic EAP structure consists of two electrodes and an ion polymer film. When an electric field is applied, ions shift attracted by an electrode. With the ions the polymer film shifts and causes the swelling of one side of the entire structure. The swelling results in a bending motion (Chang et al., 2018). Voltages of 5 V allow for large deformations. Chikhaoui et al., 2018 propose an ionic EAP continuum robot for surgical procedures. However, they respond slowly and do exhibit lower forces. The most common electronic EAP representative is the dielectric elastomer (DE). The basic function principle is a deformation of an elastomer compressed between two electrodes. When an electric field is applied, the electrodes attract each other and force the elastomer to expand. This type of EAP is fast and generates relatively high forces. They are often proposed as bionic muscles. Electric fields up to several mega volts per meter are required (Chang et al., 2018), which limits the application for surgical robots.

7.10 STIFFENING METHOD SELECTION

Table 5 shows a summary of the mentioned methods with general qualities. Table 6 illustrates selected methods integrated into a robotic manipulator. Since the dimensions of the manipulators differ in terms of diameter and length, a comparison of the Young's modulus would be ideal. To determine this, cross sections of prototypes are needed, which is rarely provided in the literature. To provide some comparability, the lengths are set to 200 mm and the resulting stiffness is calculated using beam theory. First, the product EI is determined based on the stated data in the respective work:

$$EI = \frac{k l^3}{3}, \quad (1)$$

where k is the stiffness defined as the division of the deflection force by the resulting deflection. l is the manipulator length. This definition of the stiffness is also used in Table 6 if not stated differently. Using the product EI, the stiffness k_{200} at length $l_{200} = 200$ mm is calculated as follows:

$$k_{200} = \frac{3EI}{l_{200}^3}. \quad (2)$$

In the following, the stiffening methods are evaluated based on their characteristics and the above-mentioned requirements for partial nephrectomy.

safety Several methods cannot be considered for the desired application due to safety requirements. Wax, LMPP, and LMPA exhibit high temperatures to achieve phase transition and utilize high currents to provide heating. With temperatures of about 70°C , these methods are hazardous to the human body. Rheological methods (ERF/MRF), SMA, or electronic EAP are not safe for use within the human body, either due to high voltages/currents, high temperatures, or high electric fields. Further, thermo-active approaches provide low stiffness transition rates of several seconds. This can prevent the surgeon from performing time-critical surgical steps, such as tumor resection, which occurs during ischemia (interrupted blood supply).

stiffness and stiffening factor In terms of stiffness, the tendon tensioning approaches provide relatively low stiffening (0.025 N/mm) and low stiffening factors (maximum 2.5). The fluidic shape locking manipulator reaches higher stiffness (0.45 N/mm) with a larger diameter. However, the stiffening factor is also comparably low (2.5). A granular jamming approach is reported to have high stiffening factors (Manti et al., 2016). The achievable stiffness depends on the integration manner. N. G. Cheng, Lobovsky, et al., 2012 use the method combined with tendon tensioning and reaches stiffness of up to 0.55 N/mm . Ranzani, Cianchetti, Gerboni, Falco, et al., 2016 implement the method within a fluidic manipulator, showing low stiffness increase factors. The layer jamming manipulator by Y. J. Kim et al., 2013 reports significantly higher stiffness (1.6 N/mm) and has been shown to reach stiffening factors of up to 10. The fluidic manipulator introduced by Suzumori et al., 2013 reaches comparably high stiffness. However, the stiffness factor is comparable to other approaches, which means that the manipulator already offers high stiffness in its soft state.

integration potential A compact stiffening method design is required to provide space for working channels and camera integration. Furthermore, the stiffening method should not obstruct the manipulator's range of movement. In fluidic manipulators, the chambers occupy most of the available space. Also, the fluidic shape locking approach is space-consuming, due to its fluidic chamber and shape locking features. The layer jamming creates a tubular structure with a thin wall that offers space and at the same time has a low weight. Granular jamming comes with rather high weight but is flexible in its use and distribution. Friction based stiffening between links is dependent on the cross-section to generate stiffening, such that little space is left for working channels. Tendon tension stiffening is the most space-efficient method and can be integrated additionally to support other methods. Thermo-active materials are broadly available and exhibit different shapes and can be 3D-printed. Further, they possess a self-healing quality. In case of failure in the stiff state, the material becomes a liquid homogeneous mass again by softening.

dynamics In terms of dynamic, fluidic stiffening is slower than tendon tension stiffening and jamming approaches since the fluidic chamber inflation is countered by the rising material resistance. Powerful pumps are required to increase dynamics. Jamming approaches can be stiffened fast as the ambient pressure promotes air evacuation. However, they are slower in softening, since they are usually designed to passively inflate. The smaller the pressure difference, the slower the air flows back between the membranes. Active inflating control using a pump could increase the softening procedure. Tendon tension stiffening depends on the utilized actuators. Normally the actuators are designed to provide sufficient force to bend the

manipulator, which is higher than the force required for stiffening. The required tendon displacement is in the order of millimeters. Therefore, the dynamics of tendon tension stiffening is higher compared to previous methods. Rheological fluids and electronic EAP provide high state transition rates.

7.11 CONCLUSION

In summary, jamming methods offer an adequate solution considering all requirements. They are safe, space-efficient, exhibit relatively high stiffness, and stiffness increase factors. Further qualities of jamming methods are the simple mechanical activation stimuli, requiring only a vacuum pump as an additional device. Usually, a vacuum supply is provided in the operation room, such that only an interface is needed. The particles or sheets are easily available and cost-efficient. They are more explored, have proven to be feasible in the field of continuum robotics and have been proposed by several researchers for medical applications. A decision for or against one of the jamming methods cannot be made at this stage and will be evaluated in one of the following chapters of this thesis.

Table 5: Overview of stiffening methods including activation manner and their advantages and disadvantages.

Method	Activation	Dynamic	Qualities	Citations
Tendon Tension	Mechanical	+	+simple design -low stiffness increase	Table 6
Friction	Mechanical	+	+simple design +high stiffness -space intensive	Table 6
Fluidic	Pressure	o	-space intensive	Table 6
Fluidic Shape Locking	Pressure	o	-space intensive	Table 6
Granular Jamming	Vacuum	+	+soft -space intensive	Table 6
Layer Jamming	Vacuum	+	+space efficient	Table 6
Thermo active	Temperature	-	+high forces -high temperatures (70 °C) -high currents(8 A) -slow	N. G. Cheng, Gopinath, et al., 2014 Yufei et al., 2017
Electro Rheological	Electric field	++	+fast -low forces(2-5 kPa) -high voltages(2-5 kV)	Olabi et al., 2007
Magneto Rheological	Current	++	+fast -low forces(50-100 kPa) -high currents(1-2 A)	(Olabi et al., 2007)
SMA	Current	o	+space efficient -heat(47 °C)	Y. Kim, S. S. Cheng, and Desai, 2018
EAP ionic	Voltage (5 V)	-	-slow -low force	Chang et al., 2018
EAP electronic	Electric Field	++	+fast -high electric fields (100 MV/m)	Chang et al., 2018

Table 6: Explicit research work presenting designs with integrated stiffening methods for flexible robots and quantitative stiffening evaluation results.

¹ including fluidic pressurized chambers

² force until a motion is registered

³ including tendon tensioning

⁴ calculated based on beam theory

Work	Stiffness Increase Factor	Stiffness	Size (\varnothing in mm/ length in mm)	Stiffness 200 mm long probe ⁴
Tendon Tension				
(Shiva et al., 2016) ¹	2.3x	0.3 N/mm	23/47	0.004 N/mm
(Y. J. Kim et al., 2014)	2.5x	0.529 N/mm	20/87	0.025 N/mm
Friction				
(Mahvash et al., 2011)	-	2.5 N ²	6/40	-
Fluidic				
(Suzumori et al., 2013)	3-5x	0.25 N/mm	57/1500	105.5 N/mm
(Manti et al., 2016)	10x	-	-	-
Fluidic Shape Locking				
(Yamashita et al., 2009)	-	1.6 N	16/150	-
(Moses et al., 2013)	2.5x	0.23 N/mm	40/250	0.45 N/mm
Granular Jamming				
(Ranzani, Cianchetti, Gerboni, Falco, et al., 2016)	1.73x	0.53 N/mm	50/-	-
(A. J. Loeve et al., 2010)	-	0.15 N/mm	17.8/100	0.019 N/mm
(N. G. Cheng, Lobovsky, et al., 2012) ³	-	0.08 N/mm	20/380	0.55 N/mm
(Manti et al., 2016)	40x	-	-	-
Layer Jamming				
(Y. J. Kim et al., 2013)	-	0.2 N/mm	22/400	1.6 N/mm
(Manti et al., 2016)	10x	-	-	-
Low Melting Point Materials				
(Wang et al., 2018)	4.12x	1.84-4 N/mm	8.5/140	1.37 N/mm
SMA				
(Y. Kim, S. S. Cheng, and Desai, 2018)	4x	0.15 N/mm	12.6/66.5	0.006 N/mm

8

ROBOTIC SYSTEM DESIGN

This chapter presents specific designs for the previously discussed units of the robot system, in particular, the articulated port, the actuation unit, the coupling, and the translational DoF. For each unit, possible solutions are discussed in order to meet the above mentioned requirements. Especially the sterility concept influences the applied concepts.

8.1 ARTICULATED PORT DESIGN APPROACHES

First, a basic structure of a tendon-driven continuum robot (TDCR) is introduced. A TDCR consists of a flexible backbone, spacer disks for tendon routing rigidly attached to the backbone, and tendons routed through the spacer disks and attached to an end disk. An end disk marks also the end of a segment. A single segment can bent in 3D space with 2DoF using at least three tendons. To increase the maneuverability, several segments can be stacked upon each other. Figure 33a shows the basic structure of a tendon-driven continuum robot with two segments. The tendon channels are distributed circumferentially on each spacer at a certain distance from the backbone. Two different actuation approaches exist, using either three tendons or two antagonistic tendon pairs (Figure 33a). The version with three tendons foresees an independent tendon actuation, but for the robot control it is important to adjust the tendon displacements to each other. Tension in all three tendons together can increase stiffness, but if tension is too high, it can lead to buckling and backbone damage. An antagonistic tendon pair can be actuated by one motor, such that if one tendon of a tendon pair is tensioned, the antagonistic tendon is released. The antagonistic approach avoids the simultaneous tensioning of all tendons. Both approaches provide 2DoF per segment. Robots with three tendons are proposed in several designs, e.g. Xu et al., 2015, Simaan, Xu, et al., 2009. If a robot consists of several segments, the tendons from the distal segment run through the proximal segments. The tendons of different segments can be routed through the same tendon channels or dedi-

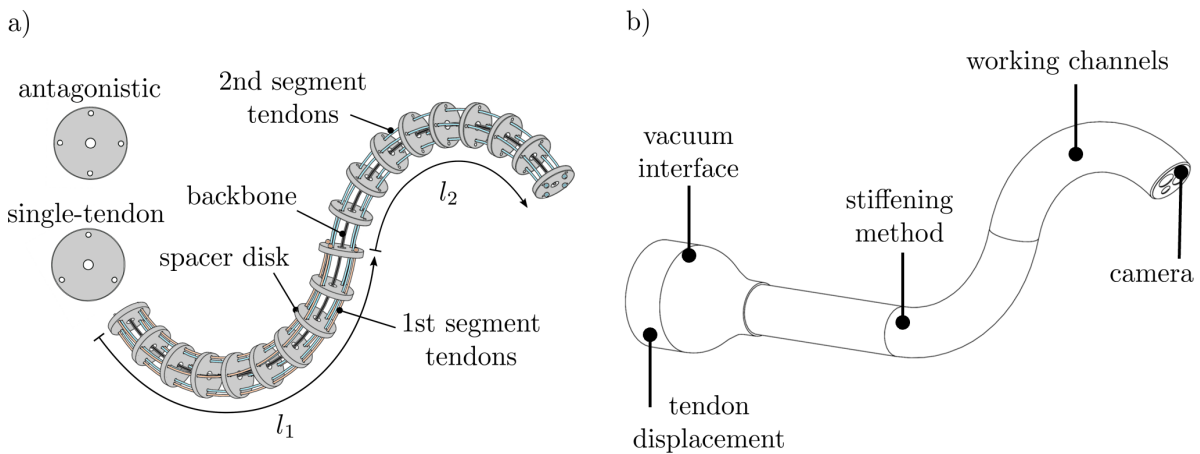


Figure 33: a) General structure of a tendon-driven continuum robot, showing single-tendon and antagonistic actuation manner. b) General components of an articulated port.

cated channels. Due to the flexible nature of continuum robots, bending of the distal segment affects the shape of the proximal segment as well.

In addition to the basic structure, application-specific components are included in the design of the articulated port: working channels, a visualization unit, and the selected stiffening methods (e.g. granular jamming and layer jamming), as shown in Figure 33b.

8.1.1 Tendon Routing

The common way of routing is parallel to the backbone (Figure 34b). An alternative is to route the tendons helically around the backbone (Gerboni et al., 2015). This enables manipulator twisting and thus 3D motion with only one tendon. This is advantageous for designing robots with few actuators establishing complex shapes in confined tortuous environments (Starke et al., 2017¹). A helical routing is shown in Figure 34c. Besides helical routing, any arbitrary tendon path can be chosen. For the application in this thesis it is required to establish a large variety of shapes in an relatively unconstrained space. Therefore, helical routing is not beneficial.

To reduce the influence of distal bending segments on the shape of proximal segments, Y. Kim, S. S. Cheng, Diakite, et al., 2017 propose an alternative routing manner. The tendons of the distal segment run close to the backbone of the proximal segments. Once they reach the associated segment, they are arranged on the outer diameter of the spacer disks to maximize the bending effect (Figure 34d). This shows to be effective, but increases the friction between the tendons and routing channels and requires additional space in the manipulator's center. This could interfere with the working channels.

Tendons of concatenated segments can be routed as shown in Figure 34a in the same channels or distributed on a circle, or with a shift towards the backbone.

¹ this work originated from a master thesis supervised during the duration of the Ph.D. program

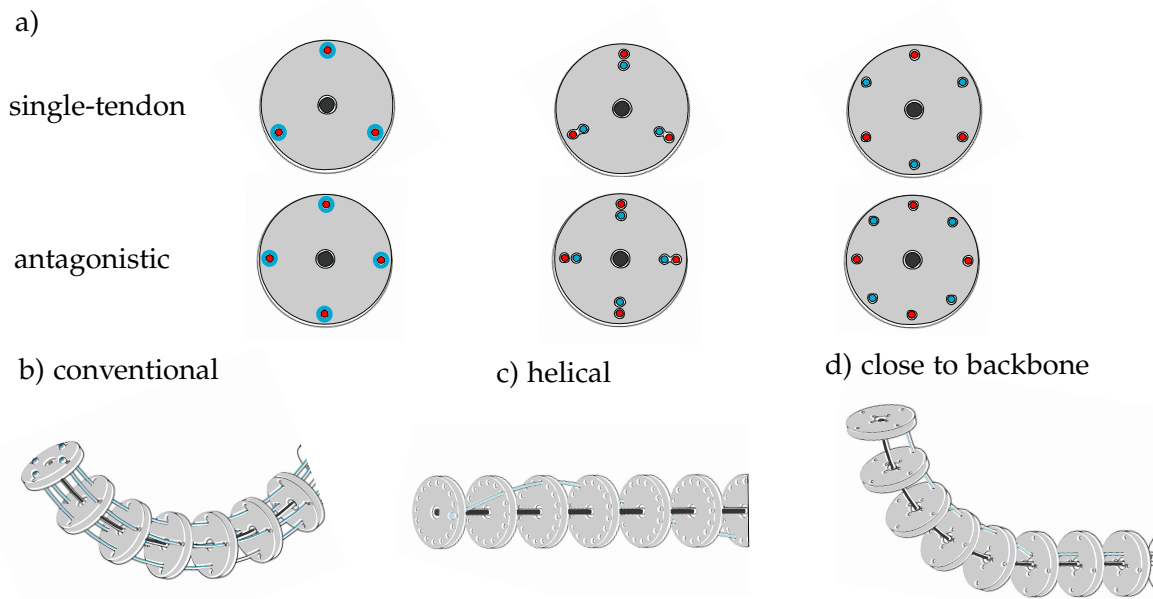


Figure 34: Different tendon routing strategies for tendon-driven continuum robots: a) Tendon routing for several segments, showing single-tendon and antagonistic actuation approaches, blue and red indicate tendons belonging to a segment; b) Parallel to backbone tendon routing; c) Helically routed tendon; d) Tendon routed close to the backbone in the proximal segment.

8.1.2 Backbone Design

This basic structure with a central backbone (Figure 35a) can be varied in different ways as well. The backbone in the center allows for 2DoF bending between two spacer disks. One could place two parallel backbones between two spacer disks, as shown in Figure 35b, and arrange the backbones to the neighboring spacer disks with 90° angular displacement. This backbone alternates its position along the entire robot structure. This way, the large lumen within the center can be used. However, the maximum curvature is halved for the same manipulator length, since only every second space between the discs can be bent in the same direction.

A similar approach of alternating backbones can be achieved with two crossed backbone pairs between two spacer disks, as shown in Figure 35c. The use of the crossed arrangement increases the torsional stiffness.

The backbone can further be a larger flexible tube with notches, reducing the bending stiffness (Figure 35d). This structure is proposed by Lee et al., 2015 and provides a large inner lumen for instrument deployment². The notches have to be cut in an alternating manner to provide bending in two directions. Due to the larger diameter, the torsional stiffness increases. A variation of notches can be designed and optimized. Due to the alternating arrangement of the notches, this approach shows reduced curvature compared to a central backbone.

Instead of a rod or a tube as a backbone, springs can be used (Tonapi et al., 2014). They can be applied to all the mentioned structures. It is a cost-effective approach and offers the pos-

² a manipulator with this backbone structure is investigated during this thesis with the focus on increasing the DoF in Amanov, Granna, et al., 2017

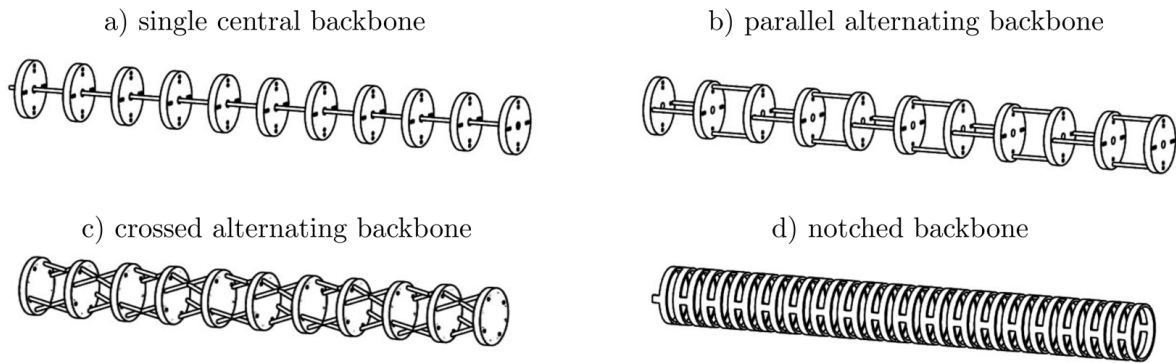


Figure 35: Backbone structures of a tendon-driven continuum robot.

sibility to vary the manipulator length by compressing all springs simultaneously. However, the spring compression, which occurs during bending, is challenging to model.

8.2 WORKING CHANNEL DESIGN

For the specific application of partial nephrectomy in this thesis, working channels need to be integrated into the tendon-driven continuum robot. As stated in the previous chapter, 3 working channels are required, two larger (8 mm) and one smaller channel (4 mm). A compact arrangement of the working channels is shown in Figure 36a. The channels can consist of dedicated flexible tubes made of rubber, plastic, etc., (Figure 36b) or a meshwork of metals or plastics (Figure 36c). As the manipulator is flexible and can be highly deformable, the working channels must deform accordingly without causing jamming of the tools or blocking of the channel. This can occur if the channel buckles at certain curvatures and changes its cross-section. Using plastic tubes surrounded by a tension spring can be a solution (Figure 36d). The spring holds the cross-section and can elongate and contract during bending. Similarly, a plastic tube with integrated flat helical spring coils can be used (Figure 36e). Alternatively, solely a spring coil can be utilized (Figure 36f). Spring coils offer only little contact surface due to the circular rod cross-section. However, spring coils and meshwork approaches are not air-proved, which has to be considered for a jamming method integration.

8.2.1 Jamming Method Integration

The integration of both jamming methods, granular and layer jamming is presented here. Along with the granules or flexible flaps, jamming methods generally require a vacuum interface and air-prove chambers.

layer jamming As suggested by Y. J. Kim et al., 2013, the most common structure for layer jamming suggests a helical wrapping of flaps along the robot structure, where the flaps are sewn together with a thread or wire (Figure 37a). To integrate this structure, a membrane (inner membrane) is placed around the continuum robot, the flaps are wrapped around, and an outer membrane is placed around the flaps. The two membranes are then attached to the base of the articulated port and are glued at its tip. In this way, the layer jamming is separated

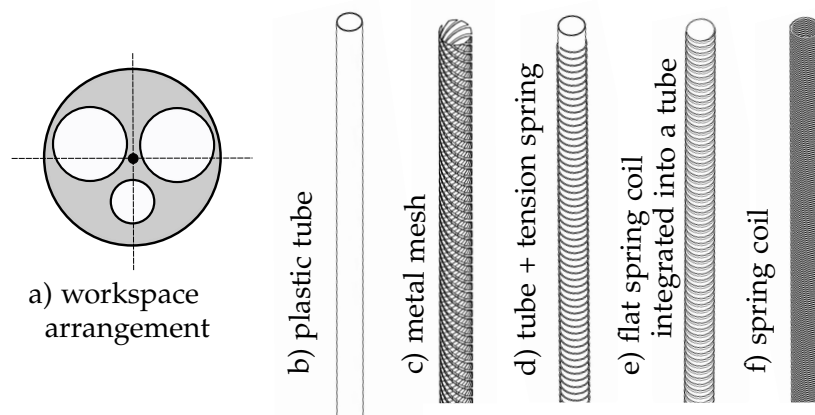


Figure 36: Working channel arrangement and different approaches of working channels.

from other components (working channels and tendons).

Another approach suggests a fixation of flap rings onto the spacer disks as shown in Figure 37b. This way, the flaps are parallel to each other and their positions are defined. Threads or wires are no longer needed to hold the structure together. Air proof encapsulation is challenging since the flaps are directly attached to the continuum robot. A possible approach is to use the working channels as inner membranes and place an outer membrane around the flaps. To ensure the air-proof chamber, the tendons have to be encapsulated in an extra membrane as well. This design offers the possibility to use the inner membranes as working channels simultaneously. The disadvantage is the smaller overlapping area, because only the flaps overlap and not, as with the helical approach, also the middle stripe as well. Further, there is a dependency on the disks. Relative motion of a spacer disk during bending means a displacement of the flaps, reducing the overlapping surface on the outer side of the bent manipulator and therefore the stiffening. This reduction also holds for the helical approach, but it is smaller due to minor incremental displacements.

granular jamming The integration of the granular jamming can be implemented by including separated vacuum chambers into the manipulator filled with granules (Figure 38a), as proposed by Cianchetti et al., 2014. Using this, the chamber is air-proof. However, this approach requires a dedicated space for the chamber, conflicting with the working channels and overall articulated port diameter.

Alternatively, the available space between the working channels and an outer membrane can be filled with granules (Figure 38b). The granules should not be compressed to enable for some deformation during manipulator bending. To ensure air-proof integration, tendons (located inside the vacuum chamber) need to be encapsulated into extra membranes themselves. Otherwise air can flow into the vacuum chamber through the tendon path to the actuation unit. The advantage of the second approach is the more efficient use of space.

8.3 TENDON DISPLACEMENT

Since the articulated port is supposed to be detachable from the actuation unit, some means of tendon displacement need to be integrated into this unit. No motorization, but an interface

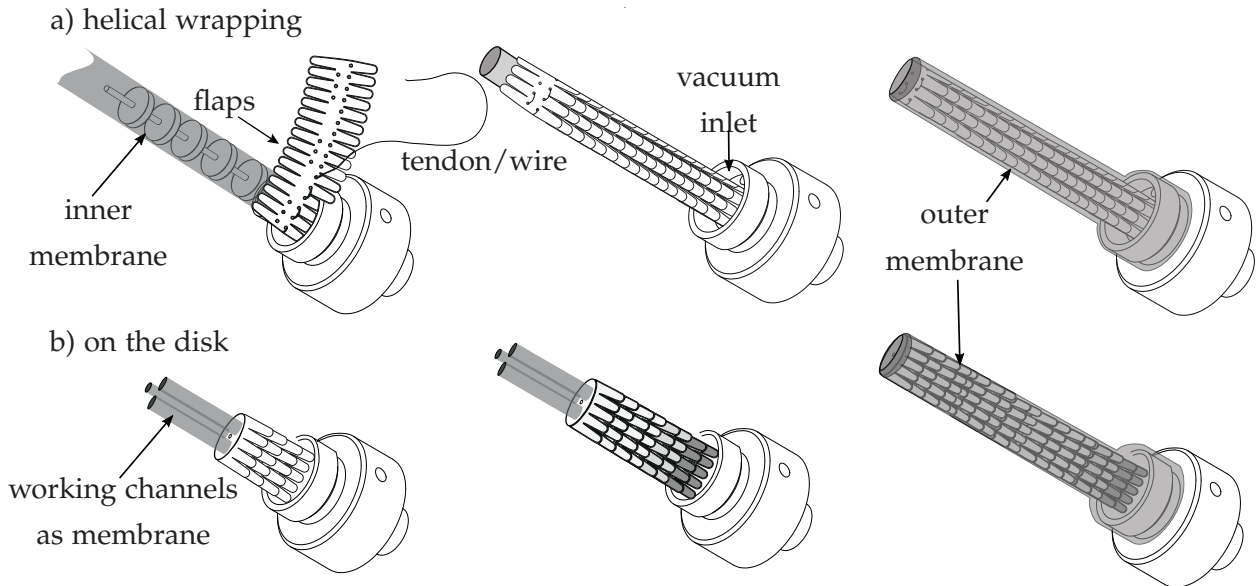


Figure 37: a) Helical wrapping layer jamming integration; b) Layer jamming integrated directly on a spacer disk.

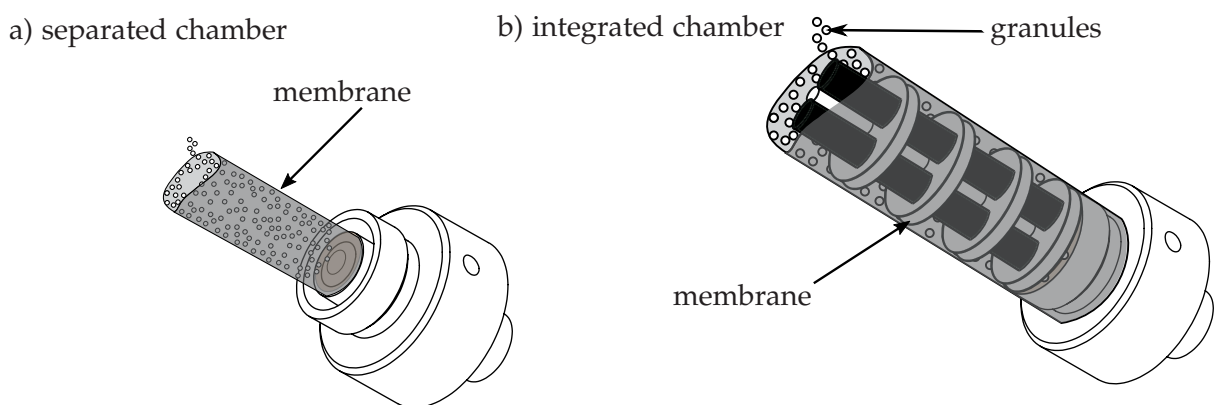


Figure 38: a) Granular jamming integrated into a separate chamber; b) Granular jamming integrated in the available space between the spacer disks.

to the coupling mechanism is necessary.

a) direct winding

b) worm winding

c) lead screw

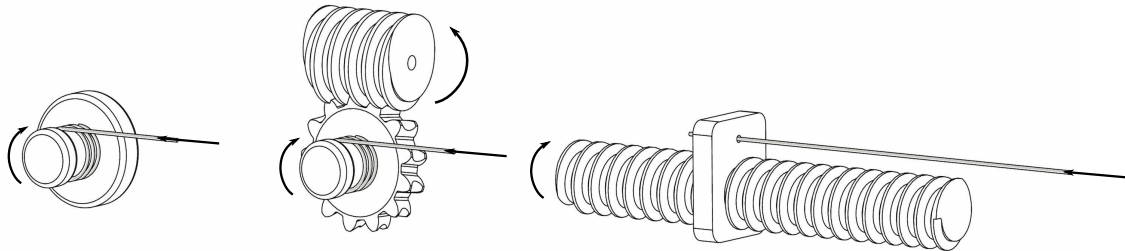


Figure 39: Tendon displacement solutions.

The tendons can be wound up on a rotating cylindrical shaft, as shown in Figure 39a. The rotation axis of the shaft is perpendicular to the tendon course. The advantage of this approach is its space efficiency. Similarly, a worm gear can be used, as shown in Figure 39b. It is space-efficient as well and the rotation axis of the worm is aligned with the tendon course. An alternative approach is to use a lead screw driven screw nut. The tendon is attached to the screw nut and is displaced translationally when the lead screw rotates (Figure 39c). The dimension of this approach depends on the required tendon displacement. The worm gear and the lead screw both provide self-locking.

8.4 MANIPULATOR DESIGN DECISION

Antagonistic tendon actuation is preferred due to the smaller number of actuators required and the inherent buckling prevention of the backbone. All tendons are guided parallel to the backbone and have the same distance to it over the entire length of the manipulator. The tendons of different segments are routed through dedicated channels. Accordingly, the number of routing tendon channels is a multiple of four. They are distributed equidistantly in the circumferential direction. The spacer disks are rigidly fixed to the backbone and are evenly distributed along it. A single central backbone is chosen because it allows for higher curvatures than other presented backbone structures. As working channels, a combination of a plastic tube with a tension spring is preferred. Due to their airtight nature, they are more suitable for use with granular jamming.

For granular jamming, granules are distributed in the available space between the spacer disks and working channels. They are encapsulated into an outer membrane, as shown in Figure 38b. Layer jamming is integrated as helically wrapped flaps which are encapsulated into two membranes, as shown in Figure 37a. It is anticipated to result in higher stiffnesses and more efficient integration.

The tendons are wound up on a worm gear individually since it is a space-efficient actuation approach and the alignment of the worm rotation axis with the tendon is beneficial as a coupling mechanism interface. Up to three segments can be actuated, resulting in 12 worm gear units distributed on a circle, as shown in Figure 40b. The worm gear circle is larger than the diameter of the articulated port.

A conic base provides the necessary space for the worm gears and guides the tendon on a non-linear path from the gears to the manipulator, as shown in Figure 40a. Additionally, the

main body includes the working channels and docking points for robotic tools (Figure 40a). Further, a vacuum interface is provided.

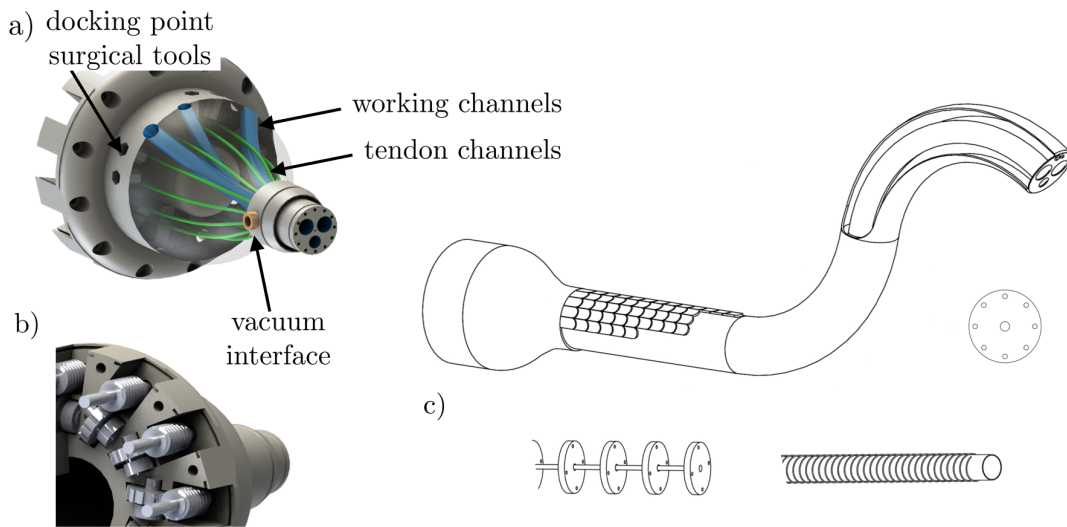


Figure 40: a) The basis with tendon and working channels; b) Tendon displacement mechanism using worm gears; c) Articulated port design showing the chosen component solutions.

8.5 COUPLING MECHANISMS DESIGN

The design of the coupling is crucial for the whole system since it transmits the tendon actuation to the manipulator. Based on the proposed articulated port design with worm gears as a tendon displacement interface, a coupling needs to provide the transmission of the worm rotation. There are different types of couplings. In this work, three approaches are considered: magnetic, friction, and shape-locking coupling.

Important qualities for the coupling mechanisms are a) separation of sterile and non-sterile components, b) efficient and slip-free transmission to ensure precise control, and c) fast and simple coupling/decoupling.

8.5.1 Magnetic Coupling

The only contact-less coupling is the magnetic coupling. When two shafts are equipped with several magnets, as shown in Figure 41a, the attracting magnetic forces will force the rotation of the driven shaft due to the rotation of the drive train. In this case, a plastic cover can be placed between both. The coupling process does not require any additional adaptation of the drive train to the output shaft, as the magnets would be forced to arrange themselves. The decoupling requires a certain force to overcome the magnetic attraction, such that in an ideal case a decoupling mechanism should be provided or an electromagnet should be used. A major drawback is the limited space for the magnets, resulting in small magnets and therefore small forces. A magnetic coupling for tendon-driven continuum robots is presented by Koller et al., 2016. One robotic segment is actuated and an actuation unit with four motors for four tendons is introduced. Per tendon 4 permanent magnets (6 mm \varnothing each) are used to

provide enough force. For several segments, this approach would result in a large size. Using an electromagnet, the size would increase even further.

8.5.2 Friction Coupling

One way of using a friction coupling would require disks with high friction coefficients on the drive train and the output shaft. The mechanism is shown in Figure 41b. High axial forces are applied to ensure slip-free transmission, which puts a high strain on the concerned parts. However, a certain slip is always present during the coupling procedure, such that the rotation of the driven shaft needs to be measured by additional sensors to determine the actual rotation angle. Additional means for the clutch in/out mechanism should be provided.

8.5.3 Shape-Locking Coupling

In contrast to the friction coupling, the shape-locking coupling is based on the fitting of geometrically compatible structures, as shown in Figure 41c. These structures can be of various types. This approach is used to couple the da Vinci® instruments. To provide shape-locking, the rotational arrangement of the disks needs to be adjusted, requiring design alternation. The coupling mechanism is efficient since it uses shape-locking which provides precise transmission and allows for relatively high forces. Although it is easy to decouple, the coupling process is complicated. A shape-locking coupling is proposed in Burgner et al., 2013 for a concentric tube continuum robot actuation unit.

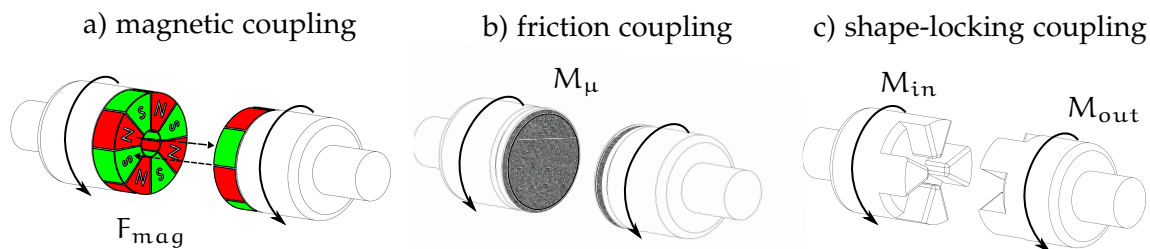


Figure 41: Overview of coupling approaches.

8.5.4 Coupling Mechanism Decision

The shape-locking coupling offers the most space-efficient, and simple, but at the same time very effective approach in comparison to the other presented mechanisms. Magnetic and friction couplings are dependent on the surface area of the magnets or friction disks. This sets limits to their miniaturization. Relying only on the shape, shape-locking mechanisms made out of durable materials provide high force transmission on a relatively small scale. Further, friction couplings rely on the magnitude of the normal force between the friction disks, which requires additional active components. In addition, shape-locking couplings were proposed, which have proven to be feasible more often in medical robotics.

Therefore, a similar approach is chosen for the coupling design in this work. The actuation unit and the manipulator possess aligned rotatory shafts. The motion from the actuation unit driveshaft has to be transmitted to the driven shaft in the manipulator. Each shaft carries an

adapter with a certain shape. To transmit the rotation, the coupling plate provides a rotating shaft with counterparts to the adapter in the operating unit and manipulator (Figure 42a). The shape of the adapters is chosen according to an Oldham coupling to compensate for possible radial shaft misalignment, as is proposed for a concentric tube robot actuation unit in Burgner et al., 2013. A sterile foil is attached to the coupling plate to cover the actuation unit. The coupling plate has to be attached to the actuation unit first (Figure 42b), and subsequently, the manipulator is attached to the coupling plate. The attachment of the coupling plate is assured by three clips, as shown in (Figure 42b). A coupling sequence is illustrated in Figure 42c. First, the coupling plate is attached to the actuation unit using a clip mechanism. In order for the coupling to engage, the corresponding shapes must be aligned. To ensure this alignment, the coupling adapter on the actuation unit side is mounted axially on the driveshaft. The drive shaft has one end with a square cross section and the adapter has the corresponding cut-out. During attachment, the adapter can be pushed inside the actuation unit compressing a spring placed between the adapter and the actuation unit front wall (Figure 42c1-c2). Shaft rotation around at least 180° has to be performed, to ensure the locking. During rotation, the driveshaft adapter, being rotationally fixed to the shaft, will turn and lock into its counterpart pushed by the spring (Figure 42c3). Subsequently, the manipulator is attached in the same manner. The adapter inside the coupling plate has to allow for some axial displacement to be pushed inside together with the driveshaft adapter (Figure 42c4). After further rotation of 180° , the manipulator will lock in as well (Figure 42c5). The coupling shown in Figure 42a is meant for a single tendon. The arrangement for several tendons is determined by the manipulator and actuation unit design.

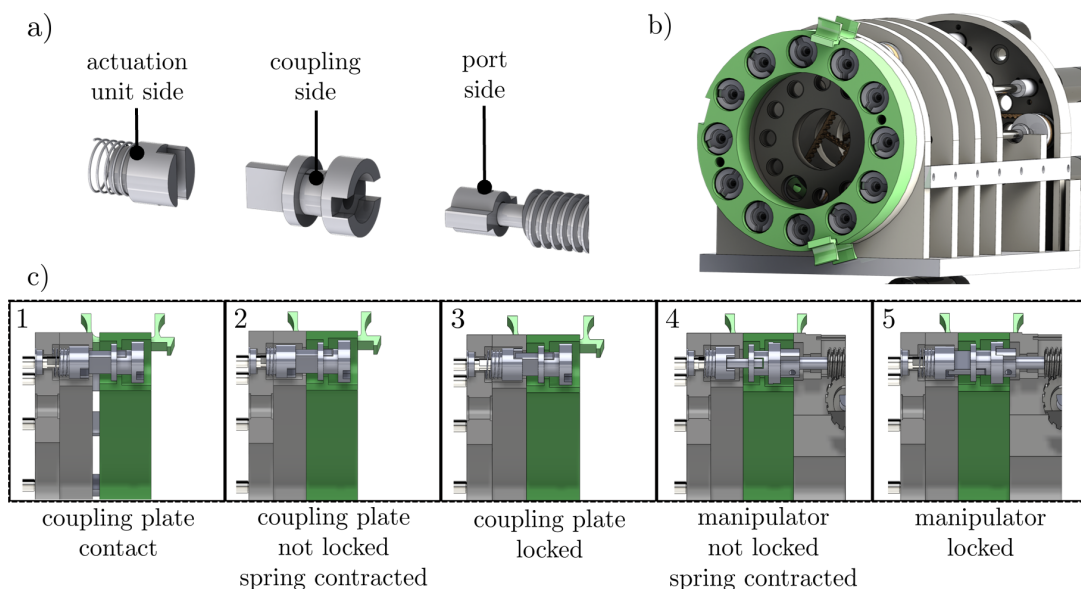


Figure 42: Coupling mechanism design and functionality: a) The corresponding shape-locking adapters on the actuation unit, coupling, and port side; b) Coupling plate attached to the actuation unit; c) Coupling sequence.

8.6 ACTUATION UNIT DESIGN

The actuation unit provides the tendon displacement in the articulated port. In this thesis, only DC motors are considered as stated in chapter 6. It further offers an interface for the coupling mechanism. Due to the chosen articulated port and coupling mechanism design, a compatible actuation concept is sought.

Twelve circumferentially distributed driven shafts in the manipulator need to be addressed. Each of these shafts could be actuated individually by a driveshaft attached to a motor. Since two driven shafts with 180° displacement correspond to an antagonistic tendon pair and have to be actuated simultaneously, they can be driven by a single motor. A motor is rigidly attached to one of the corresponding driveshafts and rotates it in one direction. The rotation

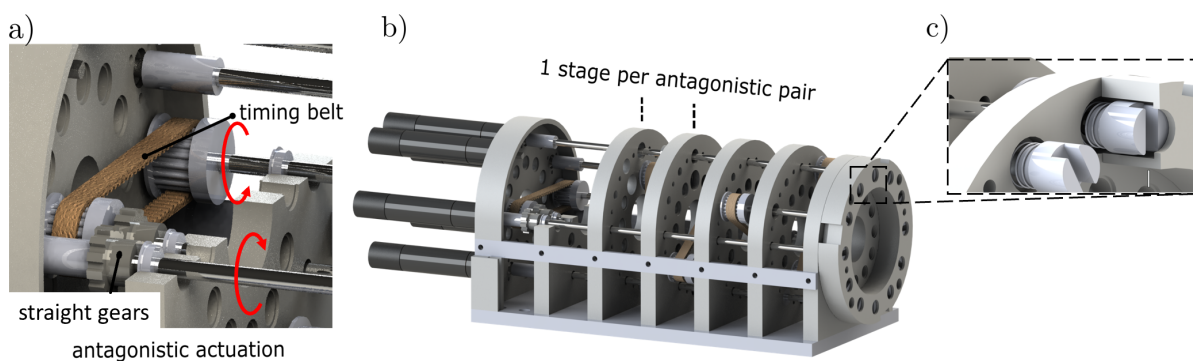


Figure 43: Actuation unit design: a) Actuation of an antagonistic tendon pair with one DC motor over a timing belt; b) Whole actuation unit; c) Locking adapter for the coupling with a compression spring.

direction of the antagonistic driveshaft has to be inverted to provide shortening/lengthening of the antagonistic pair at the same time. This is achieved by connecting both shafts by a pair of straight gears and a timing belt. The actuation assembly of one tendon pair is shown in Figure 43a. For each tendon pair, one of such stages is needed. Figure 43b shows an actuation unit example for the actuation of three segments. Each driveshaft carries an axially mounted adapter with a compression spring in the front of the actuation unit (Figure 43c).

8.7 TRANSLATIONAL DOF APPROACHES

The translational DoF provides a linear motion of the whole actuation unit. The rotation of a DC motor shaft needs to be transmitted into a translation. Several mechanical means are considered in this thesis. While the following approaches consider only the type of actuation, a linear guide is always necessary to ensure stable motion.

Lead screw An acme lead screw and screw nut combination provide a possible solution. The motor drives the lead screw and the actuation unit is rigidly attached to the screw nut (Figure 44a).

timing belt A timing belt solution is also feasible (Figure 44b). The motor arrangement would normally be perpendicular but can be in parallel with the timing belt if using e.g. bevel gears. The actuation unit is rigidly attached to a plate fixed to the timing belt.

gear rack Instead of the acme lead screw, a straight gear rack can be used. The motor is equipped with a straight gear and can directly drive the whole actuation unit along with the rack (Figure 44c). In this case, the motor has to be arranged in 90° to the rack resulting in a simple but more space-consuming design. This approach allows for the dismounting of the actuation unit when driving the gear to the end of the rack.

angled gear rack An angled gear rack and a worm combination provides a space-efficient design due to the parallel arrangement of the motor with respect to the rack (Figure 44d). It allows the actuating unit to be dismounting in the same way as the gear rack.

8.7.1 Translational DoF Design Decision

Due to the compact design and the possibility to mount/dismount the whole actuation unit, the angled gear rack is preferred. The motor will be mounted onto the actuation unit. This keeps all actuators in the same unit, facilitating cable management and actuation unit exchange. The angled gear rack is attached to a linear guide, which can be anchored on the mounting arm. The actuation unit is also equipped with slide bearings, which are complementary to the linear guide. The overall design is illustrated in Figure 44e. The worm is driven by the motor over a pair of straight gears to reduce the foot print of the mechanism. The actuation unit can be dismounted from the linear stage when driving backward.

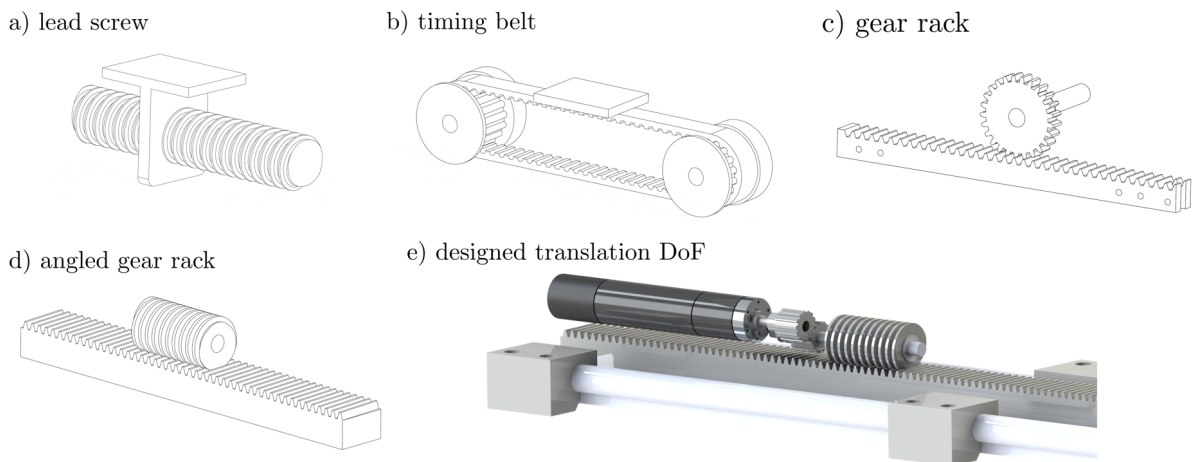


Figure 44: Translational DoF solutions in a)-d) and the chosen design using an angled gear rack and a worm in e).

9

DESIGN PARAMETERIZATION

This chapter aims to quantify the manipulator design parameters to provide efficient positioning in the abdominal space. From the selected application of partial nephrectomy, some parameters can be directly derived, such as the overall port or the working channel diameter. Segment lengths must be optimized and parameters such as the maximum outer backbone diameter can be derived from the optimization results as a function of the maximum required curvature. The parameters are classified into three different groups: direct, optimized, and derived.

An optimization algorithm framework is developed in this chapter, using several patient data sets as input. The optimization algorithm seeks a design suitable for several patients. Further, the positioning performance is investigated depending on the incision location. Subsequently, the remaining design parameters are derived from the optimization results to complete the parameterization.

9.1 PARAMETER DEFINITION AND DIFFERENTIATION

A tendon-driven continuum port is defined by the parameters listed in Table 7. Three parameter groups are identified: direct, optimization, and derived. The direct-group can be quantified based on the chosen application. For LESS, highly articulated instruments are meant to be deployed through the two larger working channels of the articulated port. Typically suggested articulated flexible tools have diameters of approximately 5 mm (Shang, Leibrandt, et al., 2017, Xu et al., 2015, Simaan, Xu, et al., 2009). To provide some space between the tool and the channel wall, the inner diameter of the large channel D_w is chosen to be 8 mm. The inner diameter of the small working channel is chosen to be 4 mm since flexible instruments for irrigation and suction require lower payloads than the primary tools and can be designed smaller. For ex-

ample, a commercial flexible ureteroscope¹ of 3 mm diameter (LithoVue™, Boston Scientific Corporation, Marlborough, MA, USA) exists with an irrigation channel. Based on the arrangement of the working channels, they occupy a certain area as shown in a cross-sectional view in Figure 45a. The tendon routing channels have to be placed radially further outside on a circle with a radius r_t . Using tendons with 0.34 mm and one tendon per channel, the diameter of the tendon routing channels is chosen to be 0.7 mm to provide enough space for the tendons to slide. This results in a tendon routing radius r_t of 10.5 mm. It is chosen as small as possible in order to provide a lower spacer disk diameter d , since the LESS incision should not exceed the usual size of 30 mm. Using the mentioned parameters, the overall spacer disk diameter can be set to 25 mm. Its thickness b is set to 3 mm to withstand forces induced by the tendons during actuation. The directly derived parameters are shown in Figure 45a.

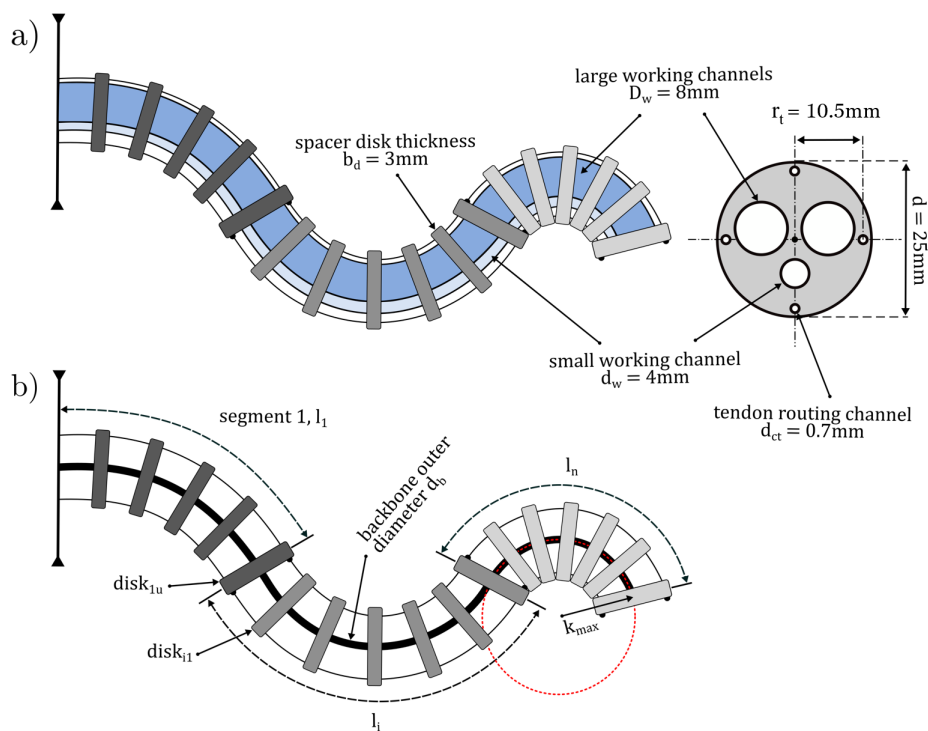


Figure 45: General continuum port design: a) Directly derived parameters in a side and cross sectional view; b) Optimization and derived parameters.

During the optimization, the segment lengths $l_1/l_2/l_3$ are optimized. The optimization is performed for a manipulator structure with two and three segments. Depending on their performance (optimization results), the number of segments n can be chosen. The optimization will provide port designs exhibiting certain curvatures. The maximum curvature, κ_{max} as shown in Figure 45b, governs the maximum backbone outer diameter d_b . As backbone material, Nitinol is considered with 8% recoverable strain. The maximum curvatures of each segment and the disk thickness determine the spacer disk number k_{1-3} of each segment. The optimized and derived parameters are shown in Figure 45b.

¹ surgical device used for transurethral kidney inspections and stone removal

Table 7: Tendon-driven continuum port parameters differentiated into groups: Direct = directly derived from the application, Optimization = require optimization, Derived = derived from the optimization results.

Parameter	Symbol	Value	Differentiation
Spacer disk diameter	d	23mm	Direct
Spacer disk thickness	b	3mm	Direct
Large working channel diameter	D_w	8mm	Direct
Small working channel diameter	d_w	4mm	Direct
Tendon routing channel diameter	d_{ct}	0.7mm	Direct
Tendon routing radius	r_t	10.5mm	Direct
Segment length 1/2/3	$l_1/l_2/l_3$?	Optimization
Segment number	n	2/3	Derived
Max. outer backbone diameter	d_b	?	Derived
number of disks	$u_1/u_2/u_3$?	Derived

9.2 KINEMATIC MODELING: CONSTANT CURVATURE APPROACH

In order to calculate the shape and the tip pose (position and orientation) of the tendon-driven continuum port, a mapping between the configuration vector \mathbf{q} and the task space \mathbf{x} is required. The configuration space is defined as the values of the robot actuation stimuli. A configuration is a specific set of \mathbf{q} leading to a specific set of \mathbf{x} . The task space is defined as the geometric description (position and orientation) of the robot body. The forward kinematic model describes this relationship.

There exist various approaches to establish the kinematic mapping between configuration and task space of continuum robots. The simplest approach defines a continuum robot as a concatenation of multiple rigid links connected by joints (Jones et al., 2006), well-known methods of rigid link robotics. In this case, the configuration vector \mathbf{q} is defined by the joint angles. A widely used approach proposes a constant curvature description, defining the robot's shape as concatenated circular arcs with constant curvatures (Simaan, Taylor, et al., 2004). For this mapping approach, the configuration vector \mathbf{q} can be defined as tendon elongations/contractions with respect to the straight robot shape. A more sophisticated approach foresees an approximation of the flexible arm with springs (Camarillo et al., 2008), or the description of a continuum robot as a thin elastic rod using Kirchhoff rod theory (Rucker et al., 2010). Here, the forces in the tendons compose the configuration vector \mathbf{q} . Further details can be found in (Burgner-Kahrs et al., 2015).

The kinematic models differ in their accuracy and calculation efficiency. While the Kirchhoff rod approach is relatively precise and computationally expensive, the approach with constant curvature arcs is relatively imprecise and the computational effort is low. However, the model accuracy is relevant if one compares how precise the robot can reach a commanded position or shape, which is defined as the absolute accuracy. For the purpose of this optimization, it is only important to discover, if configurations exist which can satisfy the objective function with the given segment lengths and segment number. Since tendon-driven continuum robots can be approximated by constant curvatures arcs neglecting friction in the tendons, all modeling approaches are suitable. As complex kinematic modeling can be computationally expensive, a time-efficient model is preferred in this work. In particular, the approach of constant curva-

ture arcs (Simaan, Taylor, et al., 2004) is chosen due to its broad application and acceptance. This model approach does not consider external forces which could be applied to the robot structure.

9.2.1 Constant Curvature Approach: General Idea

The constant curvature approach describes the continuum robot's geometry with a finite number of curved segments, each having a constant curvature along its length in a plane. Each constant curvature arc is defined by its curvature κ , length ℓ , and angle of the curve's bending plane ϕ (arc parameters). Each arc is independent of the others but is bound to a condition of equal tangent vectors at transition points. An arc is equivalent to a robot segment. Further, the curvature κ and the angle ϕ change due to actuation. The arc length can vary if the robot is capable of varying its segment length. This description allows the use of the approach for different types of continuum robots for which an assumption of constant curvature can be made. In the scope of this work, it is specifically applied to a tendon-driven continuum robot. The general approach introduces two mappings (Webster et al., 2010): the so called robot dependent mapping and the robot independent mapping. The robot dependent mapping translates from the configuration space \mathbf{q} of a specific robot with a specific design into the arc parameter description (κ, ℓ, ϕ) . The robot independent mapping translates from the arc parameter description into the task space (3D-curve) as illustrated in Figure 46.

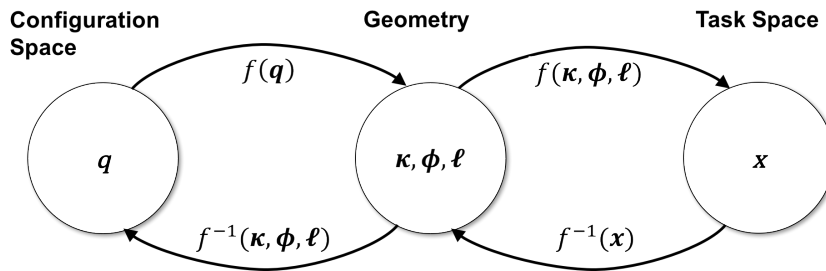


Figure 46: The constant curvature kinematic framework differentiates two mappings. The robot dependent mapping from configuration space \mathbf{q} to arc parameters κ, ϕ, ℓ and the robot independent mapping from arc parameters κ, ϕ, ℓ to task space \mathbf{x} (adapted from Webster et al., 2010).

9.2.2 Robot Dependent Mapping

In this work, a tendon-driven continuum robot with an antagonistic tendon actuation is considered. The tendon displacements, elongation/contraction of the tendons, lead to backbone bending, shaping constant curvature arcs. The constant curvature kinematics can be used to model tendon-driven continuum robots under the following assumptions:

- pure bending
- infinite torsional rigidity
- no transverse shear

- neglection of friction
- neglection of gravitational effects
- neglection of external forces.

A mapping between the configuration space and the arc parameters can be established by $(\kappa_j, \phi_j, \ell_j) = f(\mathbf{q})$, where j is the segment number and \mathbf{q} is the configuration vector, including tendon displacements, defined as:

$$\mathbf{q} = [\Delta\ell_{1_1}, \dots, \Delta\ell_{1_i}, \dots, \Delta\ell_{j_1}, \dots, \Delta\ell_{j_i}],$$

where $\Delta\ell_{j_i} = \ell_{j_i} - \ell_j$ and i is the index of tendons per segment and j the segment number. A configuration vector for a single segment is shown in Figure 47, left. In the initial configuration, the tendon-actuated continuum robot is straight and the length of each tendon ℓ_{j_i} equals the length of the segment ℓ_j , i.e. $\mathbf{q} = \mathbf{0}$. When contracted, $\Delta\ell_{j_i}$ becomes negative and for elongation $\Delta\ell_{j_i} > 0$. The following constraints hold:

$$\sum_{i=1}^{i_4} q_{j_i} = 0,$$

which implies, that it is impossible to either pull all tendons/wires simultaneously.

The arc parameters include the segment length ℓ_j , the segment curvature κ_j , and the segment rotation angle ϕ_j . The rotation angle ϕ_j specifies the angular displacement of the bending plane (defined by \mathbf{e}_{x_p} , \mathbf{e}_{y_p} , \mathbf{e}_{z_p}) of the continuum segment in reference to the x -axis of the robot base coordinate frame \mathbf{e}_{x_B} as shown in Figure 47, left. Alternatively, the relationship $\theta = \kappa s$ allows parameterization based on the angle θ through which the arc bends, where s is the arc length variable (Figure 47, left). The segment lengths ℓ_j are constant in this work. Additionally, given the number and the location of the tendon routing channels on the spacer disk, the arc parameters can be determined. In this work, four routing channels with $\beta = 90^\circ$ angular displacement per segment are used. Their distance to the backbone is defined by r_t . The tendon routing channels are indexed with $i \in [1, 4]$ and start at the x -axis of the robot base coordinate system \mathbf{e}_{x_B} running counter clock wise, as shown in Figure 47, right. As a result θ can be calculated as:

$$\theta_j(\ell_j) = \theta_j(0) - \frac{\ell_j - \ell_{j_i}}{\Delta_{j_i}}, \quad (3)$$

where ℓ_{j_i} is the length of a tendon inside the tendon-driven continuum robot. Using θ , the curvature can be calculated at any location along the backbone as:

$$\kappa_j(s_j) = \frac{\tilde{\theta}_j(s_j)}{s_j}, \quad \text{with } \tilde{\theta}_j(s_j) = \frac{\ell_j - \ell_{j_i}}{\Delta_{j_i}}, \quad (4)$$

with $\tilde{\theta}_j$ as illustrated in Figure 48 and the angle ϕ_j as:

$$\phi_j = \text{atan2}(-\Delta\ell_{j_1} \cdot \cos(\beta) + \Delta\ell_{j_2}, -\Delta\ell_{j_1} \cdot \sin(\beta)), \quad (5)$$

$$\phi_j = \text{atan2}(\Delta\ell_{j_2}, -\Delta\ell_{j_1}), \quad \text{for } \beta = \frac{\pi}{2}. \quad (6)$$

The detailed derivations are stated in Simaan, Taylor, et al., 2004.

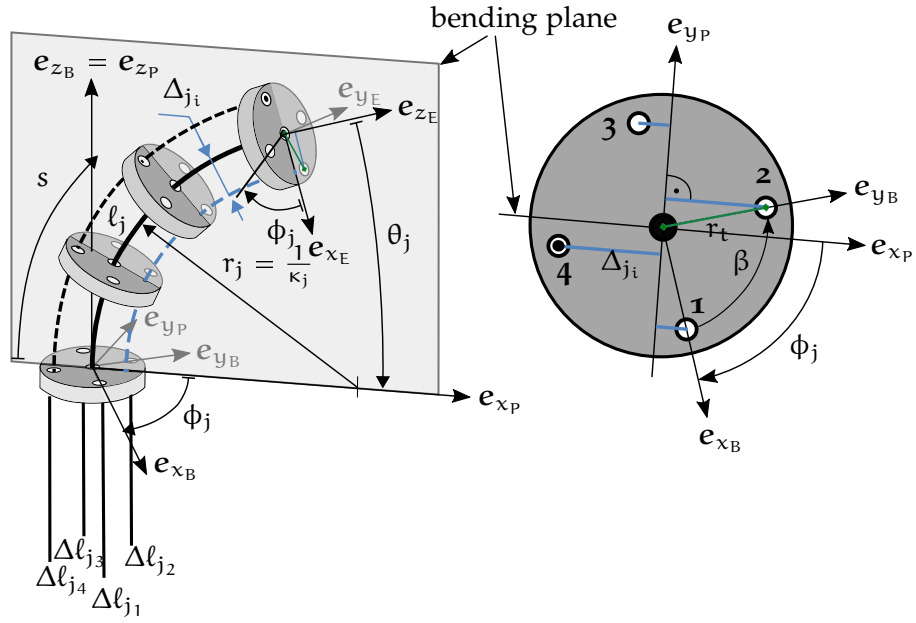


Figure 47: A single segment of the tendon-actuated continuum robot (left). The blue dashed line shows the projection of the first tendon onto the segment bending plane. Cross-sectional view of the base disk (right).

9.2.3 Robot Independent Mapping

The robot independent mapping describes the transition from the arc parameters to the task space as $\mathbf{x} = f(\boldsymbol{\kappa}, \boldsymbol{\phi}, \boldsymbol{\ell})$. For the purpose of this work, an approach where \mathbf{x} describes the pose of discrete points along the backbone is desired. Furthermore, a transformation matrix convention is used.

geometry of circular arcs Given the arc parameters, the position of each point along an arc can be determined geometrically in the arc's bending plane as

$$\mathbf{p}(s) = \begin{bmatrix} \frac{1}{\kappa} \cdot (1 - \cos(\kappa s)) \\ 0 \\ \frac{1}{\kappa} \cdot \sin(\kappa s) \end{bmatrix}, \quad (7)$$

depending on the curvature, as defined in equation 4 or the arc radius defined as κ^{-1} . A point's coordinates in the plane can also be expressed as a rotation around the y-axis e_{y_P} of the bending plane about the angle $\tilde{\theta}_j$. By additionally rotating around the z-axis e_{z_B}/e_{z_P} about the angle ϕ_j , the arc is fully described in 3D-space in the base frame (Figure 48). To calculate the locations of the tendons, it is necessary to perform a reverse rotation around the local z-axis about the angle ϕ_j resulting in the following transformation matrices:

$${}^{j-1}\mathbf{T}_j(s) = \begin{bmatrix} \mathbf{R}_z(\phi_j) & 0 \\ 0 & 1 \end{bmatrix} \begin{bmatrix} \mathbf{R}_y(\kappa_j s) & \mathbf{p}_j(s) \\ 0 & 1 \end{bmatrix} \begin{bmatrix} \mathbf{R}_z(\phi_j)^T & 0 \\ 0 & 1 \end{bmatrix}.$$

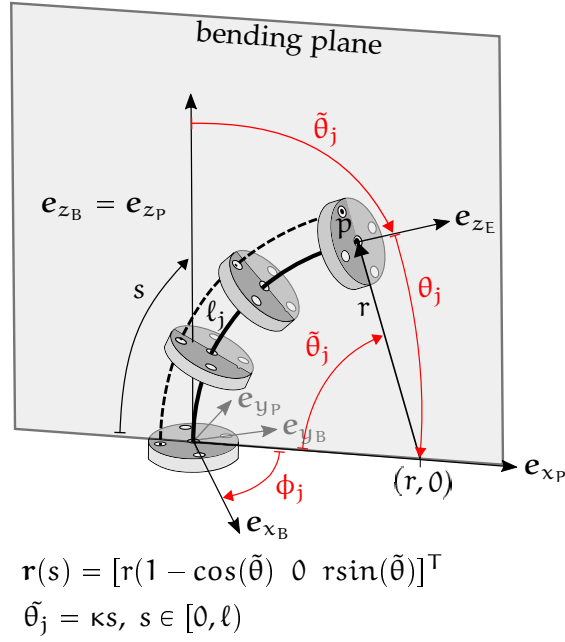


Figure 48: Rotational bending angles ϕ_j and θ_j (or $\tilde{\theta}_j$). The plane position of the tip of a circular arc is determined by the arc's radius r and opening angle θ .

9.2.4 Several Segments

A concatenation of the transformation matrices enables calculation of any point pose in the base coordinate frame of the multi-segment manipulator and therefore also the tip pose as follows:

$${}^0\mathbf{T}_j(s) = {}^1\mathbf{T}_1(l_1) \dots {}^{j-1}\mathbf{T}_j(s), \text{ for } j \in [1, n] \text{ and } s \in [1, \sum_1^n l_j]. \quad (8)$$

The frame of the previous segment defined by $\mathbf{e}_{x_{j-1}}, \mathbf{e}_{y_{j-1}}, \mathbf{e}_{z_{j-1}}$ serves as the base frame for the actual segment ($\mathbf{e}_{x_j}, \mathbf{e}_{y_j}, \mathbf{e}_{z_j}$). The robot base coordinate frame is indexed with $\mathbf{e}_{x_0}, \mathbf{e}_{y_0}, \mathbf{e}_{z_0}$ as shown in Figure 49.

9.2.5 Translational Degree of Freedom

In this work, the robot also possesses a translational DoF, moving the whole manipulator back and forth along the base axis \mathbf{e}_{z_0} . Therefore, the configuration vector is extended by Δl_1 to

$$\mathbf{q} = [\Delta l_1, \dots, \Delta l_{1_i}, \dots, \Delta l_{j_1}, \dots, \Delta l_{j_i}, \Delta l_1]$$

. The value Δl_1 defines to which extend the most proximal segment is retracted and straightened by the rigid port as shown in Figure 50, such that $\Delta l_1 \in [0, l_1]$. The effective length of the first segment, which is considered to calculate the curved shape, is defined as $\bar{l}_1 = l_1 - \Delta l_1$. If $\Delta l_1 = l_1$, then the first segment is fully retracted, meaning the number of segments is reduced to $n - 1$.

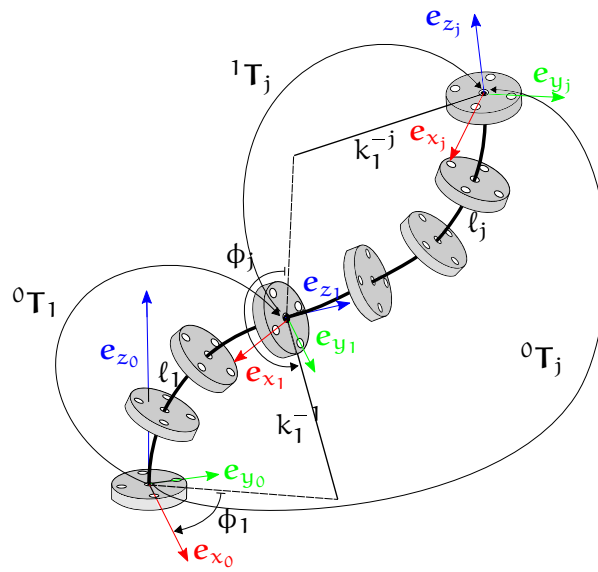


Figure 49: Concatenation of several constant curvature segments with resulting transformation matrices and resulting coordinate frames. An example for two segments is illustrated here.

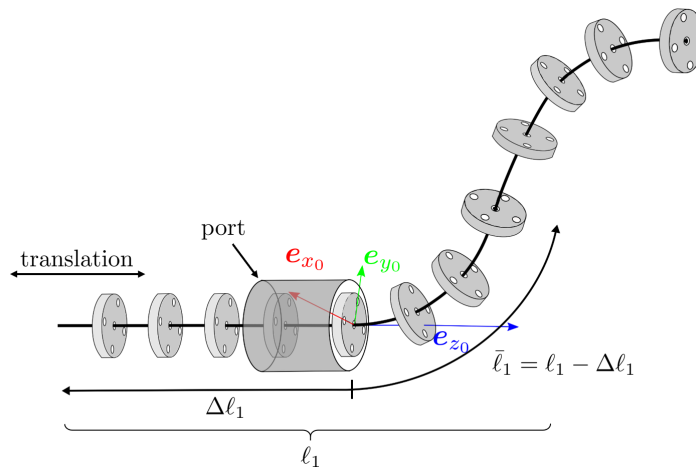


Figure 50: Scheme of the additional translational DoF straightening the most proximal segment. The deployed length $\bar{\ell}_1$ is considered to calculate the curved shape.

9.3 PARAMETER OPTIMIZATION

The purpose of the parameter optimization is to find a sufficient number of segments and corresponding segment lengths ℓ_j , which allow the tip of the articulated port to be positioned at a certain angle and distance from the kidney surface. At the same time, collisions of the robot body with the abdominal wall are minimized. An optimization algorithm is used because no analytical calculation or intuitive selection of segment lengths is possible. An overview of the structure of the optimization algorithm is illustrated in Figure 51 and explained as follows.

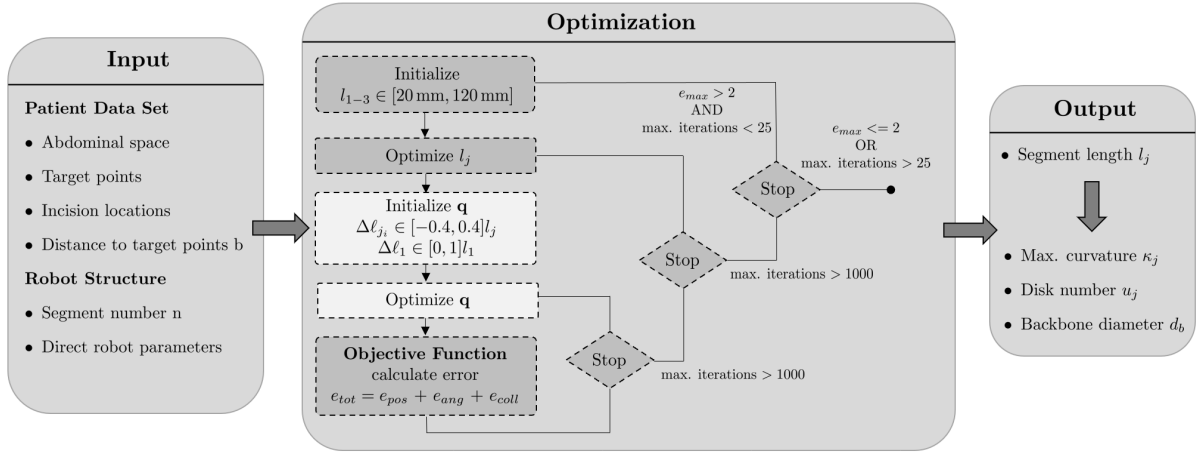


Figure 51: Design optimization algorithm scheme: input, including patient data sets and the direct continuum robot parameters; optimization structure, including optimization parameters; output, including optimized segment lengths and derived parameters.

9.3.1 Input

Input to the optimization algorithm are four abdominal spaces (AS) created from the patient measurements as presented in chapter 4, containing the region of interest (RoI) and incision location (IL). In each RoI, 9 target points are distributed manually and evenly over the surface. To enable the deployment of flexible tools through the articulated port, it needs to be positioned over the target points at a certain distance. This distance b is a further input to the optimization. Three incision locations are provided for every AS, where one of them is always at the navel. The navel incision is considered for optimization. The four abdominal spaces are illustrated in Figure 52.

Further, a tendon-driven continuum robot is given with the described parameters above. The directly derived parameters are defined as in the previous section. The total number of segments n is subject of the analysis and the segment lengths l_j are optimization parameters. Each segment provides 2DoF in the task space. Further, an additional translational DoF enables the translation of the whole robot. The number of segments can be chosen to two or three, resulting in overall 5 or 7 robot DoF respectively. The translational DoF is represented as $\bar{l}_1 = l_1 - \Delta l_1$, being the deployed length of the first segment. This representation is chosen to facilitate the optimization formulation of the outer optimization. That way, only segment lengths of the second and third segment need to be optimized in the outer optimization. The segment length of the first segment would be optimized in the inner optimization as part of the configuration vector. Its optimal value would equal to the maximum value of \bar{l}_1 over all patient data sets, since it would be the largest segment length needed. The respective configuration vector is defined as

$$\mathbf{q} = [\Delta l_{1,1}, \dots, \Delta l_{1,i}, \dots, \Delta l_{j,1}, \dots, \Delta l_{j,i}, \bar{l}_1], \text{ with } j \in [2, 3] \text{ and } i \in [1, 4]. \quad (9)$$

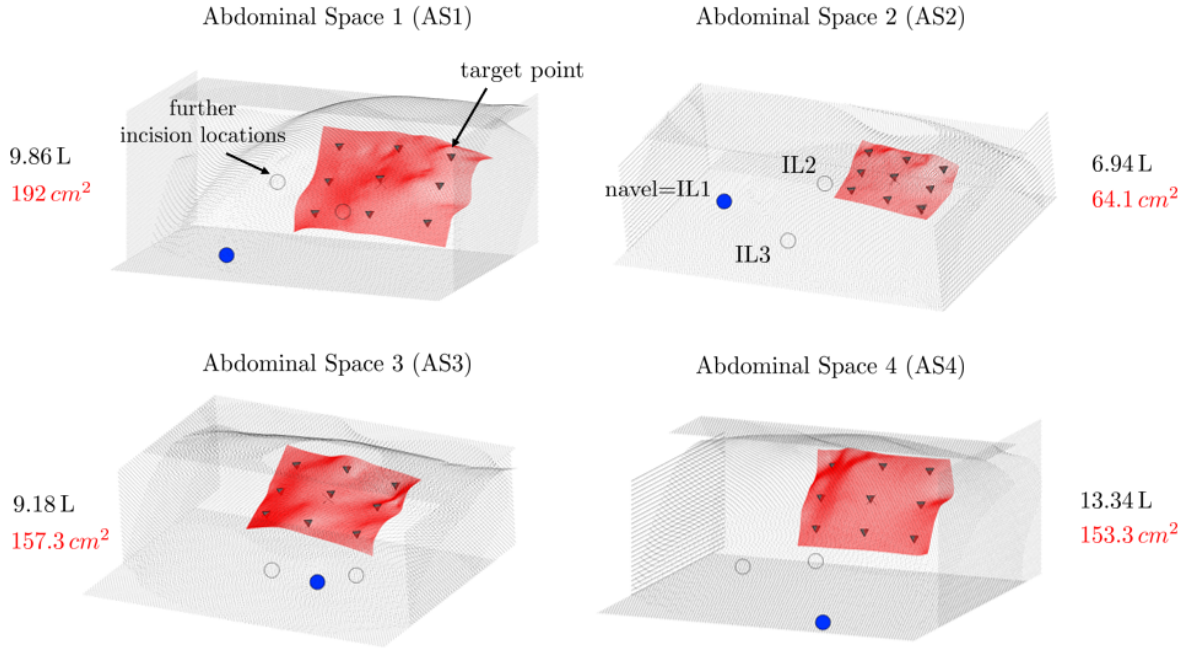


Figure 52: Patient data sets showing their region of interest and selected target points. Data sets with blue incision location (navel) are used for the optimization and the other two incision locations are used for validation.

9.3.2 Optimization

The optimization consists of two nested non-linear searching algorithms (interior-point) provided by the *fmincon* function (MATLABR2017a, MathWorks, Natwick, MA, USA). The inner optimization algorithm solves the introduced geometric kinematic model numerically to find a configuration vector \mathbf{q} minimizing the pose error and workspace collision over several points and is described in detail in the following chapter. The maximum error of the inner optimization over the 9 target points and 4 abdominal spaces is returned to the outer optimization algorithm, which searches for the optimal segment lengths by satisfying the objective defined in equation 14. The segment lengths are forwarded to the inner optimization algorithm for each iteration. The selected searching methods are assumed to be efficient to solve the complexity of this specific non-linear optimization problem.

initialization The initial values ℓ_j are generated randomly on a uniform distribution in the range of [20 mm, 120 mm]. The initial value range is estimated based on measured distances between the incision locations and the target points. For the inner optimization algorithm, the initial tendon displacements $\Delta\ell_{j_i}$ in mm are calculated in the range of $[-0.4, 0.4]\ell_j$ in mm for the respective segment length ℓ_j in mm. The translational DoF $\bar{\ell}_1$ is initialized randomly on a uniform distribution as $\bar{\ell}_1 \in [0, \ell_1]$ in mm. The number of segments is preset to two or three.

objective function The objective function is derived from the application specific use of the articulated port for LESS. In this work, the manipulator should be able to reach a certain tip position with a certain orientation and at the same time avoid collisions with the

abdominal wall. A desired tip position P_{km} is a shifted target point p_{km} on the RoI along its normal vector n_{km} by a distance of b , where $k \in [1,4]$ is indicating the data set and $m \in [1,9]$ the target point, as shown in Figure 53,right. The shift is necessary to provide space for the deployed tools. The error to minimize is the Euclidean distance in mm between P_{km} and the tip position p_{ee} , as defined in equation 10. The desired orientation is chosen to be the alignment of a target point's normal vector n_{km} and the tip's normal vector n_{ee} . The alignment would result in a perpendicular orientation of the tip towards the RoI and is chosen in this work as an indicator for the general reachability of a potential tumor. Since both vectors point in opposite directions and we are looking for a value to minimize, the angle's cosine is added to 1 resulting in a range from [0-2]. To approximately match the magnitude of e_{pos} and provide a normalized representation the value is multiplied by a factor of 50, such that e_{ang} stays in the interval of [0-100] and is defined as in equation 11. The third part is the collision avoidance with the abdominal space. A collision is not necessarily dangerous to the patient, but disadvantageous for the unpredictable shape deformation of the articulated port. Deformations can only be calculated, when the force magnitude, direction and the contact point are known. Further, the selected kinematic model includes the assumption of no external forces. To rely on the results, configurations without (or little) collision must be found. The collision error e_{coll} is defined as the relative volume of the robot (in voxels) leaving the abdominal space (in voxels) with respect to the overall robot volume (in voxels), as shown in Figure 53,left and ranges from [0-100]. The voxel size is set to 5 mm^3 , as a trade off between computational efficiency and resolution.

The overall error e_{tot} is defined as a sum of the three defined errors and is used in the inner optimization algorithm to find a configuration for each target point. The errors e_{ang} and e_{coll} range from [0-100] to approximately match the magnitude of the error e_{pos} and enable approximately equal weighting of the three errors. The explicit error definitions are as follows:

$$e_{pos} = \|P_{km} - p_{ee}\|_2. \quad (10)$$

$$e_{ang} = \left(1 + \frac{n_{ee} \cdot n_{km}}{|n_{ee}||n_{km}|}\right)50; \in [0, 100]. \quad (11)$$

$$e_{coll} = \left(\frac{v_{coll}}{v_{tot}}\right)50; \in [0, 100]. \quad (12)$$

$$e_{tot} = \frac{1}{3}(e_{pos} + e_{ang} + e_{coll}). \quad (13)$$

The outer optimization algorithm considers the maximum error over all target points (TP) for all abdominal spaces (AS) as its goal for minimization. This error e_{max} is defined as follows:

$$e_{max} = \max(e_{tot_{AS,TP}}); AS \in [1,4], TP \in [1,9]. \quad (14)$$

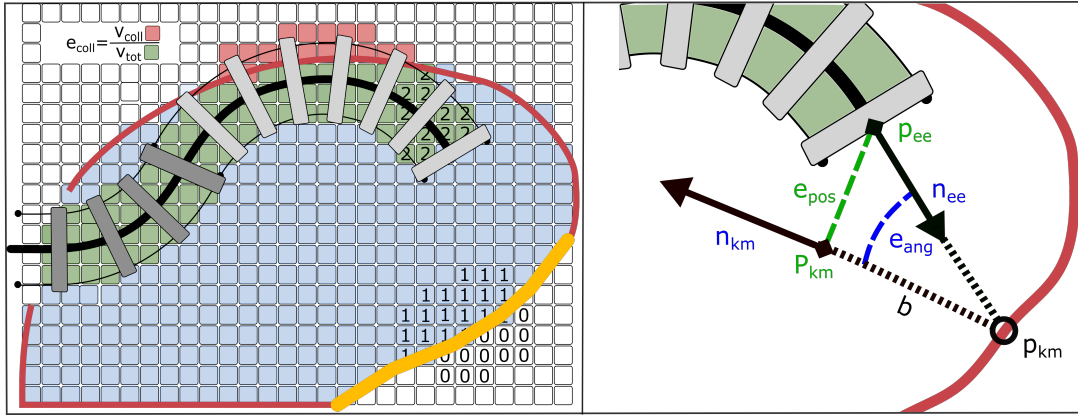


Figure 53: Error metrics of the objective function used for the inner optimization algorithm. Left: collision error e_{coll} is illustrated in a cross section of the abdominal space with the available abdominal space in blue, manipulator occupied space in green, and the collision volume in red; Right: position e_{pos} and orientation e_{ang} errors are shown with the respective points and vectors.

constraints The segment lengths l_2 and l_3 are constrained to minimum 20 mm and maximum 120 mm based on anatomical measurements, as stated in the initialization section. To prevent the robot from colliding with itself due to high curvatures, the retraction tendon displacements (negative values) are limited to a minimum of 44 % of the corresponding segment length. This calculation is done based on the manipulator parameters, stated in Table 7, considering a maximum possible curvature before the collision. There is no upper limit for tendon elongation. However, it is indirectly limited by the negative tendon displacement, since the tendons are arranged in an antagonistic manner. The sum of all tendon displacements in a single segment should always equal zero.

The translational DoF \bar{l}_1 , is limited to a minimum value of 0 mm, which is equivalent to no first segment at all. For each target point, \bar{l}_1 can vary. The maximum required value of \bar{l}_1 over all patient data sets defines the design parameter l_1 . The constraints are listed below for a better overview.

$$l_2/l_3 \in [20, 120] \text{ in mm}, \quad (15)$$

$$\bar{l}_1 \in [0, \text{Inf}] \text{ in mm}, \quad (16)$$

$$\Delta l_{j_i} \in [-0.56 \cdot l_j, \text{Inf}] \text{ in mm}, \quad (17)$$

$$\sum_i^4 \Delta l_{j_i} = 0. \quad (18)$$

stopping criteria Both used numerical search algorithms for finding the configurations and the segment lengths provided by MATLAB are parameterized with its default options, i.e. maximum iterations of 1000. Further, user-based stopping criteria are set for the segment length search. When the numerical search exits due to exceeding the maximum iteration value, the error e_{max} might not be satisfying. Therefore, the numerical search is performed as long as $e_{max} > 2$ or the user-based maximum iteration value of 25 is exceeded. In that case, any error e_{max} is accepted. The value 25 was chosen based on preliminary studies. For each of the 25 iterations, the segment lengths are regenerated randomly again.

9.3.3 Output

As output, the algorithm provides the optimized segment lengths, the errors from the objective function, configuration values, and robot shapes for each point on the target area. The maximum curvatures can be derived from the shapes and used to calculate the diameter of the backbone and the number of disks. Also, the configuration values provide information for the design of the actuation unit marking the maximum actuation values.

9.4 OPTIMIZATION EXECUTION AND RESULTS

Two optimization input sets for the optimization were created. They both include four patient data sets with an incision location in the navel and 9 target points, as shown in Figure 52 and the directly derived manipulator parameters listed in Table 7. The distance to the target points is chosen to be $b = 50$ mm. The optimization inputs differ in the number of manipulator segments, namely $n=2$ and $n=3$, resulting in 5DoF and 7DoF in configuration space respectively. The distance to the target points $b = 50$ mm was chosen to provide enough space for adequate triangulation of articulated tools.

For both input sets, the optimization was performed three times as described above (random initialization), since the selected optimization methods are not deterministic and only provide local optima. This results in 6 different optimized design parameter outputs.

To validate² the optimized parameter sets, each of the 6 designs was validated using 8 further patient data sets consisting of the same four abdominal spaces but with two other incision locations, shown in black circles in Figure 52. Further, for each validation run three distances to the target points $b = 40$ mm, $b = 50$ mm, and $b = 60$ mm were chosen. In the validation, it is investigated how well the optimized designs can perform with different incision locations and different distances to the region of interest. To execute the validation, only the inner optimization algorithm searching for valid robot configurations is used, resulting in a robot shape satisfying the same objective function. Each validation run is executed three times as well.

two segments The best result of the two segment design optimization is shown in Figure 54, top-left and reports segment lengths $l_1 = 312$ mm and $l_2 = 115.3$ mm. The graphic shows the three errors e_{pos} , e_{ang} , and e_{coll} separately as bars for several patient data sets (x-axis), where the bars include errors for 9 target points of one patient data set. The bottom and top lines of the bars show the minimum and the maximum errors, excluding outliers, respectively. The median error is marked as a horizontal black line inside a bar. The errors e_{ang} , and e_{coll} are converted to degrees and percent respectively for better representation. The validation results of the two segment design show comparable results with mostly high angle and collision errors and in some cases high position errors (Figure 54). A considerable difference in error can be observed for the different distances of b . The higher the distance, the higher are the errors. This can be explained by the constraint of the abdominal wall. At greater distances b the robot has to move away from the target points, but at the same time towards the abdomen, which eventually collides with it.

The results for the second and third abdominal cavity, regardless of the incision location, show larger errors due to their smaller volume. The two segment design seems to provide

² in general: to confirm, to make valid; in this scope: to confirm the results from one data set using other data sets

not enough DoF to satisfy all objectives simultaneously. Either the angle or the collision error rises in order to minimize the other two errors.

The maximum error e_{\max} of this optimization run design is 21.50. The results of the other two optimization runs can be found in the Appendix B and show maximum errors of 29.86 and 28.93.



Figure 54: Results of the two segment design third optimization run and validation, showing all three objective errors as box plots for different distances to target points. Errors e_{ang} and e_{coll} are converted to degrees and percent for better representation.

AS = Abdominal Space, IL = Incision Location; Indices are according to Figure 52;
Optimized segment lengths: $l_1 = 312$ mm, $l_2 = 115.3$ mm.

three segments All three optimization results for the three segment design, show better results than the two segment design (the errors e_{ang} , and e_{coll} are converted to degrees and percent respectively for better representation as well.) The results for the best optimized set are shown in Figure 55, top-left and report segment lengths of $l_1 = 333.4$ mm, $l_2 = 63.4$ mm, and $l_3 = 56.3$ mm. The superiority of a three segment design is especially significant considering the validation runs. The errors are always below 0.5 mm for the position error, 6° for the orientation error and 0.2% for the collision error. The same slight increase in error is observed for the second and third abdominal space due to the higher distance. For the distances of 40 mm and 50 mm, the orientation errors are even lower than 2° . The maximum error e_{\max} of this design is 6.29. It is not the lowest over all three optimization runs, but provides lower

errors e_{tot} for the majority of the abdominal spaces, as is shown in the Appendix B. The results clearly show the advantages of the design with three segments, whose explicit parameters are listed in Table 8. The results of the other two designs can be found in the Appendix B and show maximum errors of 23.58 and 5.77.

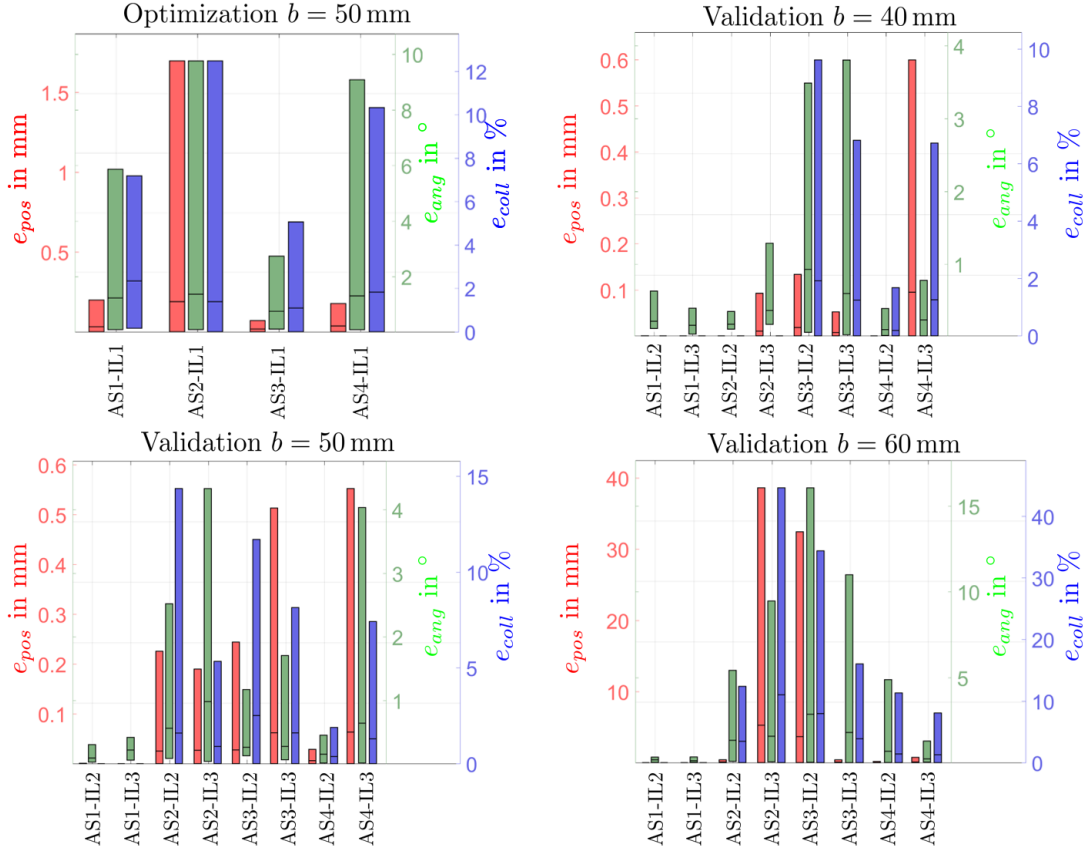


Figure 55: Results of the three segment design third optimization run and validation showing all three objective errors as box plots for different distances to target points. Errors e_{ang} and e_{coll} are converted to degrees and percent for better representation.

AS = Abdominal Space, IL = Incision Location; Indices are according to Figure 52;
Optimized segment lengths: $l_1 = 333.4$ mm, $l_2 = 63.4$ mm, $l_3 = 56.3$ mm.

state of the art parameter sets For the comparison with the state of the art, a validation was performed for the following existing designs: the previously introduced Endoport design (Amanov, Nguyen, et al., 2018), the two segment Stiff-Flop manipulator with extensible segments (Ranzani, Cianchetti, Gerboni, De Falco, et al., 2013), and the Samsung robot (Roh et al., 2015). These designs were chosen because they are meant to be used for abdominal surgeries and these are the only ones which provide the necessary segment lengths. The optimization allows the translation of the entire robot for the length of the proximal segment. The results are shown in Figure 56. All three designs are not suitable for any of the abdominal spaces since at least one or several errors exceed double digits numbers. This is clearly due to the arbitrary approach of parameter determination. Maximum errors for the Endoport, the Stiff-Flop, and the Samsung design are 58.24, 58.81, and 53.55 respectively.

Table 8: Optimized design parameters for the overall best optimization run for a three segment manipulator.

segment	1	2	3
length in mm	333.4	63.4	56.3
max. curvature [m^{-1}]	48.7	62.7	62.7
maximum OD backbone in mm	2.82	2.17	2.17
minimum distance of disks in mm	11.68	21.13	18.77
maximum number of disks in mm	28	3	3
chosen distance of disks in mm	20	22	19
chosen number of disks in mm	17	3	3

9.5 CONCLUSION

With the successful design optimization, the missing parameters can be determined. The first segments length is rather high with 333.4 mm. But it is necessary to bridge higher distances in larger abdominal spaces. The two shorter distal segments provide the required maneuverability in the confined space as they exhibit higher curvatures, as seen in Table 8. Derived from the maximum curvatures, the maximum backbone outer diameter is limited to 2.17 mm, which is a sufficient number to provide certain basic stiffness of the manipulator. Considering the disk thickness b_d , the maximum curvature, and the segment lengths, the number of disks can be calculated as stated before and is chosen to be 17, 3 and 3 for the first, second, and third segment respectively.

When comparing the results to the state of the art from chapter 2.2.3 depicted in Table 1, 2, 3 on page 31, it can be observed that none of the previous works stated, that a three segment articulated port would be necessary for surgeries in the abdomen. Furthermore, segment lengths differ for different optimizations, which proves the approach of optimizing parameters based on anatomical data. Lastly, the required curvatures resulted from the optimization exceed the reported data of existing articulated ports. Hyper-redundant structures reduce their curvatures due to their alternating joint nature. The R-LESS Samsung system presented by Y. J. Kim et al., 2014 shows only curvatures of 10 m^{-1} . The work of Rosen et al., 2017 reaches 30.2 m^{-1} for a relatively small diameter of 12 mm. Even with a small diameter, Ropenecker et al., 2014 were able to increase the curvature to 52 m^{-1} , which is sufficient for the curvature of the first segment. A fluid actuated manipulator, being a continuum structure as well, can reach curvatures of up to 39 m^{-1} , as shown in Cianchetti et al., 2014. In general, the optimization results justify the choice of the continuum robot structure and the chosen methods to parameterize the tendon-driven continuum manipulator. However, the current choice of the objective function in this work serves as an initial optimization study and other objectives, such as kinematic performance indices (e.g. dexterity) must be considered in the future. Furthermore, shape deviations due to contact forces in the event of collisions with the abdomen must be taken into account in the kinematics. To provide equally weighted errors for e_{tot} applying the tanh function to e_{pos} values can be considered.

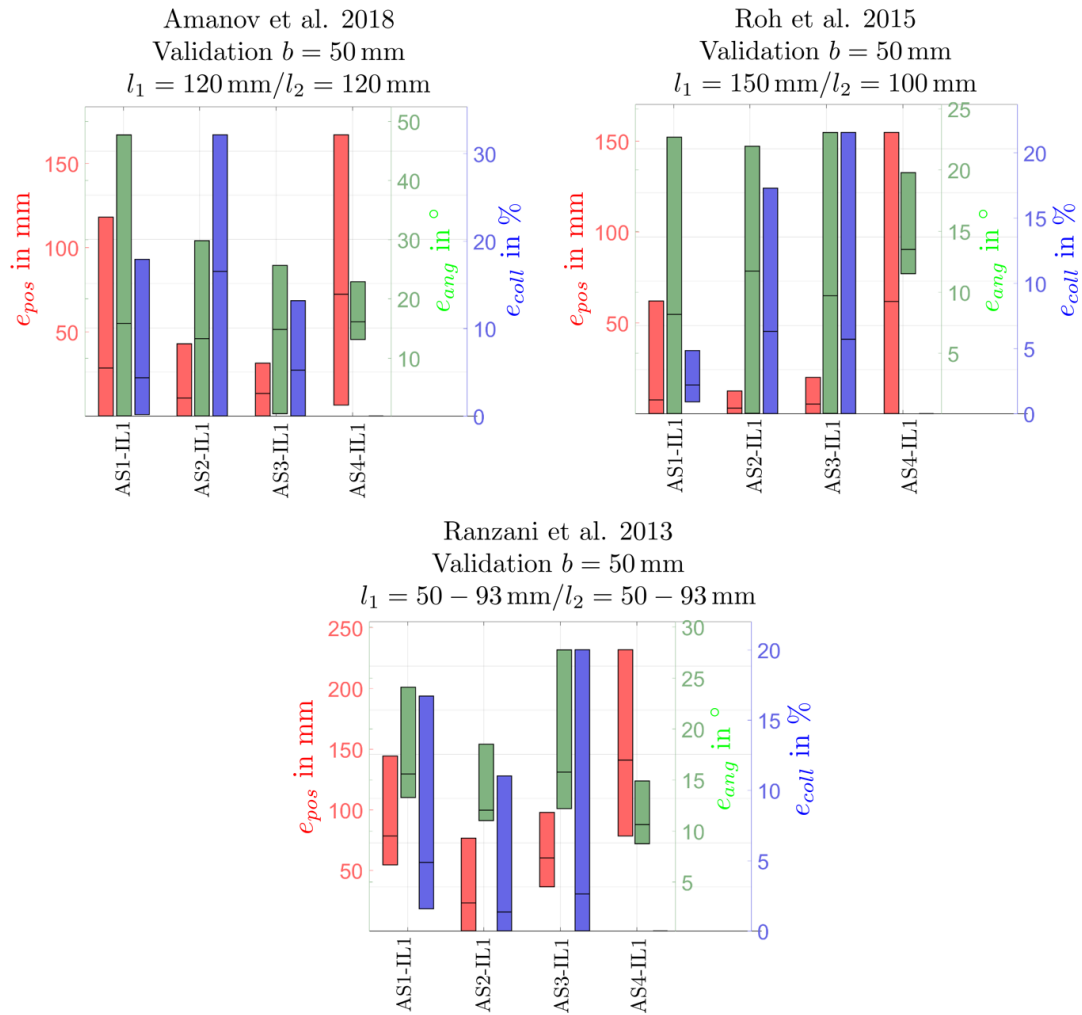


Figure 56: Validation results of the state of the art. Top-left: previous design of the articulated tendon-driven continuum Endoport (Amanov, Nguyen, et al., 2018); Top-right: Samsung robot (Roh et al., 2015); Bottom: Stiff-Flop manipulator (Ranzani, Cianchetti, Gerboni, De Falco, et al., 2013). Errors e_{ang} and e_{coll} are converted to degrees and percent for better representation. AS = Abdominal Space, IL = Incision Location; Indices are according to Figure 52

Part IV
EVALUATIONS

This chapter shows the experimental evaluation of the articulated port in an approximated use case scenario to show the feasibility of the approach in terms of reachability of important anatomical structures. A motorized prototype is used, including an actuation unit and a manipulator. Further, the prototype provides a translational DoF. A phantom is designed based on the measured patient data to imitate the abdominal space. The reachability is measured in terms of visualization of the region of interest, by capturing images of it with the integrated camera in the manipulator's tip.

10.1 REACHABILITY EVALUATION PROTOTYPE

For the reachability evaluation, a dedicated prototype is built with a unique design for this work. It is also referred to as Prototype 1 in the following. Since sterility is not required for this evaluation, the articulated port is rigidly attached to the actuation unit.

10.1.1 *Articulated Port*

The articulated port consists of three segments due to the optimization results. A single central backbone structure with evenly distributed spacer disks rigidly glued to the backbone is chosen (Figure 57b). The design disclaims working channels and stiffening methods, to investigate the reachability capability of the continuum structure alone. With the antagonistic actuation manner, 12 tendons for three segments run through 12 dedicated tendon routing channels evenly distributed circumferentially (Figure 57a). As tendons, braided steel wires coated with nylon with a diameter of 0.38 mm are used and knotted at the respective segment end disk. The spacer disks are 3D-printed (Form 2, Formlabs Inc, Somerville, MA, USA) using standard resin as printing material. For visualization, a chip-on-the-tip camera (Nan-

Eye Stereo, ams AG, Premstaetten, Austria) is installed at the manipulator's tip. Only a mono view of the camera is used. Due to the small camera size ($2 \times 4 \times 2 \text{ mm}^3$), certain surrounding light conditions are required to ensure sufficient picture quality. Therefore, a miniature LED ($2 \times 4 \times 0.5 \text{ mm}^3$) with 20 lumen is installed next to the camera, as shown in Figure 57a. The wiring is routed through the spacer disks (Figure 57b) and the whole actuation unit to its backside. Inside the actuation unit, it is guided by a rigid plastic tube to prevent contact with mechanical parts.

The manipulator is parameterized based on the results in chapter 9 and as listed in Table 8 on page 94. Two parameter adjustments were made. First, the segment length l_1 is set to 200 mm (optimized value is 333.4 mm) due to the smaller size of the abdominal space phantom, with an average size considering the four abdominal spaces. Therefore the number of discs in the first segment is also chosen differently (10 discs with a distance of 20 mm). Second, the outer backbone diameter d_b is chosen to be 0.7 mm.

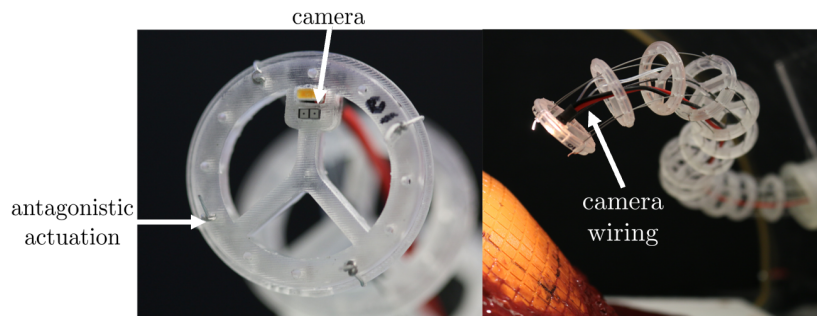


Figure 57: Prototype 1 articulated port for the reachability evaluations. Left: integrated camera and light source at the tip, tendon channel distribution; Right: 3 segments (two DoF each) articulated port.

10.1.2 Actuation Unit

The tendons exit the articulated port at its base and enter the actuation unit. The actuation unit consists of 6 identical subunits, each driving an antagonistic tendon pair. The tendons are attached to a pair of straight gear racks over swivels. The gear racks are mounted on linear guides and are actuated by a straight gear rotated by a DC motor over a worm gear. The components are attached to an acrylic glass plate. The subunit is shown in Figure 58a. Six subunits are arranged to a hexagon, as can be seen in Figure 60.

The actuation unit housing is built of square aluminum bars ($10 \times 10 \text{ mm}^2$, MakerBeam B.V., Utrecht, The Netherlands) and side, front, and back acrylic glass plates. The acrylic components are laser cut. The manipulator base is 3D-printed (Form 2, Formlabs Inc., Somerville, MA, USA). The plastic gear racks exhibit module 1, as do the straight metal gears (24 mm pitch circle diameter). The gear racks are mounted on a linear guide rail (drylin[®] TK-04-07, Igus GmbH, Cologne, Germany). The rotation of the motors is transmitted to gear racks via a metal worm gear with a transmission ratio of 20:1 and module 0.75. Six DC motors (EC 16, Maxon Motor AG, Sachseln, Switzerland) with an integrated gearbox (19:1) and absolute encoder for rotation measurement (512 increments per revolution) are used. As a motor controller, DMC-4080 (Galil Motion Control, Rocklin, CA, USA) is utilized, providing PID

control for motor shaft positioning with zero error (in encoder increments). Motor motion programming and communication is established with the software GalilSuite provided by the manufacturer. Using the mentioned actuation components, the motor shafts on the driving side (after gearbox transmission) can be positioned with a resolution of $\frac{1}{54}^\circ$. With the given tendon actuation components, the tendon displacement can be performed with a resolution of $3.8 \cdot 10^{-4}$ mm.

As an additional aspect, the tendon guidance within the actuation unit must be taken into account. Since the tendon pairs have to be guided to the gear racks, an intermediate laser cut acrylic guiding plate is placed behind the front plate of the actuation unit, redirecting the tendon path. To compensate long term tendon elongation, integrated swivels in each gear rack allow for individual tendon tension adjustment (Figure 58a).

10.1.3 Translation Degree of Freedom

The whole actuation unit is rigidly attached to a mount in the translation unit, which consists of an acme screw lead driven by a DC motor and two linear guides, as shown in Figure 58b. The translation unit housing is made of aluminum bars (15×15 mm², Bosch Rexroth AG, Lohr am Main, Germany) and 3D printed front and back walls (Ultimaker3, Ultimaker B.V., Utrecht, The Netherlands) using PLA as a material, which is provided by the printer manufacturer. The mounting platform consists of 3D printed PLA (Ultimaker3, Ultimaker B.V., Utrecht, The Netherlands) and aluminum bars (10×10 mm², MakerBeam B.V., Utrecht, The Netherlands). The slide bearings, the 10 mm guiding bars, and the acme screw lead (Tr10x2) are acquired from Igus GmbH (Cologne, Germany). A DC motor (DCX 26L, Maxon Motor AG, Sachseln, Switzerland) with an integrated gearbox (16:1) and an absolute encoder (1024 increments per revolution) for rotation measurements controlled by DMC-4040 (Galil Motion Control, Rocklin, CA, USA), offer a translation resolution of $7.2 \cdot 10^{-5}$ mm.

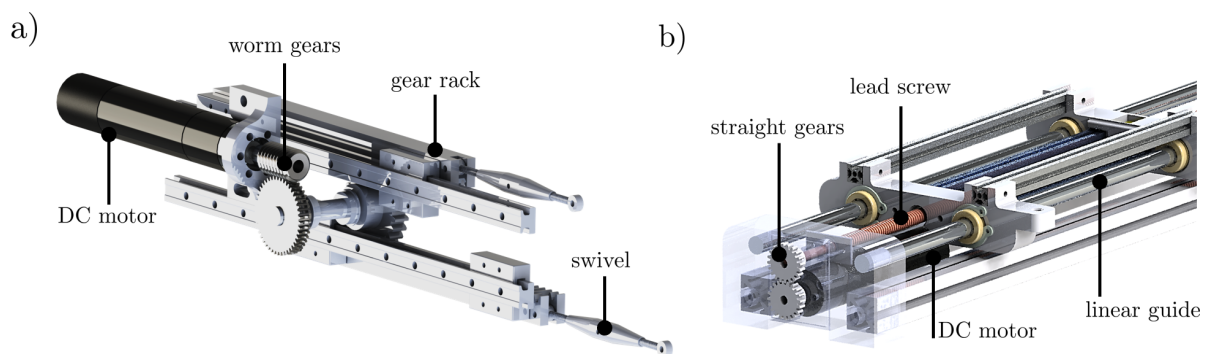


Figure 58: Prototype 1 actuation unit design: a) An actuation subunit driving an antagonistic tendon pair; b) Translational DoF design.

10.1.4 Phantom Design

The phantom mimics the insufflated human abdominal space including the region of interest, as shown in Figure 59g. This allows assessing the reachability of an approximately realistic

scenario. The dimensions of the phantom are approximated as a cut cylinder, with a circular cross-section and a specific radius, restricted by two planes, as shown in Figure 59e. Further, the distance of the geometrical balance point of the RoI to the top point of the circle is important for the adequate placement of the RoI. Derived from the average values from the abdominal spaces used for the optimization, the desired dimensions of the phantom are shown in Figure 59e. To construct the housing, wood plates are composed in 90° to each other representing the bottom and the lower part of the posterior abdominal wall. The anterior abdominal wall is composed of a flexible transparent plastic sheet with 3 mm thickness. It is held by brass bars shaped into curves on both sides towards the upper and lower pole of the kidney.

For the realistic placement of the region of interest, a fine wire mesh grid is shaped into a surface, as shown in Figure 59a. It is fixed to the wooden plates and provides a socket for the 3D-printed kidney (Agilista-3000, Keyence Germany GmbH, Neu-Isenburg, Germany) using the silicone material, which is provided by the manufacturer. The kidney dimensions and shape are extracted from a CT scan using 3D Slicer (Freeware) and converted into a STL-File for 3D-printing. Although the kidney is not required for this experiment, it is a feature of the phantom, which can be used for surgical task evaluations in future investigations. After the kidney is placed in the socket, a molded silicone (Shore A30, orange colored) layer of ca. 5 mm thickness representing the region of interest covers the printed kidney, such that it can adapt to the kidney shape, as the pararenal fat does in reality (Figure 59b-c).

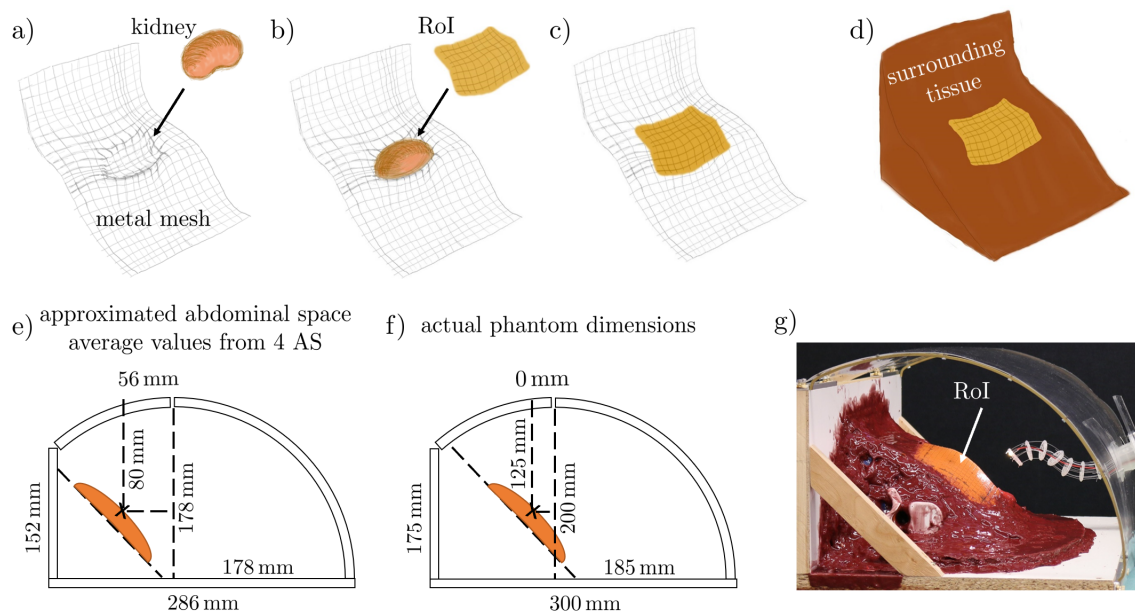


Figure 59: Detailed abdominal space phantom design. a-d) Manufacturing scheme of the region of interest; e) Abdominal space approximation based on abdominal measurement; f) Actual phantom prototype dimensions; g) Complete phantom prototype

The surface of the RoI was chosen to be $75 \times 125 \text{ mm}^2$ such that it covers the 3D-printed kidney. The remaining wire mesh is covered by red silicone, representing the surrounding tissue as shown in Figure 59d. The resulting phantom does not exactly match the average measurements, which is a result of the manufacturing process, as shown in figure 59f. The

balance center of the RoI is lower than the average value, which provides more space. However, it is also aligned with the top point of the circular cross-section, which shifts it toward the abdominal wall decreasing the available space. In summary, the phantom deviates from the average values but offers a good approximation for the reachability investigations.

10.2 EVALUATION EXECUTION

The prototype must be evaluated using the phantom in terms of its reachability, approximating the real case scenario. Although only visualization is provided, the established tip pose of the articulated port defines the access angle of the tools, which are envisioned to be deployed through the port.

A 3D-printed port rigidly attached to the actuation unit is used to place in the incision and straighten the continuum robot outside the abdomen, as discussed in chapter 8 and shown in Figure 60. The edges of the port should be round to enable the smooth deployment of the manipulator and to prevent interlocking of the spacer disks on the edges. In the real case scenario, the manipulator would be covered by a rubber or flexible thermoplastics.

The aim of the evaluation is similar to the simulations and aims to investigate how well the tip of the robot can be positioned perpendicular to certain target points on the region of interest at a certain distance from it. Preferably collisions with any part of the phantom should be avoided. The robot is assessed by inserting it through two different incisions in the anterior abdominal wall, as shown in Figure 60. In contrast to the simulations, 15TP are defined, distributed evenly over the RoI, and represented by 15 rectangular areas with a surface of $25 \times 25 \text{ mm}^2$ each (sub RoI). Fifteen target points are considered to sufficiently cover the whole RoI after some initial trials with the experimental setup. Each sub RoI is marked with a number for evaluation purposes, ranging from 1 to 15 from top left to bottom right, taking the incision perspective into account.

The focus of this investigation is the visualization of the region of interest as a representative for the positioning of the camera and the instruments. Considering the orientation of the robot's tip, camera feedback should be sufficient, since surgeons also always rely on the endoscope images as feedback during minimally-invasive surgery. Therefore, only visual feedback from the camera on the tip is used to manipulate the robot. Only the images of one camera are used for this evaluation (mono-view). In contrast to the real case scenario, the robot is controlled by manually commanding motor angles (no teleoperation¹). This is not ideal but sufficient for these evaluations. During the experiment, the robot is inserted through one of the three incisions and then moved to all 15 target points one after the other without leaving the abdominal space. Having the live camera image on a screen, the robot is positioned such that the number of a sub RoI is in the center of the image and seen straight from above. The collision detection during robot motion is additionally monitored visually (human eyes) by a side view inside the phantom, as shown in Figure 61 (top images). Each sub RoI is approached once.

¹ in this scope, teleoperation would foresee commanded tip velocities in task space, from which the joint space velocities are computed using the Jacobian.

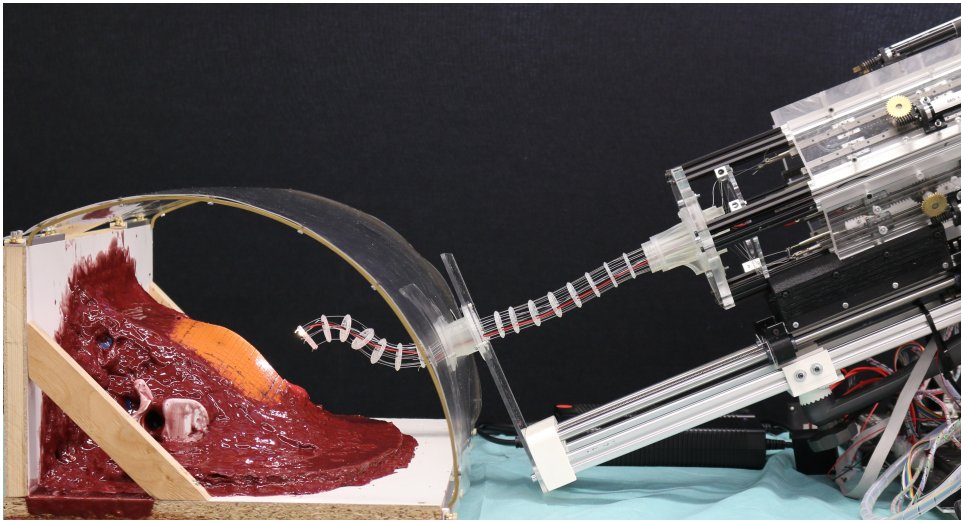


Figure 60: Experimental setup for reachability investigations showing the phantom and the corresponding prototype.

10.3 RESULTS

The images for each established configuration related to one sub RoI are depicted in Figure 61 (bottom images). It can be observed that all sub RoI can be visualized clearly such that their number is in the middle of the camera image. It is not always possible to provide the same orientation of the image, such that the numbers are not horizontally aligned. However, with teleoperation, it should be feasible since 7DoF in joint space can serve 6DoF in the task space. From the side view (Figure 61 (top images)), it can be observed that the orientation towards the target surface is approximately perpendicular. This proves that attempting to position the robot's tip above the numbers based on the visual camera feedback is sufficient to control the overall orientation. To estimate the distance, the camera feedback is not enough since only one camera of the stereo camera is used and therefore the depth can not be perceived. From the side view, the distance looks rather small and is estimated to be around 4 cm but is not measured during the evaluations. Considering the collision-free movements during the whole experiment, none of the established configurations showed contact with the anterior abdominal wall. This indicates, that greater distances to the RoI can be achieved. The additional translational DoF of the entire actuation unit is used frequently to overcome different distances from the incision to the target points.

10.4 DISCUSSION

The evaluation shows promising results in terms of reachability of relevant anatomical structures, providing initial proof of concept in an approximated use case scenario. Approximately perpendicular access to each of the sub RoI implies not only sufficient visualization but also the positioning of the instruments. As introduced in the state of the art, this improves instrument triangulation compared to access through a straight port.

Further evaluations using a manipulator with integrated working channels and membranes on phantoms of different abdominal spaces should be performed to validate the obtained

results. A study with surgeons and teleoperation algorithms under solely visual feedback from the tip camera will provide additional application-related insights. The results of the deployment through the second incision location can be found in Appendix D.

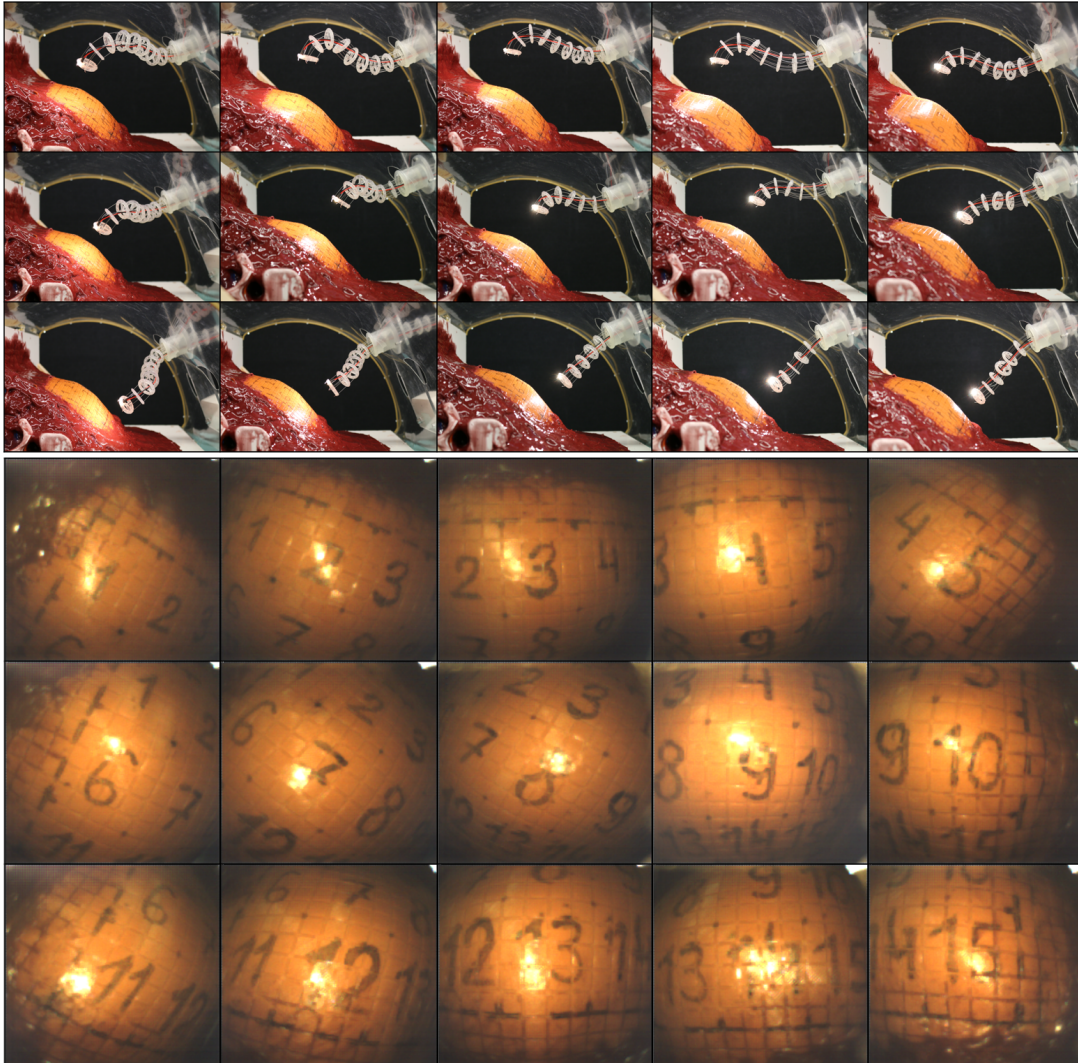


Figure 61: Experiment images of 15 configurations in the side view (top images) and the integrated camera view (bottom images).

This chapter aims to investigate the stiffness increase potentials through the structure of the backbone, and also the evaluation of the selected stiffening methods: tendon tensioning, granular jamming, and layer jamming. The torsional stiffness increase by a crossed alternating backbone structure is investigated. The tendon tension stiffening is evaluated on its own and in combination with layer jamming to unveil potential synergy effects. Lastly, the stiffness of an articulated port with integrated granular and layer jamming is investigated to discover the superior stiffening method. Throughout the chapter, the articulated port is also referred to as a manipulator.

11.1 EXPERIMENTAL TEST BENCH

To evaluate the bending and torsional stiffness, a test bench is designed and built, which is used throughout the following experiments (Figure 62a). It consists of an aluminum bar frame (30x30 mm², Bosch Rexroth AG, Lohr am Main, Germany), which holds a two-axes platform with a mounted force/torque sensor (Nano43, ATI Industrial Automation, Apex, NC, USA). The sensor has a measuring range of ± 18 N and resolution of $\frac{1}{256}$ N⁻¹ for forces and a measuring range of ± 250 Nmm with $\frac{1}{20}$ (Nmm)⁻¹ resolution for torques. Each axis consists of a linear guide system (DryLin[®] SLW, Igus GmbH, Cologne, Germany), where the acme screw is driven by a DC-motor (DCX 26L, Maxon Motor AG, Sachseln, Switzerland) with an integrated gearbox (16:1) and an absolute encoder for rotation measurement (1024 increments per revolution). As a motor controller, a DMC-4040 (Galil Motion Control, Rocklin, CA, USA) and control software provided by the manufacturer are used. The axes are arranged with 90° to each other. One axis is carried by the other and the top axis carries the sensor platform, such that the sensor can be moved in a plane (Figure 62e). Using the motor controller, a synchronized motion of the axes can be achieved, e.g. enabling a circular motion. On top of the

sensor, an adapter is mounted where the manipulator's tip is placed with 1 mm gap between the adapter wall and the end spacer disk, such that the prototype can be bent but not twisted during deflection. This setup is used for the bending experiments (Figure 62c). In the initial position, the sensor is placed directly under the manipulator so that the z-axis of the sensor is approximately aligned with the centerline of the manipulator. This corresponds to zero deflection on both motorized axes. First, a deflection on the negative y-axis of the sensor with the magnitude of the circle radius is performed, and from there the circular motion (360°) follows counter clockwise (Figure 63a). After the circular motion, the sensor moves back to its initial position (Figure 63b). The angle of the circular motion is referred to as the deflection angle in the following.

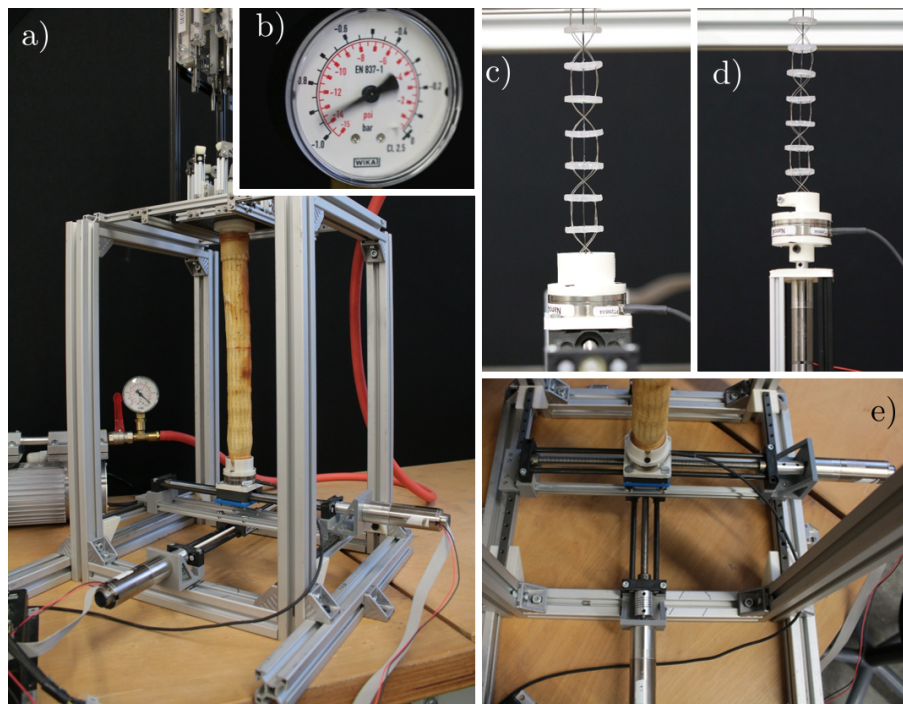


Figure 62: General stiffness evaluation setup. a) Overall test bench prototype; b) Vacuum sensor; c) Set up variation for bending evaluations; d) Set up variation for torsion evaluations; e) Closeup of the actuated axes for prototype deflection in the plane.

For the torsion stiffness measurements, an additional construction is fixed to the carrier on the top axis as shown in Figure 62d. A DC motor (EC 16, Maxon Motor AG, Sachseln, Switzerland), which is attached to the construction, is aligned with the z-axis of the sensor. The same force/torque sensor is rigidly fixed to the motor. On top of the sensor, an adapter is mounted with a clamp mechanism. Once the prototype is clamped, the motor rotates and twists the sensor and the prototype about a certain twisting angle γ counter clockwise from its initial position, where the prototype is not twisted and the sensor is unloaded (Figure 63c). Subsequently, the motor moves about 2γ clockwise. Finally, the sensor returns to its initial position. The motion is executed without time delay during the changes of direction. The torque measured during this motion corresponds to the torsional stiffness of the examined prototype.

For jamming method evaluations, a vacuum pump is utilized (MPZ86.22, hyco Vakuumtechnik GmbH, Krailling, Germany), which is capable of creating a vacuum up to $8.5 \cdot 10^3$ Pa.

Vacuum levels were measured with a mechanical manometer (Bourdon gauge¹) at the pump inlet with an accuracy of $\pm 2.5\%$ (Figure 62b). Adapters, clamps, etc. were 3D-printed using PLA (Ultimaker3, Ultimaker B.V., Utrecht, The Netherlands).

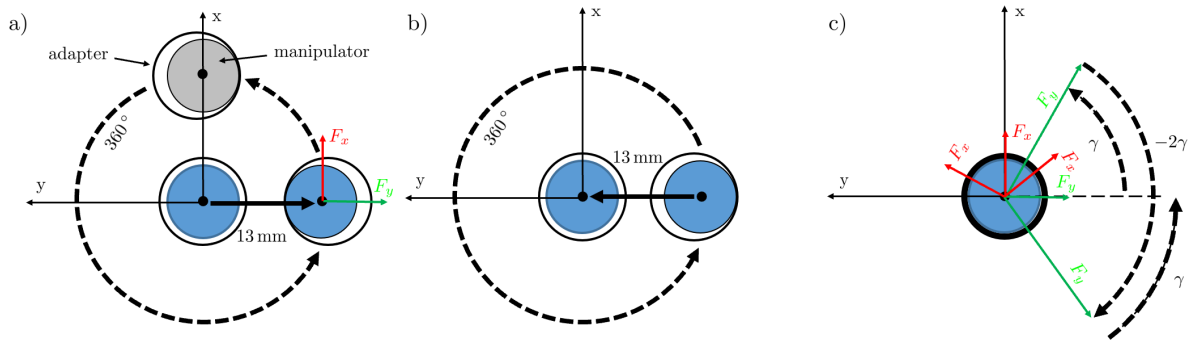


Figure 63: Stiffness evaluation motion schemes from the top view. a) Bending evaluation, the manipulator (blue) is deflected on the y-axis and then counter clockwise on a circle, intermediate position in gray; b) Manipulator moved back to the initial position; c) Torsion motion pattern.

11.2 FORCE/TORQUE SENSOR DATA PROCESSING

During a deflection motion, the sensor data is recorded using MATLAB (R2016a/R2017a, MathWorks, Natwick, MA, USA) with 40 Hz sampling rate. Per data sample, 6 values are available, three force values on the F_x , F_y , and F_z axes and three torques values about the three axes.

For the bending, the forces on the x and y-axis (in-plane movement) of the sensor are selected. The saved sensor data is trimmed to the time frame of the motor motion. The beginning of the deflection motion can be identified as a sudden force increase and is marked manually. The duration of the deflection movement can be calculated based on the set motor velocity and the deflection circle radius. The raw force data exhibits a certain noise, as shown in Figure 64a. Therefore, the data of each axis is fitted with a third-order polynomial (solid lines). The fitted data of both forces can be visualized equivalent to the circular movement to acquire information about the deflection force distribution over the bending angle (Figure 64b). The resulting force, consisting of x and y-value, is determined by the Law of Pythagoras. Since the deflection force deviates over the entire circular movement, the extreme values on the circle (max/min) and the average value of the resulting forces are calculated to compare different prototypes.

Since five repetitions per prototype are performed, the repeatability can be evaluated as well. The repeatability is defined by the variation between 5 repeated measurements, as follows:

- 1) at a particular circle point (data sample ω), a mean resulting deflection force over five repetitions is determined $\bar{F}_{res}(\omega)$
- 2) the differences between each repetition value ($F_{res_{rep}}(\omega)$) and the mean value is computed, where $rep \in [1,5]$.

¹ a c-shaped metal tube, which tends to straighten when pressurized

- 3) the resulting values are divided by the mean resulting deflection force at that circle point
- 4) this is performed for each circle point ω .

Equation 19 includes steps 1-3 and Figure 64b shows a close-up of five repetitions and the resulting mean values.

$$\text{variation}(\omega) = \frac{1}{\bar{F}_{res}(\omega)} (\bar{F}_{res}(\omega) - F_{res_{rep}}(\omega)), \text{ with } rep \in [1, 5]. \quad (19)$$

Displaying the variation as a percentage helps to interpret the repeatability in relation to the absolute values of the deflection force.

The torsion measurement data is trimmed in the same way as for the bending experiments and is fitted by a fourth-order polynomial. The raw and fitted data is shown in Figure 64c. The direction changes are marked with green circles. The variation calculation is performed in the same way as for the bending experiments, comparing samples recorded at the same time during the measurement. To be able to evaluate the hysteresis, the data is sorted with respect to the deflection angle γ , as shown in Figure 64d, where arrows indicate loading (red) and unloading (blue). The hysteresis is defined as the torque difference $\tau(\gamma) - \tau'(\gamma)$ during loading and unloading at the same angle γ , as illustrated in a closeup in Figure 64d.

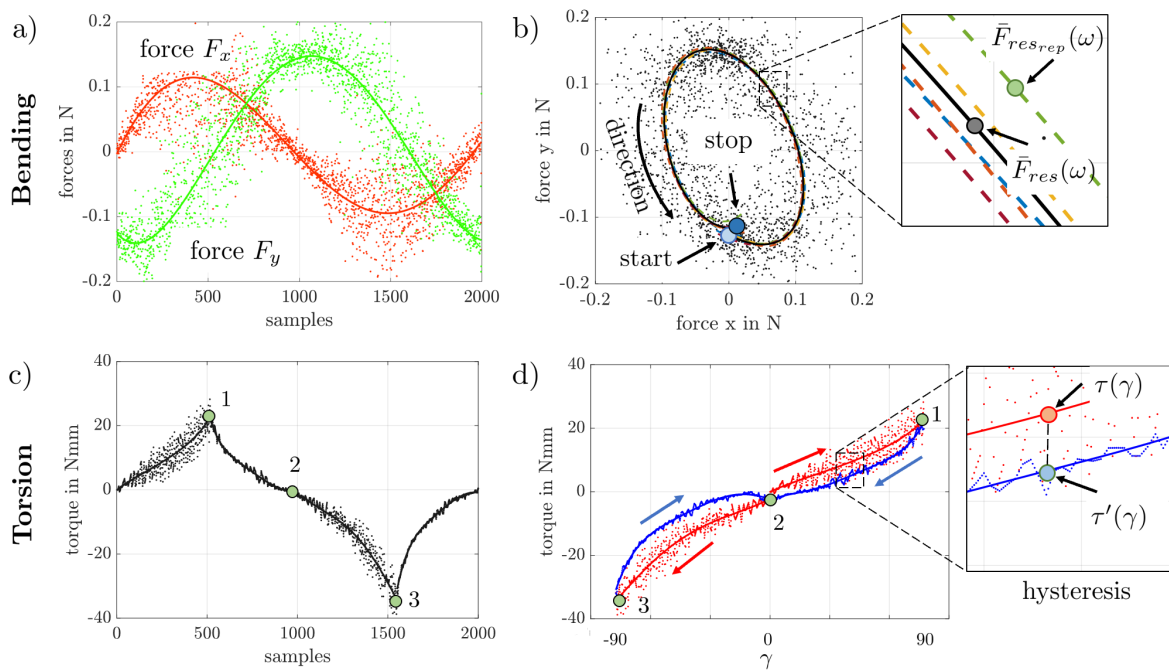


Figure 64: Stiffness evaluation data processing. a) Raw and fitted bending force values; b) Fitted bending forces arranged into a force circle showing the deflection motion direction, closeup shows 5 repetitions and the mean value of them; c) Raw and fitted data for torsion evaluations with green points marking the direction changes; d) Torque values illustrated over the twisting angle and close up showing the hysteresis.

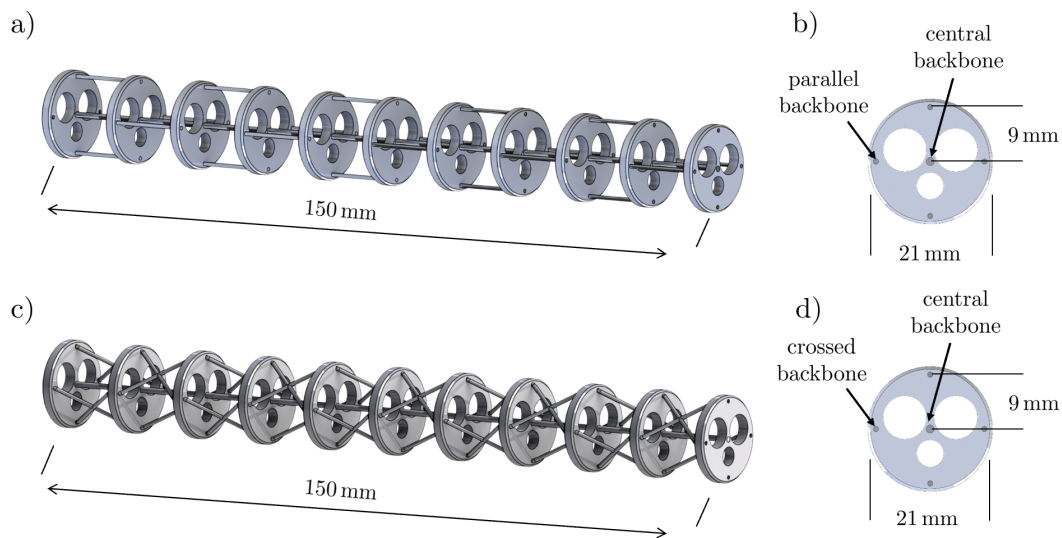


Figure 65: Two different structures to increase the torsional stiffness of the manipulator: a-b) Parallel alternating backbone structure; c-d) Crossed alternating backbone structure.

11.3 TORSIONAL STIFFNESS INCREASE BY STRUCTURE

The structure is defined as the geometric arrangements of basic manipulator parts, in particular the backbone. While the bending flexibility of continuum robots is their key feature, the torsional compliance is rather undesirable. Two approaches, generated in chapter 8 on page 69, are compared to one another: the parallel alternating backbone and the crossed alternating backbone. The parallel alternating backbone consists of two backbone rods arranged symmetrically to the center point of a spacer disk at a circle with a certain radius. They lie on the same line as the spacer disk center point and therefore in the bending plane, allowing for bending as shown in Figure 65a. The two rods are rigidly attached to two neighbored spacer disks. To allow for bending in a second plane (2nd DoF), the rods connected to the next spacer disk are displaced radially about 90° (Figure 65b). The radial displacement alternates along the manipulator length. If torsionally loaded, this design would twist and reduce its length due to twisting of the parallel alternating rods. A third backbone running through the center and attached to all the spacer disks can be placed, maintaining the manipulator length and preventing the manipulator's contraction while twisting.

The second approach, suggests a similar alternation of the backbones on a circle concentric to the spacer disk. The difference is that instead of two parallel rods, two pairs of crossed rods are used, as shown in Figure 65c. A pair of crossed rods intersects in the middle between two spacer disks. The intersection of the rods lies in the same plane as the center of a spacer disk in a straight configuration. The rods are threaded through the whole manipulator, such that they are bent close to each spacer disk. The bending stiffness of the structure is sufficient due to the flexibility of the rods, but the torsional stiffness increases due to the inclined arrangement of the crossed rods. For better comparison, a third backbone in the center of the spacer disks is added.

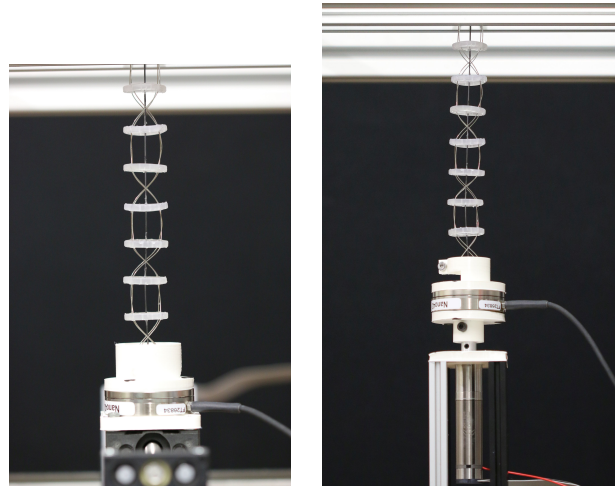


Figure 66: Experimental stiffness setup for bending (left) and torsion (right).

11.3.1 Evaluation Set Up

To evaluate the bending and torsion stiffnesses, prototypes of both structures as described in the previous section are built. Both are 150 mm long and 21 mm in diameter. Each has 10 of 2 mm thick spacer disks and nitinol rod backbones of 0.7 mm diameter for the central backbone and 0.4 mm diameter for alternating backbones. The test bench variation for torsional experiments as described beforehand is used to perform the evaluation. The set up is shown in Figure 66 for bending (left) and torsion (right). The bending deflection is performed on a circle with a radius of 13 mm and a velocity of $2.7 \cdot 10^{-1} \frac{\text{m}}{\text{s}}$.

To investigate the torsion, the parallel alternating backbone prototype is twisted about $\gamma = 90^\circ$. For the crossed alternating backbone prototype, the rotation angle is reduced to $\gamma = 17^\circ$. Five repetitions for each structure for bending and torsion are performed.

11.3.2 Results

Figure 67 shows the bending evaluation results on the left. The five repeated measurements are illustrated as dashed lines and the mean values as solid black lines and detailed results are summarized in Table 9. The bending forces for the parallel alternating backbone structure, depicted as a solid black line without markers, are considerably larger than the forces for the crossed alternating backbone structure (solid black line with triangles markers). Considering the resulting fitted deflection forces (maximum, minimum, and mean), the parallel structure shows twice as high values. These numbers are based on the mean values over five repetitions. On the other hand, the variation is higher for the crossed structure (more than doubled). Both structures show elliptic force distributions. This can be explained by the manufacturing process and needs further investigations.

Looking into the torsional stiffness results, the crossed structure shows over three times higher torques (94.85 Nmm) needed for less than a third of twisting angle (Figure 67, right). Despite the higher torque values, the variation is considerably lower for the crossed structure as well. In contrast to the parallel backbone structure, the torque to twisting angle relationship is nearly linear for the crossed backbone prototype. However, its hysteresis is higher, which is

not clearly visible in Figure 67, right due to the high slope and linear course. The disadvantage of both structures is the halved maximum curvature due to the alternating arrangement of the backbone. Only every other backbone between two spacer disks can bend in the same bending plane. For the optimized design, certain maximum curvatures are required for each of the three segments, as stated in Table 8 on page 94. Since the distal segments are much shorter, they do not necessarily need torsional stiffness increase. For a long segment as the first segment, small loads can lead to large torsion angles, affecting the shape significantly.

Table 9: Detailed results on backbone structure stiffness evaluation showing extreme force values, variations, and hysteresis.

	backbone structure	parallel	crossed
	bending		
1	mean force in N	0.125	0.066
2	max force in N	0.16	0.08
3	min force in N	0.086	0.04
4	variation min/max in %	$3.3 \cdot 10^{-5}$ -4.64	$8.3 \cdot 10^{-5}$ -11.5
5	variation mean in %	1.45	3.03
	torsion		
7	max torque in Nmm	34.14	94.85
9	variation min/max in %	$1.05 \cdot 10^{-4}$ -27	0.001-2.97
10	variation mean in %	3.14	0.95
11	hysteresis min/max in Nmm	0.013-10.26	0.004-18.5
12	hysteresis mean in Nmm	5.06	8.29

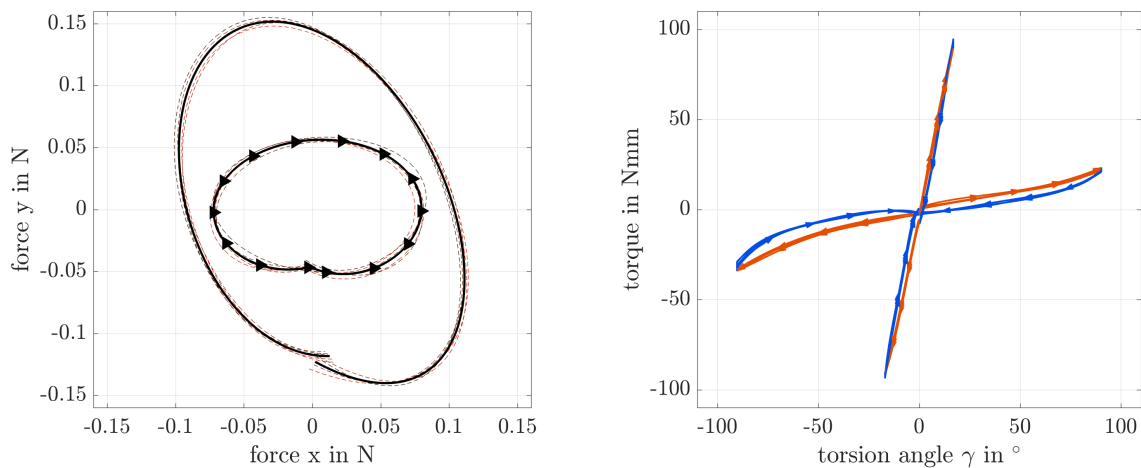


Figure 67: Backbone structure stiffness results; Left: Bending results, crossed alternating backbone is marked with triangles; Right: Torsion results, red lines indicate loading motion and blue lines unloading motion. Higher slope curves correspond to the crossed backbone structure.

11.4 JAMMING STIFFENING

This chapter aims to evaluate the tendon tension stiffening, granular jamming, and layer jamming stiffening. Therefore, two further articulated port prototypes are built and evaluated.

The prototypes are referred to as Prototype 2 and Prototype 3 to distinguish them from the previously introduced Prototype 1 for reachability investigations. Detailed parameters of the prototypes are summarized in Appendix C. Only the bending was evaluated on the presented test bench.

11.4.1 *Layer Jamming - Tendon Tension Stiffening Prototype*

This prototype is meant for investigations of layer jamming stiffening and a combination of tendon tension and layer jamming stiffening. It disclaims motorization providing manual tendon displacement actuation. This prototype is also referred to as Prototype 2 in the following. The prototype design is partially derived from the design presented in chapter 8 on page 74. It only consists of the articulated part excluding the actuation unit and the translation DoF. It has a length of 150 mm without working channels with a parallel alternating backbone structure (0.4 mm) with a central backbone (0.7 mm). Ten spacer disks (21 mm \varnothing) are equally distributed along the backbone and provide four tendon channels (0.5 mm) for antagonistic actuation at 9 mm distance to the backbone (Figure 68a-b). Four tendons (0.38 mm) made of braided steel wires covered with nylon are used. The layer jamming flaps are made of neobond (0.19 mm thick) and are integrated by wrapping it around the manipulator and interlocking the flaps every 120° , as shown in Figure 68f. An air proof chamber is achieved by the encapsulation of two membranes (Figure 68d). This results in an overall diameter of 23 mm. The dimensions of the flaps are shown in Figure 68c.

The manipulator is attached to a base equipped with worm gears to wind the tendons. Twelve metal worm gears with module of 0.75 and a transmission rate of 20:1 are integrated. The tendons are glued inside a borehole in the worm wheels' flange (13 mm \varnothing). The worms are actuated manually via a shaft (Figure 68e). The tendon displacement can be determined, based on the flange dimension and worm gear transmission. The housing is 3D-printed (Form 2, Formlabs Inc., Somerville, MA, USA). A vacuum interface is provided in the same housing (Figure 68g). A net is installed at the vacuum inlet at the base of the manipulator to prevent the membrane from being sucked in and to cut off the air flow (Figure 68h).

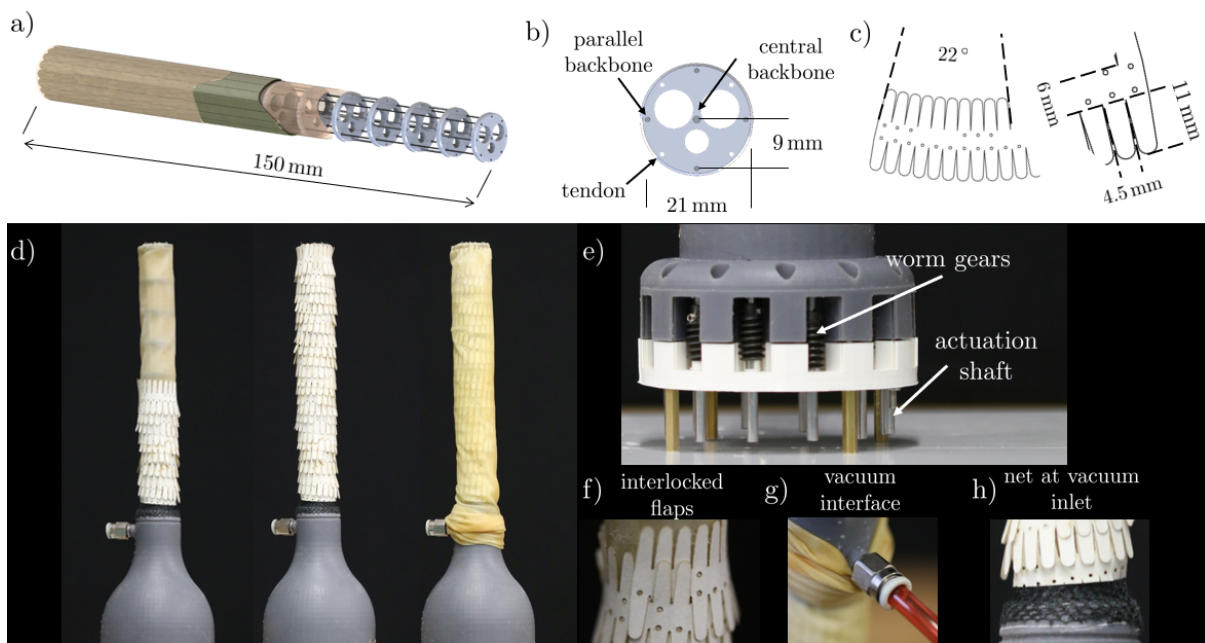


Figure 68: Prototype 2 details: a-c) Manipulator parameters; d) Layer jamming encapsulation; e) Tendon actuation by worm gears; f) Flap interlocking; g) Vacuum interface integrated at the base; h) Net at the vacuum inlet to ensure air flow.

11.4.2 Layer Jamming - Granular Jamming Prototype

In order to investigate the stiffness of an articulated port, including typical components (working channels, etc.), a dedicated manipulator prototype is evaluated in this section. Three different manipulator prototype variations of the design are introduced to understand the sources of stiffness. This prototype is further also referred to as Prototype 3. Detailed parameters for the prototype variations are shown in Appendix C.

actuation unit prototype 3 The actuation unit prototype is based on a similar design as the reachability evaluation prototype on page 100. Each antagonistic tendon pair is attached to a pair of plastic straight gear racks, driven by the metal straight gears (module 1, 24 mm pitch circle diameter). The gear racks are mounted on linear bearings, sliding on a linear guide rail (drylin[®] TK-04-07, Igus GmbH, Cologne, Germany). The rotation of a DC motor is translated to the gear racks over a metal worm gear with a transmission ratio of 20:1 and a module of 0.75 (Figure 69b). Four of the described subunits are arranged in a rectangle, as shown in Figure 69a. The housing is built of square aluminum bars (10x10 mm², MakerBeam B.V., Utrecht, The Netherlands) and side, front, and back acrylic glass plates. The acrylic components are laser cut. The manipulator base is 3D-printed (Ultimaker3, Ultimaker B.V., Utrecht, The Netherlands). Four DC motors (EC 16, Maxon Motor AG, Sachseln, Switzerland) with an integrated gearbox (19:1) and an absolute encoder for rotation measurement (512 increments per revolution) are utilized. As a motor controller, DMC-4040 (Galil Motion Control, Rocklin, CA, USA) is used, providing PID control which is able to control the motor position with zero error (in encoder increments). Motor motion programming and communication is established with the software GalilSuite provided by the manufacturer. Using the mentioned

actuation components, the motor shaft on the driving side (after gearbox transmission) can be positioned with a resolution of $\frac{1}{54}^\circ$. With the given tendon actuation components, the tendon displacement can be performed with a resolution of $3.8 \cdot 10^{-4}$ mm.

Additionally, the tendon guiding inside the actuation unit has to be considered here. Since the tendon pairs have to be guided to the gear racks, several pulleys redirect the tendon path to reduce tendon friction (Figure 69a). To compensate for e.g. long term tendon elongation, swivels are integrated into each gear rack allowing for individual tendon tension adjustment.

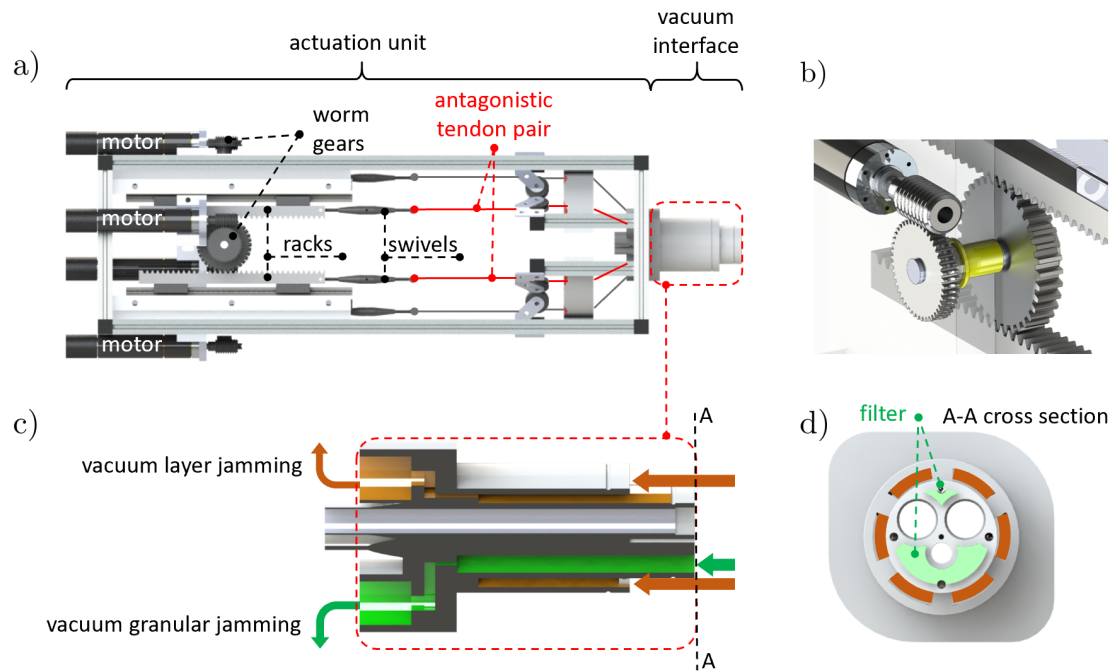


Figure 69: Actuation unit for Prototype 3: a) Overall actuation unit; b) DC motor rotation transmission to the gear racks; c) Vacuum interface cross-sectional view showing separated air pathways for granular and layer jamming; d) Separated vacuum inlets for granular and layer jamming in a cross-sectional view.

manipulator prototype 3a The first variation of the third manipulator prototype is fundamental for the following variations. It has the basic structure of a tendon-driven continuum robot including three integrated working channels made of polypropylene with two large channels of 8 mm and a small channel of 4 mm in diameter, as stated in the envisioned requirements. The larger working channels are surrounded by a tension spring to maintain the circular cross-section. Ten 3D-printed spacer disks (PLA and Ultimaker3, Ultimaker B.V., Utrecht, The Netherlands) with four tendon routing channels ($r_t = 9.5$ mm) for antagonistic actuation are fixed (glued) to a single central 1 mm thick spring steel rod backbone. The prototype is designed as a two-segment manipulator with segments of equal length of 120 mm (overall length of 240 mm), such that eight 0.14 mm Ultra-High-Molecular-Weight Polyethylene (UHMWP) (Spectra[®], Honeywell International Inc., Charlotte, NC, USA) tendons run through routing channels to the first segment end (in each channel two tendons). Four tendons are then fixed at the end of the first segment and the remaining four tendons run further

to the manipulator's tip. The overall diameter is 23 mm. This variation is illustrated in Figure 70a-b.

manipulator prototype 3b With the second manipulator variation additional granular jamming is integrated by filling the spaces between the spacer disks with granules. Granulated sugar is chosen as the most efficient granule based on the previous investigations on smaller diameter prototypes (Langer et al., 2018, Amanov, Nguyen, et al., 2018)². The tendons are separated from the granules by silicone tubes (2 mm outer diameter), as shown in Figure 70d. This ensures an air-proof vacuum chamber. The whole manipulator is then covered by a latex membrane to encapsulate the granules. The membrane is fixed to the tip and the base of the articulated port. The vacuum is introduced through a filter (coffee filter) at the base of the manipulator, as shown in Figure 69d. The overall diameter is 23.5 mm due to the additional membrane. This variation is illustrated in Figure 70c.

manipulator prototype 3c With the last variation, layer jamming with neobond flaps (0.19 mm thick) is additionally integrated. A latex membrane is placed over the previous manipulator variation and neobond flaps are wrapped around it by sewing them to each other with a UHMWP tendon (Spectra[®], Honeywell International Inc., Charlotte, NC, USA). Lastly, a further latex membrane encapsulates the layer jamming structure (Figure 70e). The vacuum is introduced at the base of the manipulator (Figure 69d). By using two membranes instead of one, the layer jamming can be activated independently from the granular jamming. This results in an overall diameter of 26 mm. Detailed flap dimensions are illustrated in Figure 70f.

11.4.3 Pure Layer Jamming Evaluation

In order to investigate only the stiffening effect of layer jamming in a tendon-driven continuum robot, the stiffening method alone without other stiffening methods must first be investigated.

evaluation set up For this investigation, Prototype 2 (Figure 68) is used. The prototype is attached to the test bench, equipped for bending evaluations (Figure 62a/c). The experiment foresees a circular displacement of the manipulator's tip with a radius of 13 mm. The measurements were conducted for a soft and stiffened state with a vacuum level of $-0.8 \cdot 10^5$ Pa. The tendons are loose, such that they do not influence the stiffness. Five repetitions for each state are performed.

results The deflection forces in the plane are shown in Figure 71, left as a circular representation. An alternative diagram shows the resulting deflection forces over the deflection angle (Figure 71, right). In the soft state, the manipulator withstands resulting forces between 0.2-0.3 N over all repetitions with a mean variation of 1 %. In the stiff state, resulting forces between 1.36-2.18 N with a mean variation of 5.15 % are reached. This corresponds to a stiffening factor of 6.34, as stated in Table 10 in the column *loose*.

² this works originated during the Ph.D. program

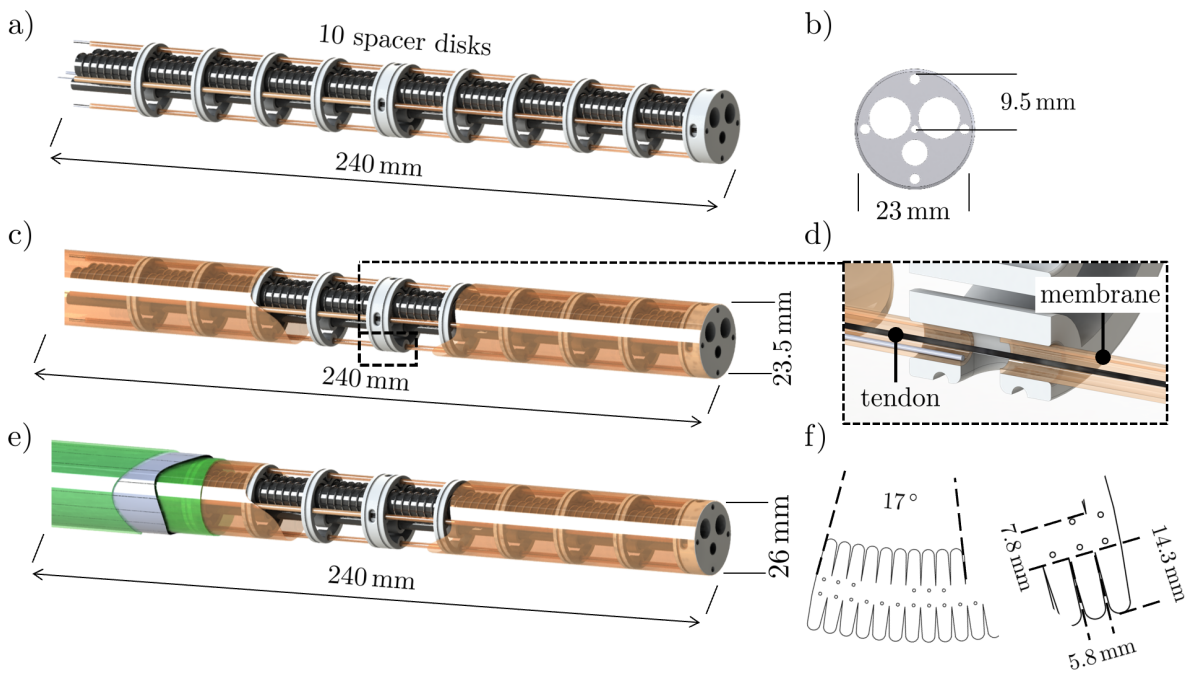


Figure 70: Prototype 3: a-b) Variation 3a with only backbone, working channels, and tendons; c-d) Variation 3b with integrated granulated sugar; e-f) Variation 3c with additionally integrated layer jamming.

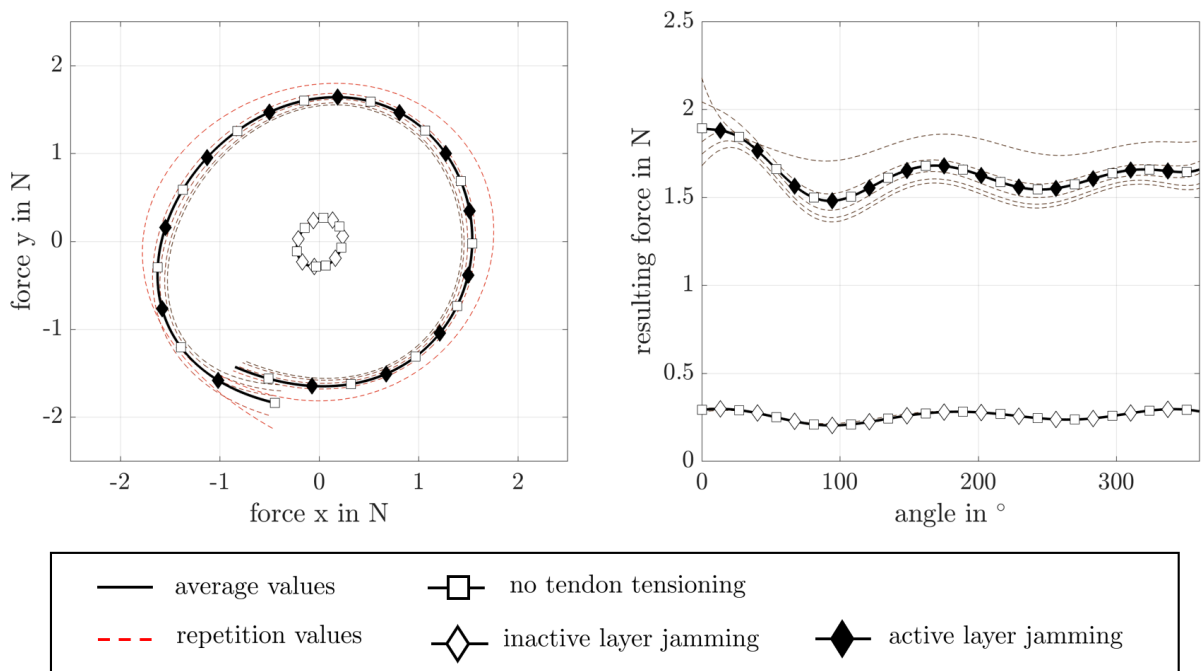


Figure 71: Results of the layer jamming stiffening with loose tendons in the soft and stiff state using Prototype 2. Left: Circular deflection force representation is shown including repetition measurements (red dashed lines); Right: Resulting deflection force over the deflection angle is depicted.

11.4.4 *Layer Jamming with Tendon Tension Stiffening Evaluation*

In this investigation, the impact of tendon tension stiffening additionally to the layer jamming is evaluated to investigate possible synergy effects.

evaluation set up Using the Prototype 2 (Figure 68), the manipulator is first stiffened by tendon tensioning of all 4 tendons for a certain tendon displacement value (in mm). Then, a full circular manipulator deflection with a radius of 13 mm is repeated five times. Subsequently, the layer jamming is activated with a vacuum of $-0.8 \cdot 10^5$ Pa and the deflection is performed 5 more times. After deactivating the layer jamming, the tendons are displaced again using a different displacement value. The following displacement values were evaluated: 0 mm, 0.5 mm, 1 mm, 1.5 mm. Higher values might cause backbone buckling as observed during initial trials beforehand and could eventually lead to backbone plastic deformation. The magnitude of the selected values is considered appropriate to monitor possible trends. The step size is chosen to be able to set the values manually (another actuation manner is not implemented in the prototype).

results Figure 72 shows the results with layer jamming in the soft state and the tensioned tendons in the top two graphs. It can be observed that already with the tendons at 0 mm tension, the stiffness is higher than with loose tendons in the previous investigation (Table 10). The stiffness increases with higher tendon displacement values. With layer jamming in the soft state at 0 mm, the manipulator prototype withstands average resulting forces between 0.4-0.69 N with a mean variation of 0.54 % and at 1.5 mm forces between 0.52-0.75 N with a mean variation of 0.72 %. Further details are found in the table 10. All force levels are higher at each tendon displacement level than with loose tendons, showing the effect of tendon tension stiffening with stiffness factors of 1.92-2.58. With layer jamming in the stiff state at 0 mm, average resulting forces between 1.54-2.54 N with a mean variation of 3.52 % and at 1.5 mm forces between 2.07-2.8 N with a mean variation of 3.26 % are observed. This corresponds to a stiffening increase factor of 1.16-1.43 in comparison to stiffening with only layer jamming, concerning the mean resulting force values. Further details are shown in Table 10.

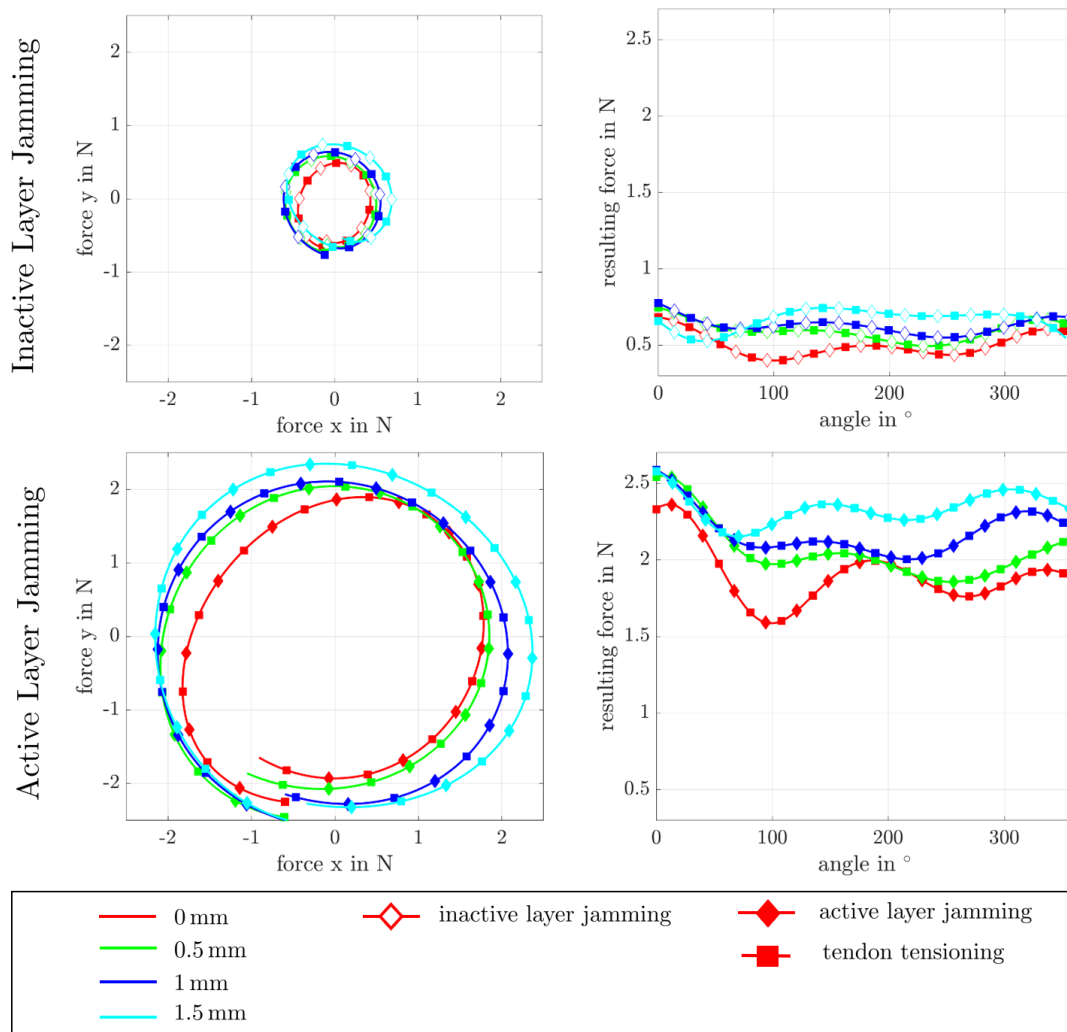


Figure 72: Results of combined layer jamming/tendon tension stiffening investigation using Prototype 2: Top: Inactive layer jamming; Bottom: Active layer jamming.

Table 10: Results of combined layer jamming/tendon tension stiffening investigation using Prototype 2. Minimum and maximum forces show the range of average (over 5 repetitions) resulting deflection forces on a circular deflection. The values in row 6 and 7 are calculated based on the average values in row 1.

	tendon displacement values	loose	omm	0.5mm	1mm	1.5mm
1	mean force in N	0.26	0.5	0.59	0.63	0.67
2	max force in N	0.3	0.69	0.75	0.79	0.75
3	min force in N	0.2	0.4	0.49	0.55	0.52
4	variation min/max in %	$3 \cdot 10^{-5}$ -6.14	$2 \cdot 10^{-4}$ -1.46	$1.1 \cdot 10^{-5}$ -1.42	$5.7 \cdot 10^{-4}$ -1.72	$1.2 \cdot 10^{-4}$ -2.44
5	variation mean in %	1	0.54	0.4	0.39	0.72
6	increase to loose tendons (row 1) in N (factor)	-	0.24 (1.92)	0.33 (2.26)	0.37 (2.42)	0.41 (2.58)
7	increase to previous in N (factor)	-	0.24 (1.92)	0.09 (1.18)	0.04 (1.07)	0.04 (1.06)
	stiffened state					
8	mean force	1.63	1.89	2.1	2.17	2.33
9	max force	2.18	2.54	2.81	2.79	2.8
10	min force	1.36	1.54	1.67	1.95	2.07
11	variation min/max in %	$5 \cdot 10^{-4}$ -15.38	$1.3 \cdot 10^{-3}$ -12.18	$5.2 \cdot 10^{-4}$ -16	0.27-9.25	$9.4 \cdot 10^{-4}$ -11.88
12	variation mean in %	5.15	3.52	3.99	2.71	3.26
13	increase from row 1 to 8 in N (factor)	1.38 (6.34)	1.39 (3.78)	1.51 (3.56)	1.54 (3.44)	1.66 (3.48)

11.4.5 Layer and Granular Jamming Evaluation

In this section, both jamming mechanisms are evaluated within the same prototype. A comparison between both should provide information about which method is superior and unveil possible synergy effects.

evaluation set up The Prototype 3a (Figure 70a-b) was evaluated to measure the basic stiffness coming with the typical articulated port components. Prototype 3b (Figure 70c-d) was evaluated in its soft and stiff state, providing information on the stiffening level using granular jamming for the articulated continuum port.

Prototype 3c (Figure 70e-f) is first evaluated without activating the stiffening methods. Secondly, only the granular jamming was activated. Then, only the layer jamming was activated. And lastly, both stiffening methods were activated simultaneously. This investigation series offers data on stiffening capabilities of both jamming methods in the same setup and aims to discover possible synergy effects of using both methods simultaneously.

Each evaluation was repeated five times. No tendon tensioning was applied. The vacuum level was always at approximately $-0.8 \cdot 10^5$ Pa.

results Prototype 3a exhibits maximum averaged (over 5 repetitions) resulting forces of 0.11 N with a mean variation of 2.55 %, as stated in Table 11. By adding granular jamming to this basic structure (Prototype 3b), the stiffness (without activating the jamming method) ranges between 0.08-0.21 N with a mean variation of 4.11 %. This shows already a significant stiffness increase by additional components such as granules and latex membranes. Activating the granular jamming leads to a deflection force increase by a factor of 5.6, resulting in a mean force of 0.84 N, as illustrated in Figure 73. The variation in the soft and stiff state are comparable.

When additionally layer jamming is integrated, the stiffness increases considerably without active jamming methods to a mean value of 0.68 N. Activating the granular jamming solely increases the stiffness by a factor of 2.54 resulting in 1.39-1.94 N deflection force. Solely layer jamming activation increases the stiffness significantly by a factor of 5.51, reaching deflection force values of 2.94-4.28 N. In the combined case, the deflection force only slightly exceeds the values of solely layer jamming. An increase by a factor of 5.97 is observed with forces ranging between 3.4-4.46 N, as shown in Figure 73. The jamming method combination provides not the accumulation of single stiffening increases, such that no synergy effect can be observed. In general, using layer jamming results in less homogeneous deflection force values compared to granular jamming, as can be observed in Figure 73, right. Granular jamming exhibits lower deflection force changes over the deflection angle.

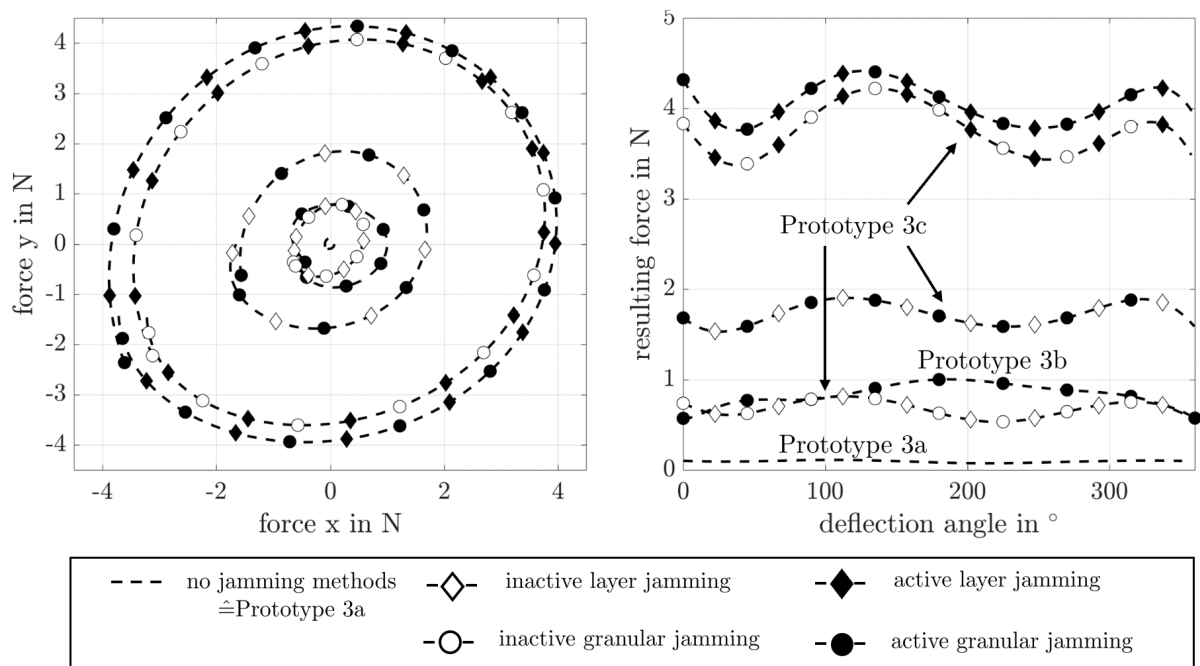


Figure 73: Results of combined granular and layer jamming evaluation using Prototype 3: Left: Circular averaged resulting force representation. Right: Averaged deflection forces over the deflection angle.

Table 11: Results of combined granular and layer jamming evaluation using Prototype 3. All values are based on the averaged data over 5 repetitions. Values in row 10 are based on the values from row 1 and 5.

	Prototype 3a	Prototype 3b	Prototype 3c Granular	Prototype 3c Layer	Prototype 3c Granular/Layer	
soft state						
1	mean force in N	0.09	0.15	0.68	0.68	0.68
2	max force in N	0.11	0.21	0.84	0.84	0.84
3	min force in N	0.07	0.08	0.53	0.53	0.53
4	variation min/max in %	$3.6 \cdot 10^{-4}$ -11.06	$4.9 \cdot 10^{-5}$ - 21.14	$7.6 \cdot 10^{-6}$ - 8.66	$7.6 \cdot 10^{-6}$ - 8.66	$7.6 \cdot 10^{-6}$ - 8.66
5	variation mean in %	2.55	4.11	1.29	1.29	1.29
stiffened state						
5	mean force in N	-	0.84	1.73	3.75	4.06
6	max force in N	-	1.06	1.94	4.28	4.46
7	min force in N	-	0.48	1.39	2.94	3.4
8	variation min/max in %	-	0.0018-17.34	$2.1 \cdot 10^{-4}$ - 9.48	-	$1 \cdot 10^{-4}$ - 10.19
9	variation mean in %	-	4.37	1.14	1.97	1.28
10	increase to soft in N (factor)	-	0.69 (5.60)	1.05 (2.54)	3.07 (5.51)	3.38 (5.97)

11.5 DISCUSSION

The generated results should be interpreted in terms of general scientific findings, comparison to the state of the art and their feasibility, concerning the selected application requirements.

general findings Considering the torsional stiffening through the structure, the results clearly show, that the crossed alternating backbone structure provides significantly higher torsional stiffness and at the same time even lower bending stiffness, maintaining the flexibility of the manipulator. It further exhibits a linear progression and has higher repeatability. The drawback is the halved maximum curvature, which has to be considered if choosing this backbone structure. For the optimized continuum port design, higher curvatures are required than can be achieved with the crossed alternating backbone for the second and third segment. Therefore, this structure can be only used for the first segment.

Looking into the Prototype 2 results with solely layer jamming stiffening, an absolute deflection force increase of 1.38 N can be observed, concerning the mean values over the whole circular motion. This is equivalent to a stiffening factor of 6.34 in comparison to the soft state. Considering the tendon tension stiffening with the same prototype, setting the tendon length equal to the backbone length (tendon displacement of 0 mm) has already an increasing effect on the deflection force. Tensioning the tendons generally, results in a deflection force increase of up to 0.41 N when layer jamming is not activated, as shown in Table 10, row 6. When both methods are activated, the effect of the tendon tensioning (force increase) rises up to 0.6 N, as shown in Table 10, row 8. The effect of layer jamming rises up to a 1.66 N force increase (Table 10, row 13). This shows that both methods support each other. However, this can be a result of a general higher basic manipulator stiffness as well. Further investigations of the relationship between the initial stiffness, and the absolute and relative stiffness increase caused by the stiffening methods are desirable in the future. Despite the supportive effect, both methods do not enhance each other. Meaning, a synergy can not be observed, since the sum of the

individually achieved force increases is greater than the force increase when both methods are activated (Table 10, row 6 and 13). In general, the layer jamming contributes considerably to the force increase. Tendon tension stiffening can be considered as a supporting stiffening method with the given manipulator design to partially increase the overall stiffness.

The evaluations with the Prototype 3b, including just granular jamming, show a mean deflection force of 0.15 N in the soft state and absolute mean deflection force increase of 0.69 N, resulting in a mean deflection force of 0.84 N in the stiff state. Prototype 3c shows higher deflection forces in the soft state (0.68 N) than Prototype 3b due to the integrated layer jamming. However, the resulting deflection force of 1.73 N with activated granular jamming shows a higher force increase (1.05 N). Here, one can observe an increased effect of granular stiffening if the basic stiffness in the soft state is higher (Table 10, row 1 and 10). The same effect can be observed in the combined assessment of layer jamming and tendon tension stiffening. An important result is observed using just the layer jamming stiffening with Prototype 3c. Having the same deflection force in the soft state, the layer jamming activation leads to a mean deflection force increase of 3.07 N. This shows a clear superiority of layer jamming using the proposed manipulator. Activating both stiffening methods simultaneously is not very beneficial since it only adds 0.31 N to the mean deflection force in comparison to solely layer jamming stiffening (Table 11, row 10).

In general, one has to consider the soft state stiffness and maneuverability of a manipulator with integrated jamming methods. Especially layer jamming, coming with two membranes, can unnecessarily increase the soft state stiffness of the manipulator, requiring higher tendon forces for actuation. The greatest resistance during actuation would come from the stretched membranes. To counter this effect, the membranes could be designed with a certain gap between them and the layer jamming. The effects of this measure on the stiffening capabilities is the subject of future work.

A relatively higher initial stiffness showed a higher force increase as a result of the stiffening method activation. At the same time, stiffening factors decrease. This effect must be investigated at different initial stiffness levels in order to obtain further insights for the design of manipulators with integrated jamming methods.

Granular jamming causes relatively low deflection forces in the soft state, however, it could be observed that at some point it inhibits the deflection of the manipulator due to jamming between spacer disks at a certain angle. They either have no space to be displaced or do not have the required viscosity (capability to move along each other). A further disadvantage of granular jamming is the lower repeatability. Over 5 repetitions, in the soft and stiff states Prototype 3b exhibits higher variations in comparison to Prototype 3c (Table 11, row 8/9). This can be caused by the arbitrary distribution of granules.

Since layer jamming has been shown as superior, granular jamming should not be used for the proposed articulated port design. This also was confirmed in further evaluations in Langer et al., 2018. In general, the experimental data should be validated by recording deflection forces in a static scenario, which would avoid the rather high measuring noise and provide more reliable results.

comparison to the state of the art To classify the evaluation results of this work with respect to the state of the art, Table 12 shows the results of this work extending the data in Table 6 from chapter 7. In particular, the results of the Prototype 3c with solely activated layer jamming are considered, since it showed the best stiffening results. Looking into the stiffness

for a 200 mm probe, the results of this thesis show the fourth-best stiffness values of $0.5 \frac{\text{N}}{\text{mm}}$. The stiffness achieved in this work exhibits a comparable value to the granular jamming prototype by N. G. Cheng, Lobovsky, et al., 2012, less than half in comparison to Wang et al., 2018, and less than one-third of the role model prototype by Y. J. Kim et al., 2013.

Low melting point alloys are excluded for this application due to the high temperatures. Granular jamming has been shown in this work's evaluations to be inferior for this particular manipulator design. Such that the prototypes using layer jamming stiffening, including this work, offer a method with the best stiffening capability for the desired application in this work. Lower stiffness compared to the role model by Y. J. Kim et al., 2013 can potentially originate from different flap materials, membrane materials, nitinol actuation rods (used by Y. J. Kim et al., 2013), or vacuum levels. The level of vacuum used in this work was $2 \cdot 10^4$ Pa lower and neobond flaps are generally less stiff as has been compared in Langer et al., 2018. This could lead to higher initial stiffness of the prototype introduced by Y. J. Kim et al., 2013, causing a higher absolute stiffening increase, as has been observed in this chapter.

On the one hand, this shows the stiffening potential which is still available using layer jamming. Further, it points out the significance of parameterization and trade-off between initial stiffness and flexibility.

Concerning the stiffening factor in this work, the second-best result (factor of 5.51) was achieved concerning the available data and stiffening methods integrated into an articulated manipulator. Only the work by N. G. Cheng, Lobovsky, et al., 2012 provides higher stiffening factors, using additional tendon tension stiffening.

Table 12: Summarized stiffening data for the assessed prototype in this thesis, complementing the state of the art data in Table 6, page 66.

Work	Stiffness Variation	Stiffness	Size (\varnothing in mm/ length in mm)	Stiffness 200 mm long probe ³
Prototype 3c Layer jamming active	5.51x	0.29 N/mm	26/240	0.5 N/mm

application feasibility To discuss the potential of the built manipulators for the chosen application, the results of the stiffening evaluation are compared with the acquired application forces in chapter 5, page 48. To provide better comparability, the deflection forces are calculated for different manipulator lengths based on the beam theory, as described in equations 1 and 2. Lengths in the interval of 144-350 mm were generated based on the results of the design optimization.

Figure 74 shows the calculated deflection forces for manipulator lengths between 144-300 mm for Prototype 2 in the stiff state with and without tendon tension stiffening, Prototype 3b in the stiff state, and Prototype 3c with solely activated granular, solely activated layer and both activated jamming methods. The top left graph further shows the load magnitudes for the three loading cases reported in the literature (horizontal dashed lines). The other three graphs include force data for the loading cases identified and measured in this thesis, partial lifting, spreading, and tearing. They are overlaid as colored background in the graph. The dark shaded area shows the values between the 25th and 75th percentile. The bottom lighter area depicts values between the minimum and the 25th percentile. The top lighter area includes values between the 75th percentile and the maximum forces recorded. The required

force values are extracted from all 6 repetitions from chapter 5.

This representation offers a way to assess the prototypes for each loading case. Further, the deployed manipulator lengths from the optimization results can be considered as well.

Prototypes 2 and 3b seem only to provide suitable forces for pulling and lifting for manipulator lengths under 200 mm. For the other cases their maximum deflection force values for the chosen segment lengths is always below the maximum and hardly exceed the 75th percentile mark.

Prototype 3b with activated granular jamming shows slightly better results and can be considered for pulling and lifting with slightly higher manipulator lengths than Prototype 2.

Prototype 3c with only active granular jamming is suitable for pulling and lifting with a length of less than 250 mm. It can be applied for all other loading cases for over 75 % of the data for a length below 175 mm.

Prototype 3c with solely active layer jamming and both activated jamming methods show similar results and should be discussed together. Lifting and pulling forces can be compensated with up to 325 mm. Manipulator length for suturing and 75 % of spreading and partial lifting data rise to about 240 mm. All measured tearing and partial lifting forces can be compensated under a manipulator length of 180 mm.

Looking into the optimization results, the manipulator lengths to reach different points in different patient data sets range between 144-450 mm. The mean deployed manipulator length is 252 mm. At this length, lifting and pulling are fully possible, tearing and suturing is feasible for most forces. However, spreading and partial lifting will result in higher articulated port shape deviations. This shows the lack of stiffness using the chosen methods. However, it needs to be pointed out, that the recorded forces originated in a first attempt to quantify the identified loading cases. The required force data acquisition needs to be further investigated and repeated to validate the initial results. Considering the reported data in the literature for pulling, lifting, and suturing, the provided stiffness in this work performs sufficient. Further, deflection forces measured during the stiffening evaluations are recorded with a straight manipulator. In the straight configuration, the whole length of the manipulator acts as a lever arm for the applied forces, resulting in a higher deflection. The deployed manipulator inside the abdomen is always bent and therefore offers a much lower lever arm, resulting in higher supported forces for the same deflections. An evaluation for loaded bent configurations must be carried out in the future.

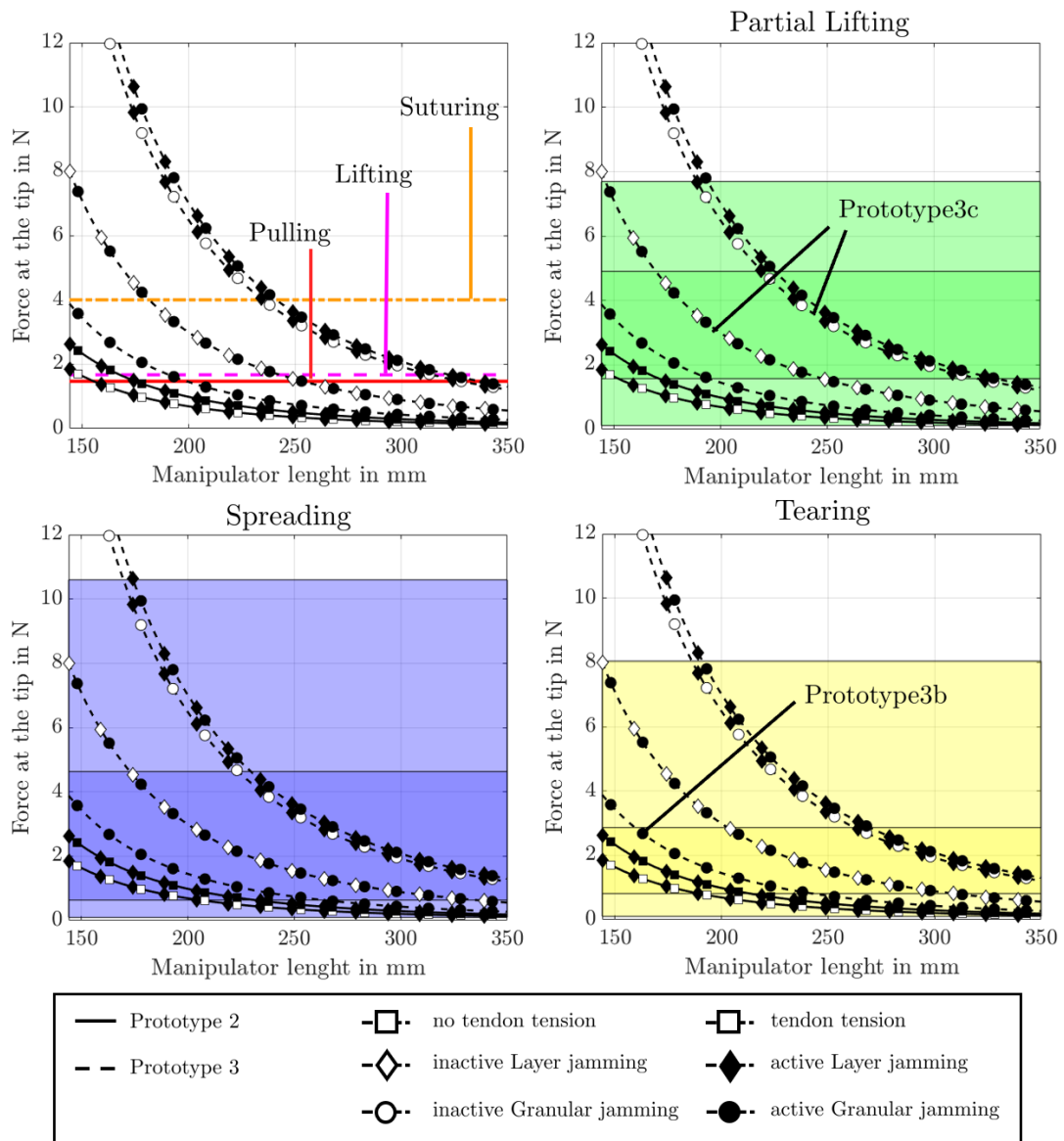


Figure 74: Evaluation of the chosen stiffening methods based on the forces required for partial nephrectomy. Shown are deflection forces as a function of the manipulator length. Top left graph shows force requirements from the literature. Other three graphs show measured force requirements in this thesis, here loading case forces are illustrated as colored areas in the background. Darker areas represent values between the 25th and 75th percentile. Lighter areas correspond to force values between the minimum and the 25th or 75th and the maximum force values.

12

STABILITY

Considering the surgical workflow, after the articulated port has been positioned in a specific configuration with sufficient access and visual feedback, the stiffening, tool deployment and tool articulation follow. During these steps, it is desirable to maintain the manipulator's shape and tip pose in order to keep the established access and visualization. In this work, stability is defined by the quality of maintaining the shape and the tip pose during the mentioned tasks in the workflow.

12.1 EXPERIMENTAL SET UP

For the setup, the Prototype 3c from the previous chapter is used. The prototype consists of a two-segment manipulator with integrated working channels and granular and layer jamming stiffening mechanisms. It also contains an actuation unit that allows to operate the manipulator with 4DoF. The prototype is fixed on a table and the manipulator is driven in 4 configurations with moderate curvature, which represent an s-curve (one segment bent in one direction, the second in another) and are rotationally symmetrical, see Figure 75 (config 1-4). Four further configurations in the same bending planes but with higher curvatures were evaluated (Figure 75, config 5-8). The bending planes are radially displaced approximately about 90° . Once the manipulator configuration is established, its shape is measured by a passive coordinate arm and a non-tactile laser scanner (FaroArm[®] and Faro ScanArm[®], Faro Europe GmbH & Co. KG, Korntal-Münchingen, Germany). The coordinate system frame of the measuring arm serves as a reference frame. After this first measurement, both stiffening methods are activated with a vacuum level of $-0.8 \cdot 10^{-5}$ Pa. This causes a certain shift of the whole manipulator shape, which is captured during the second measurement. The third measurement is performed after deploying a 3 mm ureteroscope (LithoVue[™], Boston Scientific Corporation, Marlborough, MA, USA) through an 8 mm working channel, such that it pro-

trudes 70 mm out of the manipulator's tip, as shown in Figure 75a. The fourth measurement is done after the ureteroscope is articulated randomly for 15 seconds. This should demonstrate the effect of moving tools in a real case scenario.

12.2 DATA PROCESSING

To investigate the shape and tip pose deviation resulting from the stiffening, the tool deployment, and the tool articulation, the centerline of the manipulator must be extracted from the acquired point cloud. Using the L-1 algorithm introduced by Huang et al., 2013, a 3D-point cloud can be reduced to its centerline. For the algorithm to be successful, the point cloud should be fairly homogeneous. The provided software from the laser scanner manufacturer (Cam2Measure, Faro Europe GmbH & Co. KG, Korntal-Münchingen, Germany), offers an interpolation of the measured points to a grid with equidistant distributed points. For each measured point cloud, a centerline is generated and interpolated to a curve with 100 equally distributed points.

To evaluate the visualization shift, the orientation of the tip is considered. The normal vector at the tip provides information about the orientation. By fitting a plane through the points representing the tip surface of the manipulator, provides a normal vector. The angle between vectors of different point clouds will quantify the shift in orientation. The fitting and measuring functions are provided by Cam2Measure (Faro Europe GmbH & Co. KG, Korntal-Münchingen, Germany).

12.3 RESULTS

To quantify the effect of the stiffening, the centerlines from the first and the second measurements are compared to one other by calculating the Euclidean distance between the corresponding points. For the tool deployment, the second and third measurements, and for the tool articulation, the third and the fourth measurements are compared. Lastly, the first and last measurements are compared to quantify the overall shape deviation.

The results in Figure 75b show that stiffening causes a median shape shift of 1.5 mm and maximum shift of 7 mm. The tool deployment causes smaller deviations. Tool articulation has the least effect on the shape deviation. An interesting observation is, that the overall deviation is not the sum of the three deviations and has approximately the same effect as the stiffening. With 7 mm deviation at the tip using a chip-on-the-camera, the visualized picture could be shifted by the same amount and negatively influence the view. However, the orientation of the tip is a more sophisticated indicator of the camera view. The results show angular deviations for the stiffening transition over the 8 configurations with a maximum of 3.42° and a median of 2.37° , as shown in Figure 75c. The tool deployment causes the least angular deviation and the tool articulation has slightly higher deviations than the stiffening. The overall angular deviation is here also not the accumulation of the three deviations. It reaches up to 4.23° with a median value of 2.88° .

12.4 DISCUSSION

This chapter proposes an evaluation metric to assess the stability of the articulated ports. The influence on the stability due to the tasks during the surgical procedure is shown and quantified. Especially shifting due to the stiffening methods has not been reported yet in the literature.

Overall, the deviations are considered sufficient to maintain the tip orientation established prior to the measures examined and to provide sufficient stability for the use case scenario.

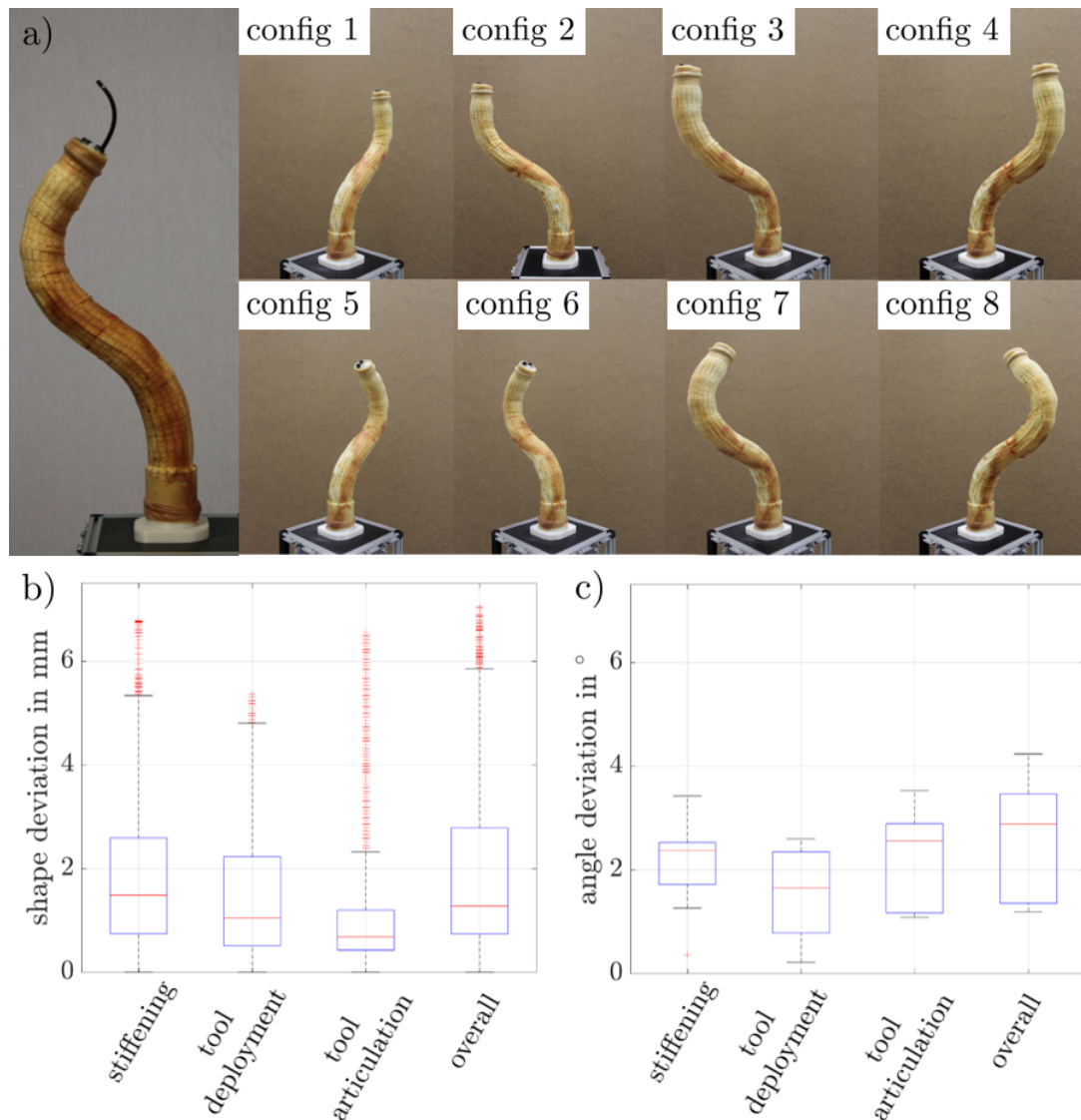


Figure 75: Stability investigations: Config 1-8: Established configurations for the evaluation; a) Example configuration with a deployed ureteroscope for tool articulation evaluation; b) Shape deviation results; c) Tip orientation shift results.

STERILE PROTOTYPE FUNCTIONALITY

In this chapter, a prototype including sterile coupling considerations based on the design in chapter 8 is evaluated. A smaller design alteration is used based on the stiffness evaluation results. The expected capability of the coupling and the actuation are shown in an initial qualitative evaluation.

13.1 MANIPULATOR PROTOTYPE

The manipulator consists of three segments as proposed by the design optimization results. The first segment is built shorter (150 mm) since the optimized length is not necessary for this evaluation. The basic manipulator structure is presented in chapter 8 on page 74. However, the first segment is additionally equipped with a crossed alternating backbone consisting of 0.4 mm nitinol rods. The central backbone is made of 0.7 mm nitinol (Figure 76a). For large working channels, a metal mesh is used and for the small working channel, a teflon tube with an implemented flat wire is used (Figure 76b). The layer jamming is used with helically wrapped neobond flaps encapsulated into two latex membranes (Figure 76c/d). The flap dimensions are illustrated in Figure 76e. Braided steel wires are knotted and glued to the end disks and routed through the 3D-printed main body (Form 2, Formlabs Inc., Somerville, MA, USA) to the metal worm gears with a transmission rate of 20:1. The tendons are wound on the worm flange (13 mm diameter), as shown in Figure 76g. For 12 tendons, 12 worm gears are installed in the main body. Each worm is mounted on a shaft equipped with a coupling adapter, as shown in Figure 76f. The size of the manipulator base is 143 mm in diameter. Detailed manipulator parameter information is given in the Appendix C.

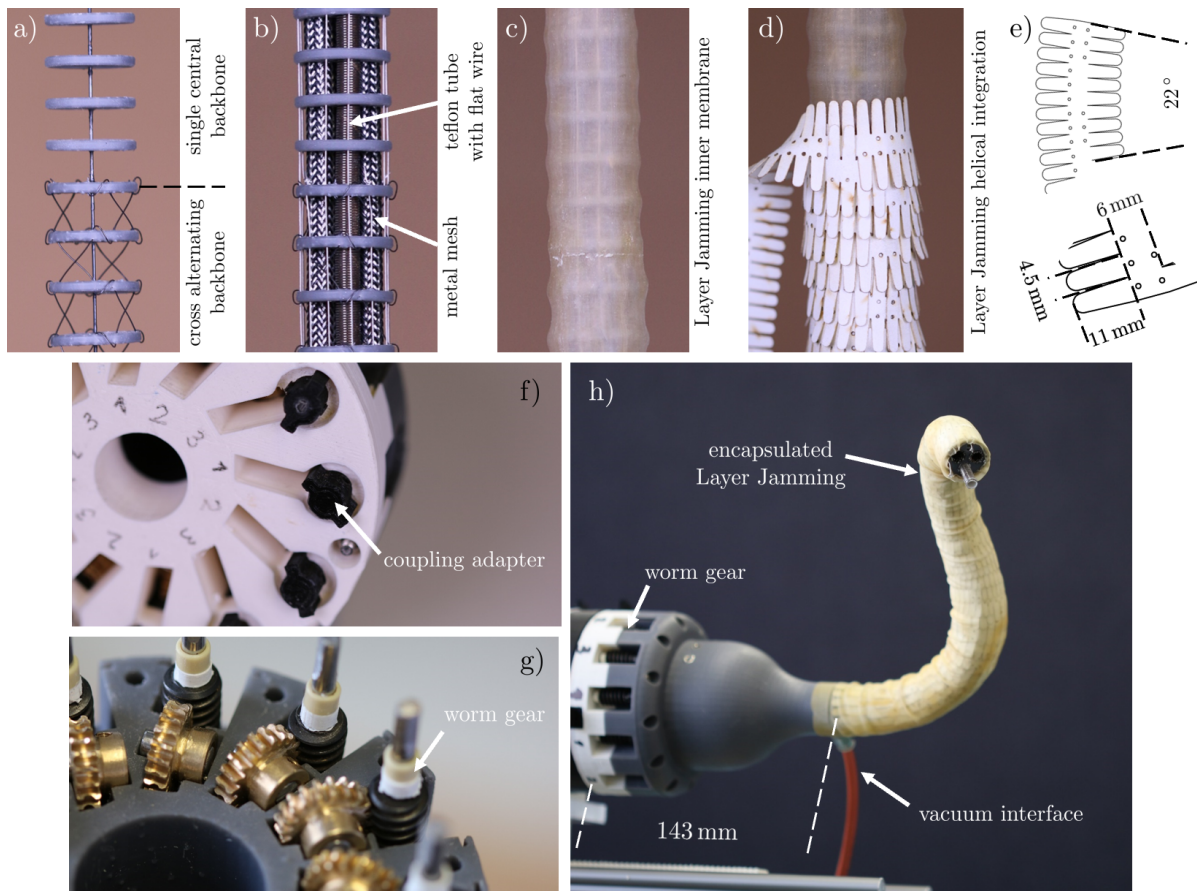


Figure 76: Detachable manipulator prototype design. a) Backbone structure; b) Working channels; c) Inner membrane for layer jamming; d) Wrapping of layer jamming e) Layer jamming flap design; f) Adapters for the coupling; g) Worm gears for tendon winding h) Complete manipulator.

13.2 ACTUATION UNIT

The actuation unit is actuated by 6 DC motors (EC 16, Maxon Motor AG, Sachseln, Switzerland) with an integrated gearbox (19:1) and an absolute encoder for rotation measurement (512 increments per revolution). As a motor controller, the DMC-4040 (Galil Motion Control, Rocklin, CA, USA) is used. The motor shafts are rigidly fixed to the driveshafts by a stiff coupling. Over straight gears with a transmission of 1:1, the rotation direction is inverted and transmitted by a timing belt with an HTD profile and a 2.5 mm pitch (Figure 77b). The shafts are mounted by radial ball bearings in the intermediate, back and front 3D-printed walls (Ultimaker3, Ultimaker B.V., Utrecht, The Netherlands).

The translation part consists of a linear guide and friction bearings (drylin[®] RJUM, Iigus GmbH, Cologne, Germany). A DC motor (same model as above) drives a metal worm (18 mm diameter) on a 3D-printed angled gear rack (Ultimaker3 + PLA, Ultimaker B.V., Utrecht, The Netherlands) with a pitch of 3 mm (Figure 77c). The dimensions of the actuation unit are shown in Figure 77.

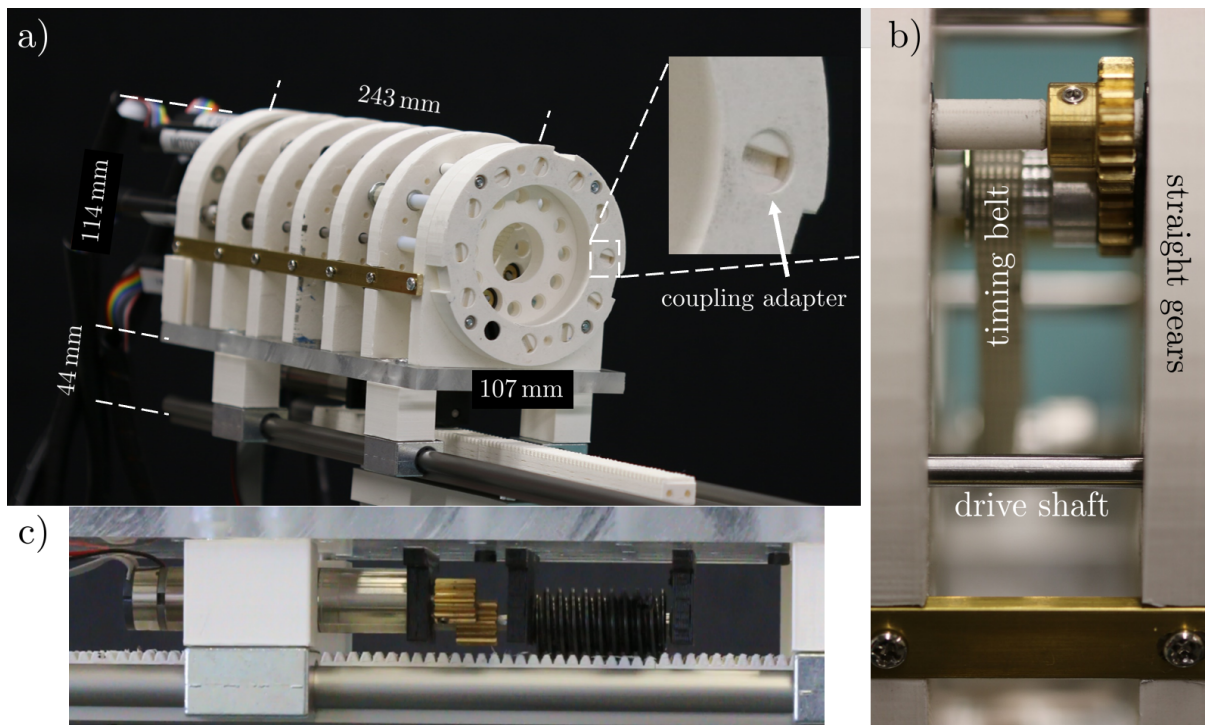


Figure 77: Detachable prototype actuation unit. a) Overall actuation unit including the dimensions; b) Antagonistic drive shaft actuation using straight gears and timing belt; c) Translational DoF.

13.3 COUPLING FLOW EVALUATION

To evaluate the coupling functionality, a coupling sequence is performed using the prototype. Figure 78a shows the front wall of the prototype actuation unit with the 12 drive shafts equipped with the coupling adapters. The coupling plate is then attached to the actuation unit, as shown in Figure 78b. The attachment via the three clips works well and mainly requires a push in the direction of the actuation unit. After rotation of the drive shafts by 180° is commanded by the motor controller, all adapters engage successfully. This can be heard and seen, when the adapters inside the coupling plate start to rotate. Finally, the manipulator is attached using the same clip mechanism and a further drive shaft rotation (Figure 78c). The adapters lock-in successfully as well and enable tendon displacement of the manipulator. The attachment requires a lot of force due to the springs, which have to be pushed back, so some effort and practice is required to perform the attachment. Springs with a lower spring rate could provide a solution. A further drawback is the unknown angle at which the locking happens, leading to a slight tendon displacement during the coupling procedure. This can be compensated when using some sort of sensor. This could be, for example, a contact sensor (closed current circuit) between the actuation unit wall and the sliding adapter at the drive shaft. During the attachment, the adapter is pushed back, triggering the contact. During the rotation, when locking happens, the contact is released and the rotation angle, at the time of contact lost, can be saved by the motor controller. To restore the initial tendon position, the motors turn counter clock wise to the saved angle. This is a cost-effective approach integrated into the actuation unit, such that the complexity of the single-use manipulator is not increased.

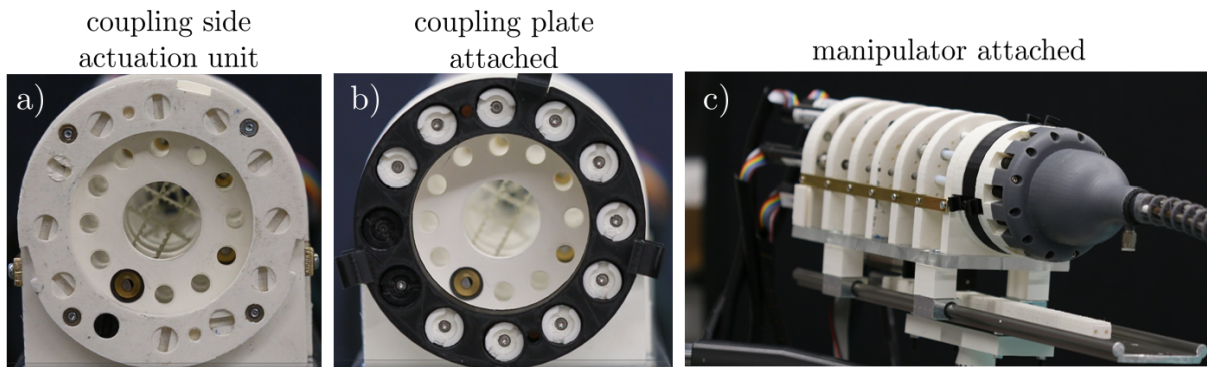


Figure 78: Coupling sequence of the detachable articulated port prototype: a) Front wall actuation unit; b) Locked in coupling plate; c) Coupled manipulator.

13.4 ACTUATION EVALUATION

In the last evaluation, the manipulator articulation functionality was investigated. After the manipulator is attached, several arbitrary configurations were established by commanding the tendon displacements manually. Five of them are shown in Figure 79. All DoF in the joint space were addressed and led to manipulator articulation.

A certain backlash during the actuation was observed as a delayed manipulator response after the motor motion started. This can be explained by the lack of tension and certain elasticity in the tendons. Partly, this may be due to the absence of sensors during the coupling process. The other error source is the uneven tendon tension during the initial winding (straight shape) of the tendons on the worm wheel and the arbitrary tendon winding path. A solution for the latter can be the implementation of helical winding notches on the worm wheel flange for a defined tendon displacement. The translation can be performed successfully over the whole range of the angled gear rack.

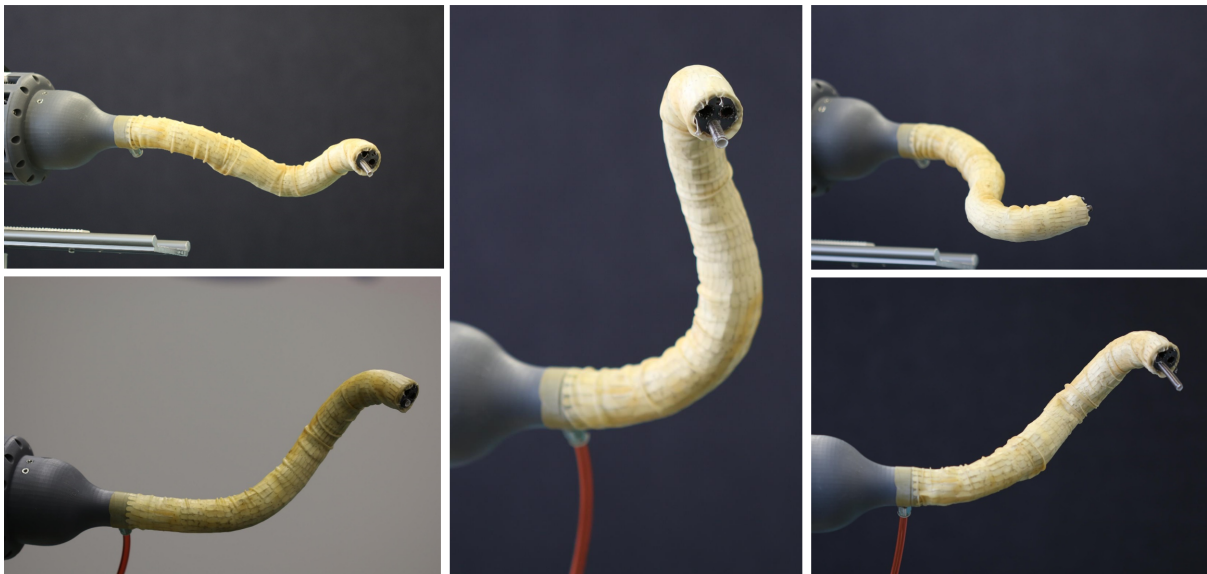


Figure 79: Example configurations established with the detachable articulated port prototype after coupling.

13.5 DISCUSSION

In this chapter, the feasibility of the prototype is shown in terms of actuation and its coupling mechanism. The overall prototype shows a compact design serving 7DoF. In terms of sterility, the coupling plate needs to be complemented by a sterile foil in the center of the coupling plate to cover the actuation unit. With this concept, the robot can be touched by the clinical staff without being contaminated. The single use of the articulated port needs to be investigated in terms of the availability of sterile components and sterile 3D-printing methods. The separation of the drive train and the driven shaft is sufficient and is also used by Intuitive Surgical for the coupling of the da Vinci® instruments. In this work, this concept is shown feasible for tendon-driven continuum robots with up to 6DoF.

EVALUATION CONCLUSION

This chapter discusses the results achieved on the basis of the requirements presented in chapter 6.4. All requirements and their fulfillment are listed in Table 13. The tendon-driven structure accommodates two large (8 mm) and one small (4 mm) working channel with the required sizes while keeping the outer port diameter (26 mm) below the required maximum value. The design offers enough space at the manipulator's tip for a chip-on-the-tip camera and light sources. Wires to supply power to the camera and to enable the data transfer can be routed inside the manipulator and the operating unit. The voltages and currents needed for the power supply of the camera and light sources are suitable for use in the human body (see Table 13). The typical light source current reaches up to 65 mA, which exceeds the safe current threshold. However, if considering the low supply voltage of 3.4 V, the current will decrease to a safe value in case of human body contact due to its electrical resistance. Since the motors are placed outside the body and do not have a conductive connection to the manipulator, they do not constitute a danger to the patient.

Although the working channels are considered large enough for tool insertion and exchange, the feasibility in a use case scenario and the required curvatures are not fully evaluated.

An effective and safe stiffness variation capability was implemented into the manipulator, which provides sufficient stability in an activated state to meet the state of the art requirements. However, the specific requirements presented in this thesis have not been realized yet and are subject to further evaluation.

A sterility concept was designed and shows promising results in the initial investigations. A proof of sterility is not provided in this thesis, such that this requirement is partially fulfilled. Overall 6 of 9 requirements are successfully fulfilled in this thesis. The partially fulfilled topics show promising first results and offer a solid base for future investigations.

Beyond the design requirements, the experimental evaluation results propose a design parameter optimization approach providing reachability of the potential kidney tumor locations, and report novel insights on granular and layer jamming stiffening methods.

Table 13: Summary of requirements and their fulfillment.

Requirement	Results	Fulfilled
Outer diameter < 30 mm	The largest diameter is 26 mm (chapter 11.4.2)	fully
2 instrument working channels	Two working channels are embedded (chapter 11.4.2)	fully
Visual Feedback	Chip-on-the-tip camera used in commercial ureteroscopes (Nan-Eye)	fully
1 additional working channel for suction or irrigation (4 mm)	Additional working channel is provided (chapter 11.4.2)	fully
Tool exchange	Tool exchange is generally possible, but was not evaluated for a variety of relevant port shapes	partially
Payload (1.47-10.6 N)	Payloads up to 4.28 N were reached	partially
Sterility	A design with a potentially sterile coupling mechanism	partially
Temperature < 40°	No heat sources in the port	fully
Voltages < 50 V or currents < 50 mA	Camera requires maximum 2.4 V/0.6 mA, light source (LED) requires maximum 3.4 V/65 mA	fully

Part V

CONCLUSION

CONTRIBUTION SUMMARY

To address current challenges in the field of Laparo-Endoscopic Single-site Surgery, this thesis focuses on the design of an articulated port for partial nephrectomy. While in the literature general application for LESS is proposed, targeting a specific application allows the formulation of a comprehensive requirements list. In cooperation with the Clinic for Urology and Urologic Oncology (Hannover Medical School), with specialists in this field, the process of the surgical procedure including important steps and surgeon demands is analyzed. As a result, a general structure of an articulated port can be defined, including 3 working channels for instrumentation deployment/exchange, a camera unit for visualization, and a stiffening method for shape stability and stiffness.

A guideline for robotic port parameterization is proposed by introducing a novel measurement method of the abdominal space, integrated into the surgical workflow. For the first time, this enables workspace acquisition inside the abdomen after insufflation and corresponding tissue shift. The collected data and developed metrics are used to perform a parameter optimization of the selected tendon-driven continuum robot structure with respect to tumor locations reachability.

Following this guideline, an articulated port design is found, which is able to access relevant anatomies in the abdomen for several patients through different incision locations. Intuitively selected parameters for LESS in the state of the art show insufficient results following the same metrics and using the same patient data sets. The feasibility of the port was shown in the first experimental investigation on an abdominal phantom.

The flexible nature of continuum robots is addressed by the investigations of human safe stiffening methods. The state of the art is extended evaluating the combination of layer jamming and tendon tension stiffening. Further, the integration of granular and layer jamming into a dedicated articulated port prototype is compared. The results reveal the superiority of layer jamming in terms of stiffening.

The overall design of the robotic system, considering the actuation unit, and especially the sterility for future clinical scenarios, is proposed. That presented design fulfills the most defined requirements for abdominal surgeries successfully and shows promising results for partially fulfilled requirements.

Although this work considers a specific application, it provides a design guideline, which can generally be applied for other abdominal surgeries, using the introduced data acquisition method.

The data acquired by the measurements can further be utilized to optimize other robotic structures for partial nephrectomy. It additionally provides a basis for clinical studies, such as correlations between the muscle mass and the created free space due to insufflation. The coupling mechanism and actuation unit design are compatible with any tendon-driven robot beyond surgical applications and can further be useful to switch between different robot sizes or tools.

Overall, this work extends the research on robotic single-port surgical procedures by exploring the potential of flexible manipulators on the example of partial nephrectomy. A comprehensive use case scenario based approach reveals and addresses shortcomings in the current research. The applied methods show successful results and offer a rich base for future works.

16

OUTLOOK

The results of this work provide possibilities for further research questions and extended evaluations. The stiffness evaluation suggested the deflection of the articulated port in its straight shape. Use case configurations exhibit curved shapes and offer a smaller lever arm. The effect on the resulting deflection in a curved shape has to be investigated in the future.

In general, the loading case study is considered a preliminary approach for force measurements. To prove the results, a more comprehensive study should be conducted, including more iterations and ideally partial nephrectomy simulations on porcine kidneys encapsulated in fat tissue.

To advance the current state, teleoperation algorithms need to be implemented and evaluated with several surgeons. To prove the benefits of the system, further articulated suitable instruments need to be provided. Docking designs, enabling fast and simple instrument exchange need to be introduced. Miniaturized flexible articulated tools proposed in research can be adopted. For the deployment of such tools and surgical consumables, further experiments are needed to evaluate the suitability of different working channel structures. With integrated flexible tools, first phantom studies with surgeons can be conducted to show the feasibility with enhanced reachability and accessibility despite the restriction of a single incision. In this context, the camera and instrument arrangements must be evaluated.

The most important future work is the assessment of the sterility of the design. In the first step, the coupling mechanism needs to be complemented by a sterile cover. The procedure of covering, coupling, uncoupling, and uncovering is the subject of investigation. Means to manufacture the articulated port with sterile components in a sterile environment are necessary to address the overall sterility concept. Sterility design assessment and further design iterations in cooperation with responsible clinical staff for instrument preparation should be a part of future work. While this work shows the benefits of an articulated port for LESS partial nephrectomy, further abdominal indications can be investigated using the proposed methods. Based on the acquired anatomical data, other robotic structures should be compared to the

articulated port in terms of proposed metrics in this thesis. The results of these investigations will provide insights on which design structure is most suitable for LESS, such that in the midterm future, a paradigm for a LESS robot design will emerge.

Further, the collected anatomical data can be used for clinical studies. They enable prediction of the created working space after inflation of the abdomen based on demographics and anatomic patient information, such as age or muscle tissue percentage. This will contribute to the progress of required soft tissue modeling.

In general, the promising results of this work enable and motivate subsequent research on the emerging topic of robotic surgery.

-
- Abbott, D. J., C. Becke, R. I. Rothstein, and W. J. Peine (2007). "Design of an endoluminal NOTES robotic system." In: *2007 IEEE/RSJ International Conference on Intelligent Robots and Systems*. IEEE, pp. 410–416.
- Amanov, E., J. Granna, and J. Burgner-Kahrs (2017). "Toward Improving Path Following Motion: Hybrid Continuum Robot Design." In: *IEEE International Conference on Robotics and Automation*, pp. 4666–4672.
- Amanov, E., T.-D. Nguyen, S. Markmann, F. Imkamp, and J. Burgner-Kahrs (2018). "Toward a Flexible Variable Stiffness Endoport for Single-Site Partial Nephrectomy." In: *Annals of Biomedical Engineering* 46.10, pp. 1498–1510.
- Andonian, S., S. Rais-Bahrami, M. A. Atalla, A. Herati, B. Lee, and L. R. Kavoussi (2010). "Laparoscopic Single-Site Pfannenstiel Versus Standard Laparoscopic Donor Nephrectomy." In: *Journal of endourology / Endourological Society* 24, pp. 429–32.
- Autorino, R., J. H. Kaouk, J.-U. Stolzenburg, I. S. Gill, A. Mottrie, A. Tewari, and J. A. Cadeddu (2013). "Current Status and Future Directions of Robotic Single-Site Surgery: A Systematic Review." In: *European Urology* 63, pp. 266–280.
- Baik, S. H. (2010). "Robotic Assisted Colorectal Surgery." In: *Robot Surgery*. Croatia: INTECH, pp. 73–94.
- Balasubramanian, A., M. Standish, and C. J. Bettinger (2014). "Microfluidic Thermally Activated Materials for Rapid Control of Macroscopic Compliance." In: *Advanced Functional Materials* 24.30, pp. 4860–4866.
- Berducci, M., H. F. Fuchs, P. Omelanczuk, R. C. Broderick, C. R. Harnsberger, J. Langert, J. Nefa, P. Jaureguiberry, P. Gomez, L. Miranda, G. R. Jacobsen, B. J. Sandler, and S. Horgan (2016). "Phase II clinical experience and long-term follow-up using the next-generation single-incision platform FMX314." In: *Surgical Endoscopy* 30.3, pp. 953–960.
- Blankemeyer, S., J. Losensky, J. Peters, and A. Raatz (2017). "Design principles for stiffness adjustment in soft material robotics using layer jamming." In: *International Conference on Engineering Science, and Applications*, pp. 39–56.
- Boron, W. and E. Boulpapep (2009). *Medical physiology: a cellular and molecular approach*. Philadelphia, PA: Saunders/Elsevier.
- Bumiller, H., M. Burgmaier, W. Eichler, B. Feustel, T. Käppel, W. Klee, J. Manderla, O. Reichmann, J. Schwarz, K. Tkotz, and U. Winter (2018). *Fachkunde Elektrotechnik*. Haan-Gruiten, Germany: Verlag Europa Lehrmittel.
- Burgner, J., P. J. Swaney, R. A. Lathrop, K. D. Weaver, and R. J. Webster (2013). "Debulking from within: A robotic steerable cannula for intracerebral hemorrhage evacuation." In: *IEEE Transactions on Biomedical Engineering* 60.9, pp. 2567–2575.
- Burgner-Kahrs, J., D. C. Rucker, and H. Choset (2015). "Continuum Robots for Medical Applications: A Survey." In: *IEEE Transactions on Robotics* 31, pp. 1–20.
- Camarillo, D. B., C. F. Milne, C. R. Carlson, M. R. Zinn, and J. K. Salisbury (2008). "Mechanics modeling of tendon-driven continuum manipulators." In: *IEEE Transactions on Robotics* 24.6, pp. 1262–1273.

- Canes, D., A. Berger, M. Aron, R. Brandina, D. A. Goldfarb, D. Shoskes, M. M. Desai, and I. S. Gill (2010). "Laparo-Endoscopic Single Site (LESS) versus Standard Laparoscopic Left Donor Nephrectomy: Matched-pair Comparison." In: *European Urology* 57.1, pp. 95–101.
- Chang, L., Y. Liu, Q. Yang, L. Yu, J. Liu, Z. Zhu, P. Lu, Y. Wu, and Y. Hu (2018). "Ionic Electroactive Polymers Used in Bionic Robots: A Review." In: *Journal of Bionic Engineering* 15.5, pp. 765–782.
- Cheng, N. G., M. B. Lobovsky, S. J. Keating, A. M. Setapen, K. I. Gero, A. E. Hosoi, and K. D. Iagnemma (2012). "Design and Analysis of a Robust, Low-cost, Highly Articulated manipulator enabled by jamming of granular media." In: *IEEE International Conference on Robotics and Automation*. IEEE, pp. 4328–4333.
- Cheng, N. G., A. Gopinath, L. Wang, K. Iagnemma, and A. E. Hosoi (2014). "Thermally tunable, self-healing composites for soft robotic applications." In: *Macromolecular Materials and Engineering* 299.11, pp. 1279–1284.
- Chikhaoui, M. T., A. Benouhiba, P. Rougeot, K. Rabenoroso, M. Ouisse, and N. Andreff (2018). "Developments and Control of Biocompatible Conducting Polymer for Intracorporeal Continuum Robots." In: *Annals of Biomedical Engineering* 46.10, pp. 1511–1521.
- Cho, E., H.-O. Adami, and P. Lindblad (2011). "Epidemiology of Renal Cell Cancer." In: *Hematology/Oncology Clinics of North America* 25.4, pp. 651–665.
- Choi, I., N. Corson, L. Peiros, E. W. Hawkes, S. Keller, and S. Follmer (2018). "A Soft, Controllable, High Force Density Linear Brake Utilizing Layer Jamming." In: *IEEE Robotics and Automation Letters* 3.1, pp. 450–457.
- Cianchetti, M., T. Ranzani, G. Gerboni, T. Nanayakkara, K. Althoefer, P. Dasgupta, and A. Menciassi (2014). "Soft Robotics Technologies to Address Shortcomings in Today's Minimally Invasive Surgery: The STIFF-FLOP Approach." In: *Soft Robotics* 1.2, pp. 122–131.
- Cooper, T. and C. R. Ramstad (2011). *Sterile drape interface for robotic surgical instrument*. US Patent 7,886,743.
- De Donno, A., L. Zorn, P. Zanne, F. Nageotte, and M. de Mathelin (2013). "Introducing STRAS: A new flexible robotic system for minimally invasive surgery." In: *2013 IEEE International Conference on Robotics and Automation*, pp. 1213–1220.
- Degani, A., H. Choset, A. Wolf, and M. A. Zenati (2006). "Highly articulated robotic probe for minimally invasive surgery." In: *IEEE International Conference on Robotics and Automation* 2006, pp. 4167–4172.
- Ding, J., R. E. Goldman, K. Xu, P. K. Allen, D. L. Fowler, and N. Simaan (2013). "Design and coordination kinematics of an insertable robotic effectors platform for single-port access surgery." In: *IEEE/ASME Transactions on Mechatronics* 18.5, pp. 1612–1624.
- Dolghi, O., K. W. Strabala, T. D. Wortman, M. R. Goede, S. M. Farritor, and D. Oleynikov (2011). "Miniature in vivo robot for laparoendoscopic single-site surgery." In: *Surgical Endoscopy* 25.10, pp. 3453–3458.
- Eickhoff, A., J. van Dam, R. Jakobs, V. Kудis, D. Hartmann, U. Damian, U. Weickert, D. Schilling, and J. Riemann (2007). "Computer-Assisted Colonoscopy (The NeoGuide Endoscopy System): Results of the First Human Clinical Trial ("PACE Study")." In: *The American journal of gastroenterology* 102.2, pp. 261–266.
- Eisenberg, D., E. Storne, and A. Belson (2010). "Use of a flexible robotic transgastric natural orifice transluminal endoscopic surgery (NOTES) platform in a cadaver to test access, navigation, maneuverability, and stability." In: *Surgical Endoscopy* 24.9, p. 2323.

- Epstein, S., E. H. Sparer, B. N. Tran, Q. Z. Ruan, J. T. Dennerlein, D. Singhal, and B. T. Lee (2018). "Prevalence of work-related musculoskeletal disorders among surgeons and interventionalists: A systematic review and meta-analysis." In: *JAMA Surgery* 153.2, pp. 1–13.
- Falahatkar, S., A. Enshaei, A. A. Allahkhan, M. M. Asli, Z. Panahandeh, and N. Okhovatpoor (2010). "Comparison of Open vs Laparoscopic Nephrectomy: Outcomes and Complications." In: *UroToday International Journal* 03.01.
- Ferlay, J., E. Steliarova-Foucher, J. Lortet-Tieulent, S. Rosso, J. W. Coebergh, H. Comber, D. Forman, and F. Bray (2015). "Reprint of: Cancer incidence and mortality patterns in Europe: Estimates for 40 countries in 2012." In: *European Journal of Cancer* 51.9, pp. 1201–1202.
- Garbin, N., C. Di Natali, J. Buzzi, E. De Momi, and P. Valdastrì (2015). "Laparoscopic Tissue Retractor Based on Local Magnetic Actuation." In: *Journal of Medical Devices* 9.1, p. 011005.
- Gerboni, G., P. W. Henselmans, E. A. Arkenbout, W. R. Furth, and P. Breedveld (2015). "HelixFlex : bioinspired maneuverable instrument for skull base surgery." In: *Bioinspiration and Biomimetics* 10.6, p. 66013.
- Haber, G.-P., R. Autorino, H. Laydner, B. Yang, M. White, S. Hillyer, F. Altunrende, R. Khanna, G. Spana, I. Wahib, K. Fareed, R. Stein, and J. Kaouk (2012). "SPIDER Surgical System for Urologic Procedures With Laparoendoscopic Single-Site Surgery: From Initial Laboratory Experience to First Clinical Application." In: *European Urology* 61.2, pp. 415–422.
- Hendrick, R. J., C. R. Mitchell, S. D. Herrell, and R. J. Webster (2015). "Hand-held transendoscopic robotic manipulators: A transurethral laser prostate surgery case study." In: *The International Journal of Robotics Research* 35.14, pp. 1559–1572.
- Henke, M. and G. Gerlach (2016). "A multi-layered variable stiffness device based on smart form closure actuators." In: *Journal of Intelligent Material Systems and Structures* 27.3, pp. 375–383.
- Huang, H., S. Wu, D. Cohen-Or, M. Gong, H. Zhang, G. Li, and B. Chen (2013). "L1-Medial Skeleton of Point Cloud." In: *ACM Trans. Graph.* 32.4, pp. 1–8.
- Hudgens, J. and R. Pasic (2007). *Fundamentals of Geometric Laparoscopy and Suturing*. Tuttingen, Germany: EndoPress GmbH.
- Hwang, M., U. J. Yang, D. Kong, D. G. Chung, J. G. Lim, D. H. Lee, D. H. Kim, D. Shin, T. Jang, J. W. Kim, and D. S. Kwon (2017). "A single port surgical robot system with novel elbow joint mechanism for high force transmission." In: *International Journal of Medical Robotics and Computer Assisted Surgery* 13.4, pp. 1–11.
- Imkamp, F., T. R. Herrmann, J. U. Stolzenburg, J. Rassweiler, T. Sulser, U. Zimmermann, S. Dziuba, M. A. Kuczyk, and M. Burchardt (2014). "Development of urologic laparoscopy in Germany, Austria, and Switzerland: a survey among urologists." In: *World Journal of Urology* 32.6, pp. 1363–1374.
- Jayaraman, S., D. Quan, I. Al-Ghamdi, F. El-Deen, and C. M. Schlachta (2010). "Does robotic assistance improve efficiency in performing complex minimally invasive surgical procedures?" In: *Surgical Endoscopy* 24.3, pp. 584–588.
- Jeong, B., Y. Park, D. Han, and H. Kim (2009). "Laparoendoscopic single-site and conventional laparoscopic adrenalectomy: a matched case-control study." In: *Journal of Endourology* 23.12, pp. 1957–1960.
- Jiang, A., T. Ranzani, G. Gerboni, L. Lekstutyte, K. Althoefer, P. Dasgupta, and T. Nanayakkara (2014). "Robotic Granular Jamming: Does the Membrane Matter?" In: *Soft Robotics* 1.3, pp. 192–201.

- Jones, B. A. and I. D. Walker (2006). "Kinematics for multisection continuum robots." In: *IEEE Transactions on Robotics* 22.1, pp. 43–55.
- Kakar, P., J. Das, P. Roy, and V. Pant (2011). "Robotic invasion of operation theatre and associated anaesthetic issues: A review." In: *Indian journal of anaesthesia* 55, pp. 18–25.
- Kaouk, J. H. and R. K. Goel (2009). "Single-Port Laparoscopic and Robotic Partial Nephrectomy." In: *European Urology* 55.5, pp. 1163–1170.
- Kaouk, J. H., R. K. Goel, G. P. Haber, S. Crouzet, and R. J. Stein (2009). "Robotic single-port transumbilical surgery in humans: Initial report." In: *BJU International* 103.3, pp. 366–369.
- Kaouk, J. H., G. P. Haber, R. Autorino, S. Crouzet, A. Ouzzane, V. Flamand, and A. Villers (2014). "A novel robotic system for single-port urologic surgery: First clinical investigation." In: *European Urology* 66.6, pp. 1033–1043.
- Kim, U., D. H. Lee, W. J. Yoon, B. Hannaford, and H. R. Choi (2015). "Force Sensor Integrated Surgical Forceps for Minimally Invasive Robotic Surgery." In: *IEEE Transactions on Robotics* 31.5, pp. 1214–1224.
- Kim, Y. J., S. Cheng, S. Kim, and K. Iagnemma (2013). "A novel layer jamming mechanism with tunable stiffness capability for minimally invasive surgery." In: *IEEE Transactions on Robotics* 29.4, pp. 1031–1042.
- Kim, Y., S. S. Cheng, and J. P. Desai (2018). "Active Stiffness Tuning of a Spring-Based Continuum Robot for MRI-Guided Neurosurgery." In: *IEEE Transactions on Robotics* 34.1, pp. 1–11.
- Kim, Y., S. S. Cheng, M. Diakite, R. P. Gullapalli, J. M. Simard, and J. P. Desai (2017). "Toward the development of a flexible mesoscale MRI-compatible neurosurgical continuum robot." In: *IEEE Transactions on Robotics* 33.6, pp. 1386–1397.
- Kim, Y. J., S. Cheng, S. Kim, and K. Iagnemma (2014). "A stiffness-adjustable hyperredundant manipulator using a variable neutral-line mechanism for minimally invasive surgery." In: *IEEE Transactions on Robotics* 30.2, pp. 382–395.
- Kitagawa, M., D. Dokko, A. M. Okamura, and D. D. Yuh (2005). "Effect of sensory substitution on suture-manipulation forces for robotic surgical systems." In: *Journal of Thoracic and Cardiovascular Surgery* 129.1, pp. 151–158.
- Kobayashi, Y., Y. Sekiguchi, T. Noguchi, Y. Takahashi, Q. Liu, S. Oguri, K. Toyoda, M. Uemura, S. Ieiri, M. Tomikawa, T. Ohdaira, M. Hashizume, and M. G. Fujie (2015). "Development of a robotic system with six-degrees-of-freedom robotic tool manipulators for single-port surgery." In: *The International Journal of Medical Robotics and Computer Assisted Surgery* 11.2, pp. 235–246.
- Koller, S., D. Ostler, T. Bachinger, M. Eblenkamr, E. Wintermantel, D. Wilhelm, and H. Feußner (2016). "Design, actuation, control and evaluation of a robot-assisted manipulator for minimally invasive surgery." In: *Annual meeting of the German Society for Computer- and Robot-Assisted Surgery*, pp. 117–122.
- Kramer, A. and O. Assadian (2008). *Wallhäufers Praxis der Sterilisation, Antiseptik und Konservierung*. Stuttgart, New York: Thieme Verlag.
- Kundrat, D., A. Schoob, L. A. Kahrs, and T. Ortmaier (2016). "First Study on a Monolithically Manufactured Variable-Length Continuum Robot with Hybrid Actuation." In: *Annual meeting of the German Society for Computer- and Robot-Assisted Surgery*, pp. 87–92.
- Langer, M., E. Amanov, and J. Burgner-Kahrs (2018). "Stiffening Sheaths for Continuum Robots." In: *Soft Robotics* 5.3, pp. 291–303.

- Lee, D. Y., J. Kim, J. S. Kim, C. Baek, G. Noh, D. N. Kim, K. Kim, S. Kang, and K. J. Cho (2015). "Anisotropic Patterning to Reduce Instability of Concentric-Tube Robots." In: *IEEE Transactions on Robotics* 31.6, pp. 1311–1323.
- Lehman, A. C., J. Dumpert, N. A. Wood, L. Redden, A. Q. Visty, S. Farritor, B. Varnell, and D. Oleynikov (2009). "Natural orifice cholecystectomy using a miniature robot." In: *Surgical Endoscopy* 23.2, pp. 260–266.
- Li, C., X. Gu, X. Xiao, C. M. Lim, and H. Ren (2019). "A Robotic System with Multichannel Flexible Parallel Manipulators for Single Port Access Surgery." In: *IEEE Transactions on Industrial Informatics* 15.3, pp. 1678–1687.
- Liatsikos, E., I. Kyriazis, P. Kallidonis, M. Do, A. Dietel, and J. U. Stolzenburg (2012). "Pure single-port laparoscopic surgery or mix of techniques?" In: *World Journal of Urology* 30.5, pp. 581–587.
- Linehan, W. M., P. A. Pinto, G. Bratslavsky, E. Pfaffenroth, M. Merino, C. D. Vocke, J. R. Toro, D. Bottaro, L. Neckers, L. S. Schmidt, and R. Srinivasan (2009). "Hereditary kidney cancer: Unique opportunity for disease-based therapy." In: *Cancer* 115.10, pp. 2252–2261.
- Liu, X., R. Y. Abdolmalaki, T. Zuo, Y. Guan, G. J. Mancini, and J. Tan (2018). "Transformable in Vivo Robotic Laparoscopic Camera with Optimized Illumination System for Single-Port Access Surgery: Initial Prototype." In: *IEEE/ASME Transactions on Mechatronics* 23.4, pp. 1585–1596.
- Ljungberg, B., L. Albiges, et al. (2019). "European Association of Urology Guidelines on Renal Cell Carcinoma: The 2019 Update." In: *European Urology* 75.5, pp. 799–810.
- Ljungberg, B., K. Bensalah, S. Canfield, S. Dabestani, F. Hofmann, M. Hora, M. A. Kuczyk, T. Lam, L. Marconi, A. S. Merseburger, P. Mulders, T. Powles, M. Staehler, A. Volpe, and A. Bex (2015). "EAU Guidelines on Renal Cell Carcinoma: 2014 Update." English. In: *European Urology* 67.5, pp. 913–924. ISSN: 1873-7560.
- Loeve, A. J., O. S. Van De Ven, J. G. Vogel, P. Breedveld, and J. Dankelman (2010). "Vacuum packed particles as flexible endoscope guides with controllable rigidity." In: *Granular Matter* 12.6, pp. 543–554.
- Loeve, A., D. Plettenburg, P. Breedveld, and J. Dankelman (2012). "Endoscope shaft-rigidity control mechanism: "Forguide"." In: *IEEE Transactions on Biomedical Engineering* 59.2, pp. 542–551.
- Mahvash, M. and M. Zenati (2011). "Toward a hybrid snake robot for single-port surgery." In: *2011 Annual International Conference of the IEEE Engineering in Medicine and Biology Society*, pp. 5372–5375.
- Manti, M., V. Cacucciolo, and M. Cianchetti (2016). "Stiffening in Soft Robotics: A Review of the State of the Art." In: *IEEE Robotics Automation Magazine* 23.3, pp. 93–106.
- Matich, S., C. Neupert, A. Kirschniak, H. F. Schlaak, and P. P. Pott (2015). "A new single-port robotic system based on a parallel kinematic structure." In: *IEEE/RSJ International Conference on Intelligent Robots and Systems*, pp. 236–241.
- Mir, M., I. Derweesh, F. Porpiglia, H. Zargar, A. Mottrie, and R. Autorino (2017). "Partial Nephrectomy Versus Radical Nephrectomy for Clinical T1b and T2 Renal Tumors: A Systematic Review and Meta-analysis of Comparative Studies." In: *European Urology* 71.4, pp. 606–617.
- Moses, M. S., M. D. Kutzer, H. Ma, and M. Armand (2013). "A continuum manipulator made of interlocking fibers." In: *Proceedings - IEEE International Conference on Robotics and Automation*, pp. 4008–4015.

- Moura, D. T. H. de, H. Aihara, P. Jirapinyo, G. Farias, K. E. Hathorn, A. Bazarbashi, A. Sachdev, and C. C. Thompson (2019). "Robot-assisted endoscopic submucosal dissection versus conventional ESD for colorectal lesions: outcomes of a randomized pilot study in endoscopists without prior ESD experience (with video)." In: *Gastrointestinal Endoscopy* 90.2, pp. 290–298.
- Netter, F. H. (H. (2019). *Atlas of human anatomy*. Philadelphia, PA: Elsevier.
- Okamura, A., C. Simone, and M. Leary (2004). "Force modeling for needle insertion into soft tissue." In: *IEEE Transactions on Biomedical Engineering* 51.10, pp. 1707–1716.
- Olabi, A. and A. Grunwald (2007). "Design and application of magneto-rheological fluid." In: *Materials & Design* 28.10, pp. 2658–2664.
- Ostrowitz, M. B., D. Eschete, H. Zemon, and G. DeNoto (2009). "Robotic-assisted single-incision right colectomy: early experience." In: *The International Journal of Medical Robotics and Computer Assisted Surgery* 5.4, pp. 465–470.
- Ou, J., L. Yao, D. Tauber, J. Steimle, R. Niiyama, and H. Ishii (2014). "jamSheets." In: *Proceedings of the 8th International Conference on Tangible, Embedded and Embodied Interaction*, pp. 65–72.
- Park, J.-Y., D.-Y. Kim, D.-S. Suh, J.-H. Kim, and J.-H. Nam (2015). "Laparoendoscopic single-site versus conventional laparoscopic surgery for ovarian mature cystic teratoma." In: *Obstetrics & Gynecology Science* 58.4, p. 294.
- Patel, N., C. Seneci, G.-Z. Yang, A. Darzi, and J. Teare (2014). "Flexible platforms for natural orifice transluminal and endoluminal surgery." In: *Endoscopy International Open* 02.02, E117–E123.
- Perretta, S., B. Dallemagne, B. Barry, and J. Marescaux (2013). "The ANUBISCOPE flexible platform ready for prime time: Description of the first clinical case." In: *Surgical Endoscopy* 27.7, p. 2630.
- Peters, B. S., P. R. Armijo, C. Krause, S. A. Choudhury, and D. Oleynikov (2018). "Review of emerging surgical robotic technology." In: *Surgical Endoscopy* 32.4, pp. 1636–1655.
- Petroni, G., M. Niccolini, A. Menciassi, P. Dario, and A. Cuschieri (2013). "A novel intracorporeal assembling robotic system for single-port laparoscopic surgery." In: *Surgical Endoscopy* 27.2, pp. 665–670.
- Prasad, S., S. Prasad, H. S Maniar, C. Chu, R. Schuessler, and R. J Damiano (2004). "Surgical robotics: Impact of motion scaling on task performance." In: *Journal of the American College of Surgeons* 199, pp. 863–8.
- Raman, J., A. Bargodia, and J. Cadeddu (2009). "Single-incision, umbilical laparoscopic versus conventional laparoscopic nephrectomy: a comparison of perioperative outcomes and short-term measures of convalescence." In: *Eur Urol* 55.5, pp. 1198–1204.
- Ranzani, T., M. Cianchetti, G. Gerboni, G. De Falco, Iris and Petroni, and A. Menciassi (2013). "A modular soft manipulator with variable stiffness." In: *Joint Workshop on New Tech. for Comp./Robot Assist. Surg. (CRAS)*, pp. 11–14.
- Ranzani, T., M. Cianchetti, G. Gerboni, I. D. Falco, and A. Menciassi (2016). "A Soft Modular Manipulator for Minimally Invasive Surgery: Design and Characterization of a Single Module." In: *IEEE Transactions on Robotics* 32.1, pp. 187–200.
- Raybourn, J. I., A. Rane, and C. Sundaram (2010). "Laparoendoscopic single-site surgery for nephrectomy as a feasible alternative to traditional laparoscopy." In: *Urology* 75.1, pp. 100–103.

- Reifsnyder, J. E., R. Ramasamy, C. K. Ng, J. DiPietro, B. Shin, S. F. Shariat, J. J. Del Pizzo, and D. S. Scherr (2012). "Laparoscopic and open partial nephrectomy: Complication comparison using the Clavien system." In: *Journal of the Society of Laparoendoscopic Surgeons* 16.1, pp. 38–44.
- Roh, K. S., S. Yoon, Y. Do Kwon, Y. Shim, and Y.-J. Kim (2015). "Single-Port Surgical Robot System with Flexible Surgical Instruments." In: *Lecture Notes in Computer Science (including subseries Lecture Notes in Artificial Intelligence and Lecture Notes in Bioinformatics)*. Vol. 9245. Switzerland: Springer International Publishing, pp. 447–459.
- Roppenecker, D. B., L. Schuster, J. A. Coy, M. F. Traeger, K. Entsfellner, and T. C. Lueth (2014). "Modular body of the multi arm snake-like robot." In: *IEEE International Conference on Robotics and Biomimetics*, pp. 374–379.
- Rosen, J., L. N. Sekhar, D. Glozman, M. Miyasaka, J. Doshier, B. Dellon, K. S. Moe, A. Kim, L. J. Kim, T. Lendvay, Y. Li, and B. Hannaford (2017). "Roboscope: A flexible and bendable surgical robot for single portal Minimally Invasive Surgery." In: *IEEE International Conference on Robotics and Automation*, pp. 2364–2370.
- Rosenblatt, A., R. Bollens, and B. Espinoza Cohen (2008). "Transperitoneal Laparoscopic Partial Nephrectomy." In: *Manual of Laparoscopic Urology*. Berlin, Heidelberg: Springer Berlin Heidelberg, pp. 35–48.
- Rucker, D. C., R. J. Webster, G. S. Chirikjian, and N. J. Cowan (2010). "Equilibrium conformations of concentric-tube continuum robots." In: *International Journal of Robotics Research* 29.10, pp. 1263–1280.
- Sethi, N., M. Gouzos, V. Padhye, E. H. Ooi, A. Foreman, S. Krishnan, and J. C. Hodge (2020). "Transoral robotic surgery using the Medrobotic Flex® system: the Adelaide experience." In: *Journal of Robotic Surgery* 14, pp. 109–113.
- Shang, J., D. P. Noonan, C. Payne, J. Clark, M. H. Sodergren, A. Darzi, and G. Z. Yang (2011). "An articulated universal joint based flexible access robot for minimally invasive surgery." In: *IEEE International Conference on Robotics and Automation*, pp. 1147–1152.
- Shang, J., K. Leibrandt, P. Giataganas, V. Vitiello, C. A. Seneci, P. Wisanuvej, J. Liu, G. Gras, J. Clark, A. Darzi, and G.-Z. Yang (2017). "A Single-Port Robotic System for Transanal Microsurgery—Design and Validation." In: *IEEE Robotics and Automation Letters* 2.3, pp. 1510–1517.
- Shields, J. M., S. B. Bhayani, and L.-M. Su (2017). "Robotic Partial Nephrectomy: Transperitoneal Technique." In: *Atlas of Robotic Urologic Surgery*. Cham: Springer International Publishing, pp. 77–91.
- Shiva, A., A. Stilli, Y. Noh, A. Faragasso, I. D. Falco, G. Gerboni, M. Cianchetti, A. Menciassi, K. Althoefer, and H. A. Wurdemann (2016). "Tendon-Based Stiffening for a Pneumatically Actuated Soft Manipulator." In: *IEEE Robotics and Automation Letters* 1.2, pp. 632–637.
- Simaan, N., R. Taylor, and P. Flint (2004). "A dexterous system for laryngeal surgery." In: *IEEE International Conference on Robotics and Automation*, pp. 351–357.
- Simaan, N., K. Xu, A. Kapoor, W. Wei, P. Kazanzides, P. Flint, and R. Taylor (2009). "Design and Integration of a Telerobotic System for Minimally Invasive Surgery of the Throat." In: *The International Journal of Robotics Research* 28.9, pp. 1134–1153.
- Starke, J., E. Amanov, M. T. Chikhaoui, and J. Burgner-Kahrs (2017). "On the Merits of Helical Tendon Routing in Continuum Robots." In: *IEEE International Conference on Robotics and Automation*, pp. 6470–6476.

- Suzumori, K., S. Wakimoto, K. Miyoshi, and K. Iwata (2013). "Long bending rubber mechanism combined contracting and extending fluidic actuators." In: *IEEE/RSJ International Conference on Intelligent Robots and Systems*, pp. 4454–4459.
- Terry, B. S., Z. C. Mills, J. A. Schoen, and M. E. Rentschler (2012). "Single-port-access surgery with a novel magnet camera system." In: *IEEE Transactions on Biomedical Engineering* 59.4, pp. 1187–1193.
- Thakkar, S., M. Awad, K. C. Gurram, S. Tully, C. Wright, S. Sanan, and H. Choset (2015). "A Novel, New Robotic Platform for Natural Orifice Distal Pancreatectomy." In: *Surgical Innovation* 22.3, pp. 274–282.
- Tonapi, M. M., I. S. Godage, and I. D. Walker (2014). "Next generation rope-like robot for in-space inspection." In: *IEEE Aerospace Conference*, pp. 1–13.
- Tonazzini, A., S. Mintchev, B. Schubert, B. Mazzolai, J. Shintake, and D. Floreano (2016). "Variable Stiffness Fiber with Self-Healing Capability." In: *Advanced Materials* 28.46, pp. 10142–10148.
- Tortora, G., M. Salerno, T. Ranzani, S. Tognarelli, P. Dario, and A. Menciassi (2013). "A modular magnetic platform for natural orifice transluminal endoscopic surgery." In: *Proceedings of the Annual International Conference of the IEEE Engineering in Medicine and Biology Society, EMBS*, pp. 6265–6268.
- Van Poppel, H. L., W. Da Pozzo, V. Albrecht, A. Matveev, A. Bono, M. Borkowski, L. Colombel, E. Klotz, T. Skinner, S. Keane, S. Marreaud, Collette, and R. Sylvester. (2011). "A prospective, randomised EORTC intergroup phase 3 study comparing the oncologic outcome of elective nephron-sparing surgery and radical nephrectomy for low-stage renal cell carcinoma." In: *European Urology* 59.4, pp. 543–552.
- Velanovich, V. (2000). "Laparoscopic vs open surgery: a preliminary comparison of quality-of-life outcomes." In: *Surgical endoscopy* 14, pp. 16–21.
- Vigneswaran, H. (2017). "FlexDex™: A Novel Articulated Laparoscopic Instrument to Perform Renorrhaphy." In: *Experimental Techniques in Urology & Nephrology* 1.2, pp. 3–5.
- Vitiello, V., Su-Lin Lee, T. P. Cundy, and Guang-Zhong Yang (2013). "Emerging Robotic Platforms for Minimally Invasive Surgery." In: *IEEE Reviews in Biomedical Engineering* 6.2, pp. 111–126.
- Wall, V., R. Deimel, and O. Brock (2015). "Selective stiffening of soft actuators based on jamming." In: *Proceedings - IEEE International Conference on Robotics and Automation*, pp. 252–257.
- Wang, J., S. Wang, J. Li, X. Ren, and R. M. Briggs (2018). "Development of a novel robotic platform with controllable stiffness manipulation arms for laparoendoscopic single-site surgery (LESS)." In: *The International Journal of Medical Robotics and Computer Assisted Surgery* 14.1, e1838.
- Webster, R. J. I. and B. A. Jones (2010). "Design and Kinematic Modeling of Constant Curvature Continuum Robots: A Review." In: *The International Journal of Robotics Research* 29.13, pp. 1661–1683.
- Wortman, T. D., J. M. Mondry, S. M. Farritor, and D. Oleynikov (2013). "Single-site colectomy with miniature in vivo robotic platform." In: *IEEE Transactions on Biomedical Engineering* 60.4, pp. 926–929.
- Xu, K., J. Zhao, and M. Fu (2015). "Development of the SJTU Unfoldable Robotic System (SURS) for Single Port Laparoscopy." In: *IEEE/ASME Transactions on Mechatronics* 20.5, pp. 2133–2145.

- Yamashita, H., S. Zuo, K. Masamune, H. Liao, and T. Dohi (2009). "Nonmagnetic rigid and flexible outer sheath with pneumatic interlocking mechanism for minimally invasive surgical approach." In: *Lecture Notes in Computer Science (including subseries Lecture Notes in Artificial Intelligence and Lecture Notes in Bioinformatics)* 5761 LNCS.PART 1, pp. 418–425.
- Yanagida, T., K. Adachi, and T. Nakamura (2013). "Development of endoscopic device to veer out a latex tube with jamming by granular materials." In: *IEEE International Conference on Robotics and Biomimetics*, pp. 1474–1479.
- Yoshiki, N. (2016). "Single-incision laparoscopic myomectomy: A review of the literature and available evidence." In: *Gynecology and Minimally Invasive Therapy* 5.2, pp. 54–63.
- Yufei, H., W. Tianmiao, F. Xi, Y. Kang, M. Ling, G. Juan, and W. Li (2017). "A variable stiffness soft robotic gripper with low-melting-point alloy." In: *36th Chinese Control Conference*, pp. 6781–6786.
- Yung, K. L., J. L. Cheung, S. W. Chung, S. Singh, and C. K. Yeung (2017). "A Single-Port Robotic Platform for Laparoscopic Surgery with a Large Central Channel for Additional Instrument." In: *Annals of Biomedical Engineering* 45.9, pp. 2211–2221.

Part VI

APPENDIX

A

ANATOMICAL ABDOMINAL SPACES

This appendix provides the complete collected anatomical patient data. The top four data sets in Figure 80 show the data used for the optimization in chapter 9. The bottom 5 show abdominal spaces which are not utilized for any evaluations or optimizations, but were collected during this thesis. Corresponding volumes and areas of the region of interest are given. Possible target points and incision locations were defined, such that the data can be used for further optimizations or validations.

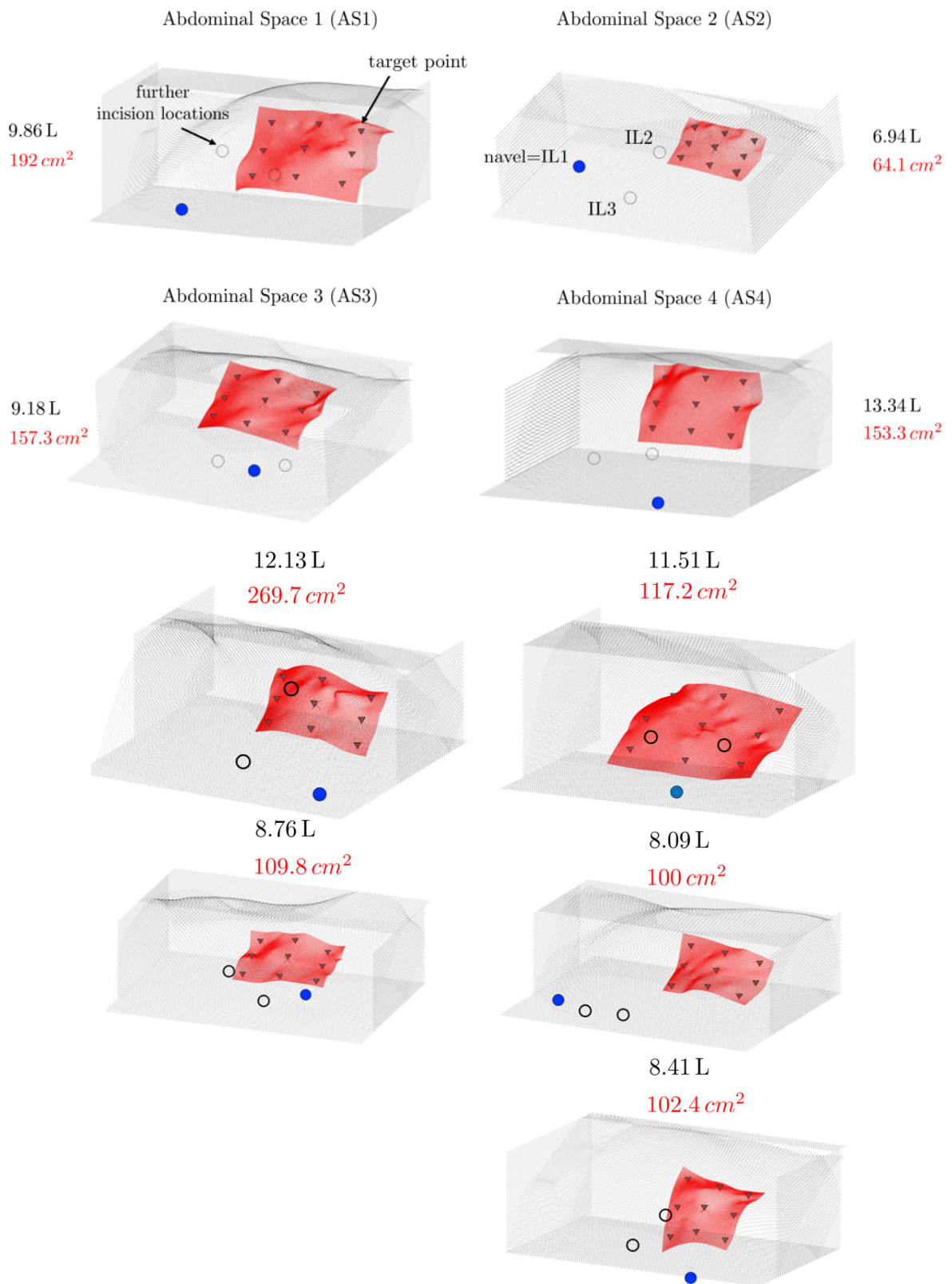


Figure 80: Patient data sets showing their region of interest and selected target points. Data sets with blue incision location (navel); Top 4 data sets are used for the optimization; 5 bottom data sets were not used in this thesis.

B

DESIGN OPTIMIZATION RESULTS

In this appendix, further design optimization results are provided. For each two-segment and three-segment optimization, two additional runs were performed, first to find a better design and second to evaluate the convergence of the algorithm. Each of the results has been validated as described in the design optimization chapter 9. The results shown here were inferior to the utilized results but should be presented to empower the stated observations in the main work, such as the negative effect of the greater distance to the target area. Figure 81 shows the results for a two segment design and Figure 83 shows the results for a three segment design.

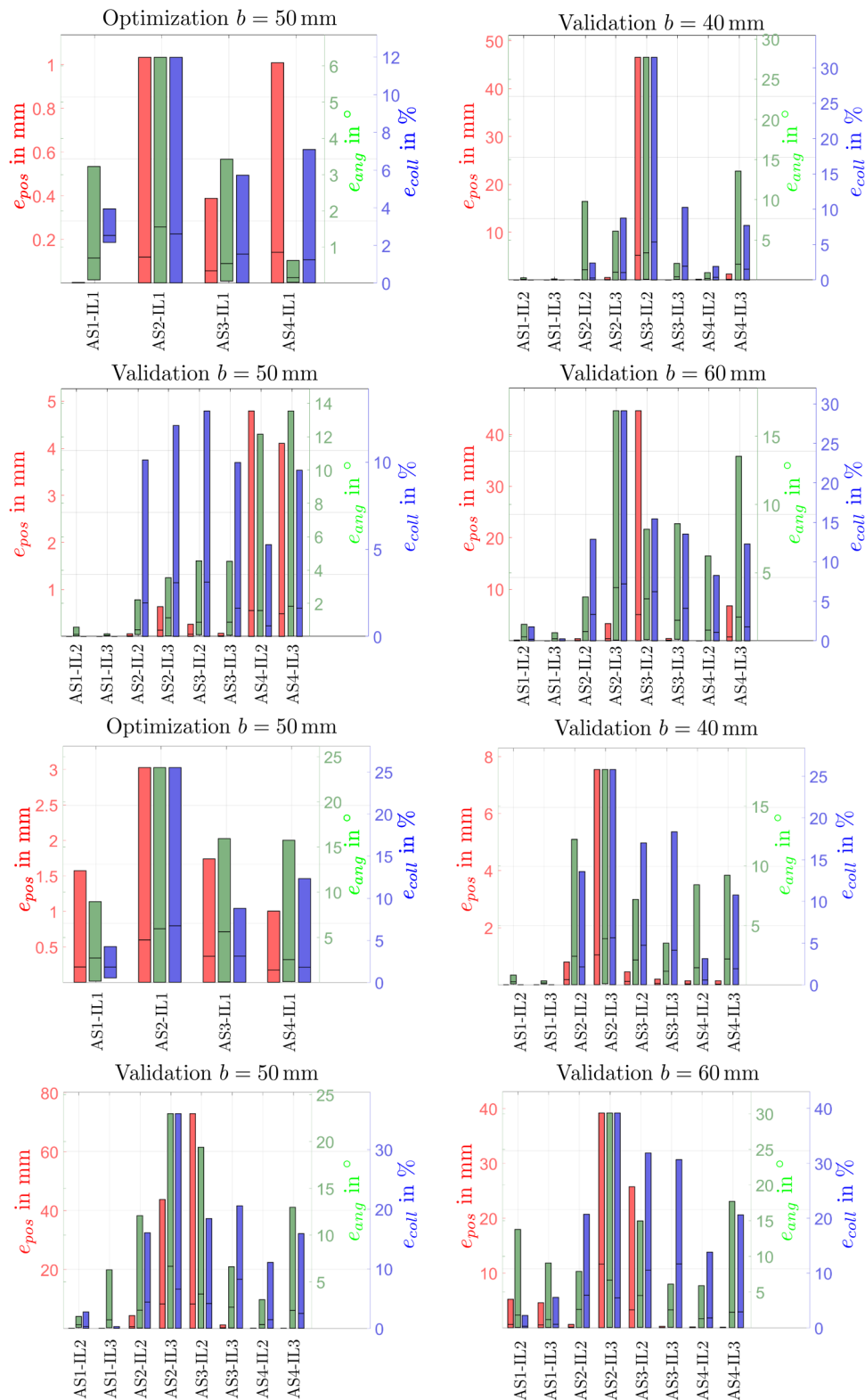


Figure 81: Results of the two-segment design optimization and validation showing all three objective errors as box plots for different distances to target points, b . AS = Abdominal Space, IL = Incision Location, Index is according to Figure 52; Top: First optimization run, $l_1 = 344.5$ mm, $l_2 = 60.3$ mm; Bottom: Second optimization run, $l_1 = 321.8$ mm, $l_2 = 101.5$ mm.

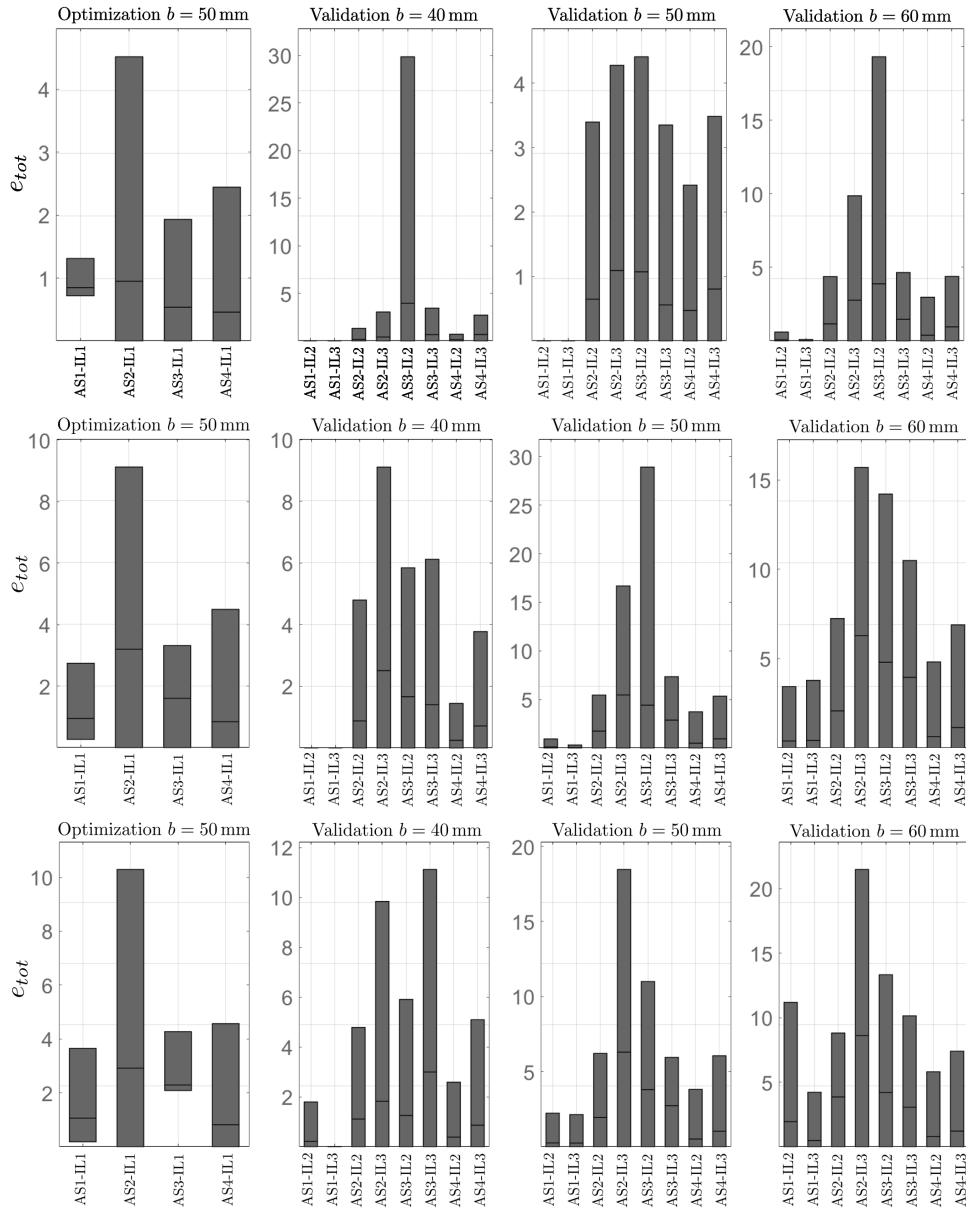


Figure 82: Results of the two-segment design optimization and validation showing the total errors ϵ_{tot} as box plots for different distances to target points, b . AS = Abdominal Space, IL = Incision Location, Index is according to Figure 52; Top: First optimization run; Middle: Second optimization run; Bottom: Third optimization run.

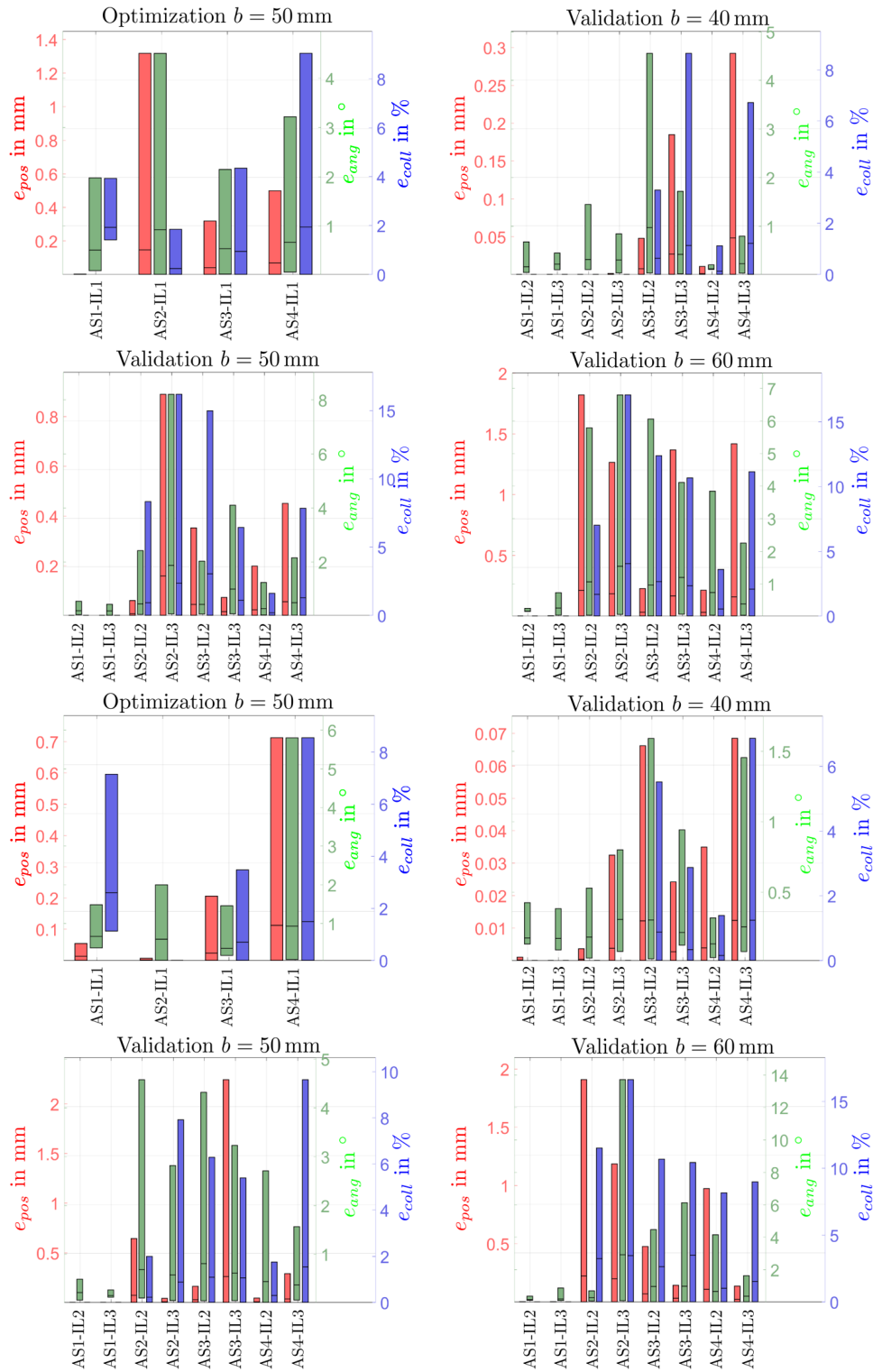


Figure 83: Results of the three-segment design optimization and validation showing all three objective errors as box plots for different distances to target points, b . AS = Abdominal Space, IL = Incision Location, Index is according to Figure 52; Top: First optimization run, $l_1 = 382.6$ mm, $l_2 = 68.6$ mm, $l_3 = 74.1$ mm; Bottom: Second optimization run, $l_1 = 355.4$ mm, $l_2 = 80$ mm, $l_3 = 28.9$ mm.

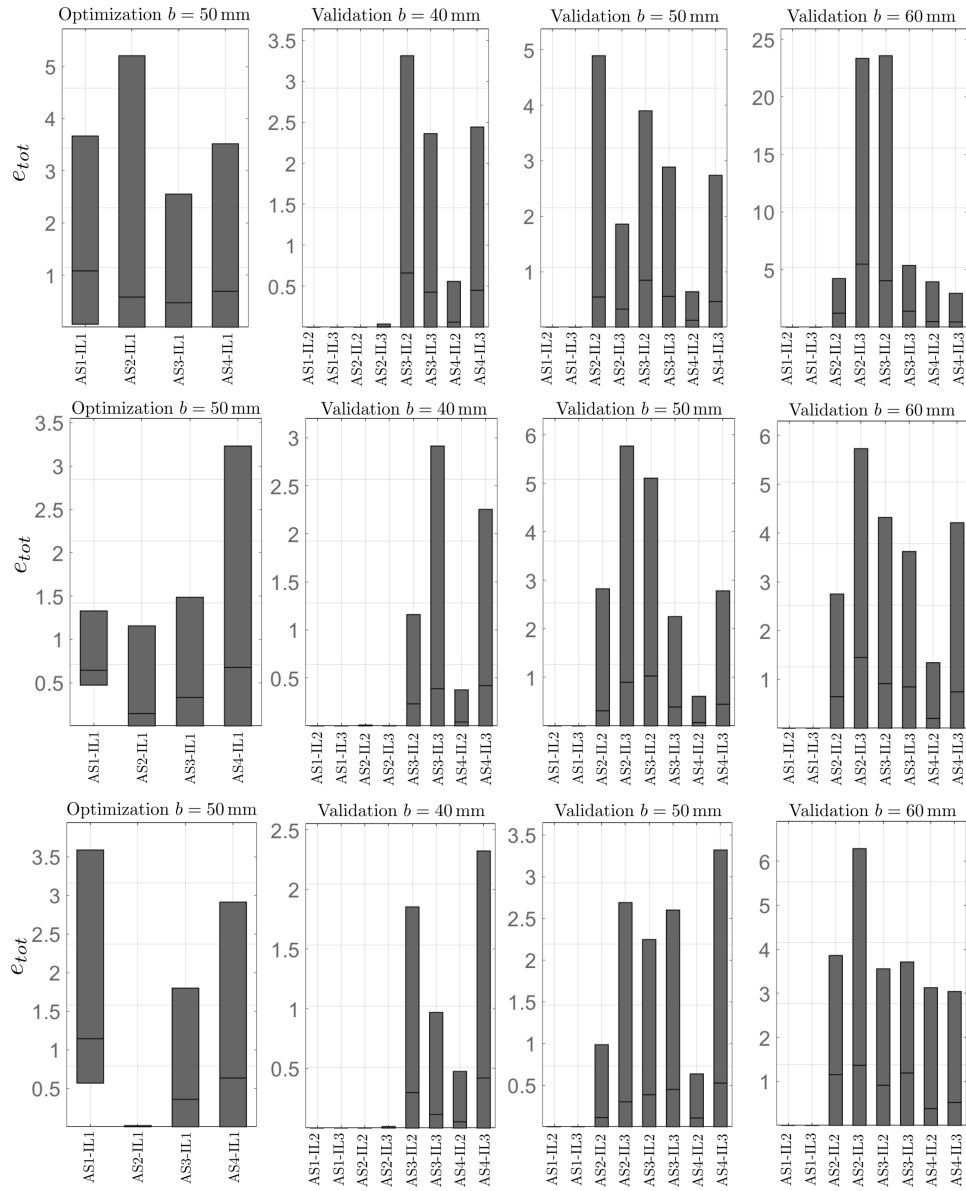


Figure 84: Results of the three-segment design optimization and validation showing the total errors e_{tot} as box plots for different distances to target points, b . AS = Abdominal Space, IL = Incision Location, Index is according to Figure 52; Top: First optimization run; Middle: Second optimization run; Bottom: Third optimization run.

DETAILED PROTOTYPE PARAMETERS

This Appendix shows a summary of manipulator prototypes. Table 14 shows the parameters of the stiffening manipulator designs: Prototype 2, Prototype 3a-c. In Table 15, the manipulator prototype design details of the detachable articulated port are summarized.

Table 14: Detailed design parameters of Prototype 2 and Prototype 3 variations.

Prototype	Prototype 2	Prototype 3a	Prototype 3b	Prototype 3c
Number of segments n	1	2	2	2
Spacer disk diameter d in mm	21	23	23	23
Segment length l_j in mm	150	240	240	240
Large working channel diameter D_w in mm	-	8	8	8
Small working channel diameter d_w in mm	-	4	4	4
Tendon routing channel diameter d_{ct} in mm	0.5	1.5	1.5	1.5
Tendon routing radius r_t in mm	9	9.5	9.5	9.5
OD backbone d_b in mm	0.7	1	1	1
OD secondary backbone d_{bs} in mm	0.4	-	-	-
Disk thickness b in mm	2	3	3	3
End disk thickness in mm	2	6	6	6
Distance of disks in mm	15	24	24	24
Number of disks	10	10	10	10

Table 15: Manipulator prototype parameters of the detachable articulated port.

Parameter	Clinical Use Case Prototype
Number of segments n	3
Segment length l_j in mm	150/63.4/56.3
Large working channel diameter D_w in mm	8
Small working channel diameter d_w in mm	4
Tendon routing channel diameter d_{ct} in mm	0.5
Spacer disk diameter d in mm	21
Tendon routing radius r_t	9
OD backbone in d_b mm	0.7
Disk thickness b in mm	2
End disk thickness in mm	3
Number of disks	10/3/3

D

EVALUATION RESULTS

D.1 REACHABILITY RESULTS

In this Appendix the reachability results using the second incision locations are shown. Figure 85 shows the side view into the abdomen phantom in the top images and the internal camera unit view in the bottom images. The region of interest (RoI) does not include the numbering of different sub RoI. However, the top images show that all regions can be accessed.

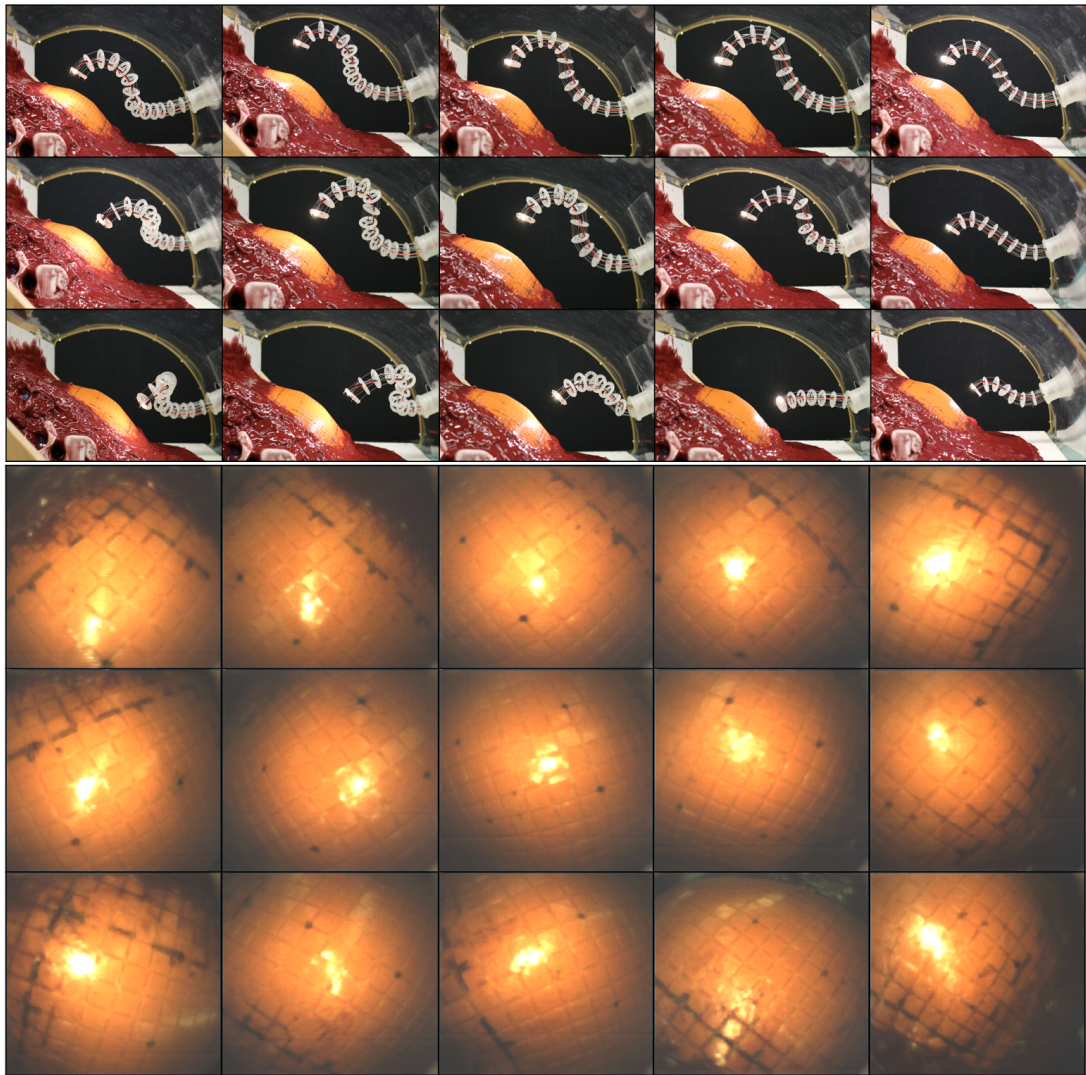


Figure 85: Reachability investigation results through further incision locations: top images show the side view from outside the abdomen; bottom images show the on tip camera view.

D.2 STABILITY RESULTS

This Appendix shows the detailed stability results. In Figure 86, the errors during each transition state and the overall error are shown for each established configuration.

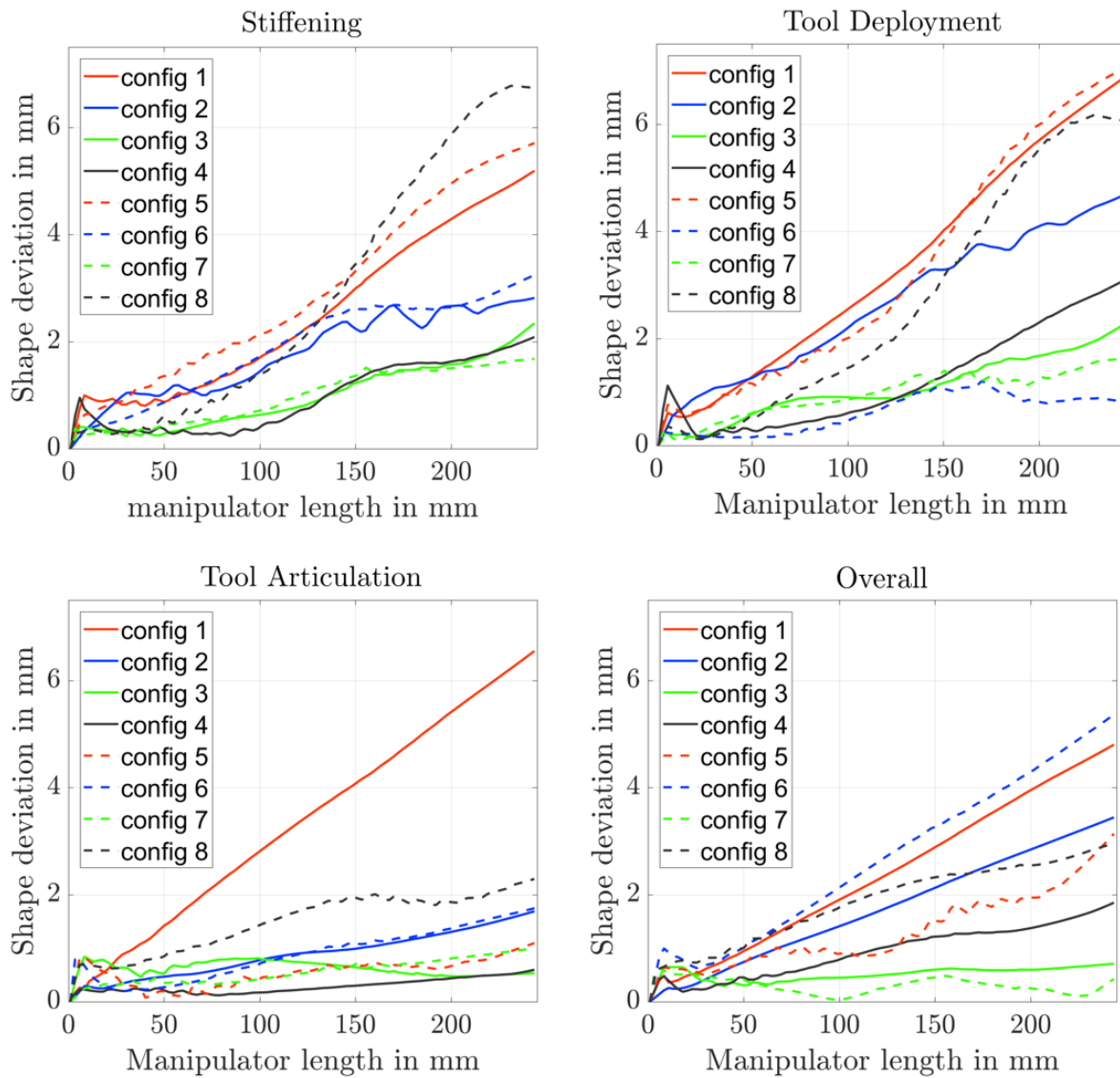


Figure 86: Shape deviation shift results of eight configurations for the three transitions and overall deviation. The dashed lines correspond to s-shapes with higher curvatures.

E

REPRINT PERMISSIONS

Table 16 lists all figures in this work that have been reproduced from third-party publications. Corresponding licenses from the Copyright Clearance Center Inc., if applicable, are provided.

Table 16: Figures reproduced from third-party publications, corresponding publishers, and licenses, if applicable.

Figure	Publication	Publisher	License
1	Netter, 2019	Elsevier	4913340987726
8d	Berducci et al., 2016	Springer Nature	4894460095268
12c	Hwang et al., 2017	John Wiley & Sons	4894461140018
14a	Xu et al., 2015	IEEE	-
14b	Wang et al., 2018	John Wiley & Sons	4894431348594
14c	Kobayashi et al., 2015	John Wiley & Sons	4894440753790
14d	Yung et al., 2017	Springer Nature	4894450495126
14e	Matich et al., 2015	IEEE	-
14f	Hendrick et al., 2015	SAGE	-
16a	Y. J. Kim et al., 2013	IEEE	-
16b	Roppenecker et al., 2014	IEEE	-
16c	Shang, Noonan, et al., 2011	IEEE	-
16d	Roh et al., 2015	Spring Nature	4894480649963
16e	Cianchetti et al., 2014	Mary Ann Liebert, Inc.	-
16f	Rosen et al., 2017	IEEE	-
17a	Tortora et al., 2013	IEEE	-
17b	Lehman et al., 2009	Spring Nature	4894480175637
32	Y. J. Kim et al., 2013	IEEE	-

CURRICULUM VITAE

PERSONAL DATA

name: Ernar Amanov
date of birth: September 5, 1986
place of birth: Karaganda, Kazakhstan
email address: ernar.amanov@gmail.com

WORK EXPERIENCE

11/2019 – PRESENT **Postdoctoral Researcher**, *Medical Engineering and Discovery Laboratory, Mechanical Engineering*, Vanderbilt University, Nashville, TN, USA
11/2014 – 04/2019 **Research Assistant**, *Laboratory for Continuum Robotics, Mechanical Engineering*, Leibniz Universität Hannover, Germany
04/2014 – 07/2014 **Student Research Assistant**, *Emmy Noether Research Group CROSS*, Leibniz Universität Hannover, Germany
07/2010 – 09/2010 **Intern**, *Department of Diesel Systems*, Bosch Automotive Diesel Systems Co., Ltd., Wuxi, China
01/2009 – 04/2009 **Intern**, *Driver Assistance Systems*, Bosch Automotive Diesel Systems Co., Ltd., Leonberg, Germany

EDUCATION

10/2011 – 09/2014 **Masters in Mechatronics**, *M.Sc.*, Leibniz Universität Hannover, Germany
10/2008 – 09/2011 **Bachelors in Mechatronics**, *B.Eng.*, Robert Bosch GmbH & Baden-Wuerttemberg Cooperative State University (DHBW) Stuttgart, Germany
06/2007 **Abitur**, *Mörike-Gymnasium*, Ludwigsburg, Germany

AWARDS

06/2018 **Best Oral Presentation Award Runner Up**, *12. Nordkongress Urologie*, F. Imkamp, E. Amanov, T.-D. Nguyen, V. Hielscher, J. Burgner-Kahrs, Die

systematische Ermittlung des chirurgischen Arbeitsraumes im Rahmen laparoskopischer Niereneingriffe: Grundlage für die Konzeptionierung eines versteifbaren Endoportsystems für die Single-Port Laparoskopie.

- 07/2017 **Best Poster Presentation Award Runner Up**, *The Hamlyn Symposium on Medical Robotics*, E. Amanov, T.-D. Nguyen, F. Imkamp, J. Burgner-Kahrs, First Results on a Flexible Variable Stiffness Endoport for Single-Site Partial Nephrectomy.
- 09/2016 **Travel Award**, *Annual Conference of the German Society for Computer- and Robot-Assisted Surgery e.V.*, Top 30% of the Paper Ranking
- 09/2015 **Travel Award**, *Annual Conference of the German Society for Computer- and Robot-Assisted Surgery e.V.*, Top 30% of the Paper Ranking

-
- Amanov, E. and J. Burgner-Kahrs (2015). "General and Application Specific Accuracy Investigations for Concentric Tube Continuum Robots." In: *Annual meeting of the German Society for Computer- and Robot-Assisted Surgery*, pp. 3–8.
- Amanov, E. and J. Burgner-Kahrs (2016). "Towards Universal Continuum Manipulators." In: *28th Conference of the international Society for Medical Innovation and Technology*, p. 82.
- Amanov, E., J. Granna, and J. Burgner-Kahrs (2017). "Toward Improving Path Following Motion: Hybrid Continuum Robot Design." In: *IEEE International Conference on Robotics and Automation*, pp. 4666–4672.
- Amanov, E., F. Imkamp, and J. Burgner-Kahrs (2016). "Initial Investigations toward a Flexible Variable Stiffness Single Port System for Partial Nephrectomy." In: *Annual meeting of the German Society for Computer- and Robot-Assisted Surgery*, pp. 93–98.
- Amanov, E., T.-D. Nguyen, and J. Burgner-Kahrs (2015). "Additive manufacturing of patient-specific tubular continuum manipulators." In: *Medical Imaging 2015: Image-Guided Procedures, Robotic Interventions, and Modeling Vol. 9415*, 94151P1.
- Amanov, E., T.-D. Nguyen, and J. Burgner-Kahrs (2016). "METABot - Magnetic Extensible Tendon Actuated Continuum Robot." In: *DGR Days (German Society of Robotics)*.
- Amanov, E., T.-D. Nguyen, and J. Burgner-Kahrs (2019). "Tendon-driven Continuum Robots with Extensible Sections - A Model-based Evaluation of Path Following Motions." In: *International Journal of Robotics Research Online First*.
- Amanov, E., T.-D. Nguyen, F. Imkamp, and J. Burgner-Kahrs (2017). "First Results on a Flexible Variable Stiffness Endoport for Single-Site Partial Nephrectomy." In: *10th Hamlyn Symposium on Medical Robotics 2017*, pp. 91–92.
- Amanov, E., T.-D. Nguyen, S. Markmann, F. Imkamp, and J. Burgner-Kahrs (2018). "Toward a Flexible Variable Stiffness Endoport for Single-Site Partial Nephrectomy." In: *Annals of Biomedical Engineering* 46.10, pp. 1498–1510.
- Imkamp, F., E. Amanov, T.-D. Nguyen, V. Hielscher, and J. Burgner-Kahrs (2018). "Die systematische Ermittlung des chirurgischen Arbeitsraumes im Rahmen laparoskopischer Niereneingriffe: Grundlage für die Konzeptionierung eines versteifbaren Endoportsystems für die Single-Port Laparoskopie." In: *12. Nordkongress Urologie*.
- Langer, M., E. Amanov, and J. Burgner-Kahrs (2018). "Stiffening Sheaths for Continuum Robots." In: *Soft Robotics* 5.3, pp. 291–303.
- Nguyen, T.-D., E. Amanov, and J. Burgner-Kahrs (Nov. 28, 2018). *Schaftmechanismus*. Application DE 10 2018 130 074.3.

- Andrae, V. (2017). "Konzept für einen miniaturisierten seilzug-aktuierten Kontinuumsroboter mit integrierter Strukturversteifung durch schichtweise Verklebung." Master's Thesis. Leibniz Universität Hannover.
- Boos, A. (2017). "Untersuchung von limitierenden Faktoren für die Miniaturisierung einer Aktuierungseinheit für tubuläre Kontinuumsroboter." Bachelor's Thesis. Leibniz Universität Hannover.
- Börger, D. (2017). "Konstruktion und Ansteuerung eines kostengünstigen mobilen hyperredundanten Schlangen-Roboters." Bachelor's Thesis. Leibniz Universität Hannover.
- Brinschwitz, D. (2019). "Konstruktion und Zusammenbau einer Kupplung zwischen einem flexiblen Endoport und einer Aktuierungseinheit für laparoskopische Eingriffe." Student Work. Leibniz Universität Hannover.
- Eberwein, M. (2015). "Kraftmessung entlang der Struktur eines tubulären Kontinuumsroboters." Master's Thesis. Leibniz Universität Hannover.
- Genc, C. (2018). "Konstruktion und Zusammenbau einer kompakten Aktuierungseinheit für seilzug-aktuierte Kontinuumsroboter." Bachelor's Thesis. Leibniz Universität Hannover.
- Hakim, S. (2018). "Modellierung eines flexiblen Endoport mit integrierten Arbeitskanälen und Steifigkeitsmechanismen." Master's Thesis. Leibniz Universität Hannover.
- Heilemann, F. (2017). "Miniaturization and evaluation of a manually actuated, statically balanced, continuous tool for medical applications." Bachelor's Thesis. Leibniz Universität Hannover.
- Hielscher, V. (2017). "Designoptimierung eines seilzug-aktuierten Kontinuumsroboters für die partielle Single-Port Nephrektomie." Master's Thesis. Leibniz Universität Hannover.
- Langer, M. (2017). "Konstruktion einer versteifbaren Ummantelung für Kontinuumsroboter für die minimalinvasive Chirurgie." Master's Thesis. Leibniz Universität Hannover.
- Mao, J. (2015). "Control of Tendon-driven Continuum Robots with Variable Section Lengths using Low-cost Hardware." Master's Thesis. Leibniz Universität Hannover.
- Markmann, S. (2017). "Design und Fertigung eines flexiblen und versteifbaren Führungskanals mit granularer Verklebung." Bachelor's Thesis. Leibniz Universität Hannover.
- Müller, H. (2018). "Modellierung der Versteifung von Layer Jamming." Project Work. Leibniz Universität Hannover.
- Neumann, M. (2015). "Kinematische Modellierung und Bewegungserzeugung für seilzugaktuierte Manipulatoren mit variabler Segmentlänge." Master's Thesis. Leibniz Universität Hannover.
- Starke, J. (2016). "Untersuchung des Arbeitsraumes und der Bewegungsabläufe seilzug-aktuierter Kontinuumsroboter mit variablen Seilführungsverläufen." Master's Thesis. Leibniz Universität Hannover.